Intrication en modes spatiaux dans des circuits photoniques semiconducteurs

Arnault Raymond

Université Paris Cité

École Doctorale 564
Physique en Île-de-France

Laboratoire
Matériaux et Phénomènes Quantiques

Spatial mode entanglement in semiconductor photonic circuits

Par
Arnault RAYMOND

Thèse de doctorat de Physique

Dirigée par Florent Baboux et Sara Ducci

Présentée et soutenue publiquement le 22/03/2023,
devant le jury composé de :

Florent Baboux	MCF	Univ. Paris Cité	Directeur de thèse
Kamel Bencheikh	CR	CNRS/Univ. Paris-Saclay	Rapporteur
Yaron Bromberg	PR	Hebrew Univ. Jerusalem	Rapporteur
Iacopo Carusotto	PR	Univ. de Trento	Examinateur
Sara Ducci	PR	Univ. Paris Cité	Directrice de thèse
Valia Voliotis	PR	Sorbonne Université	Examinatrice

Table of contents

Abstract

English

Spatial mode entanglement in semiconductor photonic circuits

Keywords: *Quantum information, integrated quantum photonics, nonlinear optics, photonic circuits, entanglement, parametric fluorescence, semiconductors, quantum simulation, quantrum metrology.*

In the last decades, the theoretical and technological developments of quantum mechanics have led to the emergence of a new research field: quantum information science. It directly exploits the peculiarities of quantum phenomena, such as superposition and entanglement, as a resource to develop new functionalities and reach performances unattainable with classical physics. Quantum information is structured into four different axes defined for the future applications of quantum information technologies: quantum computing, i.e. the use of quantum properties to achieve better complexity scaling of algorithms over their classical counterparts, quantum simulation, which exploits well-controlled quantum systems to simulate the properties of more complex and inaccessible systems, quantum metrology, where the high sensitivity of quantum systems to perturbations is harnessed to improve the precision of measurements, and quantum communication, aiming at the realization of secure information transmission. The constraining requirements for the implementation of quantum information protocols have led to the selection of several promising physical platforms, including in particular atomic systems, electronic spins, superconducting qubits and photons. Photons are particularly attractive for their propagation speed, robustness to decoherence, and large variety of degrees of freedom to encode information. In particular, high-dimensional photonic degrees of freedom, such as frequency or spatial modes, provide novel possibilities for quantum information, from fundamental tests of quantum mechanics to enhanced computation and communication protocols. In addition, optical systems have benefited in the recent years from the technological developments of photonic circuits, allowing the implementation of compact and scalable architectures for the generation, manipulation and detection of quantum states of light. In this context, the III-V semiconductor material AlGaAs, with its high second-order nonlinearity, mature fabrication technology, high electro-optic effect and integrability with superconducting nanowire single-photon detectors, is a promising candidate for the realization of integrated quantum photonic circuits in a scalable manner.

In this thesis, we demonstrate photon pair sources based on parametric fluorescence in AlGaAs photonic devices allowing to generate high-dimensional quantum states, entangled in frequency and in spatial modes.

The first investigated source employs a transverse pump geometry in a single waveg-

uide, offering the possibility to engineer the quantum state of the generated photon pairs in the frequency degree of freedom through the spatial shaping of the pump beam. We exploit it to demonstrate control over the exchange statistics of the generated biphotons.

The second demonstrated device is based on an array of evanescently coupled nonlinear waveguides, pumped in a copropagating geometry, where the generated photons can hop from waveguide to waveguide, thus implementing quantum random walks. This leads to the generation of spatially entangled states that are reconfigurable through the spatial profile of the pump beam and the parameters of the array. The photons are generated directly within the device and the generation can take place at any position along the propagation axis, leading to an increased compacity and a higher level of spatial entanglement, while opening the way to the implementation of on-chip quantum simulation tasks.

The two demonstrated devices operate at room temperature and telecom wavelength, enabling long-distance transmission of the generated photon pairs. They present a strong potential for integration within more complex AlGaAs photonic circuits, and are thus promising candidates for the all-integrated implementation of quantum information protocols on photonic chips.

Français

Intrication en modes spatiaux dans des circuits photoniques semiconducteurs

Mots-clés: *Information quantique, photonique quantique intégrée, optique non-linéaire, circuits photoniques, intrication, fluorescence paramétrique, semi-conducteurs, simulation quantique, métrologie quantique.*

Au cours des dernières décennies, les développements théoriques et technologiques de la mécanique quantique ont conduit à l'émergence d'un nouveau domaine de recherche, l'information quantique, qui exploite directement les particularités des phénomènes quantiques - comme la superposition et l'intrication - pour développer de nouvelles fonctionnalités et atteindre des performances inaccessibles aux systèmes classiques. Le champ de l'information quantique est structuré en quatre axes principaux : le calcul quantique, qui vise une meilleure scalabilité de la complexité des algorithmes, la simulation quantique, qui exploite des systèmes quantiques bien contrôlés pour simuler les propriétés et les comportements de systèmes complexes, la métrologie quantique, où la haute sensibilité des systèmes quantiques est exploitée pour améliorer la précision des mesures, et la communication quantique, qui vise à réaliser une transmission sécurisée d'information.

Les contraintes pour la mise en oeuvre des protocoles d'information quantique ont conduit à la sélection de plusieurs plateformes physiques prometteuses, comme les systèmes atomiques, les spins électroniques, les qubits supraconducteurs et les photons. Les photons sont particulièrement attractifs de par leur vitesse de propagation, leur robustesse à la décohérence et leur grande variété de degrés de liberté pour encoder l'information. En particulier, les degrés de liberté photoniques de haute dimension, comme la fréquence ou les modes spatiaux, offrent de nouvelles possibilités pour l'information quantique, pour des tests fondamentaux de la mécanique quantique comme pour des protocoles de cal-

cul et de communication améliorés. En outre, les systèmes optiques ont bénéficié ces dernières années des développements technologiques des circuits photoniques, permettant la réalisation de plateformes compactes pour la génération, la manipulation et la détection d'états quantiques de lumière. Dans ce contexte, le semi-conducteur AlGaAs, grâce à sa forte non-linéarité du second ordre, sa maturité technologique, son effet électro-optique élevé et son intégrabilité avec des détecteurs de photons uniques sur puce, est un candidat prometteur pour la réalisation de circuits photoniques quantiques intégrés.

Cette thèse étudie des sources de paires de photons basées sur la fluorescence paramétrique dans des dispositifs photoniques AlGaAs permettant de générer des états quantiques de haute dimension, intriqués en fréquence et en modes spatiaux.

La première source étudiée utilise une géométrie de pompe transverse dans un guide d'ondes, permettant de modifier l'état quantique en fréquence des paires de photons par la mise en forme spatiale du faisceau de pompe. Nous l'exploitons pour démontrer la possibilité de contrôler la statistique d'échange des biphotons générés.

Le second dispositif est basé sur un réseau de guides d'ondes non linéaires couplés de manière évanescente, pompés dans une géométrie colinéaire, où les photons générés peuvent sauter d'un guide à l'autre, implémentant des marches quantiques aléatoires. Cette configuration permet la génération d'états intriqués spatialement et reconfigurables via le contrôle du faisceau de pompe ou des paramètres du réseau. Les photons sont générés directement dans le dispositif et la génération peut avoir lieu à n'importe quelle position selon l'axe de propagation, permettant d'augmenter la compacité et le niveau d'intrication spatiale tout en ouvrant la voie à des expériences de simulation quantique sur puce.

Les deux dispositifs développés fonctionnent à température ambiante et aux longueurs d'onde télécom, compatibles avec une transmission longue-distance des états générés. Ils présentent un fort potentiel d'intégration dans des circuits photoniques AlGaAs plus complexes, et sont donc des candidats prometteurs pour la mise en oeuvre de protocoles d'information quantique intégrés sur puce.

Résumé long

Au cours des dernières décennies, les développements théoriques et technologiques de la mécanique quantique ont conduit à l'émergence d'un nouveau domaine de recherche, l'information quantique, qui exploite directement les particularités des phénomènes quantiques - comme la superposition et l'intrication - pour développer de nouvelles fonctionnalités et atteindre des performances inaccessibles aux systèmes classiques. Le champ de l'information quantique est structuré en quatre axes principaux : le calcul quantique, qui vise une amélioration de la complexité des algorithmes, la simulation quantique, qui exploite des systèmes quantiques bien contrôlés pour simuler les propriétés et les comportements de systèmes complexes, la métrologie quantique, où la haute sensibilité des systèmes quantiques est exploitée pour améliorer la précision des mesures, et la communication quantique, qui vise à réaliser une transmission sécurisée d'information.

Les contraintes pour la mise en œuvre des protocoles d'information quantique ont conduit à la sélection de plusieurs plateformes physiques prometteuses, comme les systèmes atomiques, les spins électroniques, les qubits supraconducteurs et les photons. Les photons sont particulièrement attractifs de par leur vitesse de propagation, leur robustesse à la décohérence et leur grande variété de degrés de liberté pour encoder l'information. En particulier, les degrés de liberté photoniques de haute dimension, comme la fréquence ou les modes spatiaux, offrent de nouvelles possibilités pour l'information quantique, pour des tests fondamentaux de la mécanique quantique comme pour des protocoles de calcul et de communication améliorés. En outre, les systèmes optiques ont bénéficié ces dernières années des développements technologiques des circuits photoniques, permettant la réalisation de plateformes compactes pour la génération, la manipulation et la détection d'états quantiques de lumière. Dans ce contexte, le semi-conducteur AlGaAs, grâce à sa forte non-linéarité du second ordre, sa maturité technologique, son effet électro-optique élevé et son intégrabilité avec des détecteurs de photons uniques sur puce, est un candidat prometteur pour la réalisation de circuits photoniques quantiques intégrés.

Cette thèse étudie des sources de paires de photons basées sur la fluorescence paramétrique dans des dispositifs photoniques AlGaAs permettant de générer des états quantiques de haute dimension, intriqués en fréquence et en modes spatiaux.

Dans un premier temps, nous décrivons le processus de fluorescence paramétrique dans des matériaux non-linéaires, permettant de générer des paires de photons intriquées à partir de la conversion de photons à fréquences visibles en paires de photons à fréquences télécom. Nous donnons d'abord une description théorique classique des processus optiques non-linéaires pour introduire la notion d'accord de phase, avant d'utiliser cette notion dans la description quantique de la fluorescence paramétrique pour décrire l'état quantique des paires de photons générées. Nous présentons ensuite deux géométries différentes pour réaliser un accord de phase efficace dans l'AlGaAs, d'abord une géométrie con-

trapropageante avec une pompe transverse, puis un accord de phase modal en géométrie copropageante.

Nous faisons ensuite l'étude de notre première source de paires de photons, dont le principe repose sur un accord de phase contrapropageant. L'étude théorique de l'état quantique des paires de photons générées par fluorescence paramétrique dans cette source montre tout d'abord que la symétrie d'échange de l'état dépend du profil spatial du faisceau de pompe utilisé, et ouvre la voie à la manipulation de la statistique d'échange de l'état biphoton via le contrôle de ce profil spatial. L'interférométrie de Hong-Ou-Mandel est également étudiée comme outil pour mesurer la statistique d'échange de deux particules, notamment dans le cas des anyons, qui présentent une statistique d'échange non triviale, et la possibilité d'imiter ce type de statistique d'échange à l'aide de la modulation spatiale du faisceau de pompe est démontrée. Des résultats expérimentaux sont finalement présentés, d'abord dans le cas de la mesure de l'Amplitude Spectrale Jointe des paires de photons générées, puis dans le cadre de la mesure de l'interférogramme de Hong-Ou-Mandel de paires de photons présentant une statistique d'échange anyonique. Ces résultats démontrent expérimentalement la possibilité de contrôler de manière reconfigurable la statistique d'échange de paires de photons générées par fluorescence paramétrique, à température ambiante et longueur d'onde télécom.

Nous nous concentrons ensuite sur le second dispositif, basé sur un réseau de guides d'ondes non-linéaires couplés de manière évanescente, pompés dans une géométrie colinéaire. Les photons générés peuvent sauter d'un guide à l'autre, implémentant des marches quantiques aléatoires. Cette configuration permet la génération d'états intriqués spatialement et reconfigurables via le contrôle du faisceau de pompe ou des paramètres du réseau. Les photons sont générés directement dans le dispositif à n'importe quelle position selon l'axe de propagation, permettant d'augmenter la compacité et le niveau d'intrication spatiale tout en ouvrant la voie à des expériences de simulation quantique sur puce. Nous faisons en premier lieu une étude théorique du dispositif passif, dans lequel nous introduisons un formalisme de modes de Bloch pour décrire les modes collectifs du réseau infini de guides d'ondes. En décomposant les états d'entrée sur les modes de Bloch, qui ont chacun leur propre vecteur d'onde transverse et leur constante de propagation modifiée, il est possible de calculer formellement de manière simple la propagation d'un faisceau cohérent dans le réseau. Nous faisons ensuite l'étude de la propagation de paires de photons dans le réseau, donnant lieu à des marches quantiques corrélées, et introduisons des indicateurs de non-classicalité de l'état quantique de sortie.

Nous introduisons dans un deuxième temps le concept de marches quantiques cascadées, lorsque des paires de photons sont générées directement dans le réseau par fluorescence paramétrique, et calculons l'état quantique des paires de photons ainsi obtenues. Cela permet d'étudier de manière théorique les corrélations spatiales présentées par les biphotons produits, pour la compréhension desquelles le formalisme des modes collectifs de Bloch offre un cadre adapté en permettant de considérer des corrélations de forme plus simple dans l'espace réciproque, et donnent naissance à un accord de phase modifié avec une condition supplémentaire de conservation du vecteur d'onde transverse. Nous considérons également les corrélations existant entre les degrés de liberté spatiaux et de fréquence, qui limitent la pureté des corrélations spatiales, que l'on peut quantifier en utilisant la trace partielle de la matrice densité de l'état à deux photons. Ensuite, nous introduisons un modèle théorique permettant de considérer directement l'évolution des

corrélations dans l'espace réel, et qui ne nécessite pas de calcul des modes propres, ce qui permet de l'appliquer aux réseaux finis.

Pour conclure notre étude théorique, nous effectuons une série de simulations pour mettre en lumière le rôle de différents paramètres des réseaux de guides considérés. D'abord, nous démontrons par la simulation du spectre de résonance de fluorescence paramétrique que l'existence du couplage entre les guides d'ondes conduit à un élargissement de la résonance non-linéaire. Nous étudions ensuite la pureté de la matrice densité réduite sur le degré de liberté spatial, en fonction de la largeur spectrale considérée pour les photons émis, ce qui permet, avec le tracé des spectres des photons de fluorescence paramétrique, de confirmer l'existence du couplage spatio-spectral dans l'état généré. Nous passons ensuite à la simulation d'un état pur spectralement, ainsi que de la résonance des différentes métriques pour la non-classicalité des états à deux photons, qui sont maximales autour de la longueur d'onde de fluorescence paramétrique adaptée à la dégénérescence. Finalement pour le réseau infini, nous simulons les états générés par l'injection d'un faisceau de pompe dont la distribution spatiale dans les différents guides du réseau est contrôlée en phase et en amplitude, mettant ainsi en lumière la possibilité du contrôle de l'état quantique de sortie du dispositif. Enfin, nous simulons les effets de différents paramètres en utilisant le formalisme introduit pour les réseaux finis, notamment de la propagation transverse et des pertes de la pompe, ainsi que les effets de rebond des photons sur les bords du réseau. Pour terminer, nous démontrons un effet de localisation spatiale des photons lorsque du désordre est introduit dans la constante de couplage, similaire au phénomène de localisation d'Anderson.

Nous présentons ensuite la conception et la fabrication des microstructures permettant la génération de paires de photons par fluorescence paramétrique dans les réseaux ainsi que la mesure des corrélations spatiales. Nous détaillons les simulations électromagnétiques réalisées, puis le travail de développement des techniques de microfabrication, par lithographie électronique et gravure plasma ICP, qui a constitué un aspect important et exigeant de ce travail de thèse. Nous présentons également des premières caractérisations des échantillons réalisés.

Finalement, nous introduisons les résultats expérimentaux obtenus en utilisant les échantillons ainsi fabriqués. Nous détaillons les techniques expérimentales développées pour nos mesures. Nous confirmons expérimentalement l'élargissement du spectre de résonance du processus de fluorescence paramétrique, puis mesurons la matrice de corrélation d'un échantillon sur cinq guides, en bon accord avec l'étude théorique réalisées précédemment. Les corrélations obtenues violent le critère de non-classicalité par une soixantaine de déviations standard, indiquant le caractère quantique des états produits. Ces résultats constituent la première démonstration de génération d'états de lumière intriqués spatialement dans un réseau de guide d'onde en AlGaAs, ouvrant la voie à la réalisation d'une source compacte et versatile fonctionnant à température ambiante et aux longueurs d'onde télécom.

Nous concluons ce manuscrit en donnant un aperçu des perspectives futures ouvertes par les résultats présentés.

Nous avons d'abord démontré expérimentalement la possibilité de reconfigurer les statistiques d'échange des paires de photons intriqués dans le degré de liberté de fréquence et d'imiter des statistiques d'échange arbitraires, en particulier pour reproduire le comportement des anyons dans une configuration Hong-Ou-Mandel. Cela pourrait être ex-

ploité pour la réalisation de protocoles d'information quantique exploitant la robustesse au bruit du processus de tressage (*braiding*), tels que les codes de correction d'erreurs et les protocoles de calcul quantique topologique. Le degré de liberté en fréquence peut également être couplé à la polarisation en exploitant simultanément les deux interactions pour la fluorescence paramétrique de type II supporté par la source, ce qui permet la génération d'états intriqués hybrides en fréquence/polarisation. Ce degré de liberté hybride pourrait à son tour être utilisé pour la distribution d'intrication à des systèmes quantiques ayant des niveaux d'énergie disparates ou comme ressource pour des mesures temporelles précises en métrologie. De plus, des configurations plus complexes du schéma de pompage pourraient également être mises en oeuvre pour générer une zoologie plus diversifiée d'états quantiques en fréquence, avec une structure de phase finement structurée qui peut à nouveau fournir une ressource pour la métrologie quantique.

D'autre part, nous avons démontré la génération de paires de photons intriqués spatialement à partir de marches quantiques dans des réseaux de guides d'ondes non linéaires en AlGaAs. À l'avenir, cette plateforme pourrait être utilisée pour générer une intrication spatiale contrôlable des paires de photons en adaptant la distribution spatiale du faisceau de pompe dans le réseau. Les réseaux de guides d'ondes offrent en outre une plateforme naturelle pour la simulation quantique de Hamiltoniens de liaisons fortes avec des énergies sur site et des couplages contrôlables. Les paramètres peuvent être choisis directement au stade de la fabrication ou modifiés dynamiquement en exploitant le fort effet électro-optique de l'AlGaAs. Grâce à un contrôle précis du Hamiltonien, les réseaux de guides d'ondes peuvent ainsi permettre la simulation de problèmes de matière condensée, tels que la localisation d'Anderson d'états quantiques bipartites. Ils offrent également la possibilité de simuler et d'exploiter des effets topologiques pour réaliser une transmission optique sans dissipation dans le régime quantique. En effet, il est possible de concevoir les constantes de couplage et leur périodicité à l'intérieur du réseau pour simuler des Hamiltoniens avec des propriétés topologiques, comme le Hamiltonien de Su-Schrieffer-Heeger, et d'introduire un défaut structurel pour créer une interface entre deux phases topologiques distinctes. Cela conduit à l'émergence d'états de bord topologiquement protégés qui ont des propriétés robustes au désordre. Grâce à cette configuration, les réseaux de guides d'ondes peuvent être exploités pour étudier l'interaction entre les corrélations quantiques dans le degré de liberté spatial et la protection topologique des états quantiques, notamment pour les paires de photons générées par fluorescence paramétrique.

La source contrapropageante et le réseau de guides d'ondes non-linéaires étudiés dans cette thèse permettent tous deux de générer des paires de photons intriqués de manière reconfigurable et peuvent être intégrés à des circuits photoniques pour une manipulation ultérieure des photons générés. Ils offrent diverses perspectives en termes de métrologie et de simulation quantique, et leur développement et leur intégration sur puce constituent un pas en avant vers des protocoles quantiques intégrés sur puce et à faible encombrement pour la mise en oeuvre future des technologies d'information quantique hors des laboratoires.

Introduction

Quantum information

The development of the theory of quantum mechanics since the beginning of the last century has led to a counter-intuitive description of the behaviour of the microscopic world: far from our everyday experience, particles can behave in a probabilistic manner and be in a superposition of two different states. Moreover, two quantum systems can even present *instantaneous* correlations between their measurable properties [1, 2], even when at large distances, which challenges the causality principle and gave rise to the famous Einstein-Podolsky-Rosen paradox [3]. These two properties of quantum systems - superposition and entanglement - opened the possibility for information protocols using them as a resource, creating the basis of what would later be called *quantum information* [4].

Today the research community has structured this domain into four different axes defined for the future applications of quantum information technologies: *quantum computing*, i.e. the use of quantum properties to achieve better complexity scaling of algorithms over their classical counterparts, *quantum simulation*, which exploits well-controlled quantum systems to simulate the properties of more complex and inaccessible systems, *quantum metrology*, where the high sensitivity of quantum systems to perturbations is harnessed to improve the precision of measurements, and *quantum communication*, aiming at the realization of secure information transmission. Such protocols have been theoretically developed as early as the 1980s, with the BB84 and BBM92 protocols proposed for Quantum Key Distribution (QKD) [5, 6] enabling to secure a communication channel in an absolute way using the fundamental properties of quantum mechanics. Since, other protocols have been theoretically investigated, especially in the field of quantum computing, with the emergence of algorithms potentially offering quantum advantage over their classical counterparts [7–9]. This field has attracted a growing interest over the last three decades and is now the object of concerted efforts at the international scale for further developments of potential applications, notably through public funding plans such as the European Quantum Flagship, or private research made to achieve quantum supremacy for quantum computers [10–13].

Experimental requirements for these applications are summarized by the DiVincenzo criteria [14] and were made realizable by technological developments allowing to address and measure individual quantum systems[1]. These criteria lead to the selection of suitable physical platforms to use for the encoding of quantum information, at first in the frame of two-level encoding in *quantum bits* or *qubits* (analogous to the boolean bits used in classical computing). Atomic systems, such as ultracold atoms [20] and trapped ions [21], have

[1]Notable developments include the invention of magnetic and optical traps [15,16] and of single-photon detectors [17–19].

been used to implement quantum simulation [22, 23] and quantum computation [24–26] protocols, due to the inherent possibility to encode information into the energy levels of the system. The high degree of control offered by the opto-magnetic trapping and the possibility to optically address the energy levels in a deterministic way make atomic systems prime candidates for the realization of interacting qubits with accurately controlled parameters. Electronic spins from vacancy defects in crystals [27–29] also provide natural two-level systems and are conveniently addressable through external electromagnetic fields and readable through photoluminescence, and have been used as well to implement quantum computing algorithms [30] and quantum memories in hybrid quantum information processing schemes [31, 32]. Superconducting qubits became the most advanced platform for the purpose of quantum computing [33], with the possibility to encode information in several degrees of freedom (charge [34], magnetic flux [35], phase [36]), to address the qubits electronically and to implement quantum gates in a deterministic manner [37], and have led to important advances in the scaling of the quantum computer [10]. Finally, photons, with their innate robustness against decoherence, and high propagation speed, offer characteristics of choice for the implementation of quantum communication [38] and have been used for the implementation of long-distance QKD [39]. They also have general applications in quantum information processing [40] and schemes for universal all-optical quantum computing have been proposed by Knill, Laflamme and Milburn [41] as well as Raussendorf and Briegel [42]. Since then, photons have been used for quantum simulations [43, 44], quantum algorithms [45, 46], and quantum states of lights have been instrumental for new advances in metrology [47–51]. The interfacing of photons as flying qubits with material qubits serving as quantum nodes to develop a quantum internet is also a long-term goal of the development of quantum technologies [52, 53].

Quantum photonics as a platform for high-dimensional quantum information

This PhD thesis lies in the context of photonic-based quantum technologies. One of the particular interests of photons is that they offer many degrees of freedom to encode the information, making them a versatile vector of quantum information. In the many-photons regime, the information can be encoded in the quadrature amplitudes of the electromagnetic fields, using in particular squeezed states of light [54, 55] as a resource and homodyne detection for measurements: this is the so-called *continuous variables* approach [56, 57]. The present work takes place in the framework of its counterpart, the *discrete variables* approach, in which information is encoded into few-photon states [40]. The most conventional degree of freedom to encode information in single- or few-photons systems has historically been **polarization**, used to realize quantum communication [58, 59], computing [60–62] and simulation protocols [63, 64]. However, this degree of freedom only spans a two-dimensional Hilbert space, thus limiting the quantity of information encoded for each photon. Harnessing higher-dimensional degrees of freedom offers increased density of information encoding [65], enhanced security in quantum communication protocols [66], and more versatility for quantum computation schemes [67, 68]. Degrees of freedom displaying high-dimensional Hilbert spaces for photons include **Orbital Angular Momentum** (OAM), where the information is encoded into the phase winding of the modal field amplitude along the propagation direction [69], and has been shown to be particularly suited

for long-distance QKD protocols [66, 70] with high key rates [71]; **time-bin** encoding in which the information is encoded into the time of arrival of photons, which has been used for long-distance state teleportation [72, 73] and QKD [74, 75]; **time-frequency** encoding with the spectrum of the photons being the vector of information, and **spatial** (or path) encoding where the information is contained in the occupied spatial modes, notably in photonic circuits. Frequency and spatial encoding of quantum information are especially interesting, as they both enable high-dimensional quantum information encoding with convenient transmission and manipulation. Frequency allows to convey all the information into a single spatial mode, while being integrable with already-existing telecom technology for its manipulation [76, 77]. Moreover, it is robust to propagation in fibers, allowing for reliable high-rate transmission of quantum information [78]. At the same time, the spatial degree of freedom is naturally suited for integrated photonic circuits, allowing easy high-fidelity manipulation with beamsplitters, phase-shifters and waveguide couplers, leading to advanced realizations in chip-based quantum simulation [79–83] and quantum computing [84, 85].

Integrated quantum photonics platforms

Optical-based quantum information can be implemented using photons generated from nonlinear processes in bulk crystals [86, 87], squeezed light sources [55, 88], and manipulation through bulk optical components. This type of free-space and bulk setups have been instrumental in the proof-of-principle demonstrations of the feasibility of quantum information protocols in the 1990's [89–91]. Later, the field of integrated photonics, brought by the advances in fabrication technologies from the beginning of the 2000's, especially in the semiconductor industry, has offered additional compacity and stability with low-footprint optical components, leading to increased scalability for the generation, manipulation and detection of quantum states of light integrated inside miniature chips. Efforts are currently made to combine these three fundamental stages of photonics quantum information processing on a single chip. We give in the following a quick overview of the different existing material platforms suitable for integrated quantum photonics.

Silicon-based circuits benefit from the already-developed CMOS industry, which allows for cheap manufacturing and mastered fabrication processes, and include Silicon-on-Insulator (SOI), Silica-on-Silicon (SOS) and Silicon Nitride (SiN). The mentioned materials all benefit from the presence of third-order nonlinearity, offering the possibility of photon pair generation at telecom wavelengths by Spontaneous Four-Wave Mixing (SFWM). SOI platforms have been successfully used to realize sophisticated circuits embedding several sources based on the high third-order nonlinearity of the material [92] and reconfigurable quantum gates [93]. It is compatible with the on-chip integration of high-efficiency single-photons detectors [94], making it a promising candidate for the realization of all-integrated quantum processing chips. Thanks to its high refractive index, SOI also allows to integrate components with a high density on a chip, but it suffers from two-photon absorption and non-negligible propagation losses at telecom wavelengths. SOS, on the other hand, benefits from ultra-low propagation losses [95] but also has a weaker third-order nonlinearity and lower refractive index, which decreases the integrable on-chip components density. It has been used to demonstrate the first on-chip quantum gate [96]. SiN combines both ultra-low losses and high-density components integration [95], and

presents reduced two-photon absorption, allowing to increase the pump power to compensate for its weaker third-order nonlinearity. It has been successfully used for the implementation of universal quantum gates [97, 98] and for high-dimensional entangled photon pairs using microresonators [99]. Silicon oxynitride (SiO_xN_y) has also been used to demonstrate quantum correlations in the spatial degrees of freedom in waveguide arrays [100]. We can additionally mention femtosecond laser writing in borosilicate glass, which allows for the easy fabrication of complex circuits and has been used to realize high-quality circuits, allowing to implement e.g. quantum random walks [81] and boson sampling [43]. However, this platform does not benefit from optical nonlinearity and thus cannot directly integrate photon sources.

Lithium niobate-based circuits benefit from a combination of low propagation losses, high second-order nonlinearity, and high electro-optic effect, making it a suitable platform for the implementation of efficient photon pair sources using Spontaneous Parametric Down-Conversion (SPDC) [101], as well as reconfigurable quantum circuits embedding various optical elements such as polarizing beamsplitters, electro-optic phase-shifters [102, 103] and arrays of coupled nonlinear waveguides [104]. Periodical poling, allowing to achieve a high conversion efficiency, has been used to realize bright sources and engineer the spectral properties of entanglement of the generated photon pairs [105, 106]. $LiNbO_3$ waveguides are compatible with wafer bonding, allowing e.g. to integrate photon pair sources with silicon-based circuits [107].

III-V semiconductors such as GaAs, offer high refractive index and strong field confinement, high second- and third-order nonlinearity allowing to realize efficient parametric sources based on SPDC in AlGaAs waveguides [108–112] or SFWM in waveguides [113, 114] and microring resonators [115]. GaAs can also host high-quality single-photon sources based on quantum dots [116, 117]. It benefits from a direct electronic bandgap, which is useful in the realization of electrically injected sources, either for parametric sources [118] or quantum dots [119, 120]. Additionally, they present a high electro-optic effect which can be used to implement phase-shifters and delay lines [121]. Finally, III-V semiconductors are compatible with the integration of superconducting nanowires single-photon detectors (SNSPDs) [122], opening the possibility to realize fully on-chip quantum information protocols [123].

Reconfigurable sources of biphoton states

In this thesis, we will focus on the study of SPDC photon pair sources and integrated circuits based on AlGaAs waveguides, allowing to generate frequency-entangled and path-entangled photon pairs.

The first source employs a transverse pump geometry in a single waveguide, offering the possibility to engineer the quantum state of the generated photon pairs in the frequency degree of freedom through the spatial shaping of the pump. Previous realizations of similar quantum entanglement have been realized using domain-engineered crystals [106] or spectral engineering of the pump pulse [124]. The first method fixes the shape of the spectral wavefunction of the generated photon pairs for a given source and lacks flexibility, while the second method cannot yield control over the exchanges statistics of the biphotons. On the other hand, our source displays reconfigurable spectral properties of the generated pairs, including the exchange statistics of the spectral wavefunction of

the generated biphotons.

The second device is based on an array of evanescently coupled nonlinear waveguides, pumped in a copropagating geometry, where the generated photons can hop from waveguide to waveguide, thus implementing quantum random walks. This leads to the generation of spatially entangled states that are reconfigurable through the spatial profile of the pump beam and the parameters of the array. In contrast to previous implementations of quantum random walks [81], the photons are here generated directly within the device and the generation can take place at any position along the propagation direction. This leads to an increased compacity and a higher level of entanglement, that can be exploited to realize a versatile source of spatially entangled states of light, operating at room temperature and telecom wavelength, while also opening the way to the implementation of on-chip quantum simulation tasks.

These two sources open the possibility for reconfigurable entanglement engineering of the photon pairs, either in the frequency or in the spatial degrees of freedom, which is a crucial step in the realization of chip-integrated versatile sources of quantum states.

The manuscript is organized as follows:

In the first chapter, we will introduce the theory of the second-order nonlinear process used for the generation of the photon pairs, Spontaneous Parametric Down-conversion, as well as the general characteristics of the two sources described in the thesis. Then, the second chapter will discuss the control of the exchange statistics for the photon pairs generated by the counter-propagating source, and present experimental results demonstrating, using measurements based on Hong-Ou-Mandel (HOM) interferometry, the ability to reproduce anyonic exchange statistics by engineering the joint spectral wavefunction of photon pairs. The third chapter will introduce the theory of SPDC in waveguide arrays, and present the spatial entanglement resulting from the combination of photon pair generation and quantum random walks along the array, called cascaded quantum random walks. Numerical simulations of the generated states will be presented, to offer a panel of the realizable quantum states. The fourth chapter will present the design and fabrication processes of the waveguide array source of spatially entangled photons. Finally, the fifth chapter will present the experimental demonstration of spatial correlations in the photon pairs generated using the nonlinear waveguide array.

Chapter 1

Non-linear optical processes in AlGaAs waveguides

In this chapter, we give the theoretical background necessary to describe the generation of photon pairs in AlGaAs waveguides. AlGaAs benefits from strong second and third order nonlinearities, which enables Three and Four Wave Mixing. In this manuscript, we focus on the second-order process of Spontaneous Parametric Down-Conversion (SPDC), where photons of a pump beam are converted into pairs of twin photons. We first give a classical theoretical description of the corresponding mechanisms, and then switch to a semi-classical approach to derive the quantum state of the photon pairs generated by SPDC in AlGaAs.

Contents

1.1 Nonlinear optical processes: theoretical description

The interaction between a nonlinear material medium and an electromagnetic field can give rise to diverse phenomena, such as frequency conversion of a laser beam inside a crystal, which can be used for the generation of light with interesting properties. In this section, we give a theoretical description of nonlinear optical processes, and especially Spontaneous Parametric Down-Conversion, which will serve as a tool for the generation of correlated photon pairs in an AlGaAs waveguide.

We first give a brief introduction of the concept of nonlinear polarization, then describe the evolution of fields interacting in a nonlinear crytal, and finally give a semi-classical Hamiltonian description of the SPDC process and derive the generated quantum state.

1.1.1 Nonlinear polarization

When an electric field $\mathbf{E}$ propagates through a medium, it induces a polarization in the material, which we can describe in the following way:

$$\begin{aligned}\mathbf{P} &= \epsilon_0\left[\boldsymbol{\chi}^{(1)}\cdot\mathbf{E}+\boldsymbol{\chi}^{(2)}:\mathbf{EE}+\boldsymbol{\chi}^{(3)}\vdots\mathbf{EEE}+\cdots\right]= \\ &= \underbrace{\mathbf{P}^{(1)}}_{\mathbf{P}^{L}(t)}+\underbrace{\mathbf{P}^{(2)}+\mathbf{P}^{(3)}+\cdots}_{\mathbf{P}^{NL}(t)},\end{aligned} \tag{1.1}$$

with ϵ_0 the vacuum dielectric permittivity and $\boldsymbol{\chi}^{(m)}$ the rank $m+1$ tensor representing the m-th order nonlinear susceptibility of the medium. The polarization can be written, as in the second row of the equation, as the sum of a linear ($\mathbf{P}^L(t)$) and a nonlinear ($\mathbf{P}^{NL}(t)$) term. For solid-state materials, $\boldsymbol{\chi}^{(1)}$ is of the order of 1, and the value of $\boldsymbol{\chi}^{(m)}$ decreases rapidly with m, meaning that for small values of the electric field, only the linear part of the polarization plays a significant role in the response of the medium to

the electric fields. However, for higher values of the electric fields, which can be typically achieved using laser beams, the nonlinear terms become significant as the field becomes more intense. These higher-order terms in the polarization are responsible for frequency conversion in the medium, meaning that fields at different frequencies than the external electric field can be generated.

For instance, if we consider an electric field of the form $\mathbf{E}_1(\mathbf{r},t) = \left(E_1 e^{i(\omega_1 t - k_1 z)} + \text{c.c}\right)\mathbf{e}_x$ (with c.c. the complex conjugate), then the second-order nonlinear polarization gives, from equation 1.1 (considering a simple model where the nonlinear susceptibility is independent of the involved frequencies):

$$P_i^{(2)}(z,t) = \boldsymbol{\chi}_{ixx}^{(2)} |E_1|^2 \left(e^{2i(\omega_1 t - k_1 z)} + e^{2i(-\omega_1 t + k_1 z)} + 2\right) \tag{1.2}$$

with $i = x, y, z$, and we can see that terms with frequency 2ω appear (as well as a non-oscillating term), which is called Second Harmonic Generation (SHG). If we add a term with a different frequency $\mathbf{E}_2(\mathbf{r},t) = \left(E_2 e^{i(\omega_2 t - k_2 z)} + \text{c.c}\right)\mathbf{e}_x$, then we get

$$\begin{aligned} P_i^{(2)}(z,t) =& \boldsymbol{\chi}_{ixx}^{(2)} \Big(2|E_1|^2 + 2|E_2|^2 + \Big(E_1^2 e^{2i(\omega_1 t - k_1 z)} + E_2^2 e^{2i(\omega_2 t - k_2 z)} \\ &+ E_1 E_2 e^{i((\omega_1+\omega_2)t - (k_1+k_2)z)} + E_1 E_2^* e^{i((\omega_1-\omega_2)t - (k_1-k_2)z)} + \text{c.c.}\Big)\Big) \end{aligned} \tag{1.3}$$

which corresponds to the generation of terms with frequency $\omega_1 + \omega_2$ (i.e. Sum Frequency Generation or SFG) and terms with frequency $\omega_1 - \omega_2$ (i.e. Difference Frequency Generation or DFG), giving examples of three-wave mixing processes.

1.1.2 Wave propagation in a nonlinear medium

In a material medium, the polarization induced by the electromagnetic field modifies the propagation of this field. In standard dielectric media, at low values of the electric fields, this is usually observable through a change in the propagation speed, which is quantified by the refractive index of the medium. However, for materials with high nonlinearity and/or at high optical power, the nonlinear polarization additionally creates oscillating fields at new frequencies, which act as source terms in the propagation equation of the electromagnetic field.

To derive this effect, let us consider Maxwell's equations, in a dielectric optical medium without free charges ($\rho = 0$) or currents ($\mathbf{J} = 0$) for the electric and magnetic fields $\mathbf{E}$ and $\mathbf{B}$:

$$\begin{cases} \boldsymbol{\nabla} \times \mathbf{E} = -\dfrac{\partial \mathbf{B}}{\partial t} \\ \boldsymbol{\nabla} \times \mathbf{H} = \dfrac{\partial \mathbf{D}}{\partial t} \\ \boldsymbol{\nabla} \cdot \mathbf{B} = 0 \\ \boldsymbol{\nabla} \cdot \mathbf{D} = 0 \end{cases} \tag{1.4}$$

with $\mathbf{B} = \mu_0 \mathbf{H}$ and $\mathbf{D} = \epsilon_0 \mathbf{E} + \mathbf{P}$.

By taking the curl of the first equation and using the three others to eliminate the resulting terms depending on $\mathbf{B}$, we get the propagation equation for the electric field in

the nonlinear medium:

$$\nabla^2\mathbf{E} - \frac{1}{c^2}\frac{\partial^2\mathbf{E}}{\partial t^2} = \frac{1}{\epsilon_0 c^2}\frac{\partial^2\mathbf{P}}{\partial t^2} \tag{1.5}$$

where we see the polarization appearing on the right-hand side. If we split the polarization into its linear and nonlinear part,

$$\mathbf{P} = \mathbf{P}^L + \mathbf{P}^{NL} = \epsilon_0\boldsymbol{\chi}^{(1)} \cdot \mathbf{E} + \mathbf{P}^{NL}, \tag{1.6}$$

we can take the linear part into the left-hand side, which yields

$$\nabla^2\mathbf{E} - \frac{1+\boldsymbol{\chi}^{(1)}\cdot}{c^2}\frac{\partial^2\mathbf{E}}{\partial t^2} = \frac{1}{\epsilon_0 c^2}\frac{\partial^2\mathbf{P}^{NL}}{\partial t^2}. \tag{1.7}$$

Now the left-hand side is a wave equation, and for an isotropic and lossless medium, $\boldsymbol{\chi}^{(1)}$ is simply a real scalar and the equation reduces to

$$\nabla^2\mathbf{E} - \frac{n^2}{c^2}\frac{\partial^2\mathbf{E}}{\partial t^2} = \frac{1}{\epsilon_0 c^2}\frac{\partial^2\mathbf{P}^{NL}}{\partial t^2}. \tag{1.8}$$

where $n = \sqrt{1+\chi^{(1)}}$ is the refractive index in the medium[1]. Equation 1.8 is thus a driven wave equation with a source term on the right-hand side, where the nonlinear polarization terms at new frequencies generate additional oscillations of the electric field.

The specific shape of the nonlinear polarization will then depend on the response of the material to the electric field, which we can quantify using its nonlinear electric susceptibility tensors. Here, we will focus on three-wave mixing processes, involving only the $\boldsymbol{\chi}^{(2)}$ tensor, in GaAs and AlGaAs, to put into light the phenomenon of Spontaneous Parametric Down Conversion, where a pump field at high frequency is converted into two signal and idler fields at smaller frequencies.

1.1.3 Second-order nonlinear processes in GaAs/AlGaAs

Gallium Arsenide (GaAs), and Aluminum Gallium Arsenide (AlGaAs), are III-V semiconductors that enable, thanks to their high second- and third-order nonlinearity, Three- and Four-Wave-Mixing processes. They also have additional interesting electronic and optical properties, such as their high electro-optic coefficient, high refractive index that allow for efficient confinement, direct bandgap that can be exploited to realize electrically pumped sources, and low losses at telecom wavelength.

To derive information over the shape of the second-order nonlinear tensor of GaAs and AlGaAs, we need to consider the crystalline structure of the two materials, and use symmetry conditions that help understand the shape of the tensor.

If the involved frequencies are far from resonance, and using Kleinman's symmetry condition, we can consider that the tensor element $\chi^{(2)}_{ijk}$ is independent of frequency, and

[1]Note that we can add the frequency dependence of the electric susceptibility by simply considering equation 1.8 in the Fourier decomposition of the electric field to include dispersion in the medium in our derivation. additionally, we can always consider the nonlinear susceptibility $\boldsymbol{\chi}^{(m)}$ dependent on the involved frequencies of the electric field in the tensorial product with the field.

also independent of the permutation of the indices i, j, k (e.g. $\chi^{(2)}_{ijk} = \chi^{(2)}_{ikj}$). We can then reduce the number of tensor elements to consider, by introducing

$$d_{ijk} = \frac{1}{2}\chi^{(2)}_{ijk} \tag{1.9}$$

and defining a contracted matrix d_{il} using the following correspondence table:

jk	11	22	33	23/32	31/13	12/21
l	1	2	3	4	5	6

which yields

$$d_{il} = \begin{pmatrix} d_{11} & d_{12} & d_{13} & d_{14} & d_{15} & d_{16} \\ d_{16} & d_{22} & d_{23} & d_{24} & d_{14} & d_{12} \\ d_{15} & d_{24} & d_{33} & d_{23} & d_{13} & d_{14} \end{pmatrix} \tag{1.10}$$

Additionally, GaAs/AlGaAs has a non-centrosymmetric zincblende crystalline structure, which yields a $\bar{4}3m$ (tetrahedral) symmetry. This point-group symmetry also applies to the second-order nonlinear tensor, giving relations between the tensor elements, and the final d matrix can be written, with only one non-zero independent element:

$$d = \begin{pmatrix} 0 & 0 & 0 & d_{14} & 0 & 0 \\ 0 & 0 & 0 & 0 & d_{14} & 0 \\ 0 & 0 & 0 & 0 & 0 & d_{14} \end{pmatrix}. \tag{1.11}$$

Here, the nonzero elements are d_{XYZ} and all of the elements associated with permutation of the indices, where X is the (100) direction, Y is the (010) direction, and Z the (001) direction, corresponding to the crystallographic axes, meaning that all interactions permitted by the symmetry of the crystal involve fields with polarizations components in all three crystallographic axes. In our case, we define a second coordinate system $(x, y, z) = (110, \bar{1}10, 001)$, and will consider light propagating in waveguides in the x direction, meaning that the two main permitted polarization directions for the waveguided modes are the y-direction (Transverse Electric (TE) polarization), and the z-direction (Transverse Magnetic (TM) polarization). In the case of guided modes, because of the confinement of light, it is worth noting that both the TE and TM polarized modes have a small electric field component in the x direction as well, which means that the TM-polarized modes have electric field components along all three axes of the crystal, and the TE-polarized mode only along the X and Y axes. This reduces the possible nonlinear interactions to three different types[2]:

- the interaction between three TM-polarized modes, which is called **type 0** in the context of Spontaneous Parametric Down-Conversion (SPDC),

[2]The interaction between three TE-polarized modes is prohibited because there is no component of the field in the Z direction, while the interaction between two TM-polarized and one TE-polarized modes is highly suppressed for Spontaneous Parametric Down-Conversion because the TE and TM modes have almost orthogonal field distributions in the XY plane (since the main TE component in this plane is along the y direction while the main TM component is in the x direction), giving the main component of the TM-oriented polarization $P^{TM}_Z \propto d_{XYZ}\left(E^{TE}_X E^{TM}_Y + E^{TE}_Y E^{TM}_X\right) \simeq 0$, while the polarization generated by two TM-polarized fields always have a non-zero electric field component along Z, and thus cannot be polarized along the TE direction.

- the interaction between one TM-polarized and two TE-polarized modes, which is called **type I** if the pump is TM-polarized or **type II** if the pump is TE-polarized in the context of SPDC.

1.1.4 Three Wave Mixing in a bulk medium

Having determined the shape of the nonlinear tensor, we can now shift our attention to the actual second-order nonlinear processes taking place during the interaction of the optical field within a bulk nonlinear medium. In our case, the resulting process is always stemming from the interaction between three components: one component of the induced polarization, and two components of the external electric field (which can be the same). If we consider three fields with frequencies ω_1, ω_2 and ω_3, we can consider that, for frequencies far from the resonance of the medium, the exchange of energy only occurs between the different fields involved, and not between the electric fields and the medium. The energy conservation then allows the following set of three-wave mixing processes, summarized on figure 1.1:

- **Sum Frequency Generation (SFG)** where two pump fields at frequency ω_1 and ω_2 are interacting with a nonlinear medium to create a field at frequency $\omega_3 = \omega_1 + \omega_2$.

- **Second Harmonic Generation (SHG)**, corresponding to the case of SFG where the two fields at $\omega_1 = \omega_2 = \omega$ are degenerate, and $\omega_3 = 2\omega$.

- **Difference Frequency Generation (DFG)**, also called Optical Parametric Amplification (OPA), where two fields at frequency ω_1 and ω_2 interact with the crystal to generate a field at frequency $\omega_3 = \omega_1 - \omega_2$. To ensure energy conservation, we can see that for each photon generated at frequency ω_3, a photon at frequency ω_2 must be generated as well, which means that this process also amplifies the second input field.

- **Spontaneous Parametric Down-Conversion (SPDC)**, in which the previous process can take place in the presence of the first field at frequency ω_1 only, which can generate photons at frequencies ω_2 and ω_3 by interacting with the vacuum fluctuations of the latter fields. This process does not appear in the classical description of the nonlinear interaction between the crystal and the electric field, and since it arises from the interaction with vacuum fluctuations, it induces weak fields by nature.

In the next sections, we will describe the SPDC process using the formalism of quantum mechanics, as it is the mechanism of choice to generate photon pairs. But the classical analysis of the other nonlinear optical processes still gives interesting insight on the conditions for efficient frequency conversion in nonlinear media, therefore we will first consider the phenomenon of SFG (the derivation is very similar for the cases of SHG and DFG).

Let us consider three interacting fields, with a propagation direction along the z axis (we switch to the z coordinate for the propagation direction, which is more conventional for the formalism of guided waves), verifying the energy conservation condition $\omega_3 = \omega_1 + \omega_2$:

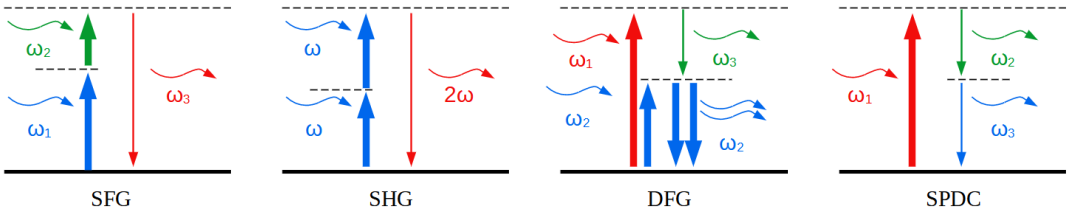

Figure 1.1: Energetical scheme of the different three-wave mixing processes, depicted as absorption and emission of photons on virtual energy levels represented by dashed lines.

$$\mathbf{E}(\mathbf{r},t) = \sum_{l=1}^{3} \left(E_l(\mathbf{r}) e^{i(\omega_l t - k_l z)} + \text{c.c.} \right) \mathbf{e}_l \tag{1.12}$$

with E_l the complex amplitude of field number l, and $\mathbf{e}_l$ its polarization. Using equation 1.8 on the corresponding frequency components, and considering the slowly varying envelope approximation (i.e. $|\frac{d^2E_l}{dx^2}|, |\frac{d^2E_l}{dy^2}|, |\frac{d^2E_l}{dz^2}| \ll |k_l \frac{dE_l}{dz}|$) and the dispersion relation $\omega_l n_l(\omega_l) = k_l c$, we get:

$$\begin{aligned}
ik_3 \frac{dE_3}{dz} e^{i(\omega_3 t - k_3 z)} &= \frac{2\chi^{(2)}_{312}\omega_3^2}{\epsilon_0 c^2} E_1 E_2 e^{i(\omega_3 t - (k_1+k_2)z)} \\
ik_2 \frac{dE_2}{dz} e^{i(\omega_2 t - k_2 z)} &= \frac{2\chi^{(2)}_{213}\omega_2^2}{\epsilon_0 c^2} E_3 E_1^* e^{i(\omega_2 t - (k_3-k_1)z)} \\
ik_1 \frac{dE_1}{dz} e^{i(\omega_1 t - k_1 z)} &= \frac{2\chi^{(2)}_{132}\omega_1^2}{\epsilon_0 c^2} E_3 E_2^* e^{i(\omega_1 t - (k_3-k_2)z)}
\end{aligned} \tag{1.13}$$

which we can re-write as

$$\begin{aligned}
i\frac{dE_3}{dz} &= \frac{d_{\text{eff}}\omega_3}{\epsilon_0 n_3 c} E_1 E_2 e^{i\Delta k z} \\
i\frac{dE_2}{dz} &= \frac{d_{\text{eff}}\omega_2}{\epsilon_0 n_2 c} E_3 E_1^* e^{-i\Delta k z} \\
i\frac{dE_1}{dz} &= \frac{d_{\text{eff}}\omega_1}{\epsilon_0 n_1 c} E_3 E_2^* e^{-i\Delta k z}
\end{aligned} \tag{1.14}$$

where $\Delta k = k_3 - k_2 - k_1$ is the wavevector mismatch, and we define an effective nonlinear coefficient $d_{\text{eff}} = 2\chi^{(2)}_{312} = 4d_{14}$.

Equation 1.1.4 shows that the three waves interact by building each other up along the propagation direction, with a phase oscillation that depends on the wavevector mismatch Δk.

If we consider the process of SFG, assuming that the field $E_3 = 0$ at $z = 0$, and if we can neglect the variation of the fields E_1 and E_2 along z (the undepleted pump approximation, which is valid for processes inefficient enough so that the two pump fields are not significantly affected by the nonlinear processes) and thus consider both fields constant, we can integrate the propagation equation over a length L:

$$E_3(L) = -\frac{2id_{\text{eff}}L\omega_3}{\epsilon_0 n_3 c} E_1 E_2 e^{i\frac{\Delta k L}{2}} \,\text{sinc}\left(\frac{\Delta k L}{2}\right). \tag{1.15}$$

The intensity given by the SFG field at the output of the medium, which we can compute as the time-average of the corresponding Poynting vector, is then

$$I_3(L) = \frac{n_3\epsilon_0 c}{2}|E_3(L)|^2 = I_3^{(0)}\,\mathrm{sinc}\left(\frac{\Delta kL}{2}\right)^2 \tag{1.16}$$

with

$$I_3^{(0)} = \frac{8d_{\text{eff}}^2 L^2\omega_3^3}{n_1 n_2 n_3 \epsilon_0^3 c^3} I_1 I_2. \tag{1.17}$$

where I_1 (respectively I_2) is the intensity corresponding to the ω_1 (respectively ω_2) frequency component of the field. The efficiency of the SFG process (and analogously, of all second-order nonlinear processes) is thus heavily conditioned by the *phase-matching term* $\mathrm{sinc}\left(\frac{\Delta kL}{2}\right)^2$: for perfect phase-matching $\Delta k = 0$, the output intensity reaches its maximal value $I_3^{(0)}$, and if the phase-matching is not perfect, the interference between the fields generated at different positions is not constructive. This results in inefficient conversion between the two pump fields and the SFG field, and in the intensity being modulated by the term $\mathrm{sinc}\left(\frac{\Delta kL}{2}\right)^2$ which has a rapidly decreasing envelope with ΔkL. It is thus a crucial point for the efficient realization of the nonlinear processes to find strategies to ensure proper phase-matching, a point we will discuss later in this chapter.

In order to compute the output power for the different modes, we need to integrate the intensity over the effective area $\mathcal{A}$ occupied by the fields,

$$P = \int_{\mathcal{A}} I dS.$$

This yields, using equation 1.16:

$$P_3 = \frac{8d_{\text{eff}}^2 L^2\omega_3^2}{n_1 n_2 n_3 \epsilon_0 c^3 \mathcal{A}} P_1 P_2\,\mathrm{sinc}\left(\frac{\Delta kL}{2}\right)^2 = \eta_{SFG} P_1 P_2 \tag{1.18}$$

with P_1, P_2 the input powers associated with fields E_1 and E_2, and η_{SFG} the SFG conversion efficiency:

$$\eta_{SFG} = \frac{8d_{\text{eff}}^2 L^2\omega_3^2}{n_1 n_2 n_3 \epsilon_0^3 c^3 \mathcal{A}}\,\mathrm{sinc}\left(\frac{\Delta kL}{2}\right)^2 \quad \left[\mathrm{W}^{-1}\right]. \tag{1.19}$$

Equation 1.19 gives the conditions for an efficient power conversion between the three fields in the medium: the non-linear effective coefficient d_{eff} should be as high as possible, the phase-matching condition $\Delta k = 0$ should be satisfied, the interaction length L between the three fields should also be as high as possible (in the lossless approximation), and finally the effective area of the fields $\mathcal{A}$ should be as small as possible[3]. In particular, this last point is interesting, since it means that waveguides, where the light intensity is confined over a small effective area, offer a powerful platform for the realization of non-linear processes. In the next section, we study specifically second-order nonlinear processes of waveguided modes of light.

[3]This last point can be understood in the following way: as the generated SFG intensity depends on the product of the two intensities, for equivalent power (i.e. integral over a surface), the scaling of the intensities is inversely linear with the effective area of the fields $\mathcal{A}$, meaning that the product of the two intensities scales as $\mathcal{A}^{-2}$, and the final output power scales as $\mathcal{A}^{-1}$, the additional linear scaling coming from integration over $\mathcal{A}$.

1.1.5 Three Wave Mixing in the guided regime

The fields we considered previously, in the slowly varying envelope approximation, had negligible divergence, and propagated only in the z direction without deformation, like plane waves. However, for actual light propagation in a bulk medium, diffraction causes the light to spread over a higher surface area, which is detrimental for the SFG conversion efficiency (from equation 1.19). To avoid this, it is possible to use waveguides to confine the interacting fields within a small effective area to increase the efficiency of the nonlinear process.

Let us consider a waveguide with a propagation direction along the z direction, the field being confined in the x and y directions. This waveguide supports modes m of the electric field which we can write as

$$\mathbf{E}_m(\mathbf{r},t) = E_m(z)e^{i(\omega_m t-\beta_m z)}\varphi_m(x,y)\mathbf{e}_m \tag{1.20}$$

where:

- φ_m is the normalized transverse distribution of the mode m, with $\int|\varphi_m(x,y)|^2dxdy = 1$;
- β_m is the propagation constant of the mode m, related to the frequency through the modal index by $\beta_m = \frac{n_m\omega_m}{c}$;
- $\mathbf{e}_m$ is the polarization of mode m;
- $E_m(z)$ is a slowly varying amplitude.

If we define, as before, three interacting fields that we decompose on modes labeled $1,2,3$, the nonlinear interaction between the three fields is now dependent on the nonlinear overlap integral[4]

$$\Gamma_{\text{eff}} = \int d_{\text{eff}}(x,y)\varphi_1(x,y)\varphi_2(x,y)\varphi_3(x,y)dxdy. \tag{1.21}$$

The SFG output power after an interaction length L is then, re-writing equation 1.18 with the effective nonlinear modal overlap:

$$P_3 = \frac{8|\Gamma_{\text{eff}}|^2L^2\omega_3^2}{n_1n_2n_3\epsilon_0^3c^3}P_1P_2\,\text{sinc}\left(\frac{\Delta\beta L}{2}\right)^2 \tag{1.22}$$

where the phase-mismatch $\Delta\beta = \beta_3-\beta_1-\beta_2$ is now dependent on the effective propagation constant of the different modes, yielding the guided SFG efficiency:

$$\eta_{SFG}^g = \frac{8|\Gamma_{\text{eff}}|^2L^2\omega_3^2}{n_1n_2n_3\epsilon_0^3c^3}\,\text{sinc}\left(\frac{\Delta\beta L}{2}\right)^2 \tag{1.23}$$

giving the nonlinear modal overlap as an additional parameter for the efficiency of the nonlinear process.

[4]Note that, for processes where the negative frequency components of the electric field are involved, such as DFG, the nonlinear modal overlap involves the conjugate of the corresponding transverse mode profile, e.g. $\Gamma_{DFG} = \int d_{\text{eff}}\varphi_1(x,y)\varphi_2^*(x,y)\varphi_3(x,y)dxdy$ if $\omega_3 = \omega_1-\omega_2$.

Here we want to study the process of SPDC for photon pair generation, which does not occur in the classical formalism, as the signal and idler field have a zero amplitude at the beginning of the process and thus do not give rise to an interaction term with the pump field. To provide a theoretical framework for the SPDC process, we need to use the formalism of quantum mechanics, which we introduce in the following paragraph.

1.1.6 Quantum formalism: Spontaneous Parametric Down-Conversion

In order to describe the nonlinear interaction within the formalism of quantum mechanics, we first need to change the interacting fields from classical fields to quantum mechanical operators. For this, we will use the creation and annihilation operators for a given mode m, $\hat{a}_m^\dagger$ and $\hat{a}_m$. The electric field operator can then be written as a sum over all existing modes:

$$\hat{\mathbf{E}}(\mathbf{r},t) = \sum_m \mathbf{E}_m(\mathbf{r}) e^{i(\omega_m t - \beta_m z)} \hat{a}_m + \text{h.c.} = \hat{\mathbf{E}}^{(+)}(\mathbf{r},t) + \hat{\mathbf{E}}^{(-)}(\mathbf{r},t) \tag{1.24}$$

where h.c. corresponds to the hermitian conjugate, $\mathbf{E}_m(\mathbf{r})$ encapsulates the amplitude and polarization of mode m, and z is the propagation direction.

If we are only interested in fields far from the resonance, we can consider that the quantum state of the nonlinear medium does not change, and only describe the Hamiltonian for the optical field, which yields:

$$\hat{H}_{NL} = \epsilon_0 \int d\mathbf{r} \boldsymbol{\chi}^{(2)}(\mathbf{r}) : \hat{\mathbf{E}}(\mathbf{r},t)\hat{\mathbf{E}}(\mathbf{r},t)\hat{\mathbf{E}}(\mathbf{r},t). \tag{1.25}$$

If we only consider the interaction between the fields for three specific sets of modes, which we label p, s, i for pump, signal and idler modes, the Hamiltonian becomes

$$\hat{H}_{NL} = \epsilon_0 \int d\mathbf{r} \chi^{(2)}_{p,s,i}(\mathbf{r}) \hat{E}_p(\mathbf{r},t)\hat{E}_s(\mathbf{r},t)\hat{E}_i(\mathbf{r},t). \tag{1.26}$$

At this point, it is useful to decompose the three interacting fields into a convenient mode basis. If we consider once again the case of optical modes confined in a waveguide in the x and y directions, and thus propagating in direction z over a length L, we can for instance decompose the modes over the propagation constants β_m, or equivalently the frequencies ω_m:

$$\begin{aligned} \hat{E}_m(\mathbf{r},t) =& \sqrt{\frac{L}{2\pi}} \int d\beta_m E_m(x,y,\beta_m) e^{i(\omega_m t - \beta_m z)} \hat{a}_m(\beta_m) + \text{h.c.} \\ =& \sqrt{\frac{L}{2\pi}} \int d\omega_m \frac{E_m(x,y,\omega_m)}{\sqrt{v_g^{(m)}(\omega_m)}} e^{i(\omega_m t - \beta_m z)} \hat{a}_m(\omega_m) + \text{h.c.} \end{aligned} \tag{1.27}$$

where we used the group velocity $v_g^{(m)} = \frac{d\omega_m}{d\beta_m}$, and the transformation $\hat{a}_m(\beta_m) \to \sqrt{v_g^{(m)}}\hat{a}_m(\omega_m)$ to ensure normalization.

additionally, we are only interested in the SPDC process where one pump photon is converted into signal and idler photons, i.e. the terms of the form $\hat{a}_p \hat{a}_s^\dagger \hat{a}_s^\dagger + \text{h.c.}$, and thus we can reduce the Hamiltonian to:

$$\hat{H}_{SPDC} = \frac{\epsilon_0}{2} \int d\mathbf{r} d_{\text{eff}}(\mathbf{r}) \hat{E}_p^{(+)}(\mathbf{r},t) \hat{E}_s^{(-)}(\mathbf{r},t) \hat{E}_i^{(-)}(\mathbf{r},t) + \text{h.c.} \tag{1.28}$$

which will be the only term giving us one photon in each the signal and idler modes.

We can additionally consider that the pump field stays undepleted during the nonlinear interaction, and treat is as a classical field:

$$\hat{\mathbf{E}}_p(\mathbf{r},t) \sim \mathbf{E}_p(\mathbf{r},t) = \int d\omega_p A(\omega_p) E_p(x,y,\omega_p) e^{i(\omega_p t - \beta_p z)} + \text{c.c.} \tag{1.29}$$

with $\mathbf{E}_p$ the spatial profile of the pump mode associated with ω_p, and $A(\omega_p)$ is the spectral distribution of the pump.

Having found the shape of the nonlinear interaction and of the interacting optical fields, we can now try to identify the quantum states produced by SPDC. To do that, we will consider that initially, the state is in the vacuum for the signal and idler modes: $|\Psi(t \to -\infty)\rangle = |0\rangle$. We can compute the evolution of this state with time using the Schrödinger equation:

$$i\hbar \frac{d}{dt} |\Psi(t)\rangle = \hat{H}_{SPDC}(t) |\Psi(t)\rangle \tag{1.30}$$

In the low pump regime, we can neglect the probability of generating multiple photon pairs during the interaction, and consider that the state evolution can be approximated at first order as:

$$|\Psi(t)\rangle = e^{-\frac{i}{\hbar}\int_{-\infty}^{t} \hat{H}_{SPDC}(t)dt} |0\rangle \approx |0\rangle - \frac{i}{\hbar}\int_{-\infty}^{t} dt \hat{H}_{SPDC}(t) |0\rangle = |0\rangle - \alpha |\psi\rangle \tag{1.31}$$

where $|\psi\rangle$ is the two-photon SPDC state.

We can compute the final biphoton state $|\psi(t=\infty)\rangle$ by using the SPDC Hamiltonian:

$$\begin{aligned}
\alpha |\psi\rangle =& -\frac{i}{\hbar}\int dt \frac{\epsilon_0}{2}\int d\mathbf{r} d_{\text{eff}}(\mathbf{r}) \hat{E}_p^{(+)}(\mathbf{r},t) \hat{E}_s^{(-)}(\mathbf{r},t) \hat{E}_i^{(-)}(\mathbf{r},t) |0\rangle \\
=& -\frac{i\epsilon_0 L}{4\pi\hbar}\int dt d\omega_p d\omega_s d\omega_i d\mathbf{r} d_{\text{eff}}(\mathbf{r}) A(\omega_p) E_p(x,y,\omega_p) e^{i(\omega_p t - \beta_p z)} \\
& \times \frac{E_s^*(x,y,\omega_s)}{\sqrt{v_g^{(s)}(\omega_s)}} e^{-i(\omega_s t - \beta_s z)} \frac{E_i^*(x,y,\omega_i)}{\sqrt{v_g^{(i)}(\omega_i)}} e^{-i(\omega_i t - \beta_i z)} \hat{a}_s^\dagger(\omega_s) \hat{a}_i^\dagger(\omega_i) |0\rangle \\
=& -\frac{i\epsilon_0 L}{4\pi\hbar}\int dt d\omega_p d\omega_s d\omega_i \frac{A(\omega_p) e^{i\Delta\omega t}}{\sqrt{v_g^{(s)}(\omega_s) v_g^{(i)}(\omega_i)}} \\
& \times \int d\mathbf{r} d_{\text{eff}}(\mathbf{r}) E_p(x,y,\omega_p) E_s^*(x,y,\omega_s) E_i^*(x,y,\omega_i) e^{-i\Delta\beta z} \hat{a}_s^\dagger(\omega_s) \hat{a}_i^\dagger(\omega_i) |0\rangle \\
=& -\frac{i\epsilon_0 L}{2\hbar}\int d\omega_p d\omega_s d\omega_i \frac{A(\omega_p)\delta(\Delta\omega)}{\sqrt{v_g^{(s)}(\omega_s) v_g^{(i)}(\omega_i)}} \\
& \times \int d\mathbf{r} d_{\text{eff}}(\mathbf{r}) E_p(x,y,\omega_p) E_s^*(x,y,\omega_s) E_i^*(x,y,\omega_i) e^{-i\Delta\beta z} \hat{a}_s^\dagger(\omega_s) \hat{a}_i^\dagger(\omega_i) |0\rangle \\
=& -\frac{i\epsilon_0 L}{2\hbar}\int d\omega_s d\omega_i \frac{A(\omega_s+\omega_i)}{\sqrt{v_g^{(s)}(\omega_s) v_g^{(i)}(\omega_i)}} \\
& \times \int d\mathbf{r} d_{\text{eff}}(\mathbf{r}) E_p(x,y,\omega_s+\omega_i) E_s^*(x,y,\omega_s) E_i^*(x,y,\omega_i) e^{-i\Delta\beta z} \hat{a}_s^\dagger(\omega_s) \hat{a}_i^\dagger(\omega_i) |0\rangle
\end{aligned} \tag{1.32}$$

and finally

$$|\psi\rangle = \int d\omega_s d\omega_i \phi(\omega_s,\omega_i) \hat{a}_s^\dagger(\omega_s) \hat{a}_i^\dagger(\omega_i) |0\rangle \tag{1.33}$$

where we define the Joint Spectral Amplitude (JSA) of the photon pair:

$$\phi(\omega_s,\omega_i) = -\frac{i\epsilon_0 L}{2\alpha\hbar}\frac{A(\omega_s+\omega_i)}{\sqrt{v_g^{(s)}(\omega_s)v_g^{(i)}(\omega_i)}} \int d\mathbf{r} d_{\text{eff}}(\mathbf{r}) E_p(x,y,\omega_s+\omega_i) E_s^*(x,y,\omega_s) E_i^*(x,y,\omega_i) e^{-i\Delta\beta z}. \tag{1.34}$$

It corresponds to the probability amplitude to find the photon in signal mode at frequency ω_s and the photon in idler mode at frequency ω_i, i.e. the spectral wavefunction of the biphoton. This JSA will serve as a tool to study the spectral properties of the SPDC photon pairs, and we will generalize it to more complex modes in chapter 3. Knowing the particular shape of the modes, it is possible to derive more information on the quantum state of the photon pairs, but we will for now extract general principles from equation 1.34, by writing it as

$$\phi(\omega_s,\omega_i) = \gamma\ \chi_\Gamma(\omega_s,\omega_i)\cdot\phi_{\text{spectral}}(\omega_s+\omega_i)\cdot\phi_{\text{PM}}(\omega_s,\omega_i), \tag{1.35}$$

where γ is a normalization constant. The efficient generation is again constrained by a phase-matching term

$$\phi_{\text{PM}}(\omega_s,\omega_i) = \int dz e^{-i\Delta\beta z},$$

which means that the JSA will be enhanced for frequencies close to perfect phase-matching while being suppressed for frequencies which do not verify the phase-matching condition. The JSA is additionally modulated by the spectral distribution of the pump appearing in

$$\phi_{\text{spectral}}(\omega_s+\omega_i) = A(\omega_s+\omega_i)$$

because of the energy conservation, and dependent on the nonlinear overlap integral

$$\chi_\Gamma(\omega_s,\omega_i) = \frac{1}{\sqrt{v_g^{(s)}(\omega_s)v_g^{(i)}(\omega_i)}}\int dxdy d_{\text{eff}}(x,y) E_p(x,y,\omega_s+\omega_i) E_s^*(x,y,\omega_s) E_i^*(x,y,\omega_i),$$

which can be dependent on the frequencies ω_s and ω_i.

We will later compute again the quantum states for specific interacting modes, which we present in the following section, along with some phase-matching strategies in AlGaAs waveguides.

1.2 Phase-matching strategies in AlGaAs waveguides

As shown in the previous section, phase-matching of the three interacting field is a key parameter for efficient nonlinear conversion in Three-Wave Mixing processes. This condition, added to the condition of energy conservation, leads to the following equation system for the SPDC process:

$$\begin{cases} \omega_3 = \omega_2 + \omega_1 \\ \boldsymbol{\beta}_3 = \boldsymbol{\beta}_1 + \boldsymbol{\beta}_2 \end{cases} \tag{1.36}$$

In materials with normal dispersion, i.e. where the refractive index n is a monotonic increasing function of ω, $\beta_3 = \frac{n_3(\omega_3)\omega_3}{c} = \frac{n_3(\omega_3)\omega_1}{c} + \frac{n_3(\omega_3)\omega_2}{c} > \beta_1 + \beta_2$ (since

$n_3(\omega_3) > n_1(\omega_1), n_2(\omega_2)$), making phase-matching in principle impossible to attain if all fields are in the same mode. Material birefringence can be exploited to achieve phase-matching in bulk crystals, such as Barium borate [86], by exploiting polarization to compensate for chromatic dispersion, but as AlGaAs is an isotropic material, this solution is not possible in the bulk material. Thus, it is necessary to implement additional phase-matching strategies, which we will discuss in this section.

The first strategy that can be implemented to satisfy the phase-matching condition is the so-called Quasi-Phase-Matching (QPM), where the material is engineered to periodically modulate the nonlinear coefficient of the medium, with a period of length $\frac{2\pi}{|\Delta\beta|}$. This allows for a modulation of $d_{\text{eff}}(\mathbf{r})$ over the propagation direction z to mitigate the effect of the spatially-dependent phase of the nonlinear generation in the material.

In the ideal case, the sign of the nonlinear coefficient is changed (figure 1.2a), which results in constructive interference of the generated fields along the propagation direction, but in a less constraining manner, it is also possible to change the value from a low to high value (figure 1.2b) to mitigate the destructive interference and allow for the build-up of the generated fields with the propagation in the material. Albeit not as effective as perfect phase-matching, this approach has allowed the realization of efficient SPDC sources in dielectric bulk crystals and waveguides (such as PPLN [125, 126][5] and PPKTP[6] [127]). In GaAs and AlGaAs, it can be realized by (1) periodical poling of the structure [128, 129] (rotating the crystal direction around the growth axis), which induces losses and is a challenging fabrication process, (2) by changing the Aluminum concentration periodically to alternate between high and low values of the nonlinear coefficient [130], or (3) by exploiting the geometry of the structure supporting the interacting fields [131–133] (e.g. using a ring resonator or gallery modes in microdisks, as sketched in figure 1.2c) to change the propagation direction along the structure and thus achieve effective periodic rotation of the crystal orientation.

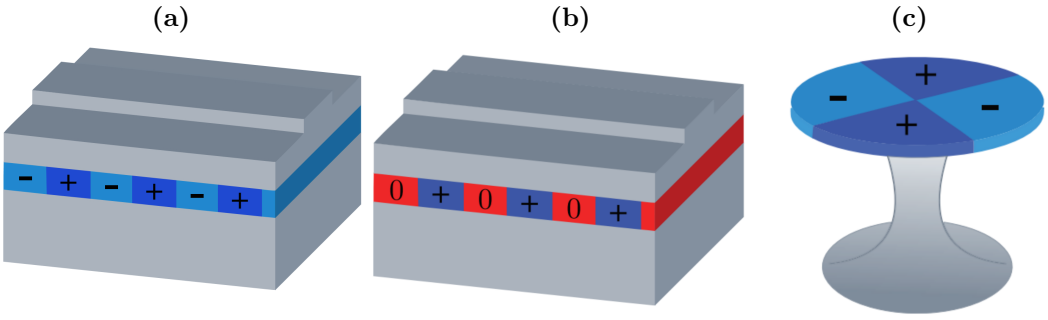

Figure 1.2: Sketch of different implementations of quasi-phase-matching strategies, a) domain-reversal QPM, where the sign of the nonlinear coefficient periodically changes along the propagation direction, b) domain-disordered QPM, were the nonlinear coefficient periodically goes from high to low values, and c) geometrical QPM in a circular structure, sketched for a microdisk.

In this thesis, we have used two other phase-matching techniques called counterpropagating and modal phase-matching; we describe them successively in the following.

[5] Periodically poled lithium niobate.
[6] Perdiodically poled potassium titanyl phosphate.

1.2.1 Phase-matching in a counterpropagating geometry

In this paragraph, we present a counterpropagating phase-matching scheme, using an AlGaAs ridge waveguide as a support. The working principle of the source is the following (see figure 1.3): a pulsed pump beam is impinging on top of an AlGaAs waveguide, producing SPDC photon pairs through nonlinear interaction with the waveguide material, with the direction propagation of the two photons in the waveguide being opposite. In this geometry, the two photons are readily spatially separated by the generation process. We first present the epitaxial structure of the source and the interacting modes, and then describe the phase-matching condition in this scheme.

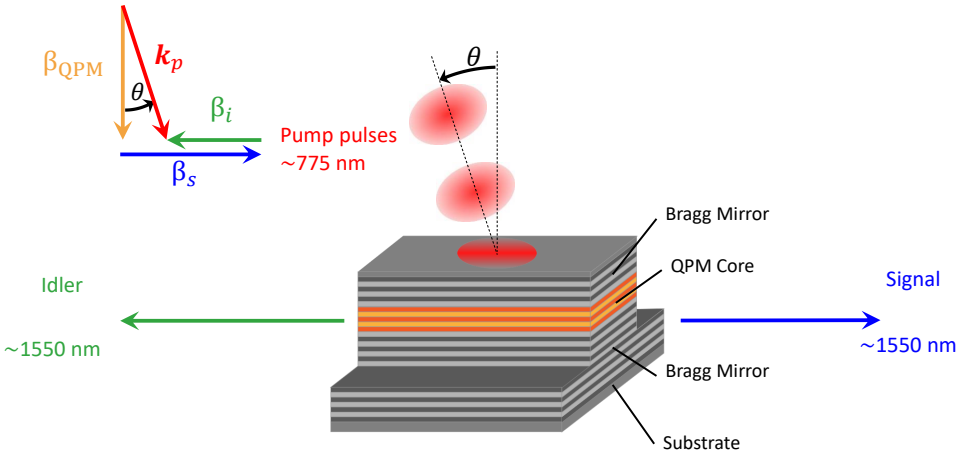

Figure 1.3: Working principle of the counterpropagating photon pair source: the pump beam impinges on top of the structure, and the signal and idler photons propagate in opposite directions inside the waveguide. The QPM core is represented in orange, while the different shades of grey indicate different Al concentrations.

1.2.1.1 Epitaxial structure and interacting modes

The source consists of an AlGaAs ridge waveguide made from a stacking of epitaxial layers with different Al concentration, as reported in table 1.1.

The design of the epitaxial structure is detailed in previous theses from our group [134, 135], and here we simply report its basic principles. The propagation core, where the SPDC photons will be generated, consists of AlGaAs layers with alternating Al concentration to implement QPM in the vertical direction, by alternating between low $\chi^{(2)}$ values and high $\chi^{(2)}$ values. It is surrounded by Bragg mirrors, which serve three different purposes: they confine the signal and idler modes produced by SPDC by total internal reflection, they provide a microcavity around the core which is resonant for the pump field wavelength at 775 nm, and finally they are engineered to prevent penetration of the

Number of periods	Role	Al content (%)	Thickness h (nm)
1	Substrate	0	
36	Bottom Bragg	90	70.8
		35	50.1
1	Buffer	90	125.1
4	Core	25	129.1
	Core	80	104.3
1	Core	25	129.1
1	Buffer	90	125.1
14	Top Bragg	35	50.1
		90	70.8
1	Cap	0	46.2

Table 1.1: Nominal epitaxial structure for the counterpropagating source.

pump field into the substrate[7]. To fabricate waveguides from this epitaxial structure, the ridges are chemically etched into the structure using photo-lithography, and we detail the fabrication process in the following chapter.

In this particular structure, the nonlinear interaction results in type II SPDC with the generation of two orthogonally polarized photons. We use the LUMERICAL software to simulate the supported modes of the waveguide, the two SPDC modes represented in figure 1.4 are the fundamental TE and TM telecom modes[8]. The two modes have slightly different effective indices $n_{TE} \simeq 3.0852$ and $n_{TM} =\simeq 3.0827$, showing a slight modal birefringence $\Delta n \simeq 0.0025$ due to the epitaxial structure and optical field confinement. It is important to note that in this case, two nonlinear interactions are possible: if we label the photon propagating to the right as signal, and the one propagating to the left as idler, the photon pairs produced can either have a signal photon with TE polarization, and an idler photon with TM polarization, or vice-versa.

1.2.1.2 Phase-matching curve

In our counterpropagating geometry, the pump beam has an incident wavevector $\boldsymbol{k_p}$ that is almost orthogonal to the propagation direction of the signal and idler modes. As mentioned in the previous paragraph, phase-matching in the vertical direction is ensured by the periodical change in Al concentration of the epitaxial layers of the core. The corresponding propagation constants (β_s and β_i for the signal and idler photons) are sketched in figure 1.3, where the pump beam impinges on top of a waveguide with a slight angle θ.[9] We can write the phase-matching condition in the waveguide direction, as well

[7]It is important that the pump field stays confined in the core and Bragg mirror layers, since absorption of the pump photons could lead to incoherent re-emission processes.

[8]Note that SPDC can in principle occur for higher-order signal and idler modes as well, but their nonlinear overlap with the pump field is reduced, and their collection in single-mode optical fibers is inefficient.

[9]Note that this angle can *a priori* result in the QPM being inefficient, because it changes the vertical component of the pump propagation constant, but the angles we use are typically below 1°, which does

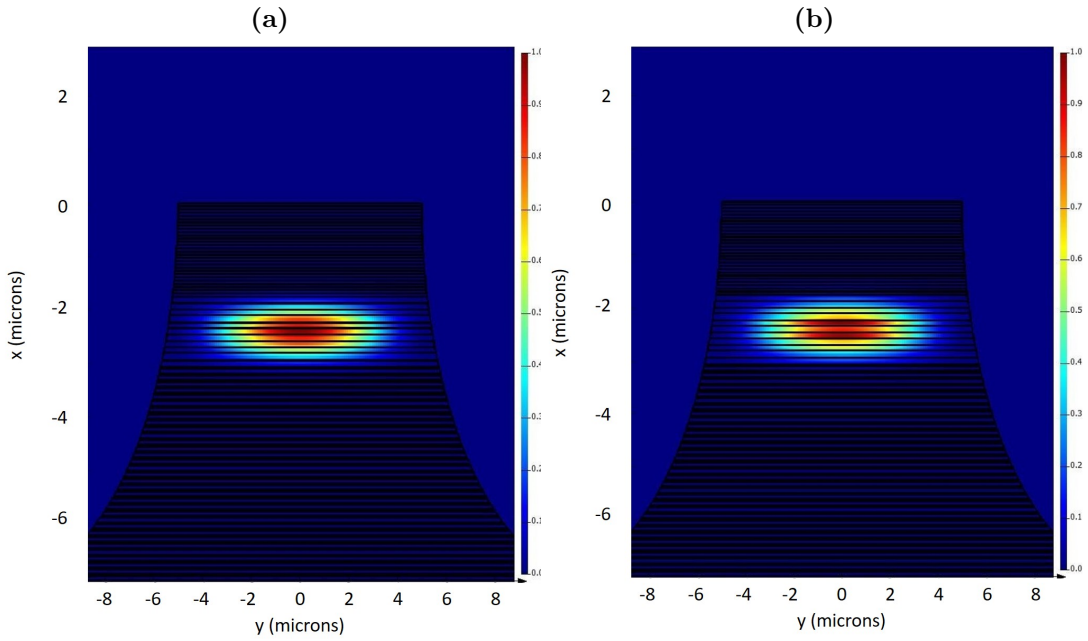

Figure 1.4: Simulated field intensity for the two fundamental TE (a) and TM (b) modes at 1550 nm, for a 5 μm wide waveguide with a wet etching profile.

as the energy conservation, as[10]:

$$\begin{cases} \omega_p = \omega_s + \omega_i \\ k_p \sin(\theta) = \beta_s - \beta_i \end{cases} \tag{1.37}$$

By substituting $k_p = \omega_p/c$, and $\beta_{s/i} = n_{s/i}(\omega_{s/i})/c$, we get:

$$\begin{cases} \omega_p = \omega_s + \omega_i \\ \omega_p \sin(\theta) = n_s(\omega_s)\omega_s - n_i(\omega_i)\omega_i \end{cases} \tag{1.38}$$

It is convenient to rewrite this equation system as an equation giving ω_i as a function of ω_s, assuming the pump frequency ω_p is fixed:

$$\begin{cases} \omega_i = \omega_p - \omega_s \\ \omega_i = \frac{n_s}{n_i}\omega_s - \frac{\omega_p}{n_i}\sin(\theta) \end{cases} \tag{1.39}$$

The equation system 1.39 defines two functions of ω_s, which are of the form $\omega_i = A - \omega_s$ and $\omega_i = B\omega_s + C$, with A and B positive values. As such, the two function always have a crossing point, meaning that for any value of the pump wavelength, *there always exists two values of* ω_s *and* ω_i *that simultaneously satisfy both the energy conservation condition and*

not significantly alter the phase-matching efficiency in the vertical direction.

[10]Here, the propagation constant along the z-axis for the pump beam is $k_p^{int} = n_p\omega_p \sin(\theta^{int})$ inside the material, where n_p is the effective index of the pump, and θ^{int} the angle inside the material, but by Snell-Descartes law, $n_p sin(\theta^{int}) = sin(\theta)$, which is valid at every interface, so we can effectively consider only the z-component of the wavevector in free space for the pump.

the phase-matching condition, and the position of the crossing point is tunable with the angle θ. The two conditions are graphically represented in figure 1.5a, as well as the signal and idler wavelengths for perfect phase-matching as a function of θ, for both interactions, in figure 1.5b. Tuning the pump angle can thus allow to change the frequencies of the generated signal and idler photons, and there is for each interaction a degeneracy angle $\theta_{deg} = \pm \arcsin \frac{n_s - n_i}{2}$ for which the signal and idler photons have degenerate frequency $\omega_p/2$. The spectral width of the generated photons is of the order of $\Delta\lambda \simeq 0.5$ nm in our typical experimental conditions, which is the value fixed by the phase-matching and energy conservation conditions. In the following, we will always select only one of the two interactions[11], by simply placing a TE-oriented polarizer on the right output of the waveguide, and a TM-oriented polarizer on the left.

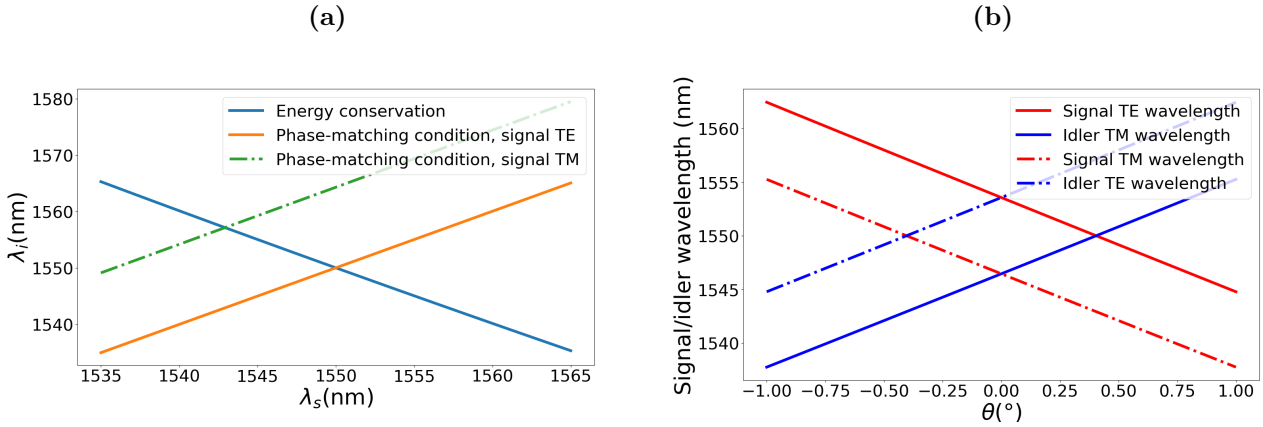

Figure 1.5: a) energy conservation and phase-matching condition for λ_i as a function of λ_s, simulated for $\lambda_p = 775$ nm and $\theta \simeq 0.40°$, which corresponds to the degeneracy angle for the interaction giving a TE-polarized signal and TM-polarized idler, and b) accordability curve giving λ_s and λ_i as a function of θ.

1.2.2 Phase-matching in a copropagating geometry

We now describe another phase-matching technique, called modal phase-matching scheme in a copropagating geometry, for the interaction of three fields in a waveguide (see figure 1.6). In order to ensure the phase-matching condition, the pump mode must have an effective refractive index approximately equal to the effective refractive indices of the signal and idler modes, while verifying the energy conservation condition $\omega_p = \omega_s + \omega_i$, which is enabled by the multimodality of the waveguide. In particular, higher-order modes tend to have heavily modified refractive indices, which is useful for phase-matching with fundamental modes at different frequencies. Here, we present a source of SPDC photon pairs with modal phase-matching based on the interaction between the TE_{00} and TM_{00} fundamental telecom modes around 1550 nm and a Bragg mode around 775 nm, where the refractive index verifies $n_{Bragg}(775\text{nm}) \simeq n_{TE_{00}}(1550\text{nm}) \simeq n_{TM_{00}}(1550\text{nm})$, allowing for degenerate phase-matching around these frequencies.

[11] Interesting quantum states can also be produced by simultaneously measuring the two interactions, which are produced coherently, as reported by Francesconi *et. al.* [136]

We first present the epitaxial structure and the interacting modes, and then describe the phase-matching condition for the copropagating geometry.

1.2.2.1 Epitaxial structure and interacting modes

The structure that we use for the generation of SPDC photon pairs in a copropagating geometry consists as previously of an AlGaAs ridge waveguide etched into an epitaxial structure made from superimposed AlGaAs layers with different Al concentrations. The corresponding epitaxial structure is reported in table 1.2. The structure is a Bragg reflection waveguide (see figure 1.6), consisting of a core surrounded above and below by Bragg mirrors, and designed to support Bragg modes consisting of three lobes around 775 nm (figure 1.7c,d), additionally to the fundamental TE and TM telecom modes around 1550 nm (figure 1.7a,b). The source and the epitaxial structure were designed and optimized by Adeline Orieux, a former PhD student of our group, in order to achieve both a high non-linear overlap, and dispersion relations which allow for phase-matching around telecom wavelengths for the signal and idler photons. This structure can support in principle both type 0, type I and type II SPDC.

Number of periods	Role	Al content (%)	Thickness h (nm)
1	Substrate	0	
6	Bottom Bragg	80	276
		25	114
1	Core	45	355.5
6	Top Bragg	25	114
		80	276
1	Cap	0	250

Table 1.2: Nominal epitaxial structure for the co-propagating source.

1.2.2.2 Interaction types and phase-matching curves

In the copropagating geometry, since the propagation direction is the same for the pump, signal and idler fields, the phase-matching condition can be written only along this direction. If we use the dispersion relation $\beta_m = n_m(\omega_m)\omega_m/c$, with $m = p, s, i$, we can then write both the energy conservation and the phase-matching condition as:

$$\begin{cases} \omega_p = \omega_s + \omega_i \\ n_p(\omega_p)\omega_p = n_s(\omega_s)\omega_s + n_i(\omega_i)\omega_i \end{cases} \tag{1.40}$$

This shows that in order to achieve phase-matching and efficient SPDC, the pump mode must have an effective index similar to the signal and idler mode at their respective frequencies.

We simulated the effective indices of the fundamental and Bragg modes in both polarizations as a function of the wavelength, which we report in figure 1.8. From the crossing points (circled), we can find the pump wavelengths allowing for perfect phase-matching

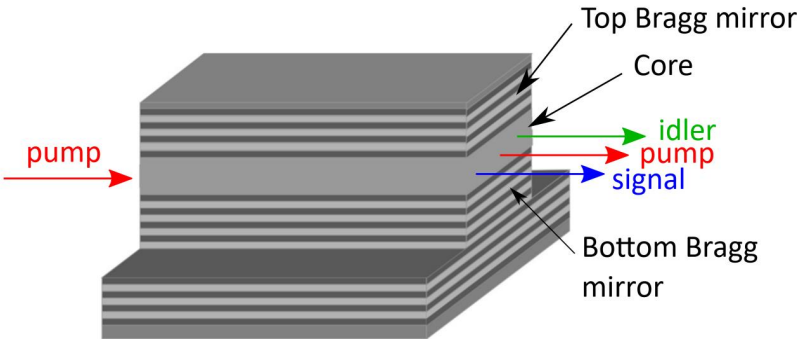

Figure 1.6: Sketch of the co-propagating modal phase-matching, where the pump photons are down-converted into signal and idler photons propagating in the same direction inside the waveguide.

at degeneracy (i.e. when both signal and idler photons have the same frequencies) for the different types of SPDC.

The corresponding conditions for phase-matching are (writing $n_{B,TE(TM)}$ the index of the pump and $n_{TE(TM)}$ that of SPDC photons):

$$\begin{cases} n_{B,TM}(\omega_p)\omega_p = n_{TM}(\omega_s)\omega_s + n_{TM}(\omega_i)\omega_i & \text{for type 0 SPDC} \\ n_{B,TM}(\omega_p)\omega_p = n_{TE}(\omega_s)\omega_s + n_{TE}(\omega_i)\omega_i & \text{for type I SPDC} \\ n_{B,TE}(\omega_p)\omega_p = n_{\sigma}(\omega_s)\omega_s + n_{\sigma_\perp}(\omega_i)\omega_i & \text{for type II SPDC where } \sigma = TE(TM) \\ & \text{and } \sigma_\perp \text{ is the orthogonal polarization} \end{cases} \tag{1.41}$$

yielding at degeneracy ($\omega_s = \omega_i = \omega_p/2$):

$$\begin{cases} n_{B,TM}(\omega_p) = n_{TM}(\omega_p/2) & \text{for type 0 SPDC} \\ n_{B,TM}(\omega_p) = n_{TE}(\omega_p/2) & \text{for type I SPDC} \\ n_{B,TE}(\omega_p) = \left(n_{TE}(\omega_p/2) + n_{TM}(\omega_p/2)\right)/2 & \text{for type II SPDC} \end{cases} \tag{1.42}$$

As in the case of SFG in a waveguide, the efficiency of the process scales as $\text{sinc}^2\left(\Delta\beta\frac{L}{2}\right)$, which depends on the frequencies of the different interacted fields, and as such influences the shape of the frequency correlations between the two photons (equation 1.34). We can simulate the phase-matching term $\text{sinc}^2\left(\frac{\Delta\beta L}{2}\right)$, as a function of the pump wavelength and the signal wavelength, as shown on the example of type 0 in figure 1.9a. The shape of the phase-matching curve shows that the efficiency of the SPDC process is maximal for the degeneracy pump wavelength (here $\simeq 773.48$ nm) and the phase-matching condition cannot be verified for pump wavelengths above this value. As the pump wavelength decreases, the curve separates in two arms, showing that tuning the pump wavelength allows to manipulate the spectral distribution of the signal and idler photons, which is given by taking the cut of the phase-matching efficiency with respect to λ_s for a fixed value of λ_p. The spectral distribution for the SPDC photons produced by the type 0

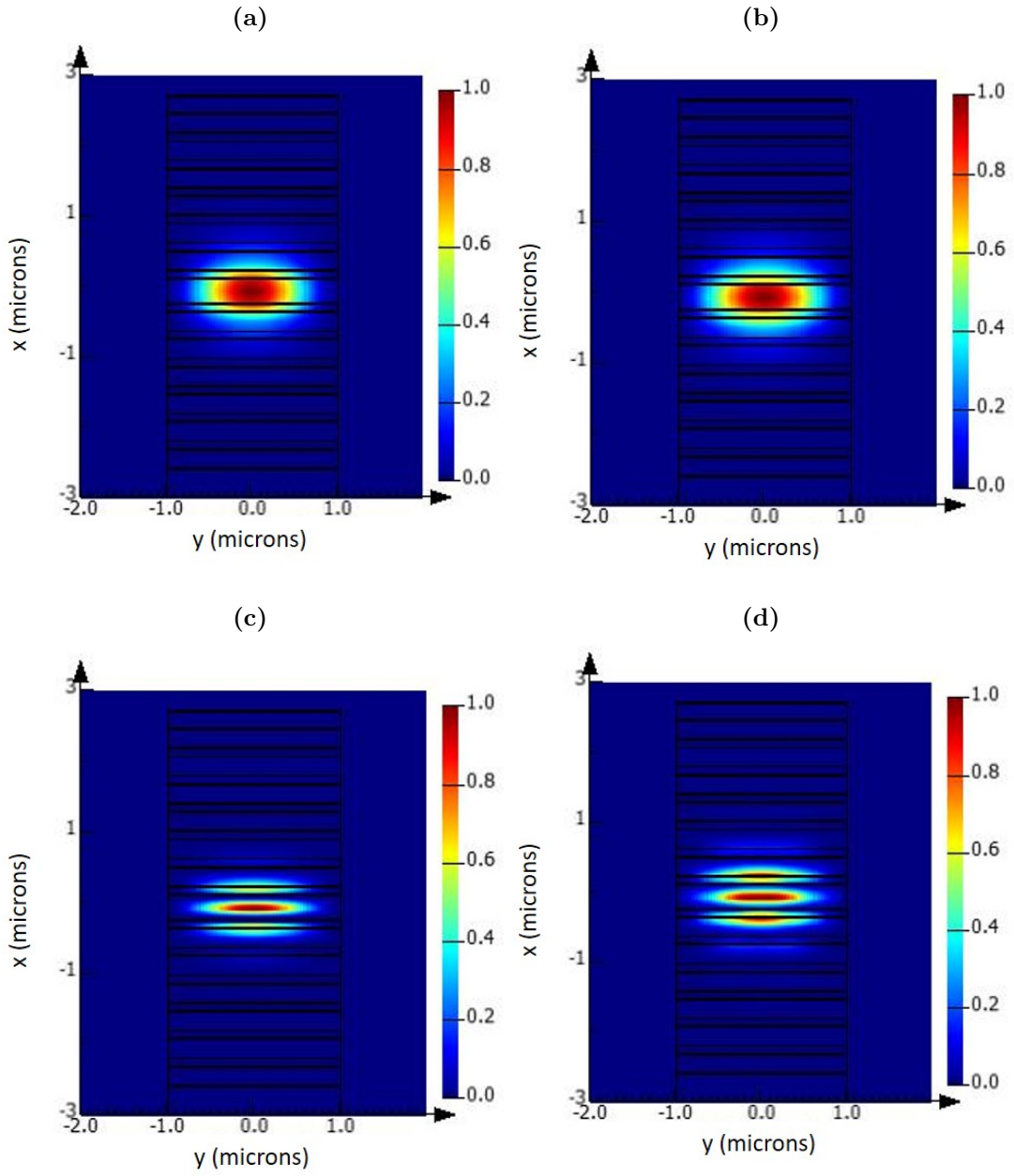

Figure 1.7: Simulated field intensity for the two fundamental TE (a) and TM (b) modes at 1550 nm, and for the Bragg TE (c) and TM (d) modes at 775 nm for a 2 μm wide waveguide with dry etching profile.

SPDC process at degeneracy wavelength is shown in figure 1.9b. The spectral width is approximately $\Delta\lambda \simeq 60$ nm for a 2 μm wide and 2 mm long waveguide, which is 2 orders of magnitude higher than the spectral width for the counterpropagating scheme.

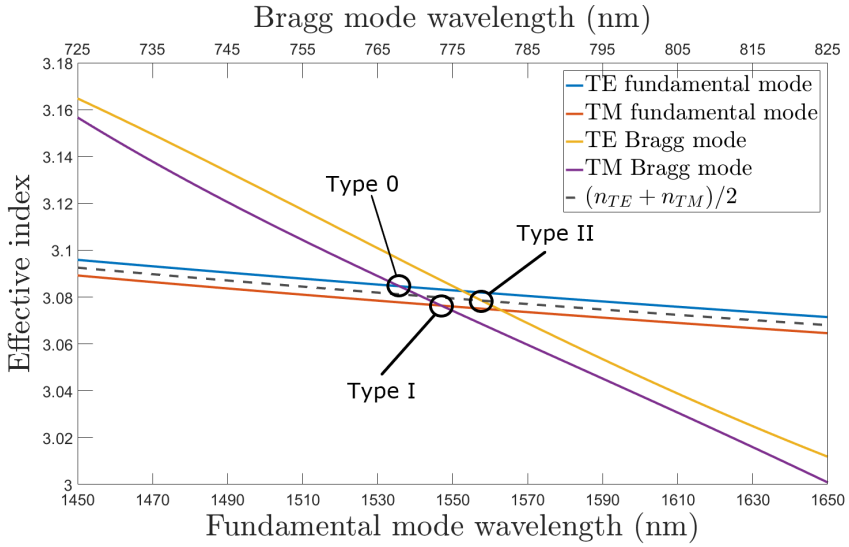

Figure 1.8: Simulated effective refractive indices for the fundamental TE and TM modes, as well as the Bragg TE and TM modes for a 2 μm wide waveguide with an ICP etching profile. The circled crossing points show where the different SPDC types are possible at degeneracy.

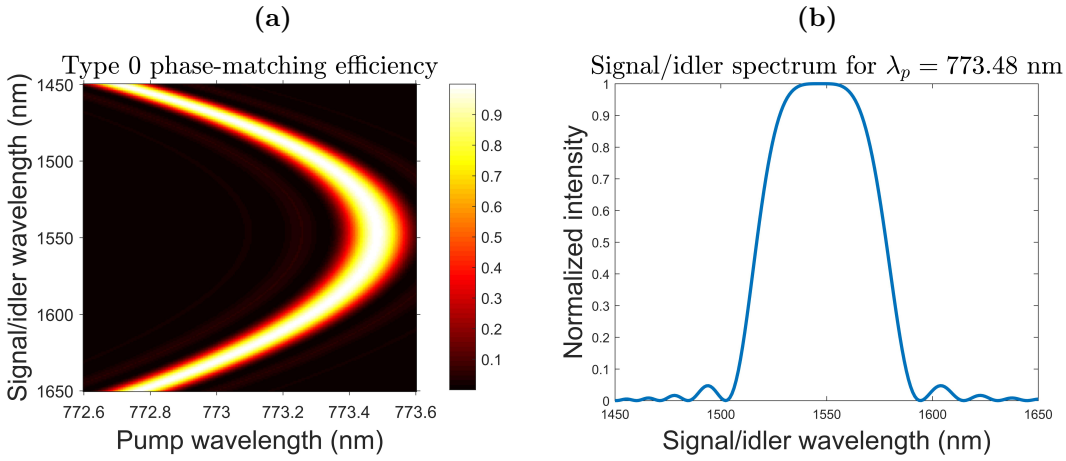

Figure 1.9: a) Simulated phase-matching efficiency for type 0 SPDC for a 2 μm wide and 2 mm long waveguide in a copropagating SPDC scheme, as a function of the pump wavelength and of the signal wavelength, the idler wavelength being determined by the energy conservation condition. b) Marginal spectrum of the SPDC photons at pump wavelength $\lambda_p = 773.48$ nm (at maximum efficiency for phase-matching at degeneracy), for the same waveguide in the copropagating scheme. The generated photons have spectral width at half maximum $\Delta\lambda \simeq 60$ nm.

Chapter 2

Biphoton exchange statistics engineering in a counterpropagating phase-matching scheme

In this chapter, we describe the generation of frequency-entangled photon pairs using a counterpropagating phase-matching scheme in an AlGaAs waveguide, allowing to manipulate the exchange statistics of the two photons. This scheme has be studied in a previous thesis of our group [137] to demonstrate the possibility to generate photon pairs with fermionic exchange statistics. Here we report the theoretical foundation of the exchange statistics manipulation, as well as the latest experimental results having led to anyonic exchange statistics for photon pairs.

Contents

2.1 Theoretical description of the quantum state

In this section, we consider the counterpropagating phase-matching scheme described in section 1.2.1 for photon pair generation using SPDC, and we describe the quantum state of the generated photon pairs by using the formalism introduced in section 1.1.6, and starting from equation 1.34. We consider a single nonlinear interaction, producing signal photon with TE polarization and idler photon with TM polarization.

2.1.1 Dependance of the biphoton wavefunction on the pump profile

Let us first consider the shape of the Joint Spectral amplitude, which we recall from equation 1.34:

$$\phi(\omega_s,\omega_i) = -\frac{i\epsilon_0 L}{2\alpha\hbar}\frac{A(\omega_s+\omega_i)}{\sqrt{v_g^{(s)}(\omega_s)v_g^{(i)}(\omega_i)}} \int d\mathbf{r} d_{\text{eff}}(\mathbf{r}) E_p(\mathbf{r},\omega_s+\omega_i) E_s^*(\mathbf{r},\omega_s) E_i^*(\mathbf{r},\omega_i) e^{-i\Delta\beta z} \tag{2.1}$$

with the phase-mismatch $\Delta\beta = k_p\sin(\theta) - \beta_s + \beta_i$. The spatial profile of the three interacting fields are involved in equation 2.1, so in order to derive the quantum state, one needs the exact spatial distributions of the considered modes. We denote the propagation direction z, the growth direction x, and the transverse direction y. The signal and idler fields have transverse profiles $E_s(\mathbf{r},\omega_s) = \varphi_{TE}(x,y,\omega_s)$ and $E_i(\mathbf{r},\omega_i) = \varphi_{TM}(x,y,\omega_i)$ which depend on the supported modes of the waveguides and their frequencies. Since the SPDC process is efficient only for a very narrow range of signal and idler wavelengths from the phase-matching term (around the crossing point between the energy conservation condition and the phase-matching condition in figure 1.5(a)), we can consider these spatial modes independent of the SPDC photons frequencies, and write them as $\varphi_{TE}(x,y,\omega_s) = \varphi_s(x,y)$ and $\varphi_{TM}(x,y,\omega_i) = \varphi_i(x,y)$. We now need to examine the shape of the pump field $E_p(\mathbf{r},\omega_p)$.

We assume that the pump beam only propagates in the x, z plane, so that its wavevector in the y direction is zero: $k_p^y = 0$. Assuming the transverse profile of the pump beam is separable in the transverse y, z plane[1], one can write the pump field spatial profile as a product of its transverse spatial profile and of the vertical microcavity response which can depend on the pump frequency ω_p:

$$E_p(\mathbf{r}, \omega_p) = f_{\mu cav}(x, \omega_p)\varphi_p^z(z, \omega_p)\varphi_p^y(y, \omega_p) \tag{2.2}$$

where $f_{\mu cav}$ is the cavity response function, dependent on ω_p and x, and φ_p^y and φ_p^z describe the pump spatial profile along the y and z direction respectively. In our case, the effective second-order coefficient d_{eff} is only dependent on x, since the material only changes along the growth direction. This yields:

$$\begin{aligned}
\phi(\omega_s, \omega_i) = &- \frac{i\epsilon_0 L}{2\alpha\hbar} \frac{A(\omega_s + \omega_i)}{\sqrt{v_g^{(s)}(\omega_s) v_g^{(i)}(\omega_i)}} \\
&\int d\mathbf{r} d_{\text{eff}}(x) f_{\mu cav}(x, \omega_s + \omega_i) \varphi_p^z(z, \omega_s + \omega_i) \varphi_p^y(y, \omega_s + \omega_i) \\
&\varphi_s^*(x, y) \varphi_i^*(x, y) e^{-i\Delta\beta z} \\
= &- \frac{i\pi\epsilon_0}{\alpha\hbar} \frac{A(\omega_s + \omega_i)}{\sqrt{v_g^{(s)}(\omega_s) v_g^{(i)}(\omega_i)}} \\
&\cdot \int dx dy d_{\text{eff}}(x) f_{\mu cav}(x, \omega_s + \omega_i) \varphi_p^y(y, \omega_s + \omega_i) \varphi_s^*(x, y) \varphi_i^*(x, y) \\
&\cdot \int dz \varphi_p^z(z, \omega_s + \omega_i) e^{-i\Delta\beta z}
\end{aligned} \tag{2.3}$$

which we write, as in chapter 1

$$\phi(\omega_s, \omega_i) = \gamma \ \chi_\Gamma(\omega_s, \omega_i) \cdot \phi_{\text{spectral}}(\omega_s + \omega_i) \cdot \phi_{\text{PM}}(\omega_s, \omega_i) \tag{2.4}$$

where the terms

$$\begin{aligned}
\phi_{\text{spectral}}(\omega_s, \omega_i) =& A(\omega_s + \omega_i) \\
\chi_\Gamma(\omega_s, \omega_i) =& \frac{1}{\sqrt{v_g^{(s)}(\omega_s) v_g^{(i)}(\omega_i)}} \int dx dy d_{\text{eff}}(x) f_{\mu cav}(x, \omega_s + \omega_i) \varphi_p^y(y, \omega_s + \omega_i) \varphi_s^*(x, y) \varphi_i^*(x, y)
\end{aligned} \tag{2.5}$$

encapsulates both the spectrum of the pump, the spectral response of the cavity, and the nonlinear overlap integral between the three fields, and the term

$$\phi_{PM}(\omega_s, \omega_i) = \int dz \varphi_p^z(z, \omega_p) e^{-i\Delta\beta z} \tag{2.6}$$

corresponds to the phase-matching condition. The latter term is of particular interest, as it gives a way of controlling the JSA of the photon pairs through the tuning of the pump spatial profile. If we rewrite the function with two new variables $\omega_+ = \omega_s + \omega_i$, and

[1]Since the beam produced by the experimental pump laser has a Gaussian profile, and since it is possible to control the spatial profile of the pump beam, which we will discuss later in the chapter, this assumption can be made reasonably.

$\omega_- = \omega_s - \omega_i$, we see that ϕ_{spectral} only depends on ω_+ and not on ω_-. Additionally, since the spectral width of the generated photons is small, we can consider the group velocities and mode profiles to be independent of the different frequencies, and thus treat χ_Γ as a constant term. Thus the only term depending on ω_- (through the phase mismatch $\Delta\beta$) is ϕ_{PM}, making it dependent upon the exchange of the two photon frequencies $(\omega_s, \omega_i) \rightarrow (\omega_i, \omega_s)$ (equivalent to the transformation $(\omega_+, \omega_-) \rightarrow (\omega_+, -\omega_-)$). In this chapter, we will specifically study the engineering of the exchange symmetry of the JSA, and we will thus be particularly interested in the ω_- parameter[2].

Let us make the dependence of ϕ_{PM} on ω_+ and ω_- explicit. First, the phase-mismatch term can be written as

$$\Delta\beta = \frac{1}{c}\left(\omega_+ \sin\theta - n_s(\omega_s)\omega_s + n_i(\omega_i)\omega_i\right). \tag{2.7}$$

Writing $\omega_{s/i} = \frac{\omega_+}{2} \pm \frac{\omega_-}{2} = \omega_{deg} \pm \frac{\omega_-}{2}$, with $\omega_{deg} = \omega_p/2$,[3] we can then use the Taylor expansion of the effective modal indices for the signal and idler modes around the degeneracy frequency, giving

$$n_{s/i}(\omega_{s/i}) = n_{s/i}(\omega_{deg}) \pm \frac{\omega_-}{2}\left.\frac{dn_{s/i}}{d\omega}\right|_{\omega_{deg}} + \frac{\omega_-^2}{8}\left.\frac{d^2 n_{s/i}}{d\omega^2}\right|_{\omega_{deg}}. \tag{2.8}$$

Injecting it into equation 2.7, and remembering that $\sin\theta_{deg} = \frac{n_s - n_i}{2}$, we obtain to second order in ω_- (where the refractive indices and their derivatives are all evaluated at ω_{deg}):

$$\begin{aligned}\Delta\beta =& \frac{1}{c}\left(\omega_+\left(\sin\theta - \sin\theta_{deg}\right) - \frac{\omega_-}{2}\left(n_s + n_i + \omega_{deg}\frac{d(n_s+n_i)}{d\omega}\right)\right.\\ &\left. -\frac{\omega_-^2}{8}\left(2\frac{d(n_s-n_i)}{d\omega} + \omega_{deg}\frac{d^2(n_s-n_i)}{d\omega^2}\right) + O(\omega_-^3)\right)\\ =& \frac{\omega_+}{c}\left(\sin\theta - \sin\theta_{deg}\right) - \omega_-\overline{v_g^{-1}} - \left(\frac{\omega_-}{2}\right)^2\delta_{GVD}\end{aligned} \tag{2.9}$$

with $\overline{v_g^{-1}}$ the mean of the inverse group velocity (evaluated at ω_{deg}):

$$\begin{aligned}\overline{v_g^{-1}} =& \frac{1}{2}\left(\frac{1}{v_g^s} + \frac{1}{v_g^i}\right) = \frac{1}{2}\left(\frac{d\beta_s}{d\omega} + \frac{d\beta_i}{d\omega}\right)\\ =& \frac{1}{2c}\left(n_s + n_i + \omega_{deg}\left(\frac{dn_s}{d\omega} + \frac{dn_i}{d\omega}\right)\right)\end{aligned} \tag{2.10}$$

and δ_{GVD} is the half-difference between the group velocity dispersions:

$$\delta_{GVD} = \frac{1}{2}\frac{d}{d\omega}\left(\frac{1}{v_g^s} - \frac{1}{v_g^i}\right) = \frac{1}{2c}\left(2\frac{d(n_s-n_i)}{d\omega} + \omega_{deg}\frac{d^2(n_s-n_i)}{d\omega^2}\right). \tag{2.11}$$

For our signal TE and idler TM modes at 1550 nm, numerical simulations done with Lumerical give Group Velocity Dispersions values of $GVD_{TE} \simeq 1.9 \cdot 10^{-4}$ fs^{2}m^{-1} and

[2]However, this source can generate other interesting states of the JSA, presented in G. Boucher's [135] and S. Francesconi's [137] theses.

[3]It is important to note that this yields $\omega_{deg} = \frac{\omega_s + \omega_i}{2}$ because of the energy conservation.

$GVD_{TM} \simeq 2.1 \cdot 10^{-4}$ fs^{2}m^{-1}, while the group velocities are $v_g^{TE} = 9.53 \cdot 10^7$ ms^{-1} and $v_g^{TM} = 9.57 \cdot 10^7$ ms^{-1}, giving $\overline{v_g^{-1}} = 1.05 \cdot 10^{-8}$ sm^{-1}. For a 5 mm long sample, the phase difference generated by the linear term $\omega_- \overline{v_g^{-1}}$ over the waveguide length is of the order of π for a frequency $\omega_- \simeq 10^{11}$ rad $\cdot$ s^{-1}, which gives a phase difference resulting from the quadratic term $\left(\frac{\omega_-}{2}\right)^2 \delta_{GVD}$ of $\Delta\phi \simeq 7.6 \cdot 10^{-17}$ rad. We can thus neglect the quadratic term in equation 2.9, since it does not generate significant phase rotations in the phase-mismatch. The phase-mismatch can thus be reduced to:

$$\Delta\beta = \frac{\omega_+}{c}\left(\sin\theta - \sin\theta_{deg}\right) - \omega_- \overline{v_g^{-1}}. \tag{2.12}$$

The first term shows that for efficient phase-matching at degeneracy (i.e. for $\omega_- = 0$), the pump beam must impinge on top of the waveguide with the correct angle θ_{deg}, and the term $\overline{v_g^{-1}}$ conditions the range of ω_- (which quantifies the deviation from degeneracy) for phase-matching, and thus dictates the width of the JSA in the ω_- direction (i.e. along the antidiagonal in the (ω_s, ω_i) coordinates). Additionally, we can consider the transverse spatial profile of the pump beam independent of the frequency, since the pump propagates in free space without dispersion: $\varphi_p^z(z, \omega_+) = \mathcal{A}_p(z)$. Taking all this into account, the phase-matching term in the JSA can finally be written:

$$\phi_{PM}(\omega_+, \omega_-) = \int_{z=-L/2}^{L/2} dz \mathcal{A}_p(z) e^{-i\left(\frac{\omega_+}{c}\left(\sin\theta - \sin\theta_{deg}\right) - \omega_- \overline{v_g^{-1}}\right)z}. \tag{2.13}$$

In the following, we will use a pulsed picosecond laser to pump our waveguide, with a central wavelength of 775 nm, and the pump angle close to the degeneracy angle, so that we can further simplify equation 2.13 by neglecting the first phase term[4]:

$$\phi_{PM}(\omega_-) = \int_{z=-L/2}^{L/2} dz \mathcal{A}_p(z) e^{i\omega_- \overline{v_g^{-1}} z}. \tag{2.14}$$

If we assume the pump spatial profile to be symmetrical around the center of the waveguide at $z = 0$ (i.e. $\mathcal{A}_p(z)$ to be even), then

$$\begin{aligned} \phi_{PM}(\omega_-) =& \int_{z=0}^{L/2} dz \mathcal{A}_p(z) \left(e^{i\omega_- \overline{v_g^{-1}} z} + e^{-i\omega_- \overline{v_g^{-1}} z}\right) \\ =& 2\int_{z=0}^{L/2} dz \mathcal{A}_p(z) \cos\left(\omega_- \overline{v_g^{-1}} z\right) \\ =& \phi_{PM}(-\omega_-) \end{aligned} \tag{2.15}$$

is a symmetrical function in (ω_s, ω_i), i.e. is invariant under the transformation $(\omega_+, \omega_-) \rightarrow (\omega_+, -\omega_-)$. However, if $\mathcal{A}_p(z) = -\mathcal{A}_p(-z)$ is now an odd function of z, we then get

$$\begin{aligned} \phi_{PM}(\omega_-) =& \int_{z=0}^{L/2} dz \mathcal{A}_p(z) \left(e^{i\omega_- \overline{v_g^{-1}} z} - e^{-i\omega_- \overline{v_g^{-1}} z}\right) \\ =& 2\int_{z=0}^{L/2} dz \mathcal{A}_p(z) \sin\left(\omega_- \overline{v_g^{-1}} z\right) \\ =& -\phi_{PM}(-\omega_-), \end{aligned} \tag{2.16}$$

[4]For a spectral width of $\Delta\omega = 10^{12}$ rad $\cdot$ s^{-1} (e.g. for a picosecond Gaussian pulse) the maximal difference in the degeneracy angle sines is $\sin\theta_{deg}^{max} - \sin\theta_{deg}^{min} = 2.5 \cdot 10^{-6}$, meaning the total phase difference over 5 mm induced by this term is of the order of 0.1 rad, i.e. a variation of less than 1% in the real part of the exponential.

which is antisymmetrical in (ω_s, ω_i), i.e. acquires a phase π under the transformation $(\omega_+, \omega_-) \rightarrow (\omega_+, -\omega_-)$. This is the most simple example of how the tailoring of the pump spatial profile can affect the exchange symmetry of the JSA, but further control of the JSA is possible. Indeed, the phase-matching term from equation 2.14 is simply analogous to the Fourier transform of the spatial profile of the pump beam [5], meaning that *any phase-matching function of ω_- can be achieved by taking the spatial profile of the pump to be its reciprocal Fourier transform.*

The next step in the shaping of the reconfigurable exchange statistics of the photon pairs is to be able to measure the exchange properties of the JSA (i.e. how it is modified when exchanging the signal and idler photons), which can be done using a Hong-Ou-Mandel experiment, a tool of choice to determine the exchange statistics of a photon pair, as we present it in the next section.

2.1.2 Hong-Ou-Mandel interferometer and exchange statistics of the photon pair

Here we recall the principle of the Hong-Ou-Mandel experiment and demonstrate its utility to measure the exchange statistics of the SPDC photon pairs.

2.1.2.1 The Hong-Ou-Mandel interferometer

The Hong-Ou-Mandel experiment, demonstrated in 1987 [138], consists in sending two photons, in our case the signal and idler photons, through the two input ports of a beamsplitter, while imposing a time delay Δt on one of the two arms. A coincidence measurement is then realized between the two output ports of the beamsplitter, and the coincidence probability as a function of the time delay is measured (figure 2.1).

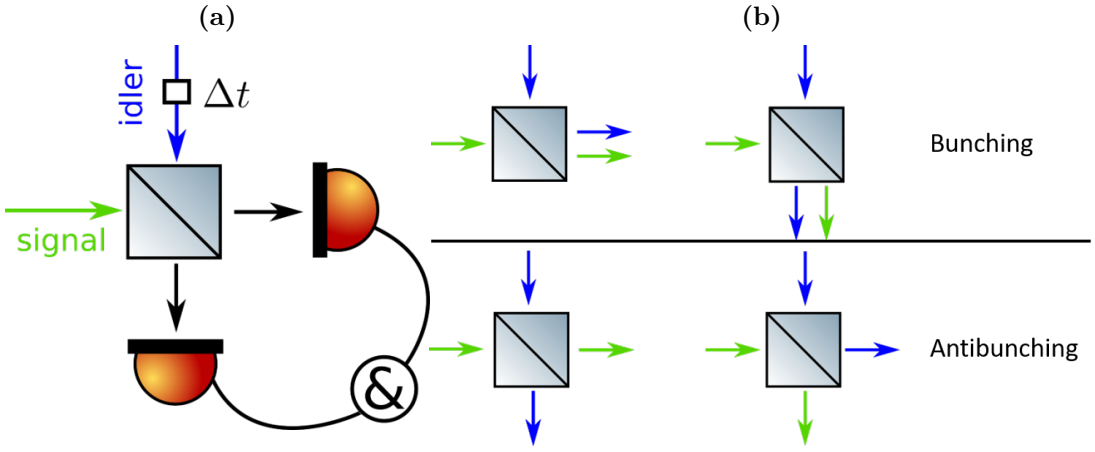

Figure 2.1: a) Schematic principle of the Hong-Ou-Mandel experiment, and b) the four possible outcomes, separated into bunching and antibunching scenarii.

If we label s, i the two input ports, and $1, 2$ the two output ports, the beamsplitter acts as the transformation for the corresponding creation operators, if the photons are

[5] Analogous, but not exactly equal, since the integral is made over a finite space, however the approximation is valid if the pump spot size is smaller than the waveguide.

indistinguishable over all degrees of freedom:

$$\begin{cases} \hat{a}_s^\dagger \to \frac{1}{\sqrt{2}}\left(\hat{a}_1^\dagger + i\hat{a}_2^\dagger\right) \\ \hat{a}_i^\dagger \to \frac{1}{\sqrt{2}}\left(i\hat{a}_1^\dagger + \hat{a}_2^\dagger\right) \end{cases} \tag{2.17}$$

We thus get, for an input state $|\Psi\rangle = \hat{a}_s^\dagger \hat{a}_i^\dagger |0\rangle$ with one photon in each input arm without added delay between them, the output state:

$$|\Psi\rangle_{out} = \frac{1}{2}\left(i\hat{a}_1^\dagger\hat{a}_1^\dagger + i\hat{a}_2^\dagger\hat{a}_2^\dagger + \hat{a}_1^\dagger\hat{a}_2^\dagger - \hat{a}_2^\dagger\hat{a}_1^\dagger\right)|0\rangle = \frac{i}{2}\left(\hat{a}_1^\dagger\hat{a}_1^\dagger + \hat{a}_2^\dagger\hat{a}_2^\dagger\right)|0\rangle \tag{2.18}$$

since $\left[\hat{a}_1^\dagger, \hat{a}_2^\dagger\right] = 0$. Thus, the photons always exit through one output arm together, and the coincidence probability $P_c = \left\langle \hat{a}_2^\dagger\hat{a}_1^\dagger\hat{a}_2\hat{a}_1 \right\rangle$ vanishes[6] because of the destructive interference between the probability amplitudes for the two antibunching outcomes. Note that if the operator were fermionic, because of the anticommutation relations, the output state would be $|\Psi\rangle_{out} = i\hat{a}_1^\dagger\hat{a}_2^\dagger|0\rangle$, meaning that the coincidence probability in this case would be $P_c = 1$.

For distinguishable particles (distinguishability can be, for instance, introduced using the time delay between the two photons), the interference between the probability amplitudes of the different paths is modified, and disappears if the particles become entirely distinguishable (i.e. if their quantum states have zero overlap), leading to the four paths having equal probability, and giving a coincidence probability of $P_c = 1/2$. The probability thus gradually increases up to 1/2 as the time delay increases, the increase speed being related to the coherence time of the photons. This is the fundamental result of the Hong-Ou-Mandel interference for independent particles, and we will look at how entangled photons behave in the interferometer in the next paragraph.

2.1.2.2 Hong-Ou-Mandel interference of spectrally entangled photons

Let us now consider a photon pair, with a JSA $\phi(\omega_s, \omega_i)$. We can write the quantum state as:

$$|\psi\rangle_{in} = \int d\omega_s d\omega_i \phi(\omega_s, \omega_i)\hat{a}_s^\dagger(\omega_s)\hat{a}_i^\dagger(\omega_i)|0\rangle \tag{2.19}$$

If we apply the beamsplitter transformation, with a time delay Δt in the idler arm, we get (identifying the signal and idler arms with the input ports of the beamsplitter, and considering every degree of freedom except for frequency to be indistinguishable between the two photons):

$$\begin{aligned} |\psi\rangle_{out} =& \frac{1}{2}\int d\omega_s d\omega_i \phi(\omega_s,\omega_i)\left(i\hat{a}_1^\dagger(\omega_s)\hat{a}_1^\dagger(\omega_i) + i\hat{a}_2^\dagger(\omega_s)\hat{a}_2^\dagger(\omega_i)\right. \\ &\left. + \hat{a}_1^\dagger(\omega_s)\hat{a}_2^\dagger(\omega_i) - \hat{a}_2^\dagger(\omega_s)\hat{a}_1^\dagger(\omega_i)\right)e^{i\omega_i\Delta t}|0\rangle \\ =& \frac{1}{2}\int d\omega_s d\omega_i \phi(\omega_s,\omega_i)\left(i\hat{a}_1^\dagger(\omega_s)\hat{a}_1^\dagger(\omega_i) + i\hat{a}_2^\dagger(\omega_s)\hat{a}_2^\dagger(\omega_i)\right)|0\rangle \\ &+ \frac{1}{2}\int d\omega_s d\omega_i \left(\phi(\omega_s,\omega_i)e^{i\omega_i\Delta t} - \phi(\omega_i,\omega_s)e^{i\omega_s\Delta t}\right)\hat{a}_1^\dagger(\omega_s)\hat{a}_2^\dagger(\omega_i)|0\rangle \end{aligned} \tag{2.20}$$

[6] Note that, in the case of bosons, this operator is restricted to the subspace with exactly two particles, otherwise it is not the correct tool to study the coincidence probability.

where the first term does not give coincidences, so we can discard it The coincidence operator $\hat{C}$ can then be defined as:

$$\hat{C} = \int d\omega_1 d\omega_2 \hat{a}_1^\dagger(\omega_1)\hat{a}_2^\dagger(\omega_2)\hat{a}_2(\omega_2)\hat{a}_1(\omega_1) \tag{2.21}$$

and the coincidence probability (which depends on Δt) as:

$$\begin{aligned}
P_c(\Delta t) =& \langle\psi|\,\hat{C}\,|\psi\rangle \\
=& \frac{1}{4}\langle 0| \int d\omega_s' d\omega_i' \left(\phi^*(\omega_s',\omega_i')e^{-i\omega_i'\Delta t} - \phi^*(\omega_i',\omega_s')e^{-i\omega_s'\Delta t}\right)\hat{a}_2(\omega_i')\hat{a}_1(\omega_s') \\
& \cdot \int d\omega_1 d\omega_2 \hat{a}_1^\dagger(\omega_1)\hat{a}_2^\dagger(\omega_2)\hat{a}_2(\omega_2)\hat{a}_1(\omega_1) \\
& \cdot \int d\omega_s d\omega_i \left(\phi(\omega_s,\omega_i)e^{i\omega_i\Delta t} - \phi(\omega_i,\omega_s)e^{i\omega_s\Delta t}\right)\hat{a}_1^\dagger(\omega_s)\hat{a}_2^\dagger(\omega_i)\,|0\rangle \\
=& \frac{1}{4}\langle 0| \int d\omega_s' d\omega_i' d\omega_1 d\omega_2 d\omega_s d\omega_i \left(\phi^*(\omega_s',\omega_i')e^{-i\omega_i'\Delta t} - \phi^*(\omega_i',\omega_s')e^{-i\omega_s'\Delta t}\right) \\
& \cdot \delta(\omega_s' - \omega_1)\delta(\omega_i' - \omega_2)\delta(\omega_s - \omega_1)\delta(\omega_i - \omega_2) \\
& \left(\phi(\omega_s,\omega_i)e^{i\omega_i\Delta t} - \phi(\omega_i,\omega_s)e^{i\omega_s\Delta t}\right)|0\rangle \\
=& \frac{1}{2}\int d\omega_1 d\omega_2 |\phi(\omega_1,\omega_2)|^2 \\
& - \frac{1}{4}\left[\int d\omega_1 d\omega_2 \phi^*(\omega_1,\omega_2)\phi(\omega_2,\omega_1)e^{i(\omega_2-\omega_1)\Delta t} + \text{c.c.}\right]
\end{aligned} \tag{2.22}$$

and finally, using the normalization of the JSA, we get:

$$P_c(\Delta t) = \frac{1}{2} - \frac{1}{2}\text{Re}\left[\int d\omega_1 d\omega_2 \phi^*(\omega_1,\omega_2)\phi(\omega_2,\omega_1)e^{i(\omega_2-\omega_1)\Delta t}\right] \tag{2.23}$$

The coincidence probability is thus the difference between a constant term 1/2 and an interference term, that will depend on the specific JSA. We can already see from equation 2.23 that at zero time delay, the second term gives $-1/2$ for a completely symmetrical JSA, thus giving a coincidence probability $P_c^{sym} = 0$, and thus a Hong-Ou-Mandel dip at $\Delta t = 0$, while for an antisymmetrical JSA, we get $P_c^{asym} = 1$, giving a "fermionic" peak in coincidences at zero time delay.

2.1.3 Exchange statistics of anyons

To derive the coincidence probability in the HOM experiment, we described the behaviour of entangled photons, using bosonic operators. However, the possibility to make photons anti-bunch at a beamsplitter, and have a fermionic-like behaviour, raises the question of the possibility to mimic arbitrary exchange statistics using entangled photon pairs, and in particular non-trivial exchange statistics, such as the fractionnal exchange statistics of anyons [139, 140]. Anyons are quasiparticles that live in 1D or 2D space and, unlike bosons or fermions, acquire a fractional phase (different from 0 or π) in their wavefunction when two of them are exchanged, and they have been first theoretically investigated in the context of the fractional quantum Hall effect [141, 142].

These types of particular exchange statistics are interesting, particularly because they open the possibility of braiding [143–145], which is the acquisition of a non-zero quantized

phase by the wavefunction through two successive directional exchanges of particles. The topological robustness to noise resulting from braiding operations makes anyons promising candidates for the implementation of fault-tolerant topological quantum computing and error correction tasks [145–147], and has attracted growing interest in the last years.

To describe the behaviour of anyons in a HOM interferometer, let us first recall the commutation relations for bosonic, fermionic and anyonic operators:

$$\begin{cases} \left[\hat{a}^\dagger(\omega_s), \hat{a}^\dagger(\omega_i)\right] = 0 & \text{for bosons} \\ \left\{\hat{b}^\dagger(\omega_s), \hat{b}^\dagger(\omega_i)\right\} = 0 & \text{for fermions} \\ \hat{c}^\dagger(\omega_s)\hat{c}^\dagger(\omega_i) = e^{i\theta(\omega_s,\omega_i)}\hat{c}^\dagger(\omega_i)\hat{c}^\dagger(\omega_s) & \text{for anyons} \end{cases} \tag{2.24}$$

where $\theta(\omega_s, \omega_i) = -\theta(\omega_i, \omega_s)$ for the operators to be well-defined. The case of bosons simply corresponds to $\theta = 0$, and the case of fermions to $\theta = \pi$. We can rewrite the state after the HOM beamsplitter for anyons with JSA ϕ_A, and post-select on the events giving coincidences between the two output arms, yielding:

$$\begin{aligned} |\psi_a\rangle =& \frac{1}{2}\int d\omega_s d\omega_i \phi_A(\omega_s,\omega_i)\left(\hat{c}_1^\dagger(\omega_s)\hat{c}_2^\dagger(\omega_i) - \hat{c}_2^\dagger(\omega_s)\hat{c}_1^\dagger(\omega_i)\right) e^{i\omega_i\Delta t}|0\rangle \\ =& \frac{1}{2}\int d\omega_s d\omega_i \left(\phi_A(\omega_s,\omega_i)e^{i\omega_i\Delta t} - e^{i\theta(\omega_s,\omega_i)}\phi_A(\omega_i,\omega_s)e^{i\omega_s\Delta t}\right)\hat{c}_1^\dagger(\omega_s)\hat{c}_2^\dagger(\omega_i)|0\rangle . \end{aligned} \tag{2.25}$$

Analogously to what we have done in equation 2.22, we can compute the probability of coincidence in the case of anyons, and we get:

$$P_c(\Delta t) = \frac{1}{2} - \frac{1}{2}\mathrm{Re}\left[\int d\omega_1 d\omega_2 \phi_A^*(\omega_1,\omega_2)\phi_A(\omega_2,\omega_1)e^{i(\omega_2-\omega_1)\Delta t}e^{i\theta(\omega_1,\omega_2)}\right]. \tag{2.26}$$

This coincidence probability is the same as for bosons with JSA $\phi_B(\omega_s,\omega_i) = e^{-i\theta(\omega_s,\omega_i)/2}\phi_A(\omega_s,\omega_i)$. Indeed, in that case, we get from equation 2.23:

$$\begin{aligned} P_c^{Bosons}(\Delta t) =& \frac{1}{2} - \frac{1}{2}\mathrm{Re}\left[\int d\omega_1 d\omega_2 \phi_A^*(\omega_1,\omega_2)e^{i\theta(\omega_1,\omega_2)/2}\phi(\omega_2,\omega_1)e^{-i\theta(\omega_2,\omega_1)/2}e^{i(\omega_2-\omega_1)\Delta t}\right] \\ =& \frac{1}{2} - \frac{1}{2}\mathrm{Re}\left[\int d\omega_1 d\omega_2 \phi_A^*(\omega_1,\omega_2)\phi_A(\omega_2,\omega_1)e^{i(\omega_2-\omega_1)\Delta t}e^{i\theta(\omega_1,\omega_2}\right] \\ =& P_c^{Anyons}(\Delta t). \end{aligned} \tag{2.27}$$

Tailoring the spectral entanglement of photon pairs (i.e. their JSA ϕ_B) thus enables to simulate the behaviour of anyons at a Hong-Ou-Mandel interferometer, by mimicking the effect of the fractional exchange statistics stemming from the operators algebra through a phase manipulation of the JSA.

2.2 Experimental measurement of the exchange statistics

Having presented the theory for the manipulation of the exchange statistics of photon pairs to mimic anyonic behaviour, we now turn to presenting the experimental realization of photon pairs with reconfigurable exchange statistics, starting with the fabrication and characterization of the sample, and going through the shaping of the pump beam and the measurement process for the exchange statistics.

2.2.1 Sample fabrication and characterization

In this paragraph we go over the different steps involved in the fabrication and characterization of the sample. The samples are fabricated from an epitaxial growth realized by Aristide Lemaître in C2N via Molecular Beam Epitaxy (following the epitaxial structure described in section 1.2.1.1), and the fabrication process described below was made in the clean room of the MPQ laboratory at Université Paris Cité.

2.2.1.1 Fabrication

The sample was fabricated using optical lithography and chemical wet etching, using the following procedure: the sample is cleaned, and a negative photosensitive resist (S1805) is spincoated on its surface. The sample then undergoes UV lithography while covered by a metallic chromium mask consisting of single lines, to realize simple waveguides. The resist is then developed, and the sample is chemically etched using a 1:1:1 BCK solution (i.e. an even mix of hydrobromic acid, chlorhydric acid and potassium dichromate). The process is summarized in figure 2.2. The process was studied and optimized by several PhD students from our group, and described in more details in Xavier Caillet's [134] and Claire Autebert's [148] theses. The sample is then cleaved to make clean facets at the input and output of the waveguides, to realize 1.9 mm long waveguides, with a 6 μm width.

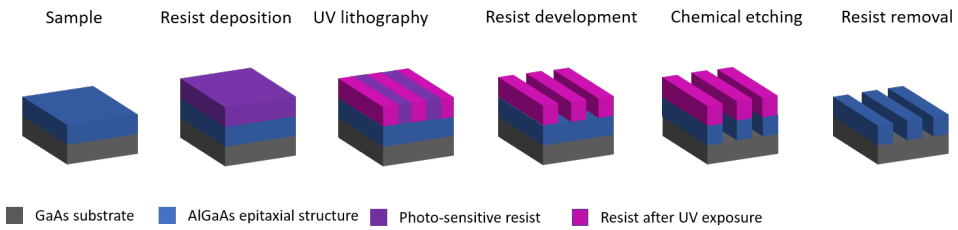

Figure 2.2: Schematical summary of the lithography and chemical etching process.

2.2.1.2 Losses characterization

When propagating inside a waveguide, photons can suffer from losses induced by several effects, such as fabrication defects, scattering from impurities, modal mismatch at domain interfaces or roughness. It is thus important to ensure that the sample has reasonable losses, so as to not lose the information carried by the generated photon pairs.

In order to measure the losses of the sample, we employ a Fabry-Pérot technique exploiting the modal reflectivity of the telecom modes at the facets of the waveguides. Optical losses lead to a decrease of the intensity of a light beam along the propagation direction z:

$$\frac{dI}{dz} = -\alpha I \tag{2.28}$$

where α is the propagation loss coefficient. If we couple a laser beam into the waveguide, and take into account the reflectivity of the input and output facets, the waveguide acts

as a Fabry-Pérot cavity, resulting in a transmitted power at the output that depends on the wavelength:

$$P_t = \frac{\eta P_0 T^2 e^{-\alpha L}}{(1 - Re^{-\alpha L})^2 + 4Re^{-\alpha L} \sin^2\left(\frac{4\pi n_{\text{eff}} L}{\lambda_0} + \phi_0\right)} \tag{2.29}$$

with η the coupling efficiency of light inside the waveguide, P_0 the input power, T and R the modal transmission and reflection coefficients at the facets, L the length of the waveguide, n_{eff} the effective index of the guided mode, λ_0 the free-space wavelength, and ϕ_0 the reflection-induced phase.

The reflection coefficients can be estimated by using numerical simulations, giving values of $R = 0.247$ for the TE-polarized mode, and $R = 0.285$ for the TM-polarized mode. Furthermore, by continuously varying the wavelength of the injected laser beam, one can extract the values for the maximum and minimum transmitted power P_t^{max} and P_t^{min}, and thus the ratio

$$C = \frac{P_t^{max}}{P_t^{min}}$$

allowing to determine the loss coefficient as:

$$\alpha = \frac{1}{L} \cdot \ln\left(R\frac{\sqrt{C}+1}{\sqrt{C}-1}\right). \tag{2.30}$$

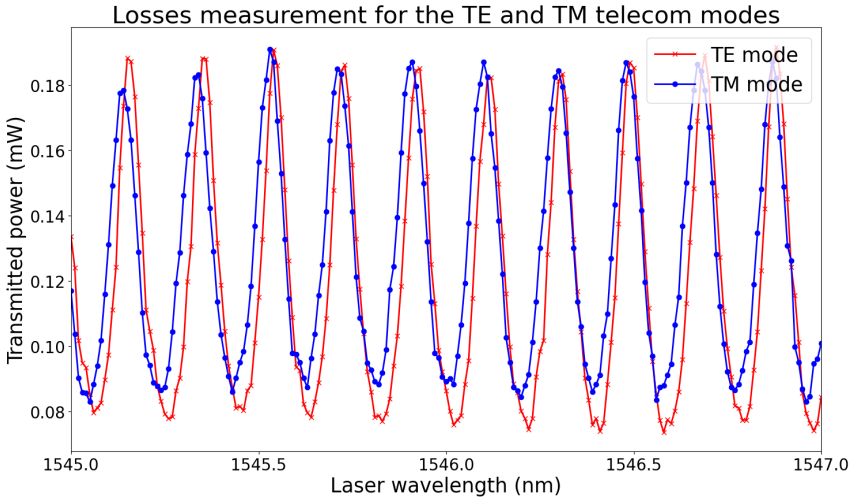

Figure 2.3: Result of the loss measurement for the TE and TM telecom modes.

Figure 2.3 shows, for the sample studied in this chapter, the measured transmitted power as a function of wavelength for the TE and TM-polarized telecom modes around 1550 nm. The extracted loss coefficients are $\alpha_{TE} = 0.9$ cm^{-1} and $\alpha_{TM} = 1.1$ cm^{-1}, obtained with the simulated values for the modal reflectivity $R_{TE} = 0.247$ and $R_{TM} = 0.285$.

2.2.2 Measurement of the exchange statistics

We now describe the measurement of the exchange statistics of the biphoton wavefunction, with the wavefront shaping technique and the Hong-Ou-Mandel coincidence measurement.

2.2.2.1 Wavefront shaping and experimental set-up

As we saw from the beginning of the chapter, the main requirement to generate photon pairs with reconfigurable exchange statistics is the ability to tailor the spatial profile of the pump beam in the waveguide propagation direction. In order to shape the pump beam, the tool we use in this work is a phase Spatial Light Modulator (SLM), which consists of an array of pixels that can reflect light while locally changing its phase. Through diffraction effects, SLMs can be used to shape the wavefront of the reflected beam by individually addressing the pixels to spatially modulate its phase. We use a Leto SLM from the Holoeye company, and the wavefront shaping techniques using this device were studied by Saverio Francesconi in a previous PhD thesis from our group [137].

As the pump laser, we use a Coherent Mira Ti:sapphire laser, pulsed with a 76 MHz repetition rate, a 4.5 ps pulse duration and 50 mW average power, set at the SPDC resonance wavelength for our source ($\lambda_p = 773.15$ nm). As shown in figure 2.4, the laser beam is then sent on the SLM through a telescope to match its dimension to the SLM, and a second telescope in a 4f configuration to image the SLM on the waveguide. Part of the beam is reflected on a 99:1 beamsplitter and sent to a Phasics SID4 wavefront analyzer (WFA) to characterize the spatial profile of the input pump beam. The pump beam with the desired spatial profile is then focused on top of the waveguide using a cylindrical lens, and the generated signal and idler photons are collected through microscope objectives. To ensure that we only consider the interaction where the signal photon is TE-polarized and the idler photon is TM-polarized, we use polarizers at the output facets of the sample.

An ideal characterization of the emitted the quantum state would consist in measuring the JSA. Unfortunately, the simultaneous measurement of the amplitude and phase of the wavefunction is a very difficult problem, which lacks measurement methods applicable in the general case, although there are techniques that have been used in specific situations [149]. It is easier to measure the Joint Spectral Intensity (JSI), which is the squared modulus of the JSA, giving information on the joint spectrum of the biphoton. In order to do so, we use a fiber spectrograph[7] as presented in figure 2.4, where the two photons are sent into highly dispersive fibers (DCF), which change the frequency information of the photon pairs into an information on time of arrival on single-photon detectors. The times of arrival of the photons relative to a trigger coming from the pulsed laser clock is then measured using a Swabian TimeTagger. After proper calibration, the JSI can be reconstructed from the coincidence counts in each time-bin.

An example of JSI measurement, when pumping the source with a standard Gaussian profile at degeneracy angle, is shown in figure 2.6a. The average value of the dispersion for the employed DCFs was around $D = -1650$ ps $\cdot$ nm^{-1} for both fibers, the detectors are Superconducting Nanowire Single-Photon Detectors (SNSPD) with a $\Delta t_D = 90$ ps jitter, and the TimeTagger resolution is $\Delta t_{TT} = 42$ ps. Thus, the best achievable spectral resolution was here

$$\Delta\lambda = \frac{\sqrt{\Delta t_D^2 + \Delta t_{TT}^2}}{|D|} \simeq 60 \text{ pm}. \tag{2.31}$$

This resolution allows to obtain the general shape of the JSI (essentially circular in figure 2.6a, and confirming the good spectral indistinguishability of the photons, as needed to

[7] Other methods exist [150, 151], but they are usually more time-consuming, although they can be more accurate.

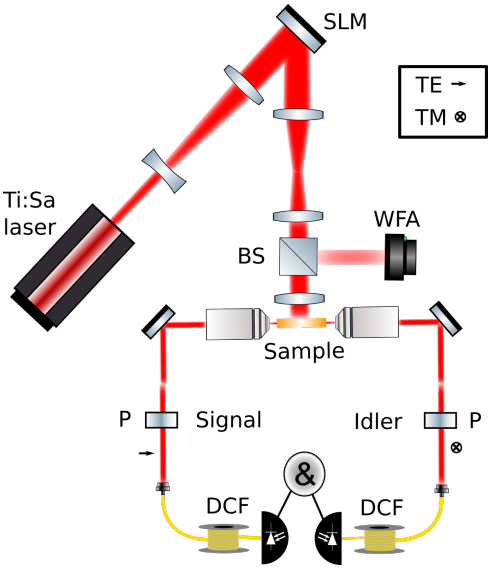

Figure 2.4: Experimental set-up for the measurement of the JSI.

perform HOM interference), but its value is of the same order than the free spectral range of the Fabry-Pérot cavity ($\Delta\lambda_{FSR} \simeq 190$ pm), and thus does not allow to precisely resolve the associated modulation of the joint spectrum.

Next, in order to measure the exchange statistics of the biphoton state, the signal and idler photons are coupled to fibers and sent into a fibered beamsplitter acting as a HOM interferometer, with its two output ports connected to single-photons detectors, as sketched in figure 2.5. We use a Fibered Polarization Controller (FPC) in the signal photon arm in the beamsplitter, to ensure that the polarization modes of the two photons at the input of the beamsplitter coincide to allow interference of the two photons. A motorized fibered delay line adds a time delay Δt at the input of the idler arm in the beamsplitter, two fibered filters are added before detection to filter out the potential luminescence noise, and the photon detection is carried out by Superconducting Nanowire Single-Photon Detectors (SNSPDs). Scanning the time delay on the delay line allows to reconstruct the HOM interferogram of the generated photon pairs, and we discuss the experimental results in the next paragraph.

2.2.2.2 Anyonic-like exchange statistics

In this paragraph, we present the experimental results for the measurement of the exchange statistics of photons for different JSA shapes. First, we show than we can indeed invert the bunching behaviour of the photons at a beamsplitter, and measure the HOM interferogram for an antisymmetrical JSA. In order to realize this, we impose a phase step $\Delta\varphi$ between the two halves of the pump spot with Gaussian intensity profile using the SLM. For $\Delta\varphi = \pi$, the pump spatial profile is thus antisymmetrical with respect to the center of the waveguide. In this case, from equation 2.16, the JSA is expected to be antisymmetrical under exchange of the two frequencies, and the two photons should anti-bunch at the HOM interferometer for a time delay $\Delta t = 0$. Figure 2.6d presents the result of the JSI measurement for $\Delta\varphi = \pi$ that we can compare to the previous measurement (figure 2.6a) at $\Delta\varphi = 0$. We observe that for $\Delta\varphi = \pi$, the JSA splits into two lobes, and

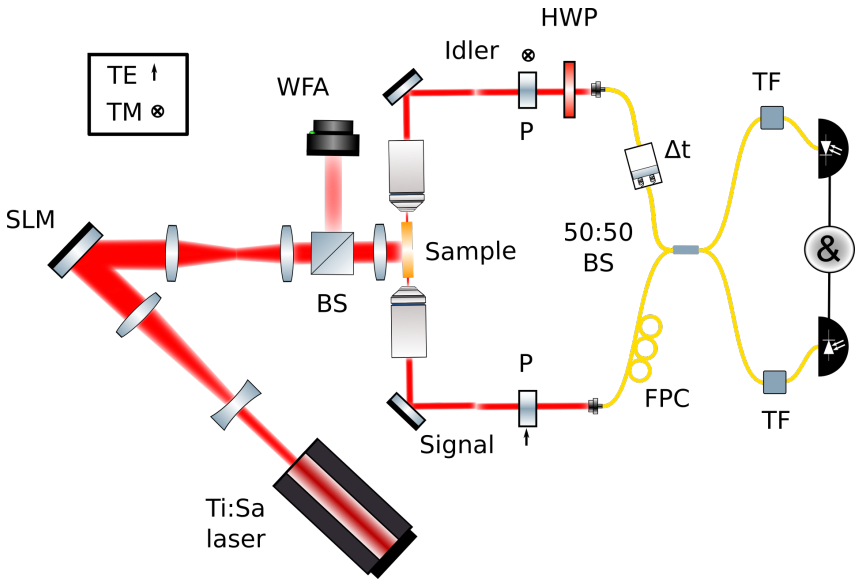

Figure 2.5: Experimental set-up for the HOM measurement.

we expect the phase difference between the two lobes to be π. The corresponding measured HOM interferograms are presented in figures 2.6b and 2.6e for $\Delta\varphi = 0$ and $\Delta\varphi = \pi$ respectively, and compared with theoretical predictions in figure 2.6c and f[8]. We observe spatial bunching of the photons through the HOM interferometer for the symmetric state $\Delta\varphi = 0$, and antibunching for the antisymmetric state $\Delta\varphi = \pi$. This experiment already shows the possibility to manipulate the exchange statistics of the photon pairs to simulate a fermionic behaviour at the beamsplitter. In order to tailor the pump beam to explore further exchange statistics, we first need to define a correct phase-matching function for the simulation of anyonic statistics, as well as the corresponding pump spatial profile.

For experimental demonstration, we chose to focus on anyons having a phase $\theta = \pm\pi/2$ under exchange, i.e. $\theta(\omega_s, \omega_i) = \text{sign}\,(\omega_i - \omega_s) \cdot \pi/2$ in the formalism of equation 2.24. The target wavefunction to implement is, as plotted in figure 2.7a:

$$\begin{cases} \phi_{PM}(\omega_-) = Ce^{i\pi/4}\sqrt{|\omega_-|}e^{-\omega_-^2/2\sigma^2} & \text{for } \omega_- \geq 0 \\ \phi_{PM}(\omega_-) = Ce^{-i\pi/4}\sqrt{|\omega_-|}e^{-\omega_-^2/2\sigma^2} & \text{for } \omega_- \leq 0 \end{cases} \tag{2.32}$$

where the term $\sqrt{|\omega_-|}$ is here to ensure the continuity of the JSA along the $\omega_- = 0$ interface, and C is a normalization constant. The corresponding pump spatial profile, which we compute numerically by inverting equation 2.14, is represented on figure 2.7b, along with the simulated HOM interferogram for this phase-matching function in figure 2.7c.

We experimentally implement the corresponding pump spatial profile, which consists in two unbalanced lobes, with the separation between the two lobes offset from the waveguide center, and a phase difference of π between the two lobes. Using this pump profile,

[8]This measurement was presented in Saverio Francesconi's PhD thesis and in [152], and realized with different single-photon detectors and a different time tagger than the one we described in the section, but the experimental set-up is essentially the same. We refer the reader to the given references for more information on the specifics of this measurement, as we included it in the thesis mainly to have a coherent progression in the measurement of the exchange statistics.

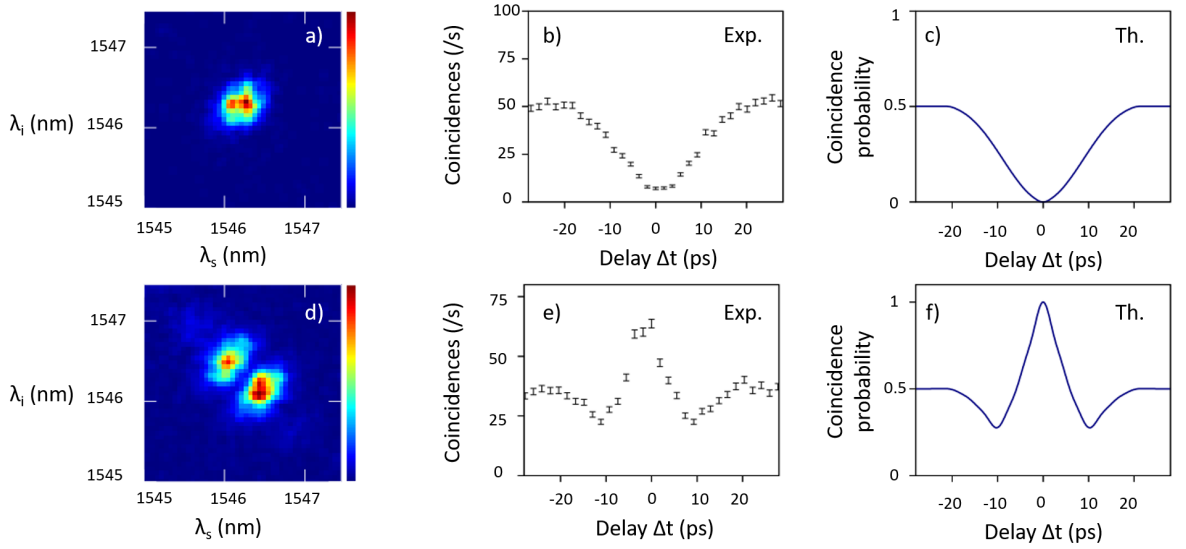

Figure 2.6: a) Experimental JSI, and b) experimental and c) theoretical HOM interferograms for a Gaussian beam with phase-shift $\Delta\varphi = 0$, and d) experimental JSI, and e) experimental and f) theoretical HOM interferograms for a Gaussian beam with phase-shift $\Delta\varphi = \pi$.

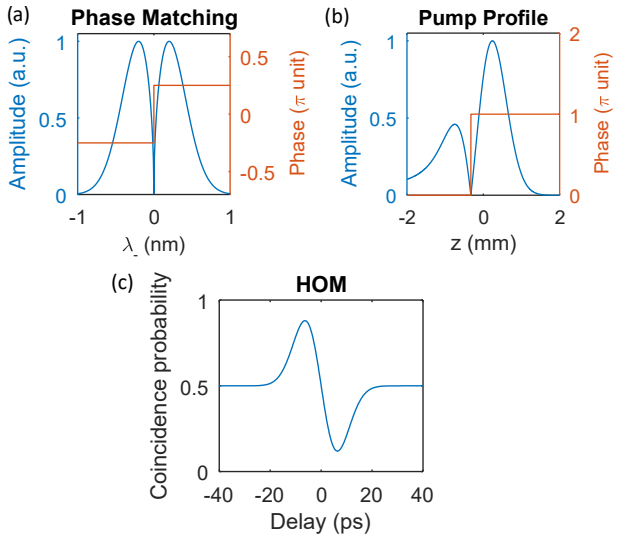

Figure 2.7: Simulated a) phase-matching function, b) pump spatial profile and c) HOM interferogram for entangled photon pairs mimicking $\pi/2$ anyons.

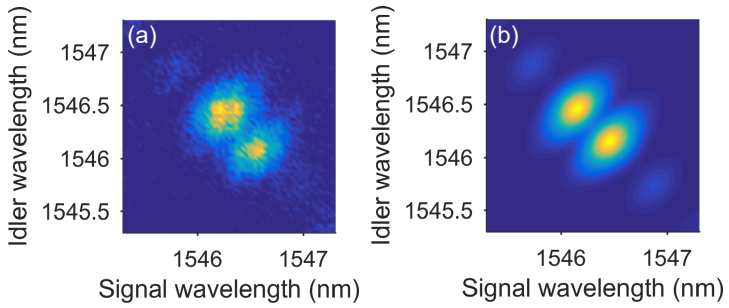

Figure 2.8: a) Experimental and b) simulated JSI for the phase-matching function described in equation 2.32, mimicking anyons with a $\pi/2$ phase over exchange.

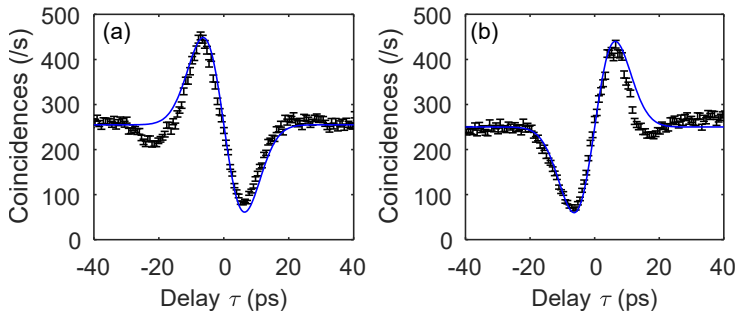

Figure 2.9: Experimentally measured HOM interferograms (dots) and theoretical prediction (blue line) for frequency-entangled biphoton states mimicking $\theta = \pm\pi/2$, with different exchange directions for a) and b).

we measure the JSI of the produced photon pairs using the experimental set-up described in the previous paragraph, and plot it on figure 2.8 along with the simulated JSI (obtained from equation 2.3). The measured JSI consists of two lobes with similar intensities along the ω_- direction, which is consistent with the target phase-matching function (figure 2.7a), and demonstrates accurate control over the joint spectrum from the tailoring of the pump profile. The generation rate of the SPDC photon pairs is estimated to be 10^7 pairs·s^{-1} from the experimental data.

Finally, we measured the HOM interferogram of the biphoton state to reveal the exchange statistics of the generated photon pairs. The results are presented on figure 2.9a (dots), and are in good agreement with the numerical simulation (blue line), showing a peculiar shape with a peak at negative delay, a dip at positive delay, and a symmetry around the central point at zero delay. The same state with an opposite phase in the anyonic operator algebra (i.e. $\theta(\omega_s, \omega_i) = \text{sign}\,(\omega_s - \omega_i) \cdot \pi/2$) is also measured on figure 2.9b, and is obtained by taking the symmetrical pump profile with respect to the center of the waveguide. Its HOM interferogram, that is mirror-symmetric to the previously measured interferogram, is also in good agreement with the theoretical prediction.

2.3 Summary and perspectives

In this chapter, we analytically described the exchange symmetry control of the JSA of photon pairs produced by SPDC using a counterpropagating phase-matched source,

through spatial tailoring of the pump beam. We investigated HOM interferometry as a tool to characterize the exchange symmetry of the spectral wavefunction of the generated photon pairs, and experimentally measured photonic states displaying bosonic, fermionic and anyonic behaviours in their HOM interferograms. The good agreement between the theory and the experimental results confirms the reconfigurable manipulation of the photon pairs statistics from the tailoring of the spatial profile of the pump beam.

We have thus demonstrated flexible exchange statistics control of photon pairs, directly at the generation stage, in a chip-integrated source, at room temperature and telecom wavelength. The possibility to generate on-demand frequency-entangled states in a controllable and reconfigurable manner is a powerful resource in quantum simulations of exchange statistics effects [63, 64, 153, 154] to simulate the behaviour of fermionic or anyonic particles and is an asset in view of the implementation of quantum information protocols on-chip. This source can also be used to generate more complex states, like hybrid polarization/frequency entangled states [136], which have applications in metrology for accurate time measurements [155] or in the interconnection of qubits with disparate energy levels [156], and like compass states [157] presenting fine phase structure which can be used as a resource for quantum metrology [158, 159].

The results presented in this chapter are published in [160].

Chapter 3

Theory of quantum walks in nonlinear waveguide arrays

With the end of the previous chapter, we conclude our study of the counter-propagating biphoton source and we now turn to the device based on nonlinear waveguide arrays. As we will discuss in this chapter, this device can be exploited to realize quantum random walks [161], in which a particle can simultaneously evolve towards all its accessible states with interference between the various probability amplitudes. Quantum walks constitute a powerful resource in quantum information, allowing e.g. the demonstration of the Shor factoring algorithm [46], boson sampling [162] and simulation of condensed matter problems [81]. Two different regimes of quantum random walks exist: **discrete-time** quantum random walks [163], where the particles evolve in discrete steps, and **continuous-time** quantum random walks [164], in which the evolution of the particles is continuous and can be described using Hamiltonian dynamics. In the case of photons, the accessible states can be path modes of a photonic circuit. Discrete-time quantum walks in the path degree of freedom have been implemented using networks of directional couplers and phase-shifters (see figure 3.1a) in femtosecond written circuits in silicate glass [81, 165] and integrated with SFWM sources in silicon-based circuits [166]. On the other hand, the natural photonic platform for the implementation of continuous-time quantum random walks consists in arrays of evanescently coupled waveguides (figure 3.1b), allowing photons to continuously hop from one waveguide to its neighbours during their propagation. This platform has first been explored in the classical regime [167] to study nonlinear effects and solid-state phenomena such as Bloch oscillations or disorder-induced localization, by exploiting the analogy between electrons in a crystal periodic potential and optical waves propagating in a periodic dielectric structure. More recently, the quantum regime has been experimentally investigated in passive arrays of silicon oxynitride waveguides [100] fed with an external source of photon pairs, then in the cascaded quantum walks regime in periodically poled lithium niobate by generating SPDC photons directly inside the waveguide array [104] and finally in silicon chips where SFWM was used inside a waveguide array to demonstrate topological protection of the generated photon pairs [82]. Nonlinear waveguide arrays have also been identified as a promising platform for the on-chip generation of continuous-variable multipartite entanglement [168–170].

The aim of this chapter is to introduce the theory necessary to the understanding of the phenomenon of quantum random walks inside a waveguide array and to study

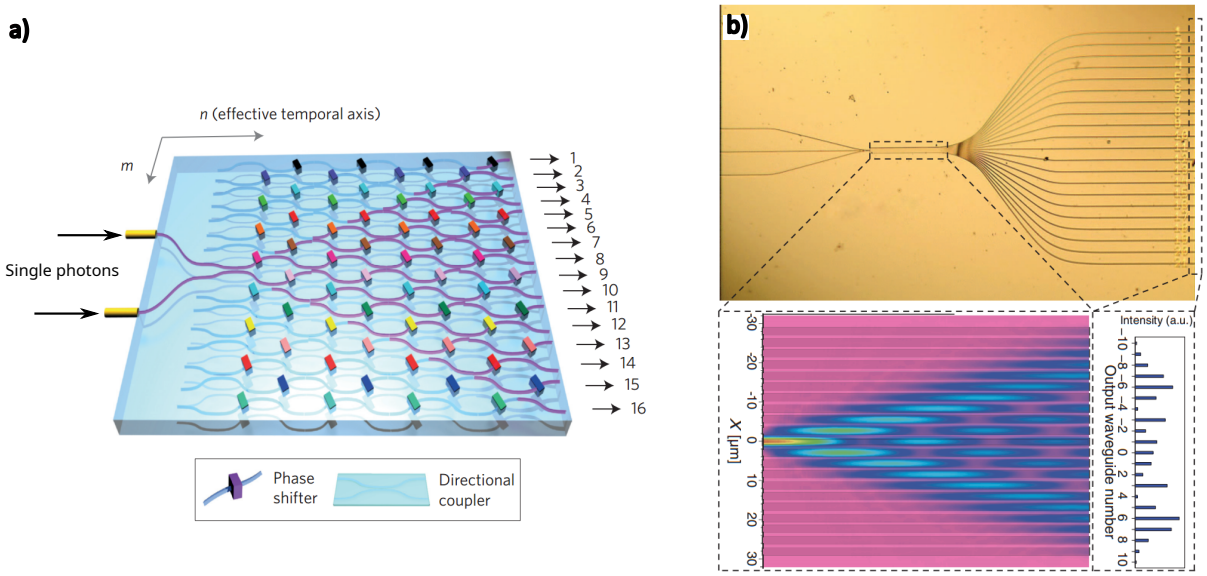

Figure 3.1: a) Lattice of photonic beam splitters and phase shifters, taken from [81] and b) array of silicon oxynitride waveguides (top) and discrete diffraction in the array (bottom), taken from [100].

its interplay with the generation of correlated photon pairs by SPDC directly inside the device, with the aim of developing a compact and versatile source of spatially entangled states, operating at room temperature and telecom wavelength. We first give a theoretical model for the evanescent coupling between the waveguides, then focus on the case of the infinite waveguide array and introduce the Bloch modes and tight-binding formalism to describe the propagation of optical fields inside the array. We then present the theory of quantum walks of correlated photons within passive arrays, before considering the case of nonlinear waveguide arrays supporting cascaded quantum walks generated by SPDC. We introduce the needed formalism both in the quasi-momentum and real space as well as the associated metrics to characterize the produced quantum states (purity, Schmidt rank, non-classicality indicator). Finally, we perform a series of numerical simulations to investigate various effects (boundary and disorder effects, pump propagation and losses) and explore the variety of spatially entangled states that can be engineered using such a device.

Contents

3.1 Continuous-time quantum walks in waveguide arrays

3.1.1 Waveguide arrays as a support for continuous quantum random walks

3.1.1.1 Coupled-mode theory for two waveguides

To get an understanding of the phenomena underlying the realization of quantum random walks in waveguide arrays, it is useful to first consider the simplest case where only two single-mode waveguides are placed near each other, so that the light from one waveguide can tunnel to the other one through evanescent coupling from the overlap of their mode profiles.

With this goal in mind, we will consider two lossless waveguides, which we label 1 and 2, supporting modes we denote $|a_1\rangle$ and $|a_2\rangle$, that we will assume to be orthogonal in this simple model. We write the modes with a ket because, although this subsection will be purely classical in its formalism, we will later work with single-photon modes, and it is useful to use this notation as of now. We assume that the guides have propagation constants β_1 and β_2. The individual propagation of the modes in waveguides 1 and 2 then yields:

$$b_i(z) = b_i(0)\, e^{-i\beta_i z} \tag{3.1}$$

where b_i denotes the field amplitude in mode $|a_i\rangle$.

Now suppose we introduce a coupling between the two fields, such that the evolution of the amplitudes b_i can be described as

$$\begin{aligned} \frac{db_1}{dz} &= -i\beta_1 b_1 + i\kappa_{1,2} b_2 \\ \frac{db_2}{dz} &= -i\beta_2 b_2 + i\kappa_{2,1} b_1 \end{aligned} \tag{3.2}$$

If the waveguides are lossless, then the total energy $|b_1|^2 + |b_2|^2$ must be conserved during the propagation, giving us:

$$\begin{aligned}\frac{d|b_1|^2}{dz} + \frac{d|b_2|^2}{dz} &= -i\beta_1 b_1 b_1^* + i\beta_1 b_1^* b_1 + i\kappa_{1,2} b_2 b_1^* - i\kappa_{1,2} b_2^* b_1 \\ &\quad - i\beta_2 b_2 b_2^* + i\beta_2 b_2^* b_2 + i\kappa_{2,1} b_1 b_2^* - i\kappa_{2,1} b_1^* b_2 \\ &= i\kappa_{1,2} b_2 b_1^* - i\kappa_{1,2} b_2^* b_1 + i\kappa_{2,1} b_1 b_2^* - i\kappa_{2,1} b_1^* b_2 \\ &= i\left(\kappa_{1,2} - \kappa_{2,1}\right)\left(b_2 b_1^* - b_1 b_2^*\right).\end{aligned} \tag{3.3}$$

Since this energy conservation does not depend on the initial conditions, we can choose the $b_i(0)$ such that $(b_2 b_1^* - b_1 b_2^*) \neq 0$, and thus we can deduce that the coupling is symmetrical:

$$\kappa_{1,2} = \kappa_{2,1} := C. \tag{3.4}$$

We can then rewrite equation 3.2 as

$$\begin{aligned}\frac{db_1}{dz} &= -i\beta_1 b_1 + iCb_2 \\ \frac{db_2}{dz} &= -i\beta_2 b_2 + iCb_1\end{aligned} \tag{3.5}$$

and simplify it even further by defining $b_1' = e^{i\beta_1 z} b_1$, $b_2' = e^{i\beta_2 z} b_2$ and $\Delta\beta = \beta_1 - \beta_2$:

$$\begin{aligned}\frac{db_1'}{dz} &= ie^{i\Delta\beta z} Cb_2' \\ \frac{db_2'}{dz} &= ie^{-i\Delta\beta z} Cb_1'\end{aligned} \tag{3.6}$$

These coupled equations can be solved analytically, by multiplying the first equality by $e^{-i\Delta\beta z}$ and taking its derivative with respect to z and using the second equality to replace $\frac{db_2'}{dz}$ by its value in the computation. This yields

$$\frac{d^2 b_1'}{dz^2} - i\Delta\beta \frac{db_1'}{dz} + C^2 b_1' = 0, \tag{3.7}$$

which is resolved through a simple second degree differential equation. Defining $\alpha = \sqrt{\frac{\Delta\beta^2}{4} + C^2}$, we finally get the shape of b_1' and b_2' (after substitution):

$$\begin{aligned}b_1'(z) &= e^{i\frac{\Delta\beta}{2}z}\left(Ae^{-i\alpha z} + Be^{+i\alpha z}\right) \\ b_2'(z) &= \frac{e^{-i\frac{\Delta\beta}{2}z}}{C}\left(A\left(\frac{\Delta\beta}{2} - \alpha\right)e^{-i\alpha z} + B\left(\frac{\Delta\beta}{2} + \alpha\right)e^{+i\alpha z}\right)\end{aligned} \tag{3.8}$$

where A and B are deduced from the initial conditions.

For instance, if we suppose that we inject power only in waveguide 1 at $z = 0$, then $b_1'(0) = A_0$ and $b_2'(0) = 0$, so we get:

$$\begin{aligned}A + B &= A_0 \\ A\left(\frac{\Delta\beta}{2} - \alpha\right) + B\left(\frac{\Delta\beta}{2} + \alpha\right) &= 0\end{aligned} \tag{3.9}$$

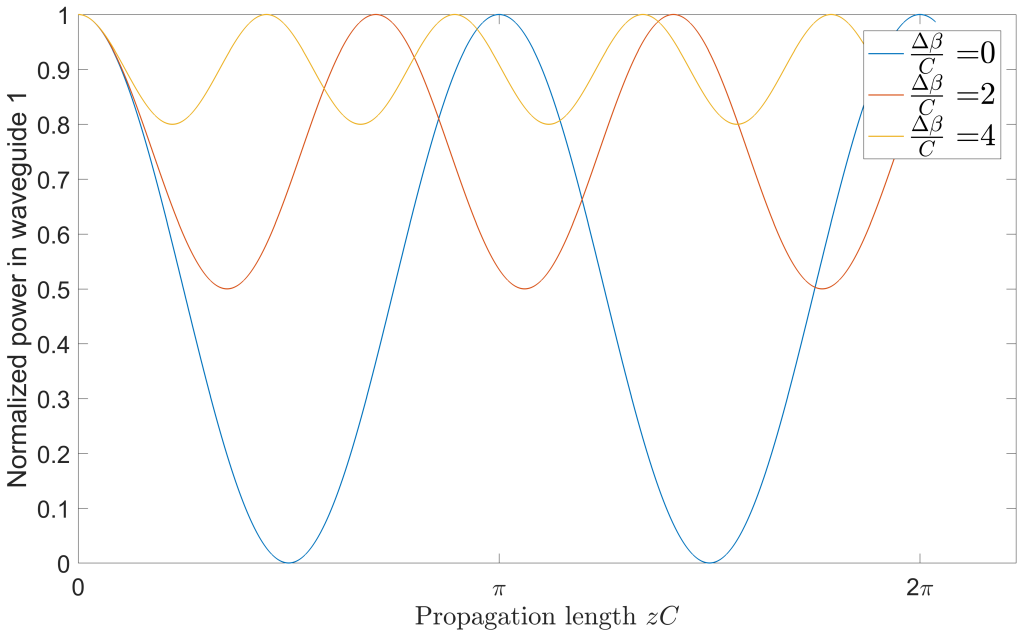

Figure 3.2: Power oscillation between the two waveguides for $\frac{\Delta\beta}{C} = 0$ (blue), $\frac{\Delta\beta}{C} = 2$ (red) and $\frac{\Delta\beta}{C} = 4$ (yellow).

which gives:

$$\begin{aligned} A &= A_0 \left(\frac{1}{2} + \frac{\Delta\beta}{4\alpha} \right) \\ B &= A_0 \left(\frac{1}{2} - \frac{\Delta\beta}{4\alpha} \right) \end{aligned} \tag{3.10}$$

If we replace it in terms of b_1' and b_2', we then have:

$$\begin{aligned} b_1'(z) &= A_0 e^{i\frac{\Delta\beta}{2}z} \left(\cos\alpha z + i\frac{\Delta\beta}{2\alpha}\sin\alpha z \right) \\ b_2'(z) &= iA_0 e^{-i\frac{\Delta\beta}{2}z} \frac{C}{\alpha}\sin\alpha z \end{aligned} \tag{3.11}$$

Equation 3.11 provides several pieces of information on the transmission of power from waveguide 1 to waveguide 2. Firstly, the power oscillates in waveguide 2 with a spatial rate $\alpha = \sqrt{\frac{\Delta\beta^2}{4} + C^2}$, dependent on both the coupling rate C between the waveguides and the mismatch $\Delta\beta$ between the two propagation constants. Secondly, we can see that as long as the mismatch $\Delta\beta$ is non-zero, the optical power can never be fully transmitted to waveguide 2. Indeed, the injected optical power is proportional to $|A_0|^2$, while the maximum power in waveguide 2 is achieved for $z = \frac{\pi}{2\alpha}$ and is proportional to $|\frac{A_0 C}{\alpha}|^2$, and $\alpha \geq C$ from its definition, with the equality only achieved for $\Delta\beta = 0$. This power oscillation between the two waveguides is shown in figure 4.4 for different values of $\Delta\beta$.

Let us now focus on the simpler case where $\Delta\beta = 0$, i.e. with no index mismatch

between the two waveguides. In this case, equation 3.5 simply reads

$$\begin{aligned} \frac{db_1}{dz} &= -i\beta b_1 + iCb_2 \\ \frac{db_2}{dz} &= -i\beta b_2 + iCb_1, \end{aligned} \tag{3.12}$$

which has for solution (from equation 3.8)

$$\begin{aligned} b_1(z) &= e^{-i\beta z}\left(Ae^{-iCz} + Be^{+iCz}\right) \\ b_2(z) &= ie^{-i\beta z}\left(-Ae^{-iCz} + Be^{+iCz}\right). \end{aligned} \tag{3.13}$$

If we define the vector $\mathbf{V}(z) = \binom{b_1(z)}{b_2(z)}$, we find that there are two modes that form a basis of solutions to the propagation equation: $\mathbf{V}_s(z) = e^{-i(\beta-C)z}\binom{1}{1}$ and $\mathbf{V}_a(z) = e^{-i(\beta+C)z}\binom{1}{-1}$, corresponding to the cases $A = 0$ and $B = 0$ in the equation above.

The mode $\mathbf{V}_s$ corresponds to a *symmetrical* superposition of the two modes of the waveguides, and has a modified propagation constant $\beta_s = \beta - C$ while the mode $\mathbf{V}_a$ is an *antisymmetrical* superposition of the two modes of the waveguides with propagation constant $\beta_a = \beta + C$. Here, we can see that much like in the case of the interaction of two two-level systems in quantum mechanics, the coupling between the waveguides induces *mode-mixing* with a shift in the propagation constant of the modes for the coupled system. In other words, the coupling of the two waveguides changes the propagation velocity in the system. If we now assume that we send, like previously, only an amplitude A_0 in waveguide 1 at $z = 0$, then we get, from equation 3.11 (it is simply the case $\Delta\beta = 0$):

$$\begin{aligned} b_1(z) &= A_0 e^{-i\beta z}\cos(Cz) \\ b_2(z) &= iA_0 e^{-i\beta z}\sin(Cz), \end{aligned} \tag{3.14}$$

or in the basis of the eigenmodes of the coupled waveguides:

$$\mathbf{V}(z) = \frac{A_0}{2}\left(\mathbf{V}_s(z) + \mathbf{V}_a(z)\right) \tag{3.15}$$

What we can see from equation 3.15 is that the power now oscillates completely from waveguide 1 to waveguide 2, with a spatial pulsation C. In terms of the eigenmodes of the two waveguides, this can be understood through a *spatial beating* between the symmetrical and antisymmetrical modes.

One parameter of interest in this model, that we will reuse in the following sections, is the *coupling length* L_c, or half-beat length, defined as the length necessary for a complete transfer of optical power from one guide to the other:

$$L_c = \frac{\pi}{2C}. \tag{3.16}$$

3.1.1.2 Tight-binding model for a waveguide array

Let us now consider a waveguide array, in the simplest case where each guide only supports one mode, which we label a_n, associated to waveguide number n which is a relative integer. Each waveguide has an associated propagation constant β_n (which for now will not depend

on n, but it can be useful to label it to consider e.g. the effect of disorder). Then we can write the initial quantum state (before propagation) in the waveguide array as a superposition of all modes:

$$|\Psi(0)\rangle = \sum_n b_n(0)\,|a_n\rangle. \tag{3.17}$$

If the quantum state propagates along the z-axis without losses, we have at position z:

$$|\Psi(z)\rangle = \sum_n b_n(z)\,|a_n\rangle = \sum_n b_n(0)\,|a_n\rangle e^{-i\beta_n z}. \tag{3.18}$$

Let us also assume that there is a coupling between the nearest-neighbour modes in the waveguide array. We denote the coupling constant between waveguides n and $n+1$ by $C_{n,n+1}$. If we then write the evolution equation for each coefficient b_n, we have:

$$\frac{db_n}{dz} = -i\beta_n b_n + iC_{n,n+1}b_{n+1} + iC_{n-1,n}b_{n-1}. \tag{3.19}$$

Equation 3.19 will serve as the basis for the theoretical description and numerical simulations of our waveguide arrays. Although it is very complex to analytically solve in the case of an array with multiple waveguides, we can still get an intuitive physical understanding of the equation: the amplitude probability of the photon in waveguide n goes through a phase rotation at a rate β_n, while also leaking with a $\pi/2$ phase to the neighbouring waveguides over time, with a rate $C_{n,n+1}$ or $C_{n-1,n}$. Note that this $\pi/2$ phase is important, as it allows for the conservation of energy. Indeed, if we compute the derivative of the energy in the waveguide array, we get:

$$\begin{aligned}
\frac{d\sum_n |b_n|^2}{dz} &= \sum_n \left(\frac{db_n}{dz}b_n^* + \frac{db_n^*}{dz}b_n\right) \\
&= \sum_n -i\beta_n\left(b_n b_n^* - b_n^* b_n\right) + iC_{n-1,n}\left(b_{n-1}b_n^* - b_n b_{n-1}^*\right) + iC_{n,n+1}\left(b_{n+1}b_n^* - b_n b_{n+1}^*\right) \\
&= \sum_n iC_{n-1,n}b_{n-1}b_n^* + iC_{n,n+1}b_{n+1}b_n^* - \sum_{k=n+1} ib_{k-1,k}b_{k-1}b_k^* - \sum_{k=n-1} ib_{k,k+1}b_{k+1}b_k^* \\
&= 0,
\end{aligned} \tag{3.20}$$

where the last two terms in the third equality are simply reindexation of the terms subtracted on the previous line. The total probability amplitude is thus conserved during the propagation along the array. This equation thus describes a lossless evolution of the optical field.

Now if we consider it closely, we can see that equation 3.19 resembles a Schrödinger-type equation, where the propagation distance z plays the role of the time. Re-writing equation 3.19 by replacing z by ct where t is the time and c the speed of light, and rearranging the equation a bit by multiplying by i and $\hbar$, we find that:

$$i\hbar\frac{db_n}{dt} = c\hbar\beta_n b_n - c\hbar C_{n,n+1}b_{n+1} - c\hbar C_{n-1,n}b_{n-1} \tag{3.21}$$

which is the equation evolution of state $|\Psi\rangle$

$$i\hbar\frac{d|\Psi\rangle}{dt} = \hat{H}\,|\Psi\rangle \tag{3.22}$$

under the action of the Hamiltonian

$$\hat{H} = c\hbar \sum_n \beta_n \left|a_n\right\rangle \left\langle a_n\right| - C_{n,n+1} \left|a_n\right\rangle \left\langle a_{n+1}\right| - C_{n-1,n} \left|a_n\right\rangle \left\langle a_{n-1}\right|. \tag{3.23}$$

$\hat{H}$ is identical to the tight-binding Hamiltonian of a one-dimensional atom chain where an electron can take positions on sites n with energies $c\hbar\beta_n$ and hop to and from the closest neighbouring sites with amplitudes $c\hbar C_{n,n+1}$ and $c\hbar C_{n-1,n}$.

This in itself is interesting, because it means that waveguide arrays can serve as a simulation platform for this type of Hamiltonian, which is encountered in many situations in condensed matter systems [167]. Additionally, the coupling constants can be engineered to reproduce simple Hamiltonians presenting interesting topological properties, such as the Su-Schrieffer-Heeger (SSH) Hamiltonian [171]. Another important feature of this type of system is that it is a suitable candidate to realize quantum random walks: as a photon is injected into a certain waveguide and propagates, its probability amplitude propagates transversally to the neighbouring waveguides and eventually to all waveguides of the array. The propagation of the photon along the waveguide array is then a realization of a continuous-time quantum random walk, on a lattice where the sites are the waveguides of the array [172].

3.1.1.3 Bloch modes and transverse propagation in infinite arrays

We will now turn our interest to the case of an infinite waveguide array: although it is a purely theoretical case, it will actually allow us to introduce the concept of transverse wavevector, which is useful to get an intuitive and physical understanding of the mechanisms behind the quantum walks in waveguide arrays. It will also serve as a good approximation in arrays where $CL \ll N$, with L the propagation length and N the total number of waveguides in the array.

In this case, we will assume that $\beta_n = \beta$ and $C_{n,n+1} = C$ for all n, so that we have a periodic array of identical waveguides. Going back to the analogy with the case of a one-dimensional atomic chain, one can find the eigenstates of the Hamiltonian of equation 3.23 using Bloch's theorem:

$$\left|\Psi\left(k_\perp\right)\right\rangle = \sum_n e^{ik_\perp \cdot n} \left|a_n\right\rangle \tag{3.24}$$

since

$$\begin{aligned}
\hat{H}\left|\Psi\left(k_\perp\right)\right\rangle &= \left(c\hbar \sum_n \beta \left|a_n\right\rangle - C\left|a_{n+1}\right\rangle \left\langle a_n\right| - C\left|a_{n-1}\right\rangle \left\langle a_n\right|\right) \sum_m e^{ik_\perp \cdot m} \left|a_m\right\rangle \\
&= c\hbar\beta \left|\Psi\left(k_\perp\right)\right\rangle - c\hbar C \sum_{m,n} e^{ik_\perp \cdot m} \left(\left|a_{n+1}\right\rangle \left\langle a_n|a_m\right\rangle + \left|a_{n-1}\right\rangle \left\langle a_n|a_m\right\rangle\right) \\
&= c\hbar\beta \left|\Psi\left(k_\perp\right)\right\rangle - c\hbar C \sum_n e^{ik_\perp \cdot n} \left(\left|a_{n+1}\right\rangle + \left|a_{n-1}\right\rangle\right) \\
&= c\hbar\beta \left|\Psi\left(k_\perp\right)\right\rangle - c\hbar C \sum_n e^{ik_\perp \cdot (n-1)} \left|a_n\right\rangle + e^{ik_\perp \cdot (n+1)} \left|a_n\right\rangle \\
&= c\hbar\beta \left|\Psi\left(k_\perp\right)\right\rangle - c\hbar C \sum_n e^{ik_\perp \cdot n} \left|a_n\right\rangle \left(e^{ik_\perp} + e^{-ik_\perp}\right) \\
&= c\hbar \left(\beta \ - 2C\cos k_\perp\right) \left|\Psi\left(k_\perp\right)\right\rangle
\end{aligned} \tag{3.25}$$

We can see from equations 3.24 and 3.25 that the eigenmodes of the waveguide array are Bloch modes with transverse wavevector $k_\perp$ ranging between $-\pi$ and π, with amplitude spread amongst all the waveguides. The most interesting feature of these eigenmodes is the dependence of the energy with $k_\perp$. In terms of optical modes, this means that each Bloch mode has its own modal propagation constant $\beta(k_\perp) = \beta - 2C\cos k_\perp$: the coupling between the waveguides gives a band structure to the dispersion relation of the modes.

Another feature worthy of note is that these eigenmodes are not normalizable; however, we can write every $|a_n\rangle$ as an integral of these modes, much like we would use a Fourier transform:

$$|a_n\rangle = \frac{1}{2\pi}\int_{-\pi}^{\pi} e^{-ik_\perp \cdot n}\,|\Psi(k_\perp)\rangle dk_\perp \tag{3.26}$$

Since we know exactly how the Bloch modes propagate, this decomposition allows us to analytically compute the optical profile after an arbitrary propagation length from any input state.

Let us consider for instance that we send a single photon into mode $|a_0\rangle$ at $z = 0$, so that $|\Psi(0)\rangle = |a_0\rangle$. After a propagation of length z, each Bloch mode associated with $k_\perp$ is simply multiplied by $e^{-i\beta(k_\perp)z}$, which gives us

$$\begin{aligned}
|\Psi(z)\rangle &= \frac{1}{2\pi}\int_{-\pi}^{\pi} e^{-i\beta(k_\perp)z}\,|\Psi(k_\perp)\rangle dk_\perp \\
&= \frac{1}{2\pi}\int_{-\pi}^{\pi}\sum_n e^{-i\beta(k_\perp)}e^{ik_\perp n}\,|a_n\rangle\, dk_\perp \\
&= \frac{e^{-i\beta z}}{2\pi}\sum_n\int_{-\pi}^{\pi} e^{2iC\cos(k_\perp)z}e^{ik_\perp n}\,|a_n\rangle\, dk_\perp .
\end{aligned} \tag{3.27}$$

The field amplitude $b_n(z)$ in guide n after a propagation length z is then

$$\begin{aligned}
b_n(z) &= \frac{e^{-i\beta z}}{2\pi}\int_{-\pi}^{\pi} e^{2iC\cos(k_\perp)z}e^{ik_\perp n}dk_\perp \\
&= \frac{e^{-i\beta z}}{2\pi}\int_{-\pi+\frac{\pi}{2}}^{\pi+\frac{\pi}{2}} e^{2iC\cos(k_\perp)z}e^{ik_\perp n}dk_\perp \\
&= \frac{e^{-i\beta z}}{2\pi}\int_{-\pi+\frac{\pi}{2}}^{\pi+\frac{\pi}{2}} e^{2iC\sin(k_\perp-\pi/2)z}e^{ik_\perp n}dk_\perp \\
&= \frac{e^{-i\beta z}}{2\pi}\int_{-\pi}^{\pi} e^{-2iC\sin(k_\perp)z}e^{ik_\perp n}e^{-in\frac{\pi}{2}}dk_\perp \\
&= e^{-i\beta z}i^{-n}J_n(2Cz),
\end{aligned} \tag{3.28}$$

where J_n is the Bessel function of the first kind associated to number n.

The presence probability of the single photon thus propagates in the transverse direction and oscillates in every waveguide. This phenomenon, called *discrete diffraction*, has been extensively studied both theoretically and experimentally in the case of coherent optical waves [167]; a unique photon has the same behaviour (quantum effects only arise when at least two photons are considered). Figure 3.3 shows the full electromagnetic simulation of transverse propagation of coherent light through a waveguide array with typical parameters (more details are given in chapter 4). The simulation, which is in excellent agreement with the tight-binding approximation, shows that the intensity in one waveguide oscillates quasi-periodically, as expected from the behaviour of the Bessel

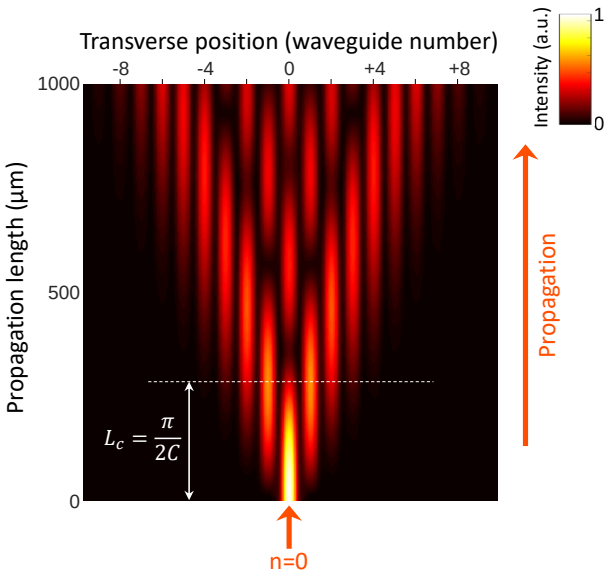

Figure 3.3: Electromagnetic simulation of the discrete diffraction of an optical wave in a waveguide array.

functions, and propagates transversally over a characteristic number of steps $2CL = \pi \frac{L}{L_c}$ after a longitudinal propagation over a length L.

3.1.1.4 Quantum walks of photon pairs

Let us now consider a pair of photons walking through the array, as for instance produced by SPDC. In this case, it is not sufficient to treat each photon individually, and we now need to consider the *joint spatial amplitude* of the two photons. If we label the photons s and i for signal and idler, so that this formalism is easily transferred to SPDC, and assuming that the waveguides now support single-photon modes $|a_{n_s}\rangle_s$ in guide n_s for the signal photon and $|a_{n_i}\rangle_i$ in guide n_i for the idler photon, then this joint spatial amplitude is simply the probability amplitude distribution b_{n_s,n_i} of the photon pair over all the possible waveguide pairs, so that we can write the biphoton state in the general case[1] as:

$$|\Psi(z)\rangle = \sum_{n_s,n_i} b_{n_s,n_i}(z) |a_{n_s}\rangle_s |a_{n_i}\rangle_i \tag{3.29}$$

The evolution of this joint spatial amplitude, represented by the matrix (b_{n_s,n_i}), is conditioned by a number of different factors. First, the waveguides still have propagation constants that have an influence on the phase evolution of the coefficients b_{n_s,n_i}. Secondly, the photons propagate transversally in the array and change waveguides, which translates to the probability amplitude moving from b_{n_s,n_i} to either $b_{n_s\pm1,n_i}$ or $b_{n_s,n_i\pm1}$, again with a phase $\frac{\pi}{2}$ as noted in section 3.1.1.1. The evolution of the joint spatial amplitude is thus governed by the set of equations

$$\frac{db_{n_i,n_s}}{dz} = -i(\beta_s + \beta_i) b_n + iC(b_{n_s,n_i+1} + b_{n_s,n_i-1} + b_{n_s+1,n_i} + b_{n_s-1,n_i}) \tag{3.30}$$

[1]Note that, in order to consider indistinguishable photons in the spatial degree of freedom, we can simply consider the matrix (b_{n_s,n_i}) to be symmetrical.

We are interested in the spatial mode correlations of the two photons, it is thus useful to consider the indicators that can be used to quantify the quantum properties of the photon pairs, such as entanglement or non-classicality. The first tool that can be used is simply the *joint spatial intensity*, which is the square modulus of the joint spatial amplitude:

$$\Gamma_{n_s,n_i} = |b_{n_s,n_i}|^2. \tag{3.31}$$

To show that this quantity reveals quantum correlations between the photons, let us temporarily come back to the simpler case of two coupled identical waveguides, in which we send two indistinguishable photons. We can here re-write equation 3.30 as:

$$\begin{aligned} \frac{db_{1,1}}{dz} &= -2i\beta b_{1,1} + 2iCb_{1,2} \\ \frac{db_{2,2}}{dz} &= -2i\beta b_{2,2} + 2iCb_{1,2} \\ \frac{db_{1,2}}{dz} &= -2i\beta b_{1,2} + iC\left(b_{2,2} + b_{1,1}\right) \\ b_{2,1} &= b_{1,2} \end{aligned} \tag{3.32}$$

Let us consider that we inject for instance one photon in each guide, so that $b_{1,2}(0) = b_{1,2}(0) = \frac{1}{\sqrt{2}}$ and $b_{1,1}(0) = b_{2,2}(0) = 0$. In terms of quantum states, if we go back to subsection 3.1.1.1, we can write the initial state as:

$$|\Psi(0)\rangle = \hat{a_1}^\dagger \hat{a_2}^\dagger |0\rangle \tag{3.33}$$

and decompose it into the symmetrical (s) and antisymmetrical (a) eigenmodes of the coupled waveguides:

$$\begin{aligned} |\Psi(0)\rangle &= \frac{1}{2}\left(\hat{a_s}^\dagger + \hat{a_a}^\dagger\right)\left(\hat{a_s}^\dagger - \hat{a_a}^\dagger\right)|0\rangle \\ &= \frac{1}{2}\left(\hat{a_s}^\dagger \hat{a_s}^\dagger - \hat{a_a}^\dagger \hat{a_a}^\dagger\right)|0\rangle . \end{aligned} \tag{3.34}$$

Since the two photons evolve independently and we know exactly how the eigenmodes behave as a function of z, we can derive the evolution of $|\Psi(z)\rangle$ and put it back in the $\{\hat{a_1}^\dagger, \hat{a_2}^\dagger\}$ basis:

$$\begin{aligned} |\Psi(z)\rangle &= \frac{e^{-i2\beta z}}{2}\left(e^{i2Cz}\hat{a_s}^\dagger \hat{a_s}^\dagger - e^{-i2Cz}\hat{a_a}^\dagger \hat{a_a}^\dagger\right)|0\rangle \\ &= \frac{e^{-i2\beta z}}{4}\left(e^{i2Cz}\left(\hat{a_1}^\dagger + \hat{a_2}^\dagger\right)\left(\hat{a_1}^\dagger + \hat{a_2}^\dagger\right) - e^{-i2Cz}\left(\hat{a_1}^\dagger - \hat{a_2}^\dagger\right)\left(\hat{a_1}^\dagger - \hat{a_2}^\dagger\right)\right)|0\rangle \\ &= \frac{e^{-i2\beta z}}{2}\left(\cos(2Cz)\left(\hat{a_1}^\dagger \hat{a_2}^\dagger + \hat{a_1}^\dagger \hat{a_2}^\dagger\right) + i\sin(2Cz)\left(\hat{a_1}^\dagger \hat{a_1}^\dagger + \hat{a_2}^\dagger \hat{a_2}^\dagger\right)\right)|0\rangle . \end{aligned} \tag{3.35}$$

From equation 3.35, we can now compute the average photon number in each waveguide [79]:

$$n_{1(2)}(z) = \cos^2(2Cz) + \sin^2(2Cz) = 1 \tag{3.36}$$

which is a constant. This is analogous to the behaviour of a coherent state of light simultaneously injected in the two guides: the power in each waveguide will never be zero, and will be a constant along the propagation direction.

However, a difference arises if we perform a coincidence measurement between the two waveguides. The coincidence probability is in this case:

$$P_c = \cos^2(2Cz) = \Gamma_{1,2} + \Gamma_{2,1}. \tag{3.37}$$

This coincidence probability oscillates between 0 and 1, and goes to zero for

$$z_0 = \frac{\pi}{4C} = \frac{L_c}{2}. \tag{3.38}$$

Hence, at propagation length z_0, which is half the coupling length L_c, the two photons bunch together and are never found in different waveguides, which shows a non-classical effect of the quantum walk of two correlated photons.

Coming back to the general case of a waveguide array, a general way to quantify the non-classicality of spatial correlations has been introduced by Bromberg *et al.* [79] and used in Refs [80,100]. It is a criterion stating that two incoherent classical beams coupled to two different waveguides generate intensity correlations that always verify the following inequality[2]:

$$\Gamma_{n_i,n_s} \geq \frac{1}{3}\sqrt{\Gamma_{n_i,n_i}\Gamma_{n_s,n_s}}. \tag{3.39}$$

A complete derivation of the criterion is given in appendix B. From this inequality, we define a non-classicality indicator

$$I_{\mathrm{NC}}(n_s, n_i) = \max\left(\frac{1}{3}\sqrt{\Gamma_{n_i,n_i}\Gamma_{n_s,n_s}} - \Gamma_{n_i,n_s}, 0\right) \tag{3.40}$$

that we use in the following section to give indication over the non-classicality of the state. This criterion gives a lower bound on Γ_{n_s,n_i} for the classical behaviour of light.

In an opposite manner, the Cauchy-Schwartz inequality, which gives an upper bound for classical behaviour $\Gamma_{n_s,n_i} \leq \sqrt{\Gamma_{n_i,n_i}\Gamma_{n_s,n_s}}$, can be used as well to define the Cauchy-Schwartz violation indicator:

$$I_{\mathrm{CS}}(n_s, n_i) = \max\left(\Gamma_{n_i,n_s} - \sqrt{\Gamma_{n_i,n_i}\Gamma_{n_s,n_s}}, 0\right) \tag{3.41}$$

The two inequalities give two different characterizations for non-classical behaviours that violate the inequation $\frac{1}{3}\sqrt{\Gamma_{n_i,n_i}\Gamma_{n_s,n_s}} \leq \Gamma_{n_s,n_i} \leq \sqrt{\Gamma_{n_i,n_i}\Gamma_{n_s,n_s}}$.

3.1.2 Cascaded quantum walks in nonlinear waveguide arrays

In most previous experimental studies of quantum walks, the photons were generated with external sources and injected into a passive array. We now want to consider the interplay between SPDC and quantum random walks in waveguide arrays made from material with second-order nonlinearity, such as AlGaAs.

[2]In that sense, it is not rigorously an entanglement witness, since we can imagine special classical states of light that would violate it. However, it can still give a good indication of non-classical correlations.

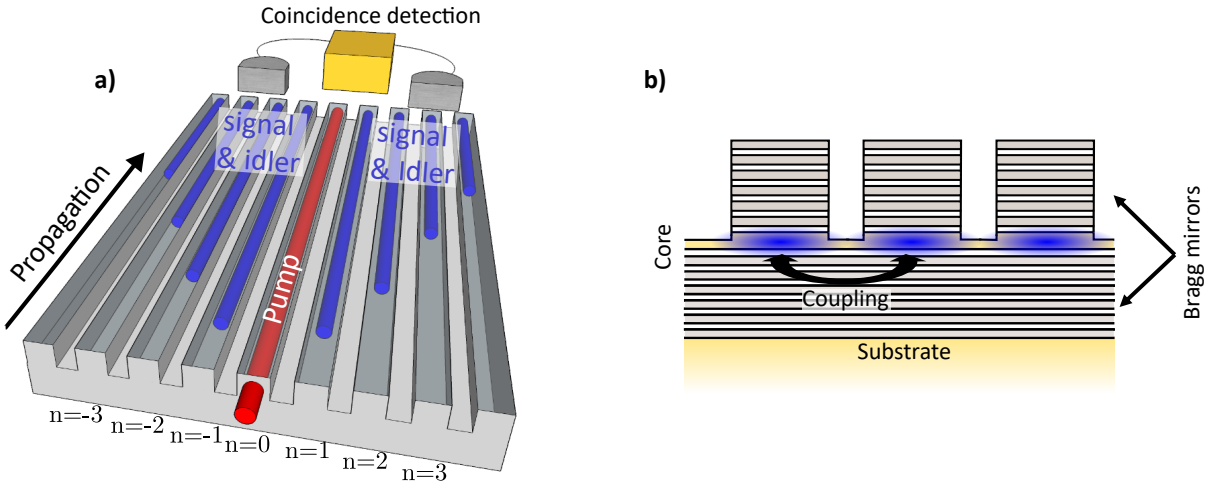

Figure 3.4: a) Working principle of the photon pair generation in a nonlinear waveguide array, where the pump is injected into the central waveguide and the generated SPDC photons can tunnel to the adjacent waveguides. b) Transverse section of an AlGaAs waveguide array with evanescent coupling between the different waveguides.

3.1.2.1 Simplest theoretical case: infinite array with no pump propagation

With this goal in mind, we will consider the simple case, in which each single waveguide of the arrays only supports three interacting modes, a pump mode that we will label p, a signal mode s and an idler mode i (they can, however, be the same transverse mode and simply differ by their frequencies or polarization). We consider the SPDC in the undepleted pump limit.

The working principle is illustrated in figure 3.4. Let us assume that we inject a pump beam (sketched in red in figure 3.4a) into the central waveguide of the array, and that this pump beam undergoes SPDC during its travel inside the array. For now, we will assume that the pump does not undergo transverse propagation throughout the array, which is naturally favored by its twice shorter wavelength. We also assume that the process is sufficiently weak so that the probability of generating two photon pairs is negligible.

In this situation, the pump beam will generate (at most) one pair of signal and idler photons (sketched in blue in figure 3.4a) inside the pumped waveguide, which will then undergo quantum walks by tunneling to the neighbouring waveguides because of evanescent coupling (figure 3.4b). Due to the probabilistic nature of the SPDC process, the photon pairs can be generated at all possible positions along the propagation axis. The output quantum state results from the interference between the various probability amplitudes from the different generation positions. This is the concept of *cascaded quantum walks*, presented by Solntsev *et al.* [80], which results in a higher level of spatial entanglement compared to the case of quantum walks in passive arrays. This principle can be generalized to the situation where several waveguides are simultaneously pumped, which allows for further tailoring of the spatial correlations as will be shown later in the chapter.

Hamiltonian

Let us consider the nonlinear Hamiltonian of the system, which is similar to what has been shown in section 1.1.6, except we now need to simultaneously consider all of the waveguides:

$$\hat{H}_{NL}(t) = \frac{\epsilon_0}{2} \sum_n \int_V d\mathbf{r} d_{\text{eff}}(\mathbf{r}) \hat{E}_{p,n}(\mathbf{r},t)\, \hat{E}_{s,n}(\mathbf{r},t)\, \hat{E}_{i,n}(\mathbf{r},t) \tag{3.42}$$

with $d_{\text{eff}}(\mathbf{r})$ the element of the second-order nonlinearity tensor of the material describing the interaction between the pump, signal and idler modes, and $\hat{E}_{j,n}$ the modal fields from waveguide n, with $j = p, s, i$. Much like in section 1.1.6, we can consider here only the interactions in which exactly one pump photon is converted into a signal and idler photon pair and its reciprocal process (which is in mathematical terms its Hermitian conjugate). The Hamiltonian then reduces to:

$$\hat{H}_{\text{SPDC}}(t) = \frac{\epsilon_0}{2} \sum_n \int_V d\mathbf{r} d_{\text{eff}}(\mathbf{r}) \hat{E}^{(+)}_{p,n}(\mathbf{r},t)\, \hat{E}^{(-)}_{s,n}(\mathbf{r},t)\, \hat{E}^{(-)}_{i,n}(\mathbf{r},t) + \textbf{h.c.} \tag{3.43}$$

If we decompose the waveguided modal fields in the Bloch mode basis, we get, treating like in section 1.1.6 the pump field as a classical field and the signal and idler fields as operators[3,4]:

$$\begin{aligned}
E^{(+)}_{p,n}(\mathbf{r},t) =& \frac{1}{2\pi} \int d\omega_p dk_p^\perp A_{spectral}(\omega_p) \tilde{A}_{spatial}(k_p^\perp) e^{i\left(\omega_p t - \beta_p\left(\omega_p, k_p^\perp\right) z\right)} e^{-ik_p^\perp n} E_{p,n}(x,y) \\
\hat{E}^{(+)}_{s,n}(\mathbf{r},t) =& \frac{1}{2\pi} \int d\omega_s dk_s^\perp e^{i\left(\omega_s t - \beta_s\left(\omega_s, k_s^\perp\right) z\right)} e^{-ik_s^\perp n} E_{s,n}(x,y) \hat{a}_s\left(\omega_s, k_s^\perp\right) \\
\hat{E}^{(+)}_{i,n}(\mathbf{r},t) =& \frac{1}{2\pi} \int d\omega_s dk_i^\perp e^{i\left(\omega_i t - \beta_i\left(\omega_i, k_i^\perp\right) z\right)} e^{-ik_i^\perp n} E_{i,n}(x,y) \hat{a}_i\left(\omega_i, k_i^\perp\right)
\end{aligned} \tag{3.44}$$

where z is the propagation direction and $E_{j,n}(x,y)$ is the normalized transverse profile of the single-waveguide mode, with $j = p, s, i$. $A_{spectral}(\omega_p)$ denotes the spectrum of the pump, while $\tilde{A}_{spatial}(k_p^\perp)$ is the Fourier transform of the spatial distribution of the pump in the array.

We can then re-write the Hamiltonian by replacing the interacting fields by their mathematical expressions:

$$\begin{aligned}
\hat{H}_{\text{SPDC}}(t) =& \frac{\epsilon_0}{2\,(2\pi)^3} \sum_n \int d\omega_p d\omega_s d\omega_i A_{spectral}(\omega_p) e^{i(\omega_p - \omega_s - \omega_i)t} \\
& \cdot \int dz dk_p^\perp dk_s^\perp dk_i^\perp \tilde{A}_{spatial}(k_p^\perp) e^{i\left(\beta_s\left(\omega_s, k_s^\perp\right) + \beta_i\left(\omega_i, k_i^\perp\right) - \beta_p\left(\omega_p, k_p^\perp\right)\right) z} e^{i\left(k_s^\perp + k_i^\perp - k_p^\perp\right) n} \\
& \cdot \int dx dy d_{\text{eff}}(x,y)\, E_{p,n}(x,y) E^*_{s,n}(x,y) E^*_{i,n}(x,y) \\
& \cdot \hat{a}_s{}^\dagger\left(\omega_s, k_s^\perp\right) \hat{a}_i{}^\dagger\left(\omega_i, k_i^\perp\right)
\end{aligned} \tag{3.45}$$

[3] We do not consider here the effect of the group velocity, that is in good approximation a constant term over the considered bandwidth, as it makes the calculation heavy, but the result is easily generalizable.

[4] We consider here the modified propagation constant of the collective Bloch modes for the pump, signal and idler $\beta_j\left(\omega_j, k_j^\perp\right) = \beta_j^{(0)} - 2C_j \cos\left(k_j^\perp\right)$ with $j = p, s, i$, where $\beta_j^{(0)}$ is the propagation constant for a single waveguide.

and using $\sum_n e^{ikn} = 2\pi\delta(k)$, we get a term $2\pi\delta\left(k_s^\perp + k_i^\perp - k_p^\perp\right)$ inside the integral and we can simplify it:

$$\begin{aligned}\hat{H}_{\text{SPDC}}(t) =& \frac{\epsilon_0 \Gamma_{\text{eff}}}{8\pi^2} \int d\omega_p d\omega_s d\omega_i A_{spectral}(\omega_p) e^{i(\omega_p-\omega_s-\omega_i)t} \\ & \cdot \int dz dk_s^\perp dk_i^\perp \tilde{A}_{spatial}(k_s^\perp + k_i^\perp) e^{i\left(\beta_s\left(\omega_s,k_s^\perp\right)+\beta_i\left(\omega_i,k_i^\perp\right)-\beta_p\left(\omega_p,k_s^\perp+k_i^\perp\right)\right)z} \\ & \cdot \hat{a_s}^\dagger\left(\omega_s, k_s^\perp\right) \hat{a_i}^\dagger\left(\omega_i, k_i^\perp\right)\end{aligned} \tag{3.46}$$

The efficiency of the SPDC process is governed by the nonlinear integral overlap of the single-waveguide modes, appearing in equation 3.46:

$$\Gamma_{\text{eff}} = \int_S d_{\text{eff}}(x,y) E_{p,n}(x,y) E_{s,n}^*(x,y) E_{i,n}^*(x,y) dxdy, \tag{3.47}$$

which does not depend on the waveguide number n since all waveguides are assumed identical and independent of frequency.

Equation 3.46 shows that in terms of Bloch modes, the SPDC must satisfy an additional condition in the case of waveguide arrays which is the *conservation of the transverse wavevector*, similar to an exact phase-matching condition for the Bloch modes. In the case of an infinite periodic array, this exact conservation condition is related to the translational invariance of the system in the transverse direction.

Biphoton state at the array output

The Hamiltonian evolution of a photonic quantum state is then given by the Schrödinger equation for the nonlinear interaction:

$$i\hbar \frac{d|\Psi\rangle}{dt} = \hat{H}_{\text{SPDC}}(t)|\Psi\rangle. \tag{3.48}$$

In actual semiconductors, the probability to generate a photon pair from a single pump photon is very low, so if we assume that we are initially in the vacuum state $|0\rangle$, we then have, neglecting the events of multiple pairs creation:

$$|\Psi(t)\rangle = e^{-\frac{i}{\hbar}\int_{-\infty}^{t} \hat{H}_{\text{SPDC}}(t)dt}|0\rangle \approx |0\rangle - \frac{i}{\hbar}\int_{-\infty}^{t} \hat{H}_{\text{SPDC}}(t)dt\,|0\rangle. \tag{3.49}$$

Our final state is

$$|\Psi\rangle = |0\rangle - \frac{i}{\hbar}\int_{-\infty}^{+\infty} \hat{H}_{\text{SPDC}}(t)dt\,|0\rangle \tag{3.50}$$

Here, we will as before post-select the quantum state on the subspace in which there is a photon pair, meaning that we are only interested in the second term of the equality, which is (for now without normalization):

$$
\begin{aligned}
|\Psi\rangle =& -\frac{i}{\hbar}\int_{-\infty}^{+\infty}\hat{H}_{\text{SPDC}}(t)dt\,|0\rangle \\
=& -\frac{i}{\hbar}\int_{t=-\infty}^{+\infty}dt\frac{\epsilon_0\Gamma_{\text{eff}}}{8\pi^2}\int d\omega_p d\omega_s d\omega_i A_{spectral}(\omega_p)e^{i(\omega_p-\omega_s-\omega_i)t} \\
&\cdot\int dk_s^\perp dk_i^\perp \tilde{A}_{spatial}(k_s^\perp+k_i^\perp)\int_0^L dz e^{i\left(\beta_s\left(\omega_s,k_s^\perp\right)+\beta_i\left(\omega_i,k_i^\perp\right)-\beta_p\left(\omega_p,k_s^\perp+k_i^\perp\right)\right)z} \\
&\cdot\hat{a_s}^\dagger\left(\omega_s,k_s^\perp\right)\hat{a_i}^\dagger\left(\omega_i,k_i^\perp\right)|0\rangle \\
=&\frac{i\epsilon_0\Gamma_{\text{eff}}}{\hbar 8\pi^2}\int d\omega_p d\omega_s d\omega_i A_{spectral}(\omega_p)e^{i(\omega_p-\omega_s-\omega_i)t}\delta\left(\omega_p-\omega_s-\omega_i\right) \\
&\cdot\int dk_s^\perp dk_i^\perp \tilde{A}_{spatial}(k_s^\perp+k_i^\perp)L\,\text{sinc}\left(\Delta\beta\left(\omega_s,\omega_i,k_s^\perp,k_i^\perp\right)\frac{L}{2}\right)e^{-i\left(\Delta\beta\left(\omega_s,\omega_i,k_s^\perp,k_i^\perp\right)\frac{L}{2}\right)} \\
&\cdot\hat{a_s}^\dagger\left(\omega_s,k_s^\perp\right)\hat{a_i}^\dagger\left(\omega_i,k_i^\perp\right)|0\rangle \\
=&\frac{i\epsilon_0\Gamma_{\text{eff}}L}{\hbar 8\pi^2}\int d\omega_s d\omega_i dk_s^\perp dk_i^\perp A_{spectral}(\omega_s+\omega_i)\tilde{A}_{spatial}(k_s^\perp+k_i^\perp)\,\text{sinc}\left(\Delta\beta\left(\omega_s,\omega_i,k_s^\perp,k_i^\perp\right)\frac{L}{2}\right) \\
&\cdot e^{-i\left(\Delta\beta\left(\omega_s,\omega_i,k_s^\perp,k_i^\perp\right)\frac{L}{2}\right)}\hat{a_s}^\dagger\left(\omega_s,k_s^\perp\right)\hat{a_i}^\dagger\left(\omega_i,k_i^\perp\right)|0\rangle
\end{aligned}
\tag{3.51}
$$

where we have defined the phase mismatch $\Delta\beta\left(\omega_s,\omega_i,k_s^\perp,k_i^\perp\right)=\beta_p\left(\omega_p,k_p^\perp\right)-\beta_s\left(\omega_s,k_s^\perp\right)-\beta_i\left(\omega_i,k_i^\perp\right)$.

Spatio-Spectral Amplitude

We can thus write the post-selected state after SPDC:

$$
|\Psi\rangle=\int d\omega_s d\omega_i dk_s^\perp dk_i^\perp\phi\left(\omega_s,\omega_i,k_s^\perp,k_i^\perp\right)\hat{a_s}^\dagger\left(\omega_s,k_s^\perp\right)\hat{a_i}^\dagger\left(\omega_i,k_i^\perp\right)|0\rangle \tag{3.52}
$$

This state is a superposition of spatio-spectral modes, which is a generalization of the case of SPDC in a single waveguide where we had a superposition of spectral modes. The distribution of spatio-spectral modes is given by the Joint Spatio-Spectral Amplitude ϕ, which is a generalization of the Joint Spectral Amplitude from section 1.1.6. From equation 3.51, it reads:

$$
\begin{aligned}
\phi\left(\omega_s,\omega_i,k_s^\perp,k_i^\perp\right)=&\frac{1}{\sqrt{N}}A_{spectral}(\omega_s+\omega_i)\tilde{A}_{spatial}(k_s^\perp+k_i^\perp) \\
&\cdot\,\text{sinc}\left(\Delta\beta\left(\omega_s,\omega_i,k_s^\perp,k_i^\perp\right)\frac{L}{2}\right)e^{-i\left(\Delta\beta\left(\omega_s,\omega_i,k_s^\perp,k_i^\perp\right)\frac{L}{2}\right)}
\end{aligned}
\tag{3.53}
$$

with N a normalization constant.

One can see that there are three terms in ϕ. The first term $A_{spectral}\left(\omega_s+\omega_i\right)$ represents the spectrum of the pump beam, and it encapsulates the energy conservation in the SPDC process: photon pairs at frequency (ω_s,ω_i) can only be produced if the pump's spectrum at $\omega_p=\omega_s+\omega_i$ is non-zero. The second term $\tilde{A}_{spatial}(k_s^\perp+k_i^\perp)$ is the Fourier transform of the spatial shape of the pump, or equivalently its amplitude in the transverse wavevector space, and it incorporates the conservation of transverse wavevectors during the SPDC process, which we have shown in equation 3.46. The last term is

$\text{sinc}\left(\Delta\beta\left(\omega_s,\omega_i,k_s^\perp,k_i^\perp\right)\frac{L}{2}\right)$, and is the origin of the phase-matching condition of SPDC processes. It makes an interesting property of the SPDC in waveguide arrays apparent: the phase-matching is modified by the coupling between the waveguides. Indeed, from equation 3.25, the effective propagation constant for the Bloch modes of the waveguide array is $\beta(k^\perp) = \beta^{(0)} - 2C\cos(k_\perp)$ (where $\beta^{(0)}$ is the propagation constant of an uncoupled waveguide). If we assume that the array is perfectly periodic and the coupling between the waveguides is homogeneous, but that it can still depend on the frequencies of the specific modes and on their properties (for instance their polarization), we have

$$\begin{aligned}\Delta\beta\left(\omega_s,\omega_i,k_s^\perp,k_i^\perp\right) =& \beta_p\left(\omega_p,k_p^\perp\right) - \beta_s\left(\omega_s,k_s^\perp\right) - \beta_i\left(\omega_i,k_i^\perp\right)\\ =& \beta_p^{(0)}\left(\omega_s+\omega_i\right) - \beta_s^{(0)}\left(\omega_s\right) - \beta_i^{(0)}\left(\omega_i\right)\\ &+ 2C_s\left(\omega_s\right)\cos\left(k_s^\perp\right) + 2C_i\left(\omega_i\right)\cos\left(k_i^\perp\right)\\ =& \Delta\beta^{(0)}\left(\omega_s,\omega_i\right) + \Delta\beta^C\left(\omega_s,\omega_i,k_s^\perp,k_i^\perp\right)\end{aligned} \tag{3.54}$$

with $\Delta\beta^{(0)} = \beta_p^{(0)}\left(\omega_s+\omega_i\right) - \beta_s^{(0)}\left(\omega_s\right) - \beta_i^{(0)}\left(\omega_i\right)$ the phase mismatch in the case of a single waveguide, and $\Delta\beta^C$ the additional mismatch stemming from the coupling between the waveguides[5]. We will discuss this phase-matching term in more details in the following section, when we will talk about the correlations between the spatial and spectral degrees of freedom that it encapsulates.

Spatial intensity correlations

Having derived the shape of the biphoton state $|\Psi\rangle$, we can first turn our interest to its spatial correlations. To this end, we first define the intensity correlations in transverse wavevector space:

$$\tilde{\Gamma}_{k_s^\perp,k_i^\perp} = \int d\omega_s d\omega_i |\phi\left(\omega_s,\omega_i,k_s^\perp,k_i^\perp\right)|^2. \tag{3.55}$$

Although this quantity is useful from a formal point of view, since it quantifies the correlations between the two photons in the transverse momentum space, it is of less practical interest, since it is hard to experimentally measure the distribution of the two photons in the Bloch modes basis. What we can more directly access experimentally is the probability distribution for the two photons to be in the waveguide pairs (n_s, n_i), which is Γ_{n_s,n_i}. Here, we can decompose the creation operators for the Bloch modes[6] $\hat{a_j}^\dagger\left(\omega_j,k_j^\perp\right) = \sum_n e^{-ik_j^\perp n} e^{2iC_j\cos\left(k_j^\perp\right)L}\hat{a_j}^\dagger\left(\omega_j,n\right)$, with $j = s,i$. Starting from equation 3.52 this gives:

[5]The modified phase-matching does not include the coupling constant for the pump, as we have assumed that it was negligible, but at this stage, the result is easily generalizable to the case of a pump propagating in the transverse direction.

[6]We consider the modes after a propagation length L, which imposes a phase difference between the collective Bloch modes and the single-waveguide modes of $2C_j\cos\left(k_j^\perp\right)L$.

$$
\begin{aligned}
|\Psi\rangle =& \frac{1}{\sqrt{N}} \int d\omega_s d\omega_i dk_s^{\perp} dk_i^{\perp} \sum_{n_s,n_i} \phi\left(\omega_s,\omega_i,k_s^{\perp},k_i^{\perp}\right) e^{-ik_s^{\perp}n_s} e^{-ik_i^{\perp}n_i} \\
& e^{2i\left(C_s\cos\left(k_s^{\perp}\right)+C_i\cos\left(k_i^{\perp}\right)\right)L} \hat{a_s}^{\dagger}\left(\omega_s,n_s\right)\hat{a_i}^{\dagger}\left(\omega_i,n_i\right)|0\rangle \\
=& \frac{1}{\sqrt{N}} \int d\omega_s d\omega_i \sum_{n_s,n_i} \left(\int dk_s^{\perp} dk_i^{\perp} \phi\left(\omega_s,\omega_i,k_s^{\perp},k_i^{\perp}\right) e^{-ik_s^{\perp}n_s} e^{-ik_i^{\perp}n_i} \right. \\
& \left. \cdot e^{-2i\left(C_s\cos\left(k_s^{\perp}\right)+C_i\cos\left(k_i^{\perp}\right)\right)L} \right) \hat{a_s}^{\dagger}\left(\omega_s,n_s\right)\hat{a_i}^{\dagger}\left(\omega_i,n_i\right)|0\rangle \\
=& \frac{1}{\sqrt{N}} \int d\omega_s d\omega_i \sum_{n_s,n_i} \tilde{\phi}\left(\omega_s,\omega_i,n_s,n_i\right)\hat{a_s}^{\dagger}\left(\omega_s,n_s\right)\hat{a_i}^{\dagger}\left(\omega_i,n_i\right)|0\rangle
\end{aligned}
\tag{3.56}
$$

with $\tilde{\phi}\left(\omega_s,\omega_i,n_s,n_i\right)$ the 2-dimensional spatial Fourier transform of

$$
\phi\left(\omega_s,\omega_i,k_s^{\perp},k_i^{\perp}\right) e^{-2i\left(C_s\cos\left(k_s^{\perp}\right)+C_i\cos\left(k_i^{\perp}\right)\right)L}.
$$

We thus obtain:

$$
\Gamma_{n_s,n_i} = \int d\omega_s d\omega_i |\tilde{\phi}\left(\omega_s,\omega_i,n_s,n_i\right)|^2, \tag{3.57}
$$

generalizing equation 3.31. The real-space variables n_s and n_i are more readily accessible experimentally, and directly usable, for instance by connecting the end of each waveguide in the array to a specific channel (a fiber, an integrated waveguide structure on a photonic chip ...). Quite similarly to the case of SPDC in single waveguides, we can see that both the constraints given by the transverse wavevector conservation and the modified phase-matching term contribute to creating correlations in the transverse wavevector space (and thus in real space) since the phase-matching term is not separable as a function of the variables $k_s^{\perp}, k_i^{\perp}$.

3.1.2.2 Spatio-spectral correlations and purity of the spatial state

Let us now go back to the analysis of the modified phase-matching. Equation 3.54 can be written by using the effective indices for the pump, signal and idler modes:

$$
\begin{aligned}
\Delta\beta\left(\omega_s,\omega_i,k_s^{\perp},k_i^{\perp}\right) =& \Delta\beta^{(0)}\left(\omega_s,\omega_i\right) + \Delta\beta^{C}\left(\omega_s,\omega_i,k_s^{\perp},k_i^{\perp}\right) \\
=& \frac{1}{c}\left(\left(\omega_s+\omega_i\right)n_p\left(\omega_s+\omega_i\right) - \omega_s n_s(\omega_s) - \omega_i n_i(\omega_i)\right) \\
& + 2C_s\left(\omega_s\right)\cos\left(k_s^{\perp}\right) + 2C_i\left(\omega_i\right)\cos\left(k_i^{\perp}\right)
\end{aligned}
\tag{3.58}
$$

An important feature of this phase-matching is that it induces spatio-spectral correlations in the biphoton state, since the phase mismatch needs to be close to zero in order for the SPDC process to take place efficiently. If there were no coupling between the waveguides, the phase mismatch would simply be, like in the single-waveguide case:

$$
\Delta\beta^{0}\left(\omega_s,\omega_i\right) = \frac{1}{c}\left(\left(\omega_s+\omega_i\right)n_p\left(\omega_s+\omega_i\right) - \omega_s n_s(\omega_s) - \omega_i n_i(\omega_i)\right). \tag{3.59}
$$

As shown in section 1.2.2 (figure 1.9a), if we consider the SPDC efficiency as a function of the pump frequency, such a phase-matching induces a very narrow resonance: indeed, it is only possible for the phase mismatch to be close to zero, and thus for the generation to be maximally efficient, in a narrow range of pump frequency where the modal index of the pumping mode at ω_p is close to the mean of the modal indices of the signal and idler modes close to degeneracy $\omega_s \approx \omega_i \approx \frac{\omega_p}{2}$. If we now consider the coupling between the waveguides in the array, the phase-mismatch has an additional term than can compensate for the spectral part of the phase mismatch, up to $\Delta\beta^C_{max} = 2\left(C_s + C_i\right)$. This means that *exact* phase-matching is still possible for frequencies that satisfy $|\Delta\beta^0| \leq \Delta\beta^C_{max}$ and thus there is a wider pump frequency range where SPDC can be conducted efficiently: the coupling between the waveguide relaxes the constraints on the pump frequency for efficient photon pair generation. This effect can be quantified if we know the particular frequency dependence of the involved modal indices, and we will present numerical simulations of the enlargement of the SPDC spectrum in the following section.

The coupling between the spatial and spectral degrees of freedom can have interesting effects, and a detailed study of this coupling is given in [173], which we will summarize here. The phase mismatch 3.58 and its frequency and transverse wavevector dependence is inherent to the waveguide array, and determines the shape of all possible correlations, while the spectral and spatial shape of the pump can serve as a selection of a subspace of the correlations.

Indeed, by selecting a frequency ω_p for the pump, one selects a line along the antidiagonal in the (ω_s, ω_i) space, and thus the spectral shaping of the pump allows to select a specific subspace of values for the frequency phase-mismatch $\Delta\beta^{(0)}$. In a similar way, the spatial shaping of the pump on a specific transverse wavevector selects an antidiagonal in the $\left(k_s^\perp, k_i^\perp\right)$ space, and thus a specific subspace of values for the possible coupling phase-mismatch $\Delta\beta^C$. Note here that the space of interest for the $\left(k_s^\perp, k_i^\perp\right)$ variables is a two-dimensional torus, which has an effect on the specific shape of the selected subspace. Is is interesting to note here that both the energy conservation and the transverse wavevector conservation add constraints on the variety of subspaces that can be selected, while the modified phase-matching term act as an envelope for the possible joint spatio-spectral amplitude that can be achieved with this source. Thus, both the spectral and spatial shaping of the pump can be used as a form of control over the quantum state produced, making the nonlinear waveguide array a reconfigurable source of spatio-spectral correlations (albeit not giving fully arbitrary control over the final biphoton state).

Shape of the spatial correlations

It is possible to get a general idea of the shape of the spatial correlations by making a rough analysis of the single-waveguide phase-matching condition. Let us assume we are in the simple case where $C_s = C_i = C$ and that perfect phase-matching at degeneracy is permitted by the pump frequency, i.e. $\Delta\beta^{(0)}(\omega_p/2, \omega_p/2) = 0$. In this case, the phase-mismatch $\Delta\beta^C$ takes values in a symmetrical interval around 0, whose width is dictated by the coupling constant C. Perfect phase-matching condition around degeneracy is then given by the condition $\Delta\beta^C(\omega_p/2, \omega_p/2, k_s^\perp, k_i^\perp) = 0$, i.e. $2C\left(\omega_p/2\right)\left(\cos\left(k_s^\perp\right) + \cos\left(k_i^\perp\right)\right) = 0$. The modified phase-matching condition thus selects transverse wavevectors around the

square defined in the torus $(k_s^\perp, k_i^\perp)$-space by the condition $k_s^\perp = \pi \pm k_i^\perp$.

If we now discard the frequency degree of freedom to study the shape of the spatial correlations for a pump equally spread over all transverse wavevectors (e.g. when pumping a single waveguide) and consider the case where the transverse wavevector condition is perfectly respected, the state can be written as[7]:

$$\begin{aligned}
|\Psi\rangle \simeq & \frac{1}{\sqrt{N'}} \int_{-\pi}^{\pi} dk_s^\perp \left(\left| k_s^\perp, \pi - k_s^\perp \right\rangle + \left| k_s^\perp, \pi + k_s^\perp \right\rangle \right) \\
= & \frac{1}{\sqrt{N'}} \int_{-\pi}^{\pi} dk_s^\perp \sum_{n_s,n_i} \left(e^{i(k_s^\perp n_s + \pi n_i - k_s^\perp n_i)} + e^{i(k_s^\perp n_s + \pi n_i + k_s^\perp n_i)} \right) |n_s, n_i\rangle \\
= & \frac{1}{\sqrt{N'}} \sum_{n_s,n_i} e^{i\pi n_i} \left(\int_{-\pi}^{\pi} dk_s^\perp e^{ik_s^\perp (n_s - n_i)} + \int_{-\pi}^{\pi} dk_s^\perp e^{ik_s^\perp (n_s + n_i)} \right) |n_s, n_i\rangle \\
= & \frac{2\pi}{\sqrt{N'}} \sum_{n_s,n_i} e^{i\pi n_i} \left(\delta_{n_s,n_i} + \delta_{n_s,-n_i} \right) |n_s, n_i\rangle \\
= & \frac{2\pi}{\sqrt{N'}} \sum_{n} e^{i\pi n} \left(|n, n\rangle + |n, -n\rangle \right).
\end{aligned} \tag{3.60}$$

From this hand-waving reasoning, the correlations can thus be expected to be mainly localized on the diagonal and antidiagonal terms of the matrix Γ_{n_s,n_i}, i.e. terms of the type $\Gamma_{n,n}$ and $\Gamma_{n,-n}$. This effect will become apparent when we present simulations for the spatial correlations in the case of a pure state pumped at degeneracy (see paragraph 3.2.1.5 and figure 3.11) and can be interpreted as a *simultaneous bunching and antibunching* of the generated photon pairs in the waveguide array[8].

Reduced spatial density matrix

Although these spatio-spectral correlations can be used as a resource for quantum information, in the following we will mainly be interested in the spatial part of the Joint Spatio-Spectral Amplitude and in our case the spatio-spectral correlations will be a limiting effect on the purity of the spatial state that we measure. Indeed, we will experimentally only have access to the measurement of the spatial correlations without any spectral resolution, which will yield a mixed state for the spatial state. This is not a fundamental problem, since one can always spectrally filter the signal and idler photons in a narrow range around specific frequencies, which is mathematically equivalent to a projection in the total Hilbert space, giving access to a pure spatial state.

A useful metric to quantify the spatio-spectral correlations in the absence of filtering is the reduced spatial density matrix. To define it, we start from the pure biphoton state $|\Psi\rangle$ defined in the previous section (equation 3.52) and write the associated density matrix

[7]There is no phase in the Fourier transform in this case, since the condition $k_s^\perp = \pi \pm k_i^\perp$ precisely cancels the phase term $2C\left(\omega_p/2\right)\left(\cos\left(k_s^\perp\right) + \cos\left(k_i^\perp\right)\right)$.

[8]The intensity correlations are spread over all guides in the waveguide array in the case of an infinite propagation length and perfect phase-matching, but in a practical situation the spread of the state will be limited by the propagation length.

$$\begin{aligned}\hat{\rho} =& \left|\Psi\right\rangle \left\langle\Psi\right| \\ =& \frac{1}{N}\int d\omega_s d\omega_i dk_s^{\perp} dk_i^{\perp} \phi\left(\omega_s, \omega_i, k_s^{\perp}, k_i^{\perp}\right) \hat{a_s}^{\dagger}\left(\omega_s, k_s^{\perp}\right) \hat{a_i}^{\dagger}\left(\omega_i, k_i^{\perp}\right) \left|0\right\rangle \\ & \cdot \int d\omega_s' d\omega_i' dk_s'^{\perp} dk_i'^{\perp} \phi^*\left(\omega_s', \omega_i', k_s'^{\perp}, k_i'^{\perp}\right) \left\langle 0\right| \hat{a_s}\left(\omega_s', k_s'^{\perp}\right) \hat{a_i}\left(\omega_i', k_i'^{\perp}\right) \\ =& \frac{1}{N}\int d\omega_s d\omega_i dk_s^{\perp} dk_i^{\perp} \phi\left(\omega_s, \omega_i, k_s^{\perp}, k_i^{\perp}\right) \left|\omega_s, k_s^{\perp}\right\rangle \left|\omega_i, k_i^{\perp}\right\rangle \\ & \cdot \int d\omega_s' d\omega_i' dk_s'^{\perp} dk_i'^{\perp} \phi^*\left(\omega_s', \omega_i', k_s'^{\perp}, k_i'^{\perp}\right) \left\langle\omega_s', k_s'^{\perp}\right| \left\langle\omega_i', k_i'^{\perp}\right|\end{aligned} \tag{3.61}$$

where $\left|\omega_j, k_j^{\perp}\right\rangle$ denotes the state of a single photon in the mode $j = s, i$ at frequency ω_j and with transverse wavevector $k_j^{\perp}$. In terms of matrix element, one has

$$\rho\left(\omega_s, \omega_i, k_s^{\perp}, k_i^{\perp}, \omega_s', \omega_i', k_s'^{\perp}, k_i'^{\perp}\right) = \phi\left(\omega_s, \omega_i, k_s^{\perp}, k_i^{\perp}\right) \phi^*\left(\omega_s', \omega_i', k_s'^{\perp}, k_i'^{\perp}\right) \tag{3.62}$$

The reduced spatial density matrix $\hat{\rho}_{spatial}$ is then simply the partial trace in the spectral domain of $\hat{\rho}$:

$$\begin{aligned}\hat{\rho}_{spatial} =& Tr_{spectral}\hat{\rho} \\ =& \int d\omega_s d\omega_i \left\langle\omega_s\right| \left\langle\omega_i\right| \hat{\rho} \left|\omega_s\right\rangle \left|\omega_i\right\rangle\end{aligned} \tag{3.63}$$

with matrix element:

$$\rho_{spatial}\left(k_s^{\perp}, k_i^{\perp}, k_s'^{\perp}, k_i'^{\perp}\right) = \int d\omega_s d\omega_i \phi\left(\omega_s, \omega_i, k_s^{\perp}, k_i^{\perp}\right) \phi^*\left(\omega_s, \omega_i, k_s'^{\perp}, k_i'^{\perp}\right) \tag{3.64}$$

One can then see that $\tilde{\Gamma}_{k_s^{\perp}, k_i^{\perp}}$ (equation 3.55) is simply the diagonal element of the reduced spatial density matrix, i.e. $\rho_{spatial}\left(k_s^{\perp}, k_i^{\perp}, k_s^{\perp}, k_i^{\perp}\right)$.

Thus the measurement of spatial correlations at the output of the waveguide array actually corresponds, in the general case, to the observation of a mixed state, which has reduced spatial entanglement compared to a pure spatial state. This is a limiting effect in the use of entanglement as a resource to encode information. The purity of the reduced spatial density matrix $\hat{\rho}_{spatial}$ (defined by $Tr(\hat{\rho}_{spatial}^2)$) thus allows to assess the quality of the measured spatial state if no information on the photons frequencies is collected during the measurement process.

Effect of the pump transverse propagation

Up to now, we considered that the coupling constant for the pump beam was zero, but in the case of a infinite array, the results we found are easily generalized, since the only effect of the coupling is to modify the propagation constant of the collective modes of the waveguide array and thus the phase-matching. If we consider a coupling $C_p \neq 0$ for the pump mode, the expression for the Joint Spatio-Spectral Amplitude then stays the same,

but the phase-mismatch from equation 3.58 becomes:

$$\begin{aligned}\Delta\beta\left(\omega_s,\omega_i,k_s^{\perp},k_i^{\perp}\right) =&\Delta\beta^{(0)}\left(\omega_s,\omega_i\right)+\Delta\beta^{C}\left(\omega_s,\omega_i,k_s^{\perp},k_i^{\perp}\right)\\ =&\frac{1}{c}\left(\left(\omega_s+\omega_i\right)n_p\left(\omega_s+\omega_i\right)-\omega_s n_s(\omega_s)-\omega_i n_i(\omega_i)\right)\\ &-2C_p\left(\omega_p+\omega_i\right)\cos\left(k_s^{\perp}+k_i^{\perp}\right)\\ &+2C_s\left(\omega_s\right)\cos\left(k_s^{\perp}\right)+2C_i\left(\omega_i\right)\cos\left(k_i^{\perp}\right).\end{aligned} \tag{3.65}$$

The pump transverse propagation can thus be interpreted as a modification of the phase-mismatch, and creates a different selection pattern for the spatio-spectral correlations, without changing the general structure of the Joint Spatio-Spectral Amplitude.

3.1.2.3 SPDC in finite waveguide arrays

The case of a perfectly periodic infinite array has given us insight into interesting effects coming from the coupling of the waveguides, such as spatio-spectral correlations and enlargement of the SPDC resonance spectrum, but it has limitations for the study of real-life systems. For example, in presence of disorder in the coupling or propagation constants, the collective modes of the system become impossible to analytically compute. It is interesting in this case to introduce a real-space formalism for finite arrays, which gives a more realistic approach to simulate actual waveguide arrays. It is possible in this approach to account for non-constant coupling between the waveguides, enabling the simulation of topological Hamiltonians with different topological domains and the emergence of topologically protected modes. Such formalism also allows to consider boundary effects and rebounds of the photons along the edge of the array, which can have interesting effects. Finally, this formalism is very practical to transfer to numerical simulations in matrix form for specific arrays.

Let us consider here the case of SPDC in a finite array of N identical waveguides, equally spaced and thus with identical coupling between nearest-neighbours. If we assume that each waveguide supports exactly one mode with propagation constant β, it is possible to show, similarly to what has been done in the case of the Bloch modes, that the array now supports N collective modes that we label by $1 \leq k \leq N$, with modified propagation constants $\beta_k = \beta - 2C\cos\left(\frac{k\pi}{N+1}\right)$.

Knowing that, it is possible for a specific array to compute the collective eigenmodes and then to apply the Hamiltonian formalism in the same way as it has been done in the previous paragraphs, by taking the nonlinear overlap between the different collective modes for the pump, signal and idler fields and then deriving the quantum state in the basis of these eigenmodes. Although it is the most rigorous theoretical way to derive the biphoton state at the output of the array, it involves tedious calculations, is dependent on the specific array and the number of waveguides, and this theoretical formalism is generally unpractical for the purpose of numerical simulations. It is thus useful to take a different approach in order to simulate finite arrays of waveguides.

To reproduce the main features of the different physical phenomena involved in the creation of the SPDC photon pairs, we will follow here the approach of Blanco-Redondo *et al.* in [82]. We will consider that the biphoton state consists of the vacuum state at the entrance of the nonlinear waveguide array at $z = 0$, and that it evolves along

the propagation direction. We will denote the state by $|\Psi(z)\rangle$, and derive its evolution equation along z.

We will consider as previously that the pump beam is not depleted by the low efficiency SPDC process, and that it evolves according to a classical wave equation. We model the pump field through a vector amplitude $A_{p,n}(\omega_p, z)$ which denotes the pump amplitude in each waveguide n at frequency ω_p and position z. The evolution equation for the pump beam can be written as:

$$\begin{aligned}\frac{dA_{p,n}(\omega_p, z)}{dz} =& -i\beta_p(\omega_p) A_{p,n}(\omega_p, z) - \alpha_p A_{p,n}(\omega_p, z) \\ &+ iC_p(\omega_p)\left(A_{p,n+1}(\omega_p, z) + A_{p,n-1}(\omega_p, z)\right)\end{aligned} \tag{3.66}$$

where $C_p(\omega_p)$ is the coupling constant for the pump mode at frequency ω_p (which can be set to zero in the case of an uncoupled pump beam) and α_p accounts for the losses of the pump. This equation can then be solved with the initial conditions for the pump beam to get $A_{p,n}(\omega_p, z)$ for all z.

If we write $\Psi_{n_s,n_i}(\omega_s, \omega_p, z)$ the vector element of the state with one photon in guide n_s and one photon in guide n_i, at frequencies ω_s and ω_i and position z, we now have 3 effects to take into account in our model:

- the propagation of the two photons along the waveguides, with propagation constants $\beta_s(\omega_s)$ and $\beta_i(\omega_i)$

- the coupling between the waveguides, which we model by considering that the signal photon can go from waveguide n_s to waveguide $n_s \pm 1$ with coupling constant $C_s(\omega_s)$ and the idler photon from waveguide n_i to waveguide $n_i \pm 1$, with a coupling constant $C_i(\omega_i)$

- the creation of photon pairs by SPDC, whose probability amplitude is proportional to the pump amplitude $A_{p,n}$ and to the nonlinear overlap Γ_{eff} (equation 3.47) and is a local interaction that can only produce two photons in the same waveguide[9].

Here we neglect the losses for the SPDC photons since for our sample they are very low compared to the optical losses for the pump beam[10,11]. The evolution equation for the term $\Psi_{n_s,n_i}(z)$ is then

[9] It is also possible to consider non-local SPDC generation [174].

[10] The effect of losses can be understood in the following intuitive picture: if the SPDC modes have high losses, then the photon pairs produced close to the input of the waveguide will have a much greater probability of being lost than the ones produced close to the output. Photons generated close to the output will have less time to undergo quantum walks in the transverse direction and thus the output quantum state will be more localized around the pumped waveguide. An opposite reasoning can be made for the losses of the pump, where the output state will get closer to the case of ballistic propagation in a passive array as the pump losses increase.

[11] We refer the reader to reference [175] for a more detailed study of the effect of losses for the SPDC modes.

$$\begin{aligned}\frac{d\Psi_{n_s,n_i}(\omega_s,\omega_p,z)}{dz} =& -i\left(\beta_s(\omega_s)+\beta_i(\omega_i)\right)\Psi_{n_s,n_i}(\omega_s,\omega_p,z)\\ &+iC_s(\omega_s)\left(\Psi_{n_s+1,n_i}(\omega_s,\omega_p,z)+\Psi_{n_s-1,n_i}(\omega_s,\omega_p,z)\right)\\ &+iC_i(\omega_i)\left(\Psi_{n_s,n_i+1}(\omega_s,\omega_p,z)+\Psi_{n_s,n_i-1}(\omega_s,\omega_p,z)\right)\\ &+\Gamma_{\text{eff}}\delta_{n_s,n_i}A_{p,n_s}(\omega_s+\omega_i,z)\end{aligned} \tag{3.67}$$

with the initial condition $\Psi_{n_s,n_i}=0$ at $z=0$, and where the last term is the source term for the creation of SPDC photon pairs. This is equivalent to the formulation given by Blanco-Redondo *et al.* [82], where the effective Hamiltonian[12] is given by

$$\hat{H}(z) = \hat{H}_{\text{propagation}}(z)+\hat{H}_{\text{coupling}}(z)+\hat{H}_{\text{generation}}(z) \tag{3.68}$$

with

$$\begin{aligned}\hat{H}_{\text{propagation}} =& \hbar\sum_{n_s}\int d\omega_s\beta_s(\omega_s)\hat{a}_s^\dagger(\omega_s,n_s)\,\hat{a}_s(\omega_s,n_s)\\ &+\hbar\sum_{n_i}\int d\omega_i\beta_i(\omega_i)\hat{a}_i^\dagger(\omega_i,n_i)\,\hat{a}_i(\omega_i,n_i)\end{aligned} \tag{3.69}$$

$$\begin{aligned}\hat{H}_{\text{coupling}} =& -\hbar\sum_{n_s}\int d\omega_s C_s(\omega_s)\left(\hat{a}_s^\dagger(\omega_s,n_s+1)\,\hat{a}_s(\omega_s,n_s)+\hat{a}_s^\dagger(\omega_s,n_s-1)\,\hat{a}_s(\omega_s,n_s)\right)\\ &-\hbar\sum_{n_i}\int d\omega_i C_i(\omega_i)\left(\hat{a}_i^\dagger(\omega_i,n_i+1)\,\hat{a}_i(\omega_i,n_i)+\hat{a}_i^\dagger(\omega_i,n_i-1)\,\hat{a}_i(\omega_i,n_i)\right)\end{aligned} \tag{3.70}$$

$$\hat{H}_{\text{generation}}(z) = \hbar\Gamma_{\text{eff}}\sum_n\int d\omega_s d\omega_i A_{p,n}(\omega_s+\omega_i,z)\,\hat{a}_s^\dagger(\omega_s,n)\,\hat{a}_i^\dagger(\omega_i,n) \tag{3.71}$$

and the state is described in the Fock basis as

$$|\Psi(z)\rangle = \Psi_0|0\rangle+\sum_{n_s,n_i}\int d\omega_s d\omega_i\Psi_{n_s,n_i}(\omega_s,\omega_i,z)\hat{a}_s^\dagger(\omega_s,n)\,\hat{a}_i^\dagger(\omega_i,n)|0\rangle+... \tag{3.72}$$

Here we are only interested in the part of the state having exactly one photon in each of the signal and idler modes and we disregard the other modes. We have

$$i\hbar\frac{d|\Psi\rangle}{dz} = \hat{H}(z)|\Psi\rangle \tag{3.73}$$

and we retrieve equation 3.67 by projecting on the the post-selected state and taking $\Psi_0=i$. Since the evolution equation 3.67 is very well adapted to discretize and put into a matricial form, it is a suitable formalism to realize numerical simulations of the output quantum state after interaction of the pump beam in the array with an easily adaptable and generalizable algorithm, which we will develop in section 3.2.2.

[12]It is important to keep in mind that this Hamiltonian does not have the dimension of an energy and does not act as a derivative over time but over distance.

3.2 Numerical simulations

In this section, we introduce various kinds of numerical simulations that we performed to help quantify and visualize the effects described in the previous sections. We will describe the process and the method for the numerical simulations, and then present the results in a graphical way. The software used for the numerical simulations is MATLAB, which is efficient for manipulating arrays, vectors and matrices.

3.2.1 Case of infinite arrays: Bloch-mode formalism

We first consider in this subsection the case of infinite arrays described within the Bloch modes formalism.

3.2.1.1 Passive arrays and correlated quantum walks

The first effect that is interesting to simulate is the case of correlated quantum walks, when we send two single photons in a passive waveguide array, as described in section 3.1.1.4. In order to properly simulate this effect in a realistic way, one needs to access the coupling constant of the array, which we can numerically simulate. These simulations will be described in chapter 4, but the value for the coupling length at telecom wavelength is typically around $L_c \simeq 350$ μm for the waveguide arrays that we will use, with an array length $L \simeq 2$ mm, giving $\frac{L}{L_c} \simeq 6$. Intuitively, this quantity is related to the mean number of "steps" the photons will take in the transverse direction during the quantum walks, with the relation $N_{steps} \simeq \frac{\pi L}{L_c}$ (see equation 3.28).

To simulate the quantum walk of two photons in a passive array, we will then simply give an input state $|\Psi_0\rangle$ in a matricial form with the coefficient b_{n_s,n_i} and then discretize the evolution equation 3.30 along z.

We can consider different possible input states. For instance, following Bromberg *et al.* [79], it is interesting to look at three particular cases, and compare them to the corresponding classical propagation of incoherent beams in a similar setting. For this we will consider the three input states $|\varphi_0\rangle = \frac{1}{\sqrt{2}}\hat{a}_0^\dagger\hat{a}_0^\dagger|0\rangle$, $|\varphi_1\rangle = \hat{a}_0^\dagger\hat{a}_1^\dagger|0\rangle$ and $|\varphi_2\rangle = \hat{a}_1^\dagger\hat{a}_{-1}^\dagger|0\rangle$, and compare them to the cases where we inject two incoherent beams in the corresponding waveguide pairs (either $\{0,0\}$, $\{0,1\}$ or $\{1,-1\}$). We know from the criterion given in [79] that some properties of the Joint Spatial Amplitude cannot be reproduced by such a classical input. We present, for the three input states considered, the graph of the Joint Spatial Intensity Γ_{n_s,n_i} (equation 3.31), the non-classicality indicator defined in equation 3.40 as $I_{\mathrm{NC}}(n_s,n_i) = \max(\frac{1}{3}\sqrt{\Gamma_{n_s,n_s}\Gamma_{n_i,n_i}} - \Gamma_{n_s,n_i}, 0)$ and the violation of the Cauchy-Schwartz inequality defined in equation 3.41 as $I_{\mathrm{CS}}(n_s,n_i) = \max(\Gamma_{n_s,n_i} - \sqrt{\Gamma_{n_s,n_s}\Gamma_{n_i,n_i}}, 0)$ in figure 3.5 (first, second and third column, respectively).

The spatial correlations at the lattice output for the input state $|\varphi_0\rangle = \frac{1}{\sqrt{2}}\hat{a}_0^\dagger\hat{a}_0^\dagger|0\rangle$ (first line in figure 3.5) present four lobes at the corners of the matrix, giving evidence of the ballistic propagation of the photons in the passive array over approximately 20 sites, consistently with the value of $\pi L/L_c$. These correlations do not generate a non-zero value of the non-classicality indicator nor a violation of the Cauchy-Schwartz inequality. This is coming from the fact that the output state in this case is simply the product of the output states of single photons injected in the central waveguide and undergoing quantum

random walks, and thus is analog to the classical case of two incoherent beams injected in the central waveguide[13].

The case of $|\varphi_2\rangle = \hat{a}_1^\dagger \hat{a}_{-1}^\dagger |0\rangle$ (third line in figure 3.5) is more interesting, since the correlations also present four strong lobes in the corners of the matrix, but the intensity along the lines joining the corners is suppressed compared to the case of $|\varphi_0\rangle$. This state also presents a strong violation of both the non-classicality and Cauchy-Schwartz inequality along these same lines, showing signs of a highly non-classic behaviour of the photon pairs, coming from the interference between the paths of the two photons. This can be interpreted as a *simultaneous bunching and antibunching of the photons in the ballistic lobes*.

The case of $|\varphi_1\rangle = \hat{a}_0^\dagger \hat{a}_1^\dagger |0\rangle$ (second line in figure 3.5), corresponding to the injection of two photons in adjacent waveguides gives a different shape for the spatial correlations of the biphoton states: the correlations are now concentrated in two strong lobes in the diagonal corners of the matrix, and the violation of the non-classicality criterion is strongest in the antidiagonal corners of the matrix, consistent with the fact that the antibunching terms are now suppressed, leaving only *bunching of the photons in the ballistic lobes*.

3.2.1.2 Joint Spatio-Spectral Amplitude

Let us now consider the case of photon pairs generated by SPDC in an infinite waveguide array. As seen in section 3.1.2.1, in the case of an infinite array, one can directly write the Joint Spatio-Spectral Amplitude as a function of the spatial and spectral profiles of the pump beam, and of the phase-matching term. Let us recall equation 3.53, to identify the different simulation steps:

$$\begin{aligned}\phi\left(\omega_s, \omega_i, k_s^\perp, k_i^\perp\right) =& \frac{1}{\sqrt{N}} A_{spectral}(\omega_s + \omega_i) \tilde{A}_{spatial}(k_s^\perp + k_i^\perp) \\ & \cdot \operatorname{sinc}\left(\Delta\beta\left(\omega_s, \omega_i, k_s^\perp, k_i^\perp\right)\frac{L}{2}\right) e^{-i\left(\Delta\beta\left(\omega_s,\omega_i,k_s^\perp,k_i^\perp\right)\frac{L}{2}\right)}\end{aligned} \tag{3.74}$$

To compute it numerically, we simply need to discretize the $\left(k_s^\perp, k_i^\perp\right)$ space, and the (ω_s, ω_i) space, and then compute the functions $\tilde{A}\left(k_p^\perp\right)$ from the input spatial profile of the pump, and simply compute for every point in the discretized spaces the product

$$A_{spectral}(\omega_s + \omega_i)\tilde{A}_{spatial}(k_s^\perp + k_i^\perp) \operatorname{sinc}\left(\Delta\beta\left(\omega_s, \omega_i, k_s^\perp, k_i^\perp\right)\frac{L}{2}\right).$$

In our case, we will limit ourselves to a single pump frequency ω_p, since our source for the pump beam will be a continuous wave laser with a narrow bandwidth. This yields through energy conservation $\omega_i = \omega_p - \omega_s$, and thus:

$$\phi\left(\omega_s, \omega_i, k_s^\perp, k_i^\perp\right) = \phi\left(\omega_s, \omega_p - \omega_s, k_s^\perp, k_i^\perp\right).$$

[13]Since the photons in the array evolve independently, if the input state is a separable one (e.g. $|\varphi_0\rangle = |a_0\rangle \otimes |a_0\rangle$, the output state is also separable, of the form $U|a_0\rangle \otimes U|a_0\rangle$, where U is the unitary operator representing the evolution of the state in the array. The spatial correlations are then just the product of "classical" spatial correlations.

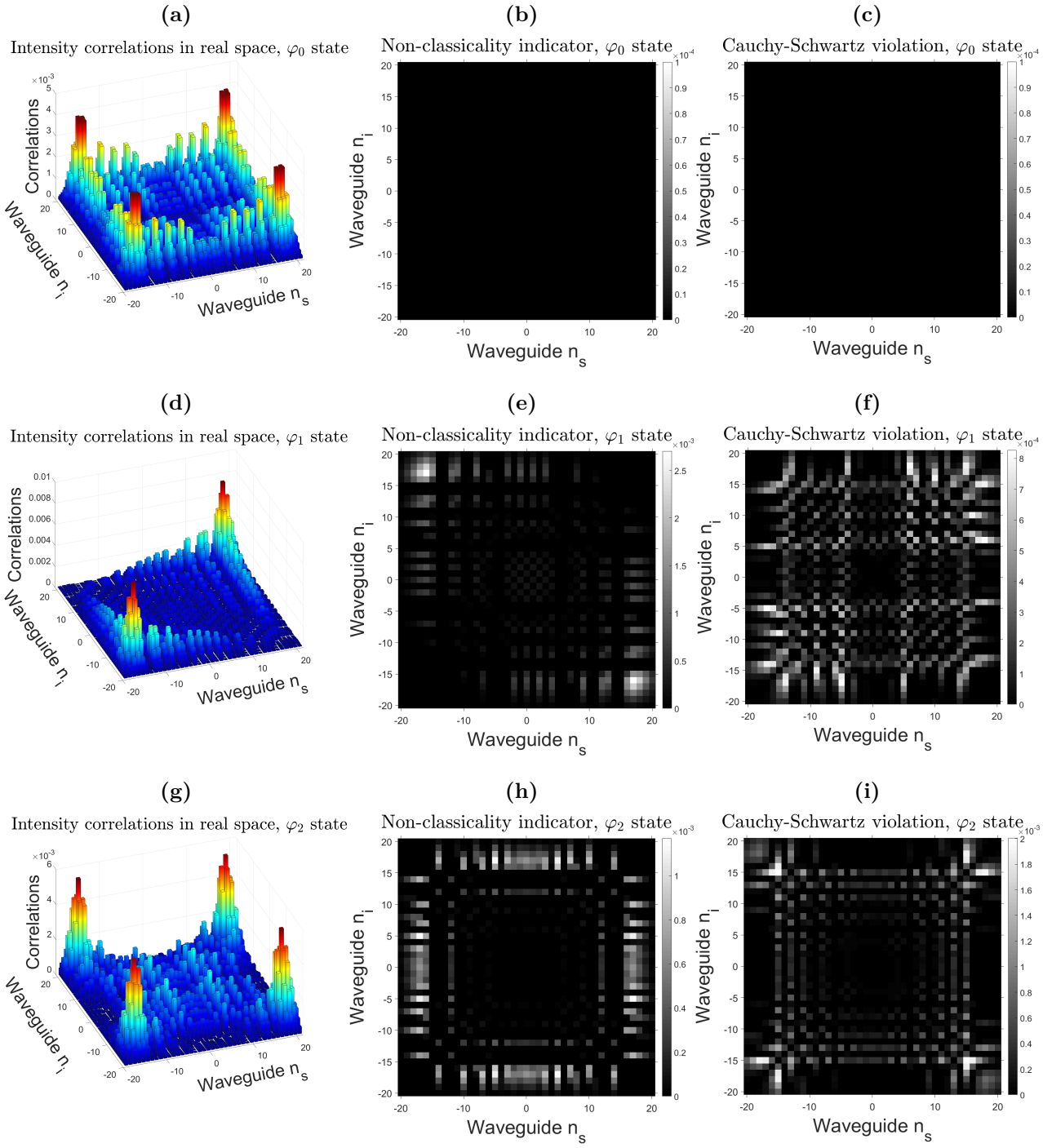

Figure 3.5: Spatial correlations, non-classicality indicator and Cauchy-Schwartz inequality violation for the three input states $|\varphi_0\rangle$, $|\varphi_1\rangle$ and $|\varphi_2\rangle$ (first, second and third lines respectively), with a 2 mm long waveguide array, yielding $L/L_c \simeq 6$. In every case, the correlations propagate up to $\pi L/L_c \simeq 20$ guides in the transverse direction.

Here, our structure supports three different interactions for the SPDC process: type 0 interaction, where the pump, signal and idler photons all have the same TM polarization, type I interaction, where the pump is TM polarized and the signal and idler photons are both TE polarized, and type II interaction where the pump is TE polarized and the signal and idler photons have crossed polarization (see section 1.1.3). To compute the phase-mismatch $\Delta\beta$, we have to simulate the relevant parameters for the considered interactions. These simulations are detailed in chapter 1 for the modal indices and in chapter 4 for the coupling constants. We will consider here, in agreement with the experiment presented in chapter 5, a waveguide array with a typical gap of 500 nm between the waveguides. The simulations will focus on type 0 SPDC, which is very similar to the case of type I except for a scaling factor in the coupling constants. The case of type II SPDC is more complicated, as the coupling constants for both photons are different. This gives rise to interference between two possibilities with the signal photon being either TE- or TM-polarized. We will briefly present simulations for the case of type II correlations in paragraph 3.2.1.5 in the case of a pure state, but for the most part will use type 0 SPDC as a support for a more pedagogical display of the possibilities offered by nonlinear waveguide arrays.

We present in the following paragraphs the results of the simulations while studying the effect of different parameters. Initially, we will only consider the case of a non-propagating pump, injected in the central waveguide of the array.

3.2.1.3 Enlargement of the SPDC spectrum

The first effect we can simulate is the enlargement of the SPDC resonance spectrum. For that, we can compute the joint spatio-spectral amplitude ϕ for a certain pump frequency ω_p and integrate its square modulus over ω_s, ω_i, $k_s^\perp$ and $k_i^\perp$, which gives the probability of producing a photon pair in any couple of transverse modes and at any couple of frequencies. We can then plot the result as a function of ω_p, which gives the SPDC efficiency for different pump frequencies. We made the simulation for a propagation length of 2 mm and taking into account signal and idler photons generated over a 800 nm band centered on $\omega_p/2$, and plotted the results in figure 3.6, where we used the pump wavelength λ_p as a parameter for convenience. Three different cases were considered: the case where the coupling constant was taken from the numerical simulations ($C(\omega_p/2) \simeq 4.6$ mm^{-1}), the case where the value of the coupling constant was half of the simulated value ($C(\omega_p/2) \simeq 2.3$ mm^{-1}), and the case where there was no coupling, corresponding to a single waveguide. The SPDC efficiency is asymmetrical with respect to the pump wavelength and presents a maximum for perfect phase-matching at degeneracy, as explained in section 1.2.2. The efficiency stays maximal at the same wavelength in the case of waveguide arrays. The plot also shows a correlation between the coupling constant and the Full Width at Half Maximum (FWHM), which goes from 0.2 nm for the case of the single waveguide, to 1.44 nm in the case of the halved coupling constant, and finally to 2.76 nm in the case of the full simulated coupling constant, corresponding to an almost-linear relationship between the FWHM and the coupling between the waveguides (which we verified by additional simulations). We additionally computed the marginal spectrum of the generated SPDC photons for two different values of the pump wavelength, $\lambda_{p,deg} = 773.48$ nm (figure 3.7a) giving perfect single-waveguide phase-matching $\Delta\beta^{(0)}$ at degeneracy for type 0 SPDC and at a wavelength 2 nm below, $\lambda_p = 771.48$ nm (figure

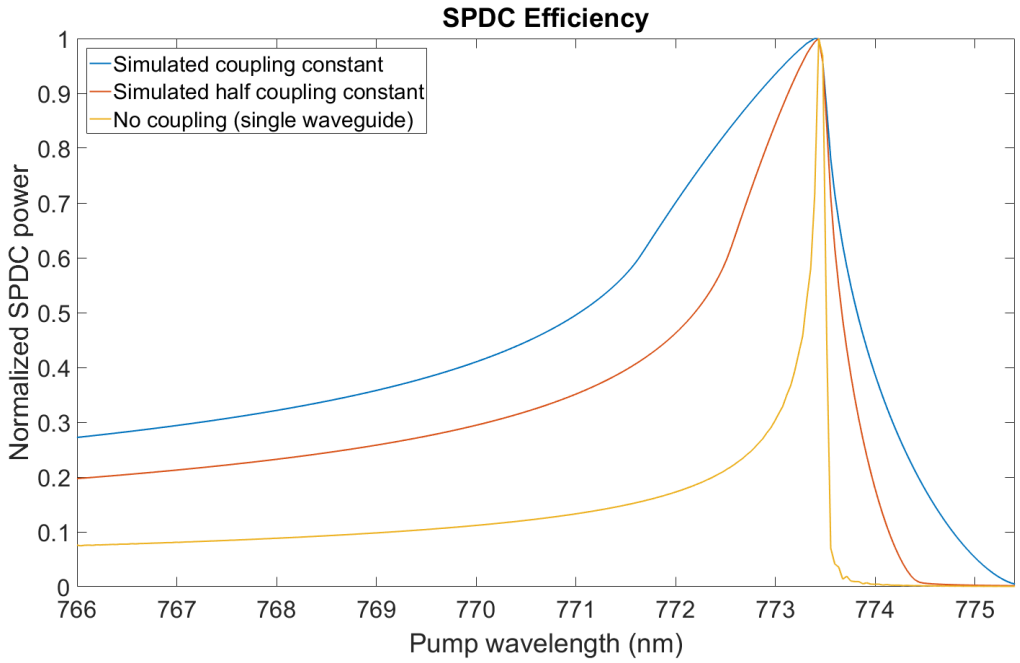

Figure 3.6: Simulated SPDC resonance spectrum for different coupling constant values.

3.7b). We see that the FWHM of the spectrum for $\lambda_{p,deg}$ is of the order of 330 nm, meaning that the spectrum of the generated photons is also enlarged by the coupling compared to the case of a single waveguide (figure 1.9b) where the FWHM is $\simeq$ 70 nm. The spectrum of the generated photons splits into two lobes as the wavelength decreases (figure 3.7b), similarly to the case of a single waveguide yielding a branched shape in the SPDC efficiency (figure 1.9a).

3.2.1.4 Spatio-spectral correlations and purity of the state

As we have seen in the previous section, the phase-matching term in the Joint Spatio-Spectral Amplitude induces a coupling between the spatial and spectral degrees of freedom, which can limit the purity of the measured spatial state if the measurement is not spectrally resolved. To visualize the effect of the spatio-spectral correlations, one can look at the single counts[14] of each waveguide or at the diagonal coincidences as a function of the signal/idler photon wavelength. We consider here a 800 nm bandwidth for the signal and idler photons around degeneracy.

The results of the simulation are shown in figure 3.8, for the same two values of the pump wavelength as in figure 3.7. In agreement with figure 3.7a, we can see that, for pump wavelength $\lambda_{p,deg}$ (figure 3.8a), the distribution of the signal wavelength is mainly concentrated in a lobe around degeneracy, while for a smaller pump wavelength (figure 3.8c), the signal distribution forms two lobes that shift away from the degeneracy wavelength. We also observe that the spatial distribution of both the single counts and diagonal coincidences (figures 3.8b and 3.8d) varies with the signal wavelength, indicating that the Joint Spatio-Spectral Amplitude cannot be simply written as a product of a

[14] We compute the single counts in waveguide n_s as the sum of the matrix elements Γ_{n_s,n_i} over n_i: $S(n_s) = \sum_{n_i} \Gamma_{n_s,n_i}$.

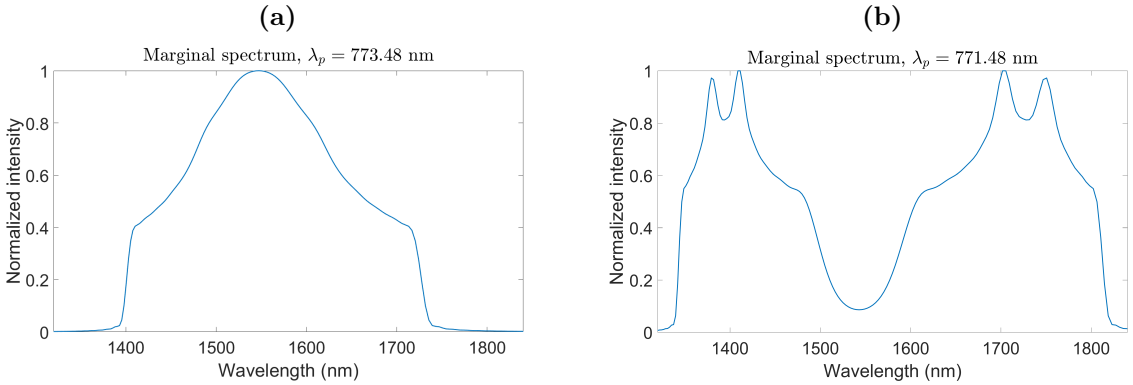

Figure 3.7: Marginal spectrum of the emitted SPDC photons for pump wavelengths a) $\lambda_p = \lambda_{p,deg} = 773.48$ nm, corresponding to the maximum of SPDC efficiency, and b) $\lambda_p = 771.48$ nm. $L/L_c \simeq 6$ at degeneracy.

spatial term and a spectral term, and showing the presence of spatio-spectral correlations in the output quantum state.

Another useful quantity to simulate is the purity of the state at the output of the array. This requires the simulation of the density matrix, and its tracing over the spectral degree of freedom (see section 3.1.2.2), which can be a heavy operation for the memory of the computer[15]. Thus, simulations of the purity imposed harsher computational constraints than the other simulations.

Figure 3.9 shows the simulation of the purity of the reduced spatial density matrix for different filtering widths of the output state, i.e. where we computed the reduced density matrix and its purity by only considering a certain range of values for ω_s (and ω_i) around the degeneracy. One can see that the purity goes to one when the filtering width goes to zero, which is expected from the continuous character of the Joint Spatio-Spectral Amplitude, and the fact that we filter the state into a single frequency component, meaning it is now a pure spatial state. Interestingly, the purity can go down to almost 0.1 when the filtering width increases, showing that the output state without filtering is a highly mixed state, which confirms again the presence of spatio-spectral correlations. Spectral filtering of the state is thus required to yield a state with pure spatial correlations unaffected by spatio-spectral coupling, e.g. filtering at 40 nm yields a purity of 95%.

Although the spatio-spectral correlations and the purity of the reduced density matrix indicate that the output spatial state that we measure is highly mixed, we can investigate the spatial intensity correlations in the waveguide number (Γ_{n_s,n_i}) and transverse wavevector ($\tilde{\Gamma}_{k_s^\perp,k_i^\perp}$) spaces even for non-filtered states. The corresponding correlations for a 2 mm long array with a bandwidth of 400 nm for the signal and idler photons are shown in 3.10a for the correlations in real space and figure 3.10b for the correlations in transverse wavevector space. One can see from these correlations that although the state is highly mixed, the intensity correlations still present interesting features (that we will find again later in the case of narrow filtering): the photons tend to either exit through

[15]If we want to discretize the transverse wavevector space using 100 points, and the spectral space using 400 points for a 400 nm width, which is a reasonable discretization to have satisfying precision, the total size of the matrix is $100^2 \cdot 100^2 \cdot 400^2 = 1.6 \cdot 10^{13}$ points.

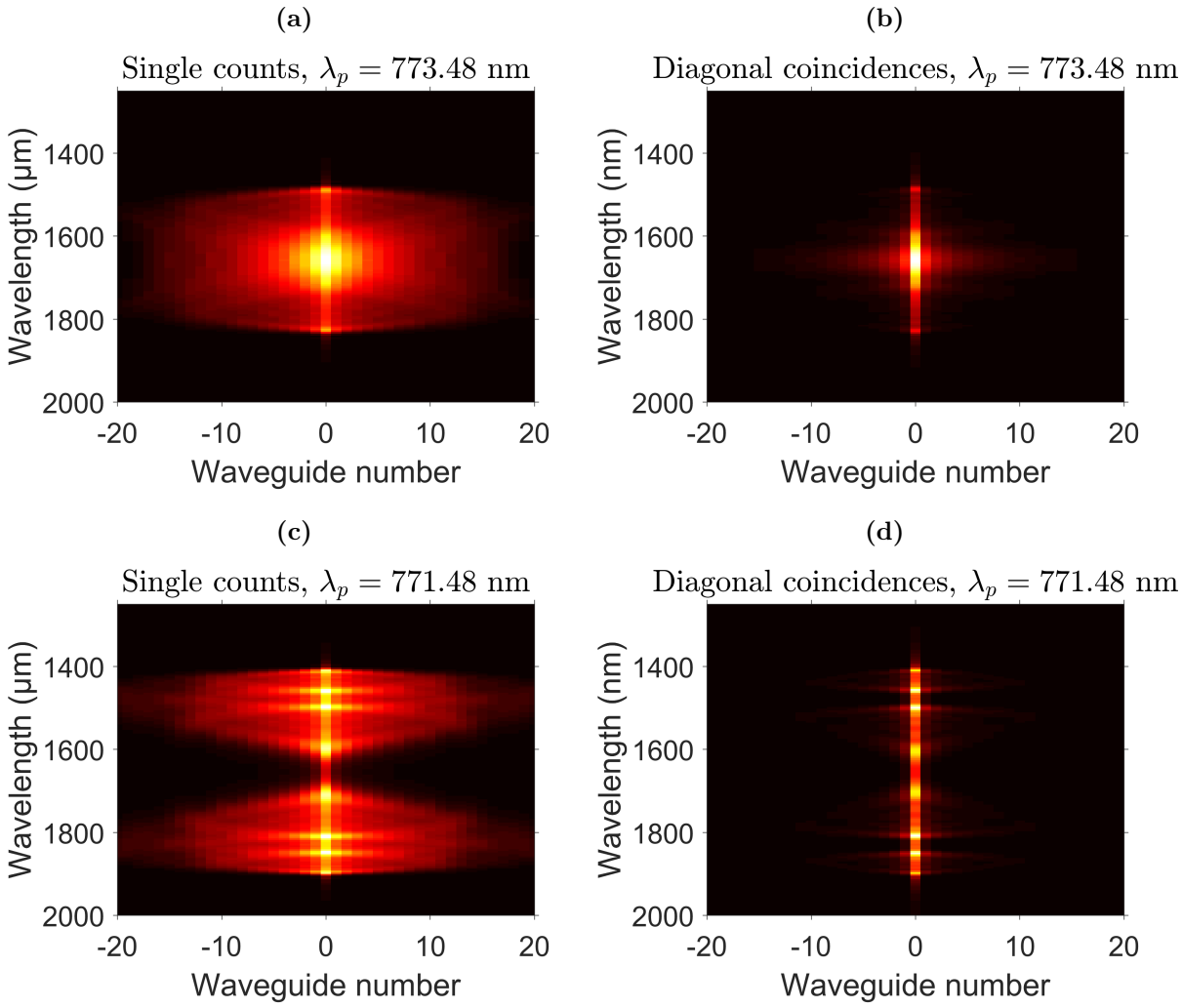

Figure 3.8: Normalized single counts and diagonal coincidences distribution as a function of the signal wavelength, for two different pump wavelengths $\lambda_p = \lambda_{p,deg} = 773.48$ nm (first row) and $\lambda_p = 771.48$ nm (second row), with $L/L_c \simeq 6$ at degeneracy.

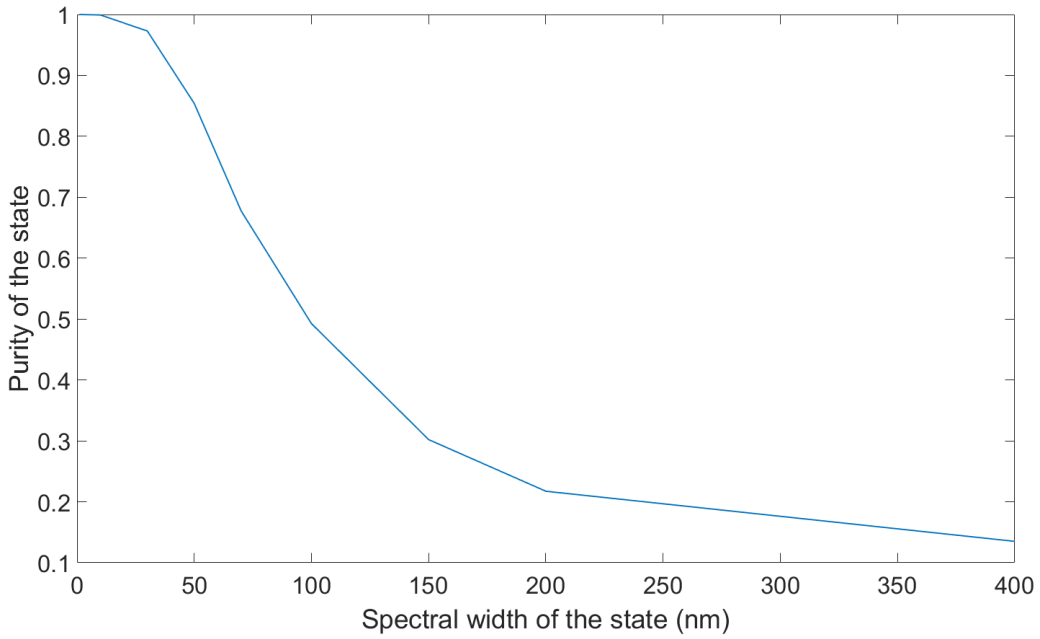

Figure 3.9: Purity of the reduced spatial density matrix as a function of the spectral filtering width of the SPDC photons.

the same output waveguide or through opposite waveguides, giving a correlation pattern located mainly on the diagonal and antidiagonal, as anticipated in paragraph 3.1.2.2 (see equation 3.60). In terms of transverse wavevector, one can see that the wavevectors are preferentially selected along the $\cos\left(k_s^{\perp}\right) + \cos\left(k_i^{\perp}\right) = 0$ curve, giving $k_s^{\perp} = \pi \pm k_i^{\perp}$ on the torus space, as expected from the modified phase-matching condition around the degeneracy, which gives the square-like shape in the correlations visible in figure 3.10b.

3.2.1.5 Non-classicality of the pure state

In all the following, we will focus on the case of spectral filtering with a narrow bandwidth near degeneracy to only take into consideration the spatial correlations of the photon pair and discard the spatio-spectral correlations. We will thus only consider the matrix elements close to $\phi\left(\omega_p/2, \omega_p/2, k_s^{\perp}, k_i^{\perp}\right)$ for the Joint Spatio-Spectral Amplitude, corresponding to a pure spatial state.

Figure 3.11 shows the corresponding correlations in real space (figure 3.11a) and in transverse wavevector space (3.11b). We can first compare figure 3.11 to figure 3.10, and see that the main features of the intensity correlations in both cases are very similar: the transverse wavevectors are selected around the $k_s^{\perp} = \pi \pm k_i^{\perp}$ square, and the spatial correlations in real space are located on the diagonal or antidiagonal of the matrix. Although the main features and the general shape remain the same, we can observe that filtering makes the transverse momentum correlations more tightly concentrated around the square defined by $k_s^{\perp} = \pi \pm k_i^{\perp}$ and increases the transverse propagation of correlations along the array as well as the relative weight of the correlations located along the diagonal and antidiagonal (compared to other points of the matrix).

Figure 3.12 shows the corresponding distribution of the non-classicality indicator, i.e.

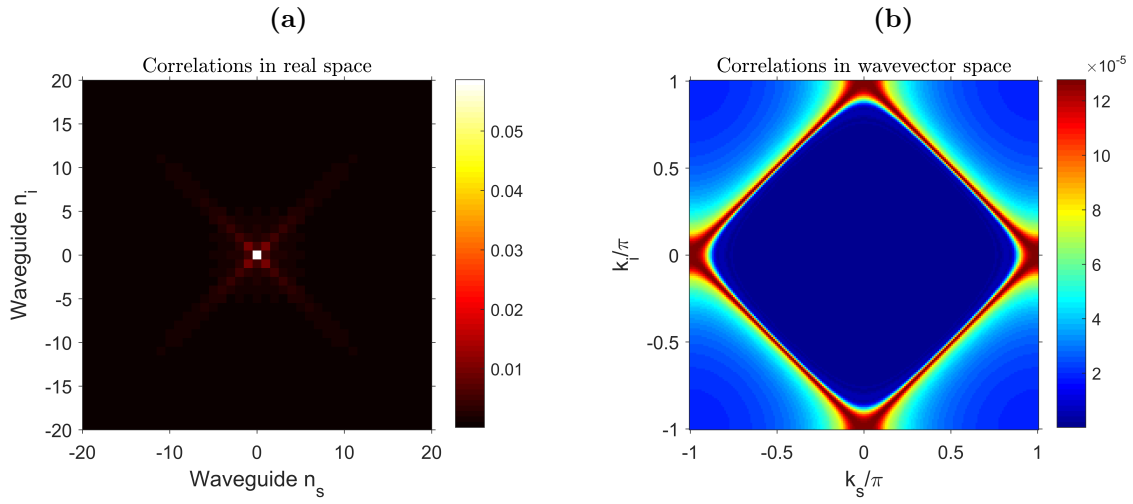

Figure 3.10: a) Real space and b) transverse wavevector-space intensity correlations for a pump wavelength $\lambda_{p,deg}$ injected in the central waveguide, with filtering width 400 nm and $L/L_c \simeq 6$ at degeneracy.

the quantity $I_{\mathrm{NC}}(n_s, n_i) = \max(\frac{1}{3}\sqrt{\Gamma_{n_s,n_s}\Gamma_{n_i,n_i}} - \Gamma_{n_s,n_i}, 0)$ (equation 3.40) as well as the violation of the Cauchy-Schwartz inequality, i.e. $I_{\mathrm{CS}} = \max(\Gamma_{n_s,n_i} - \sqrt{\Gamma_{n_s,n_s}\Gamma_{n_i,n_i}}, 0)$ (equation 3.41). We can note that the maximum attainable value (for any state) is $\frac{1}{6}$ in the case of the non-classicality indicator, and 1 in the case of Cauchy-Schwartz assuming a normalized Joint Spatial Intensity ($\sum_{n_s,n_i}\Gamma_{n_s,n_i} = 1$). These quantities give insight into how the distribution of the correlations affects the non-classical character of the matrix. The first remark we can make is that the output state, although entangled and thus highly non-classic, as discussed below, does not violate Cauchy-Schwartz inequality, since the correlations are only located on the diagonal and antidiagonal. It is also visible that the non-zero values of the non-classicality indicator is mainly located in two vertical and horizontal lines crossing at the center of the correlation matrix, away from the diagonal and antidiagonal points. This is expected since the considered non-classicality criterion gives a *lower bound* for classical behaviour, so the points that are most likely to violate the criterion are the one giving the lowest relative intensity.

Going back to the real-space intensity correlations of a pure state, the increase in the transverse propagation, mentioned before, is of particular interest, as intuitively, it is expected to be closely related to entanglement. Indeed, in the simplest case in which all the correlations are located either on the diagonal or on the antidiagonal, with the same amplitude, then one can write the Schmidt decomposition [176] of the state (i.e. its decomposition in the form of a sum $\sum_k \sqrt{\alpha_k}\,|a_k\rangle\,|b_k\rangle$ where $|a_k\rangle_k$ and $|b_k\rangle_k$ are two sets of orthonormal states):

$$|\Psi\rangle = \sum_n b_n \left(|n\rangle_s + |-n\rangle_s\right)\left(|n\rangle_i + |-n\rangle_i\right) \tag{3.75}$$

which is an entangled state with Schmidt number

$$K_{|\Psi\rangle} = \frac{1}{\sum_n |b_n|^4}. \tag{3.76}$$

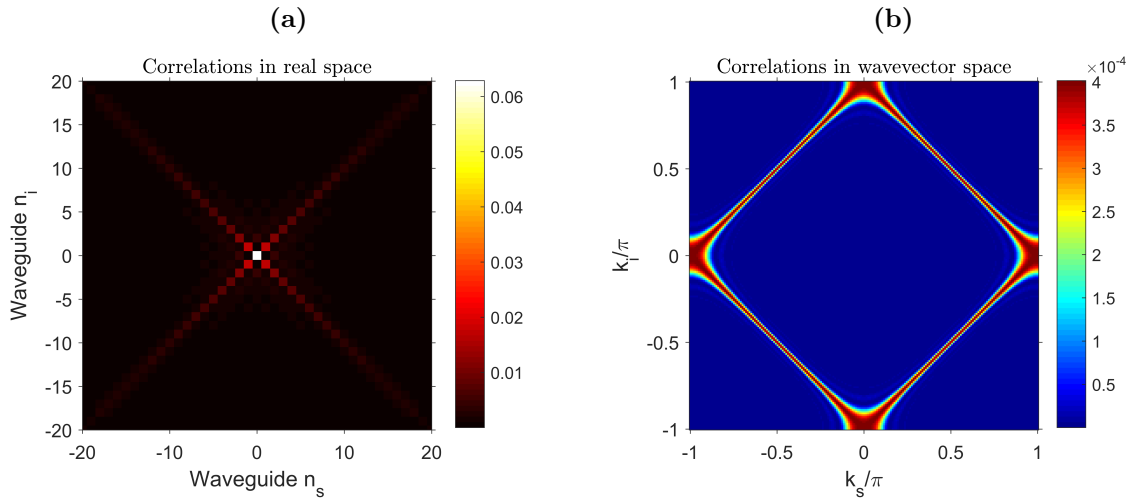

Figure 3.11: a) Real-space and b) transverse wavevector-space intensity correlations for a pump wavelength $\lambda_{p,deg}$ injected in the central waveguide, for a pure state at degeneracy and $L/L_c \simeq 6$.

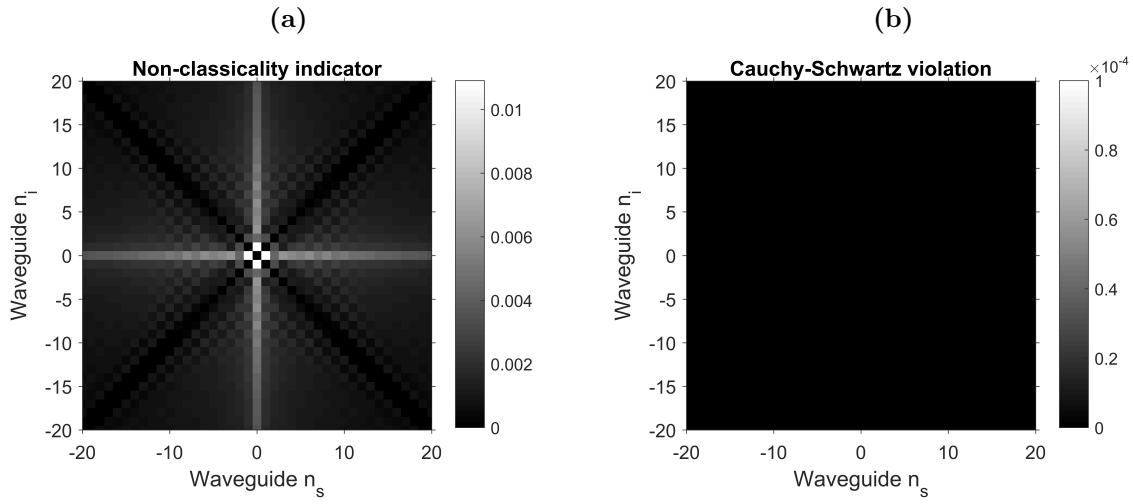

Figure 3.12: a) Non-classicality and b) Cauchy-Schwartz violation from the correlation matrix of the pure state, for $L/L_c \simeq 6$.

This quantity is maximal when all non-zero b_n are equal, and corresponds in this case exactly to the number of non-zero coefficients. Thus, the more spread out along the diagonal and antidiagonal the state is, the larger its Schmidt number (i.e. the number of involved spatial modes). As stated previously, the relevant quantity to determine the transverse propagation along the waveguide array is the ratio between the array length L and the coupling length L_c (equation 3.16), as it is related to the number of "steps" in the quantum random walks that the photons can undergo during the propagation inside the array. Figure 3.13 shows the simulated Schmidt number as a function of the dimensionless product $C_s\left(\frac{\omega_p}{2}\right)L = \frac{\pi L}{2L_c\left(\frac{\omega_p}{2}\right)}$. We can see that the Schmidt number increases monotonically with the propagation length.

Another parameter that influences the quantum properties of the considered state is the pump frequency ω_p, as it gives a degree of control over the phase-matching condition of the SPDC process. By filtering the state around $\omega_s = \omega_i = \omega_p/2$, we can compute the Schmidt number $K_{|\Psi\rangle}$ and the total non-classicality indicator (i.e. the sum of the indicator values I_{NC} over all the waveguide pairs) as a function of the pump wavelength, as plotted on figures 3.14a and 3.14b respectively. The figure demonstrates a resonance in both the Schmidt[16] number and non-classicality indicator around $\lambda_{p,deg}$.

It is also interesting to quantify the sharpness of the diagonal and antidiagonal correlations. A good indicator for this is the quantity

$$\Gamma_{diag} = \Gamma_{1,1} + \Gamma_{-1,-1} + \Gamma_{-1,1} + \Gamma_{1,-1},$$

quantifying the bunching and antibunching on the first diagonals and antidiagonals, which can be compared to

$$\Gamma_{non-diag} = \Gamma_{0,1} + \Gamma_{0,-1} + \Gamma_{1,0} + \Gamma_{-1,0},$$

giving the off-diagonal coincidence probability in the 3×3 square around the central waveguide. Figure 3.15a shows the simulated Γ_{diag} (blue line) and $\Gamma_{non-diag}$ (red line) as a function of the pump wavelength (without state normalization, i.e. taking into account SPDC efficiency). The results show a resonance around $\lambda_{p,deg}$ for Γ_{diag} and on the contrary an essentially flat behaviour for $\Gamma_{non-diag}$. The concentration of correlations along the diagonal and antidiagonal is thus maximal at $\lambda_{p,deg}$ and progressively fades out as we move away from this resonance, as directly shown in figure 3.15b displaying the ratio between Γ_{diag} and $\Gamma_{non-diag}$ as a function of the pump wavelength.

Type II SPDC and spatial correlations

We now turn to the case of type II SPDC. In this case, the correlations are the result of the interference between two possibilities, where the signal photon is either TE- or TM-polarized (and vice versa for the idler photon). We plot the simulated real-space correlations of a pure state generated by type II SPDC for a longitudinal propagation length of $L = 1$ mm in 3.16a and for a longitudinal propagation length of $L = 2.5$ mm in 3.16b.

At low propagation distance, the correlations are still mainly located around the diagonal and antidiagonal (see figure 3.16a), while at higher propagation distance, they split

[16] Although the local maxima for the Schmidt number are reached slightly off the degeneracy pump wavelength, which might stem from a more complex correlation pattern off-resonance.

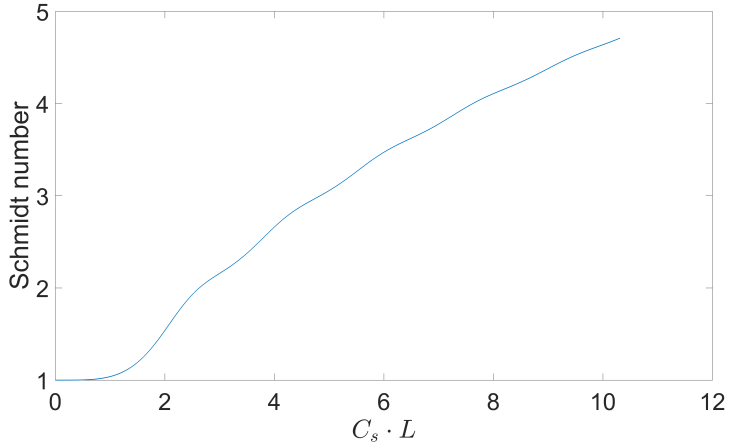

Figure 3.13: Schmidt number of the output state with increasing propagation length.

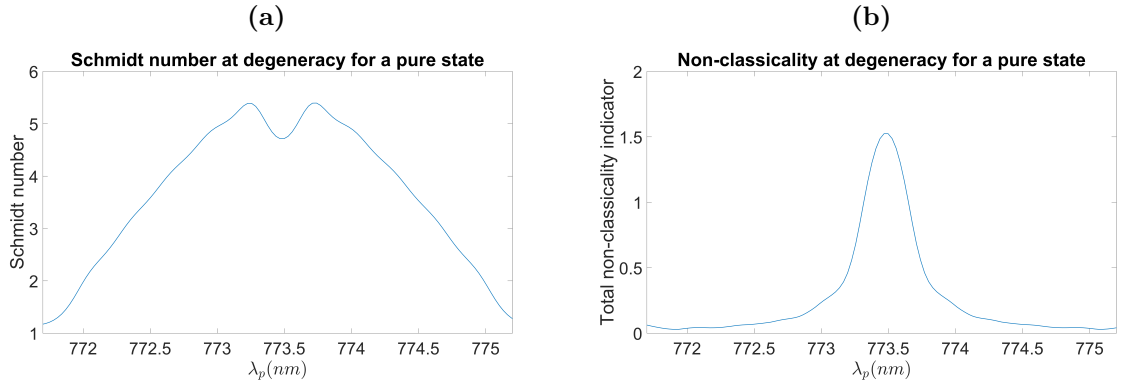

Figure 3.14: a) Simulated Schmidt number, and b) simulated total non-classicality indicator as a function of the pump wavelength, with $L/L_c \simeq 6$.

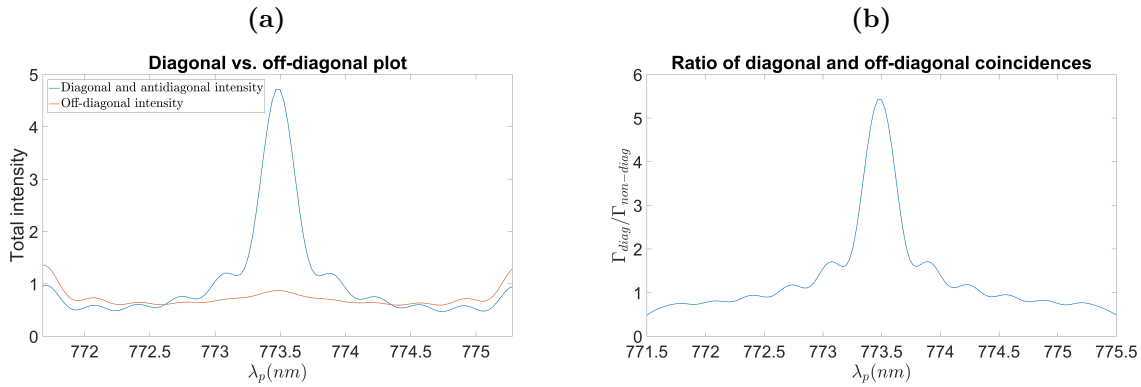

Figure 3.15: a) Absolute diagonal and anti-diagonal correlations (taking into account SPDC efficiency) Γ_{diag} (blue) and off-diagonal correlations $\Gamma_{non-diag}$ (red) and b) ratio $\Gamma_{diag}/\Gamma_{non-diag}$ as a function of the pump wavelength, for $L/L_c \simeq 6$.

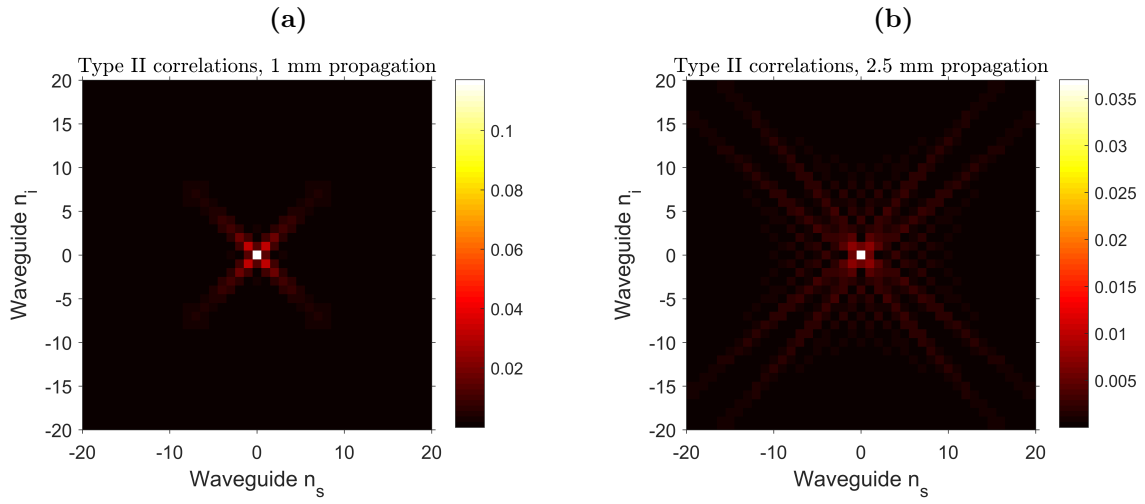

Figure 3.16: Type II spatial correlations in real space for propagation length a) $L = 1$ mm ($L/L_c \simeq 3$ at degeneracy) and b) $L = 2.5$ mm ($L/L_c \simeq 7.5$ at degeneracy), for a pump wavelength $\lambda_{p,deg}$ injected in the central waveguide, with filtering width 400 nm.

into two branches that correspond to the two possibilities mentioned above (see figure 3.16b); this splitting is governed by the polarization-dependence of the coupling constant.

Although the correlations are more complex in their shape, type II SPDC can be more efficient and thus easier to access experimentally than type 0 or type I SPDC, and we will present in chapter 5 experimental spatial correlations generated by type II SPDC.

However, for the remainder of this chapter, we will continue to focus on simulations of spatial correlations generated by type 0 SPDC, as they give a more straightforward understanding of the possibilities offered by nonlinear waveguide arrays.

3.2.1.6 Pump tailoring for the reconfiguration of the correlations

In this paragraph, we will take interest in the ability to control the output spatial correlations by tailoring the pump beam, through several examples, which put in light interesting points about the spatial correlations engineered in the array. Figure 3.17 shows four different cases: simultaneous pumping of guides 0 and 1 in phase (3.17a) or with a π relative phase (3.17c) and of guides -1 and 1 in phase (3.17b) or with a π relative phase (3.17d).

The shape of the correlation matrix is heavily modified by the tailoring of the pump spatial profile, giving control over the spatial correlations. One can observe selective enhancement or suppression of either diagonal or antidiagonal bands.

Looking at the case of the transverse wavevector correlations (figure 3.18) gives a nice numerical confirmation of the point made in paragraph 3.1.2.2: tailoring of the pump beam allows to select a subset of the $k_s^\perp = \pi \pm k_i^\perp$ square permitted by the modified phase-matching condition. Another interesting observation is that the correlations are strikingly similar if we pump guides 0 and 1 in phase or if we pump -1 and 1 with a π relative phase, and vice-versa. This is because the transverse wavevector distribution of the pump beam is intrinsically related to the relative phase between two adjacent waveguides in its spatial profile.

It is even possible to make more complex input states to control the correlations,

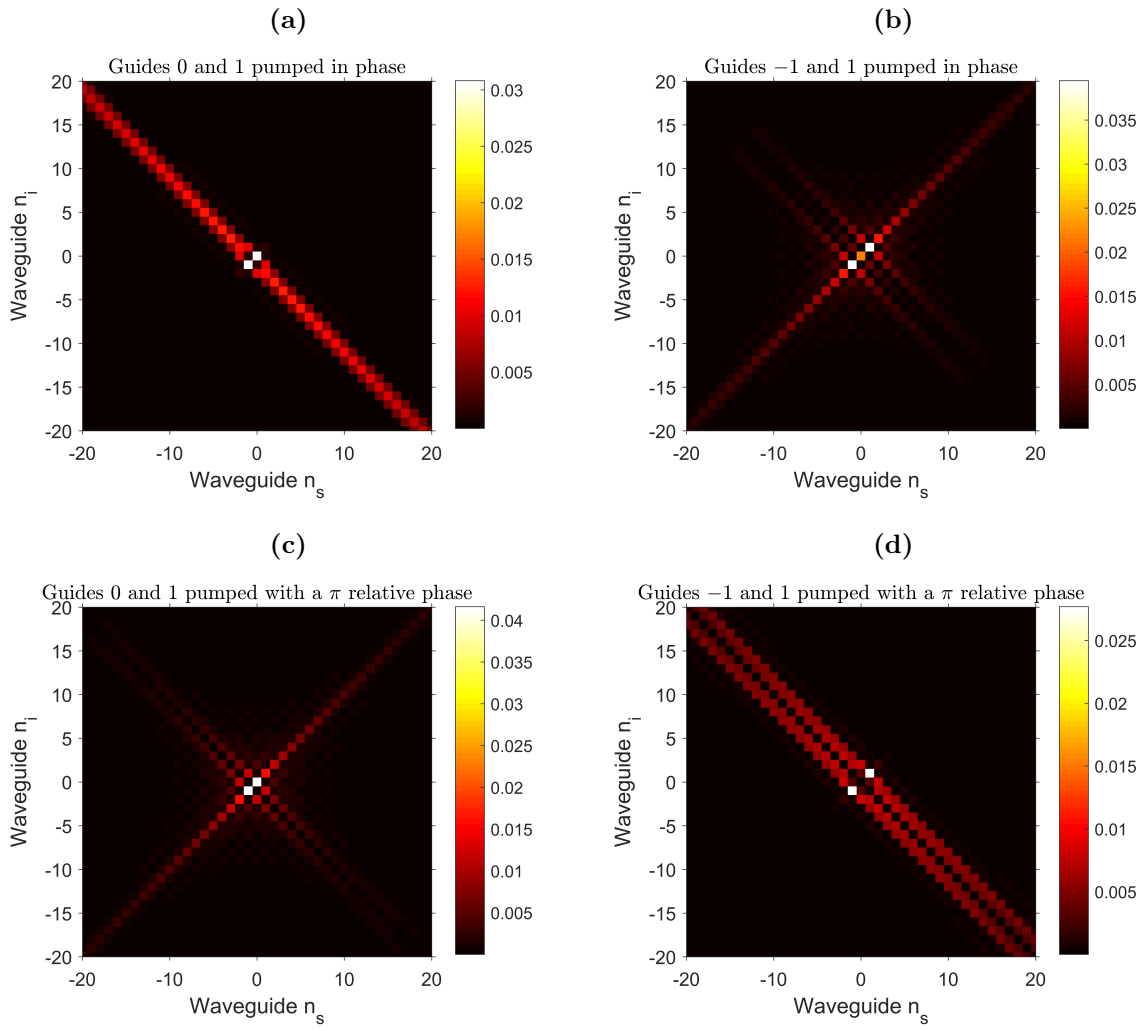

Figure 3.17: Correlations in real space while pumping two guides simultaneously, a) 0 and 1 in phase, b) -1 and 1 in phase, b) 0 and 1 with a π relative phase, and d) -1 and 1 with a π relative phase, for $L/L_c \simeq 6$.

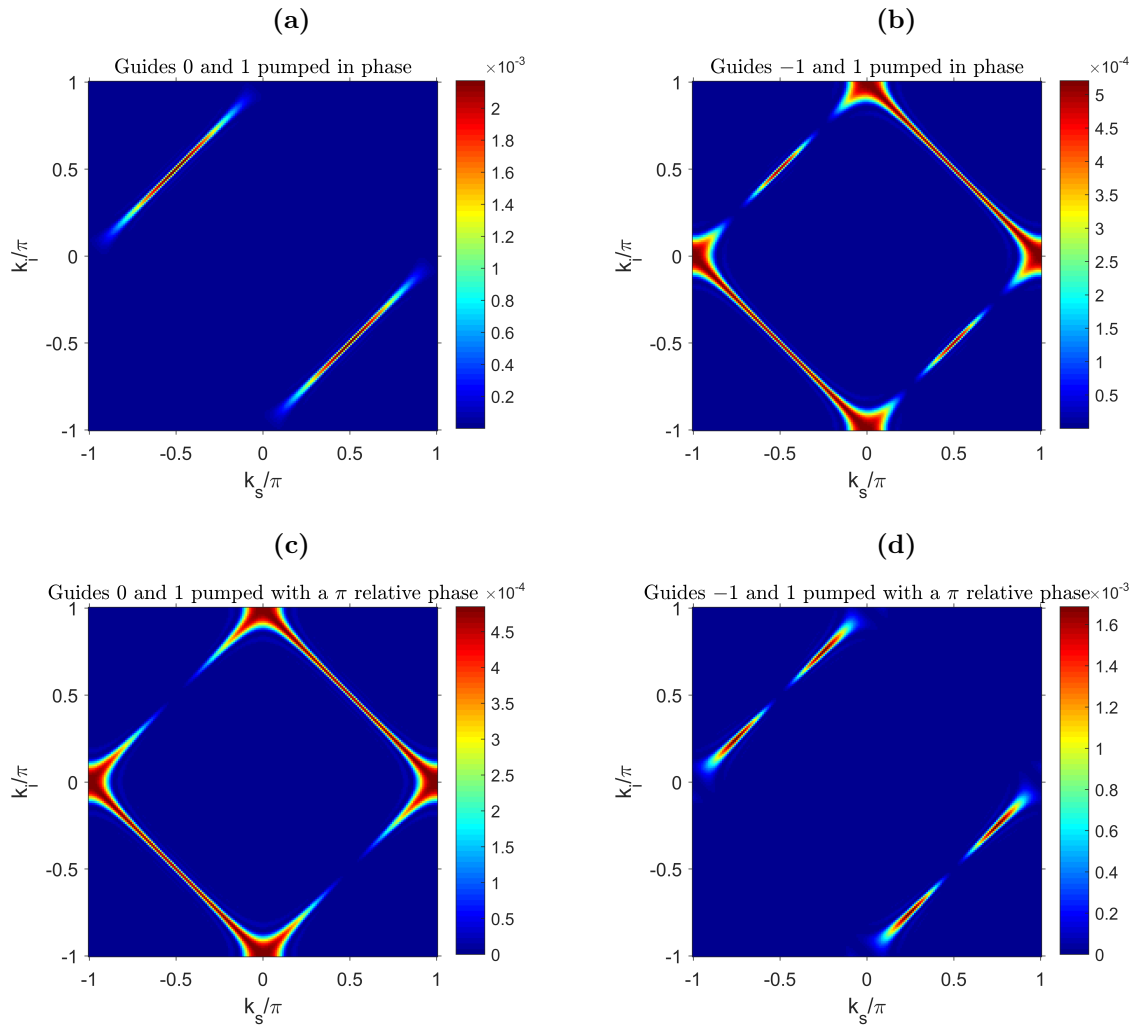

Figure 3.18: Correlations in transverse wavevector space while pumping two guides simultaneously, a) 0 and 1 in phase, b) -1 and 1 in phase, b) 0 and 1 with a π relative phase, and d) -1 and 1 with a π relative phase, for $L/L_c \simeq 6$.

which can yield interesting spatial shapes for the correlations. For instance, it is possible to obtain perfect diagonal correlations by using the pump spatial profile such that $\tilde{A}_{spatial}\left(k_p^{\perp}\right) = \delta_{k_p^{\perp},\pi}$, i.e. pumping all waveguides with alternate 0 and π phase, yielding $A_{spatial}(n) = (-1)^n$. The resulting correlations when pumping the waveguide array in this scheme is shown in figure 3.19a (real space) and b (transverse wavevector space). The wavevector correlations verify in this case $k_s^{\perp} + k_s^{\perp} = \pi$, taking only the two sides of the square oriented along the antidiagonal. In this case, we can also observe that the non-classicality indicator (figure 3.19c) is maximal on every point outside of the diagonal, while the Cauchy-Schwartz inequality (figure 3.19d) is never violated, because the non-diagonal terms are all zero.

In the same spirit, it is also possible to select the antidiagonal by selecting *every pump transverse wavevector except for* π, giving complementary correlations to the previous case in transverse wavevector space. The results for the simulation are given in figure 3.20, where in contrast to the perfect diagonal case, we observe a high violation of the Cauchy-Schwartz inequality on the antidiagonal.

These results show that nonlinear waveguide arrays constitute a versatile platform for the reconfigurable generation of spatially entangled photon pairs.

3.2.2 Real-space simulations for finite arrays

In this subsection, we introduce the simulations in real space for finite arrays, using the formalism derived in paragraph 3.1.2.3. Because equation 3.67 is very easy to put in a discrete matricial form, it is a convenient and efficient formalism for MATLAB-supported computation. Numerical simulations for finite arrays also allow to simulate systems closer to actual experimental photonic chips, with the possibility to add in a convenient manner losses, pump propagation, disorder in the propagation or coupling constants and boundary effects from the edges of the array.

The simulation is performed in the following way: we discretize the propagation direction of the array into pieces of size $dz = L/N_z$, where N_z is the number of points we consider for the propagation. We first compute (if present) the transverse propagation of the pump, taking losses into account. For this we define a variable vector for the pump beam $\{A_{n_p,n_z}\}_{1\leq n_p\leq N, 0\leq n_z\leq N_z}$, where N is the total number of waveguides, and A_{n_p,n_z} is the pump amplitude in guide n_p at position $z = n_z dz$. Starting from the desired initial condition $\{A_{n_p,0}\}$, corresponding to the spatial profile of the pump at the array input, we can then define

$$dA_{n_p,n_z} = \left(-i\beta_p\left(\omega_p\right)A_{n_p,n_z} - \alpha_p A_{n_p,n_z} + iC_p\left(\omega_p\right)\left(A_{n_p+1,n_z} + A_{n_p-1,n_z}\right)\right)dz \qquad (3.77)$$

where β_p is the propagation constant of the pump, α_p its loss coefficient, and C_p its (potentially zero) transverse coupling constant. We then redefine $A_{n_p,n_z+1} = A_{n_p,n_z} + dA_{n_p,n_z}$, and repeat the process N_z times, which gives the distribution of the pump beam along the array. We can then use this pump beam distribution in our computation of the generation of SPDC photon pairs along the array.

For the next step, we need to discretize equation 3.67. For this, we now define a

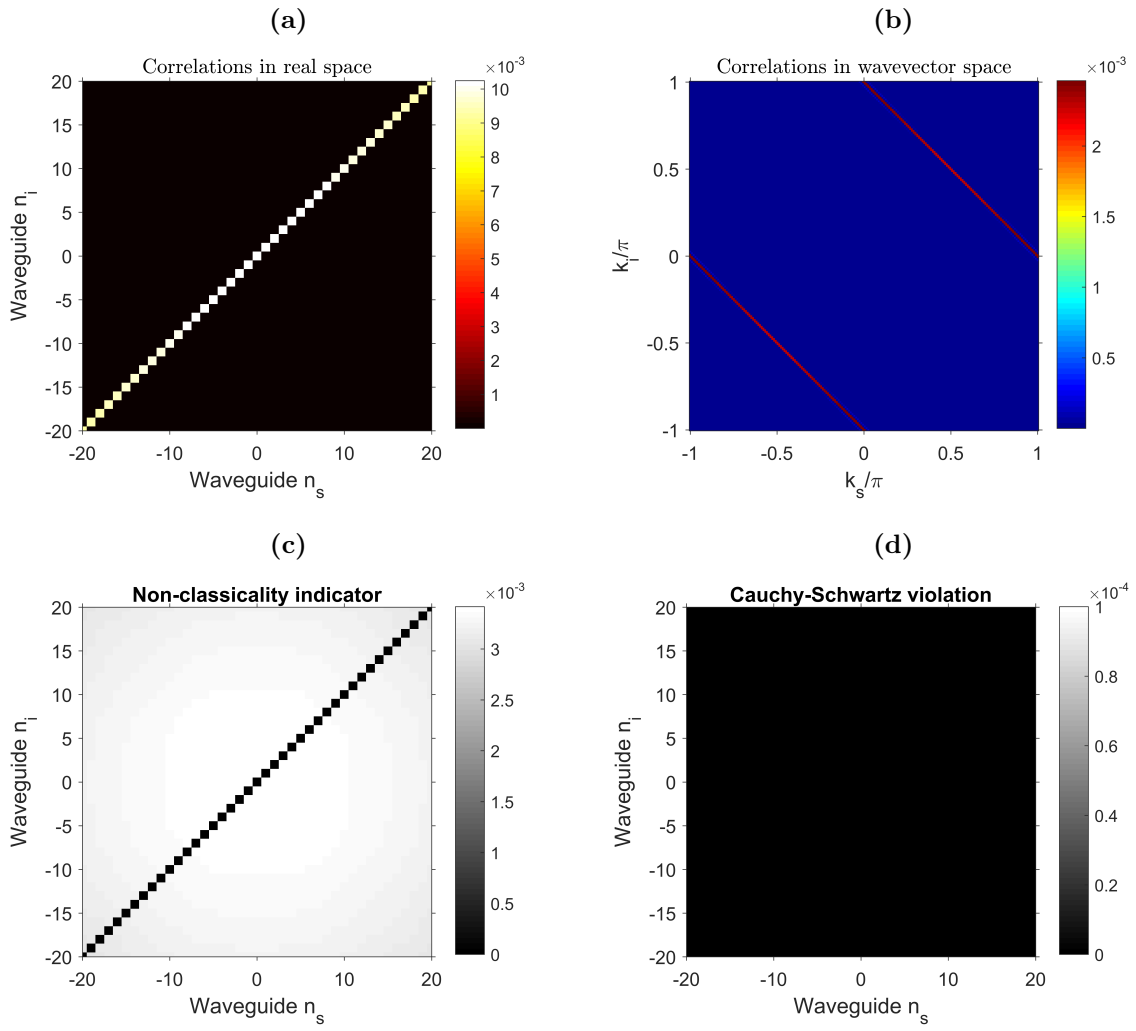

Figure 3.19: Correlations in a) real and b) transverse wavevector space and c) non-classicality indicator and d) Cauchy-Schwartz inequality violation when pumping every waveguide with alternating sign, for $L/L_c \simeq 6$.

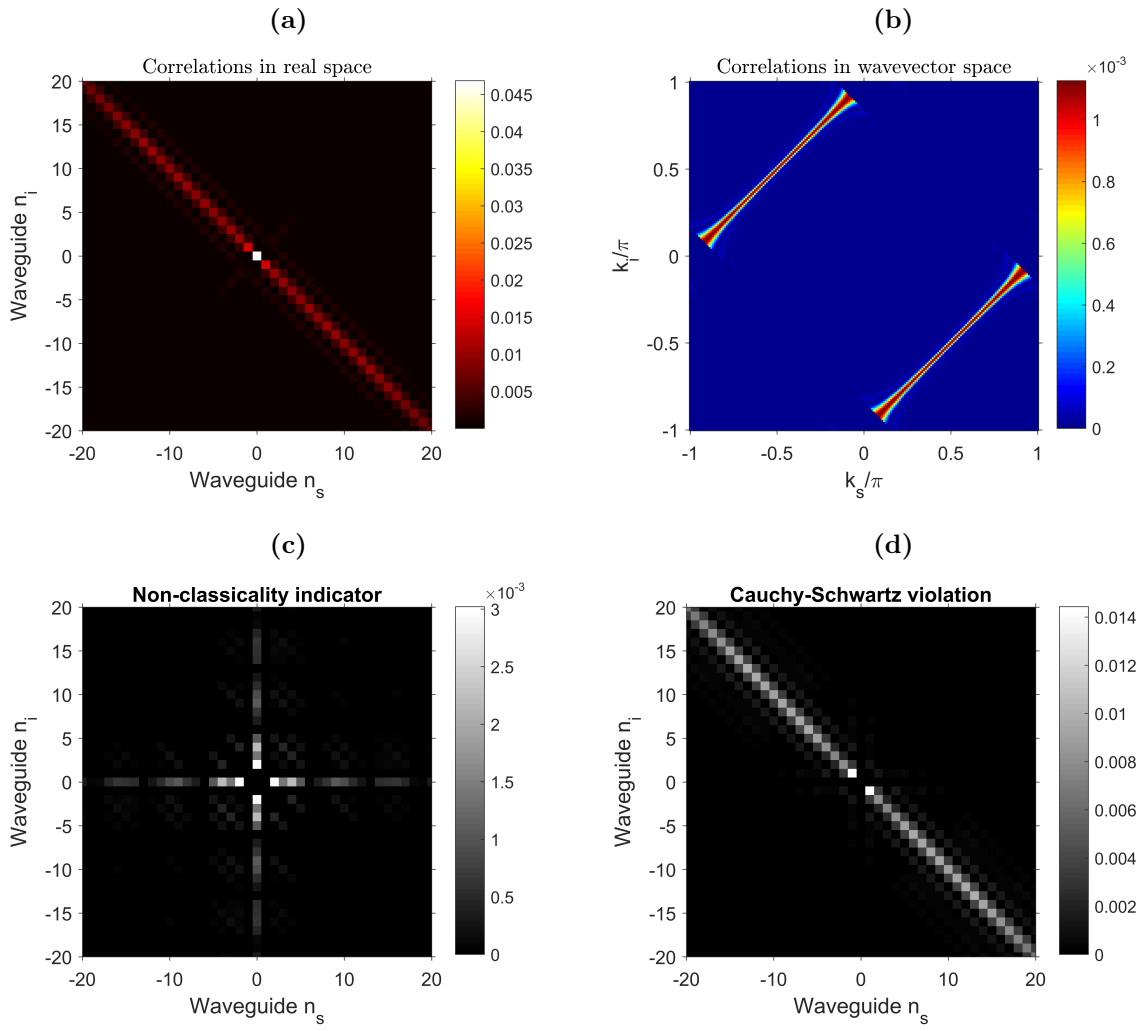

Figure 3.20: Correlations in a) real and b) transverse wavevector space and c) non-classicality indicator and d) Cauchy-Schwartz inequality violation for antidiagonal correlations, for $L/L_c \simeq 6$.

matrix[17] $\{\Psi_{n_s,n_i}(\omega_s)\}_{1\leq n_s,n_i\leq N}$, and two coupling matrices for the signal and idler modes

$$CM_i(\omega_i) = \begin{bmatrix} 0 & iC_i(\omega_i) & & & & \\ iC_i(\omega_i) & 0 & iC_i(\omega_i) & & & \\ & iC_i(\omega_i) & 0 & \ddots & & \\ & & \ddots & \ddots & iC_i(\omega_i) & \\ & & & iC_i(\omega_i) & 0 & iC_i(\omega_i) \\ & & & & iC_i(\omega_i) & 0 \end{bmatrix}$$

and

$$CM_s(\omega_s) = \begin{bmatrix} 0 & iC_s(\omega_s) & & & & \\ iC_s(\omega_s) & 0 & iC_s(\omega_s) & & & \\ & iC_s(\omega_s) & 0 & \ddots & & \\ & & \ddots & \ddots & iC_s(\omega_s) & \\ & & & iC_s(\omega_s) & 0 & iC_s(\omega_s) \\ & & & & iC_s(\omega_s) & 0 \end{bmatrix}.$$

Equation 3.67 can then be put into the matricial form at step n_z (omitting the frequency dependence for readability and considering the case of a pure state in the spatial degree of freedom):

$$d\Psi_{n_z} = \left[-i(\beta_s+\beta_i)\Psi + \Psi CM_i + CM_s\Psi + \Gamma_{\text{eff}}\delta_{n_s,n_i}\text{diag}(A_{1,n_z},...,A_{N,n_z})\right]dz \quad (3.78)$$

with $\text{diag}(\lambda_1,...,\lambda_n)$ the square matrix with diagonal coefficients $(\lambda_1,...,\lambda_n)$. We then redefine $\Psi = \Psi + d\Psi_{n_z}$ and repeat the process N_z times to get the final state at the output of the array.

Note that the matricial formalism is convenient, since it allows to introduce disorder in a simple manner in the matrix, by modifying over- and under-diagonal coefficients of CM_i and CM_s. It is also possible to introduce disorder in the propagation constants by multiplying Ψ in the equation evolution by $\text{diag}(i\beta_{s,1},...,i\beta_{s,N})$ on the left and $\text{diag}(i\beta_{i,1},...,i\beta_{i,N})$ on the right instead of using scalar multiplication in equation 3.78, although we will not consider this effect in the following simulations.

3.2.2.1 Effect of pump propagation and losses

As mentioned before, the pump can potentially undergo transverse propagation in the waveguide array, and it is important to quantify the effect of the pump propagation on the correlations, since it can potentially complexify the correlations compared to the simpler case where the pump stays confined in its input waveguides. For this we can simulate the propagation using different values of the pump transverse coupling constant C_p, and consider the intensity correlations in real space (since the intensity correlations in transverse wavevector space are no longer well-defined in the case of a finite array).

[17] Here the matrix only depends on one variable ω_s, since the energy conservation condition and monochromatic pump completely determine $\omega_i = \omega_p - \omega_s$. In practice, we will only consider pure states here, with $\omega_s = \omega_p/2$.

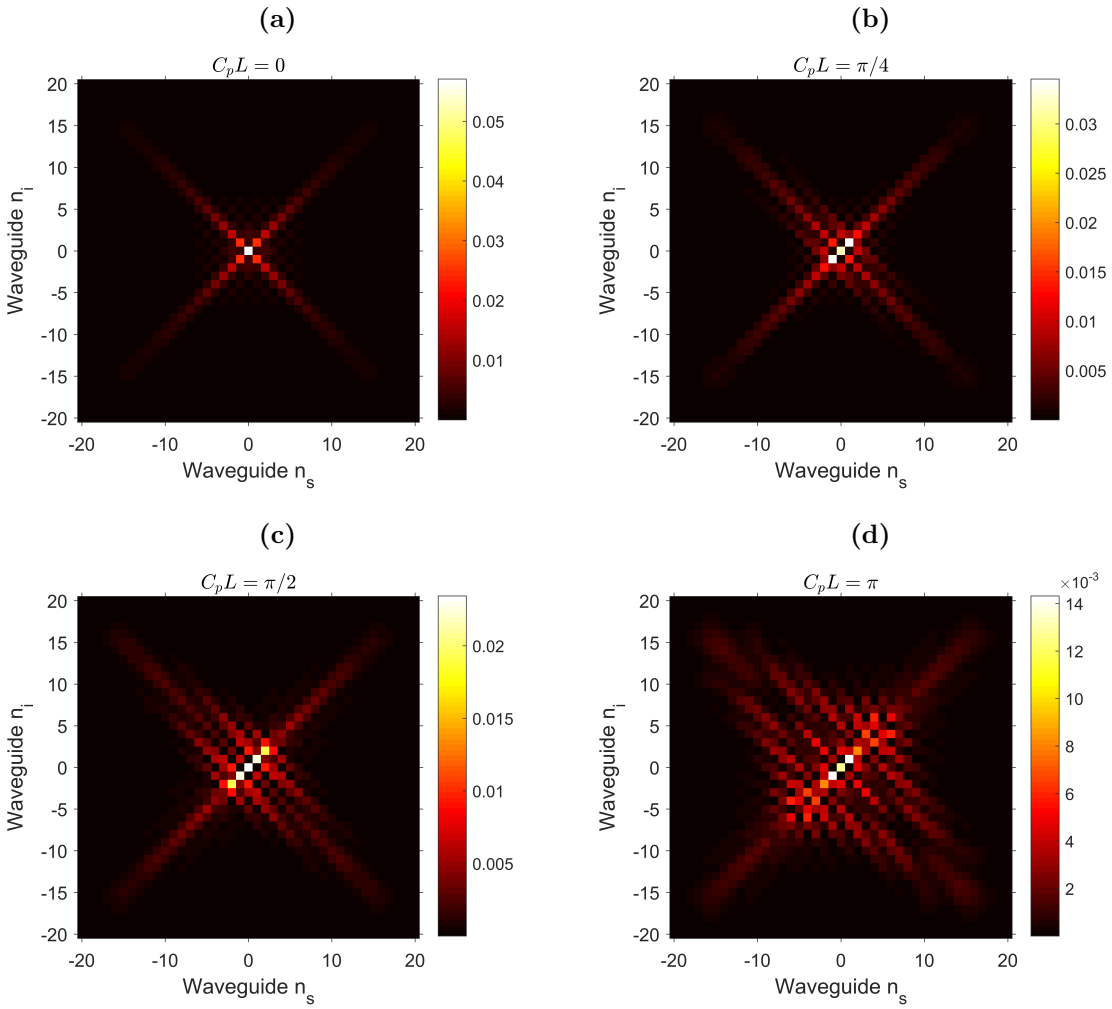

Figure 3.21: Simulated spatial correlations with a pump propagating transversally. From a) to d), the coupling constant of the pump increases. $L/L_c \simeq 6$ for the telecom fundamental modes.

We present in figure 3.21 numerical simulations for different values of the pump propagation, given in units of C_pL, which is the relevant dimensionless parameter in this case, while pumping the central waveguide of the array $n = 0$. One can see that as the propagation of the pump increases (from panel a to d), the central diagonal points have a higher coincidence rate compared to the antidiagonal ones (which is expected from the generation of photon pairs in different waveguides), and an interference pattern appears near the antidiagonal. The effect of the pump transverse propagation is complex to understand, but its main feature seems to be enhancing of the diagonal coincidences and scrambling of the antidiagonal coincidences through interference of the photon pairs produced in different waveguides in which the pump has significant intensity.

Another parameter that can affect the produced output state is the pump propagation losses, since in our samples the losses for the pump mode (Bragg mode) can be relatively high ($\simeq 5$ cm^{-1}) compared to the losses for the telecom modes of the SPDC photons (≤ 1 cm^{-1}). Intuitively, what is expected in the limit of extremely high losses is that the output state will tend to the output state for a passive array with input state $|\varphi_0\rangle$

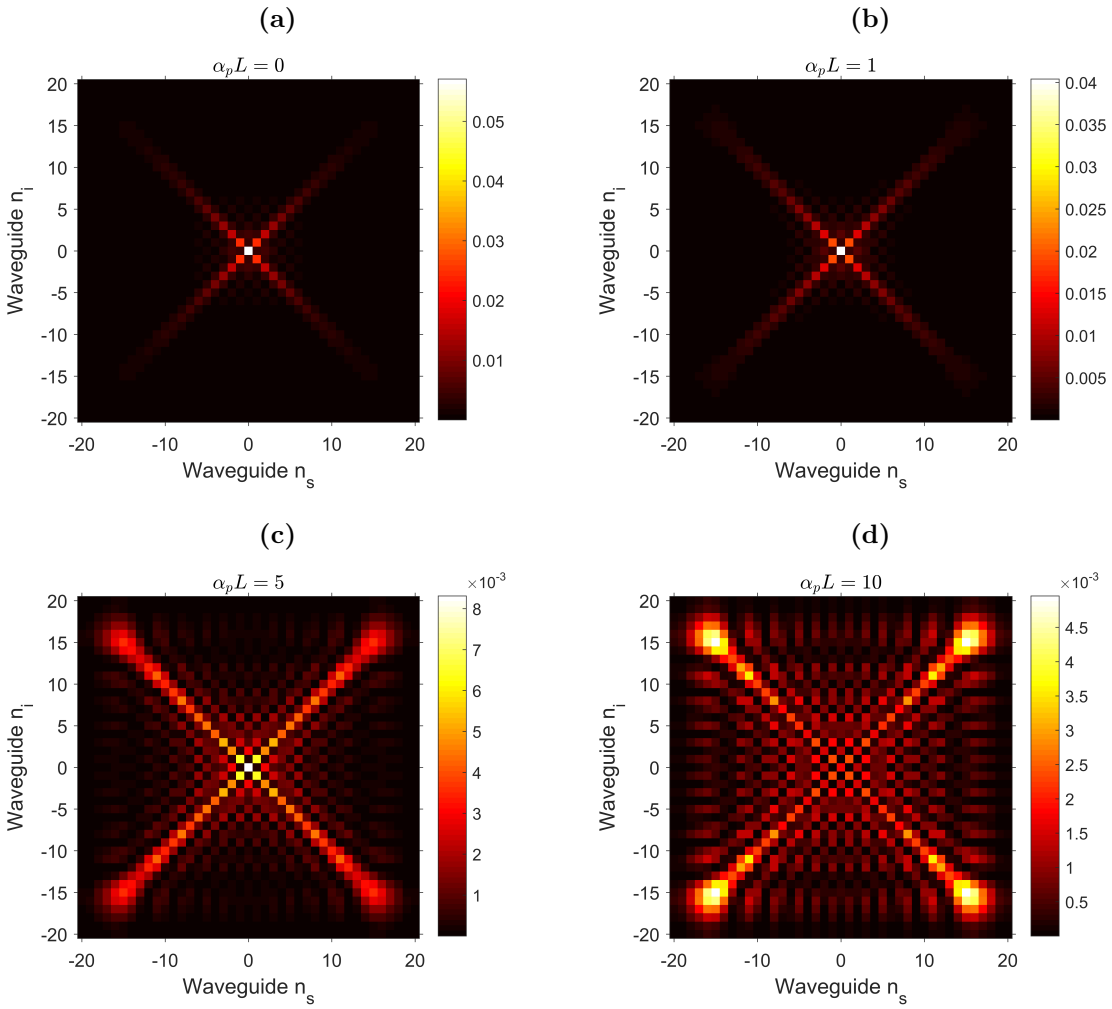

Figure 3.22: Simulated spatial correlations with losses in the pump propagation. From a) to d), the losses of the pump increase. $L/L_c \simeq 6$ for the telecom modes.

(see figure 3.5, first line), since in a very local and simplified picture, the photons would be preferentially created at the beginning of the waveguide array, as the pump intensity decreases fast with propagation, and the interference between the quantum walks starting at different positions along the propagation direction would be suppressed. We plot the simulations for different values of $\alpha_p L$ in figure 3.22 (increasing from panel a to d). With increasing pump loss, the intensity of the correlations gradually go from the correlations propagating in the diagonal and the antidiagonal from the center waveguide to ballistic lobes located in the corner of the correlation matrix, which is similar to the case studied in paragraph 3.2.1.1.

Experimentally, in our samples (see chapter 4) the pump losses and propagation constant verify $\alpha_p L \leq 1$ and $C_p L \leq 0.5$, thus we are close to the ideal case of a lossless pump without transverse coupling, which we will consider in the following.

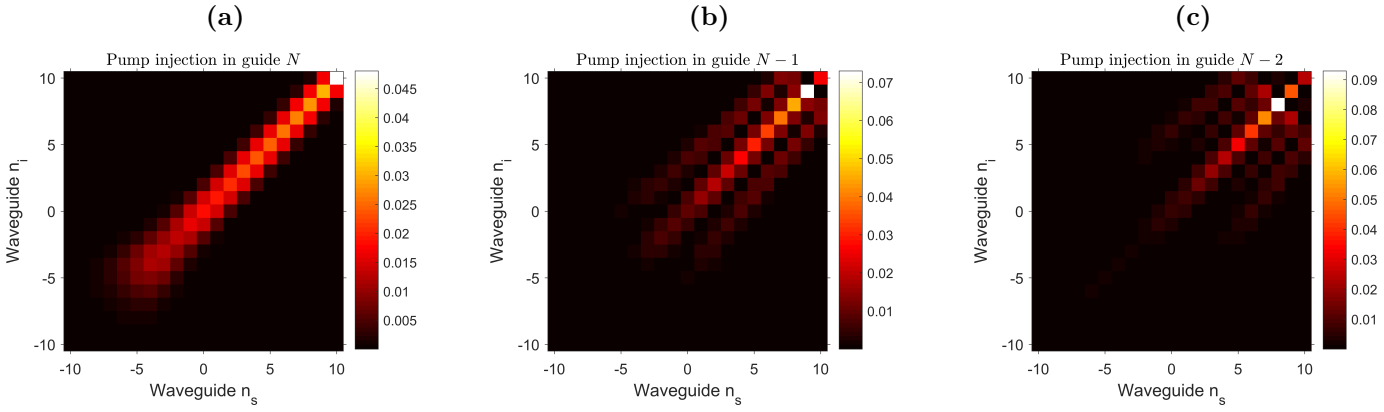

Figure 3.23: Simulated correlation matrix for injection of the pump beam near the edge of the array, a) in the rightmost waveguide, b) in its nearest neighbour, and c) in the next-nearest neighbour, for $L/L_c \simeq 6$.

3.2.2.2 Boundary effects and rebounds

The boundary effects in the waveguide array can be useful to study, since they provide interesting effects like the *rebound* of the photons at the edges of the array, changing the interference pattern and the transverse propagation direction of the photons. For instance, figure 3.23 presents the simulated spatial correlations when we inject the pump beam near one edge of the array, either in the rightmost waveguide labeled N (panel 3.23a) or in its two closest neighbours $N-1$ (panel 3.23b) and $N-2$ (panel 3.23c). The rebound pattern is visible for the case where waveguide $N-1$ or $N-2$ is pumped: we can see that the antidiagonal component is *reflected* along the edge of the correlation matrix, indicating that the photons change transverse propagation direction when reaching the boundaries of the array, since the boundaries restrict the accessible space for the photon pair. Solntsev *et al.* [104] provide a theoretical description of the phenomenon in terms of virtual sources located in a formal extension of the waveguide array. This type of boundary reflection can be used as a tool in the control of the quantum correlations in the spatial degree of freedom.

3.2.2.3 Disorder in the coupling constants

In condensed matter physics, disorder can give rise to interesting phenomena, such as Anderson localization [177], in which the wavefunction of electrons in disordered media tends to be localized because of the interference between different scattering paths. The effect of disorder is strikingly similar in the case of SPDC in waveguide arrays, where disorder in the propagation or coupling constants can lead to the localization of the photon pairs near the waveguide they were generated in, leading to a two-photons localization [178, 179]. While Lahini *et al.* [178] study diagonal disorder (corresponding to a disorder in the propagation constants $\beta_{s,n}$ and $\beta_{i,n}$), we will here, as Bai *et al.* [179] consider the effect of off-diagonal disorder, corresponding to a randomization of the values of C_s and C_i depending on the sites in the lattice. To study the effect of disorder in this case, we can add a random value between $-\Delta C$ and ΔC to C_s and C_i for each site. We can plot the correlations for different values of the disorder ΔC. Figure 3.24 shows the result of the

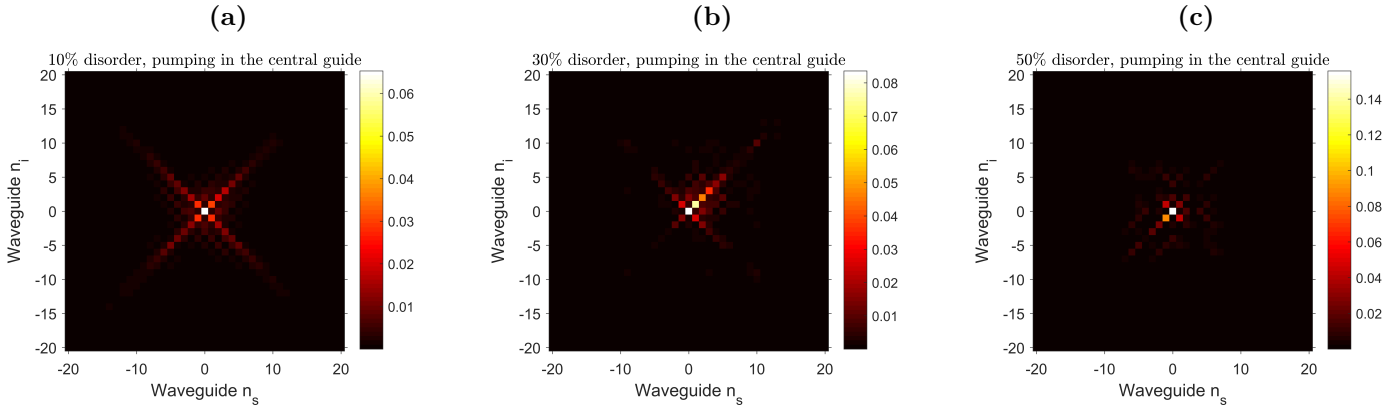

Figure 3.24: Simulated correlation matrix for injection of the pump beam in the central waveguide, with different realizations of disorder in the coupling constants, with a) $\Delta C = 0.1C_s$, b) $\Delta C = 0.3C_s$, and c) $\Delta C = 0.5C_s$, around the mean value given by $L/L_c \simeq 6$.

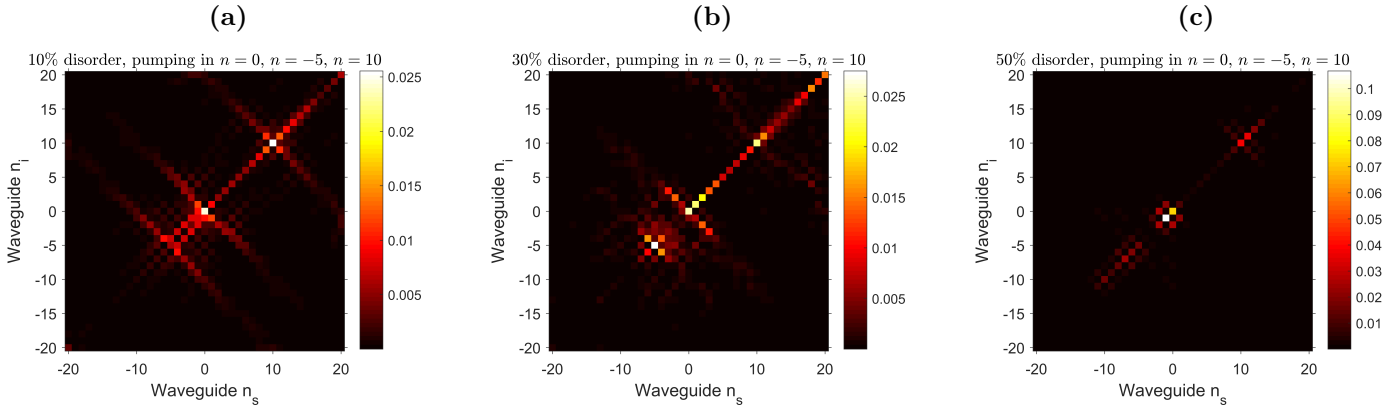

Figure 3.25: Simulated correlation matrix for injection of the pump beam in waveguides $n = 0$, $n = -5$ and $n = 10$, with different realizations of disorder in the coupling constants, with a) $\Delta C = 0.1C_s$, b) $\Delta C = 0.3C_s$, and c) $\Delta C = 0.5C_s$, around the mean value given by $L/L_c \simeq 6$.

simulation for different realizations of increasing disorder (from a to c) while pumping only the central waveguide. The result indicates that the photon pair transverse propagation is highly reduced by disorder, so that the photon pairs tend to be confined in the vicinity of the pumped waveguide ($n = 0$) as the disorder increases, demonstrating a localization phenomenon. If we pump several waveguides simultaneously ($n = 0, -5$ and 10 in figure 3.25), we see that as the disorder increases, the photons tend to be localized around the pumped sites, further confirming that the transverse propagation generally tends to be suppressed by disorder. Disorder has been explored experimentally in the context of quantum walks in passive circuits [81], but never for cascaded quantum walks. We will discuss the perspective of using nonlinear waveguide arrays to simulate such localization effects in cascaded quantum walks at the end of chapter 5.

3.2.3 Summary and conclusion

In this chapter, we have theoretically studied photonic quantum walks in waveguide arrays. After studying passive waveguide arrays, we have introduced the theory of cascaded quantum random walks in nonlinear waveguide arrays and studied the spatio-spectral correlations generated by SPDC in the case of infinite periodic arrays by introducing Bloch eigenmodes of the array. This has allowed to introduce the reciprocal spatial degree of freedom, i.e. the transverse wavevector space, as a convenient tool to describe spatial correlations. We have also presented a real-space formalism well-suited to the description of finite waveguide arrays, which allows to study some key parameters for quantum simulations of condensed matter systems, such as disorder or topological effects. Additionally, we presented two indicators for the non-classicality of the generated biphoton states in the spatial degree of freedom, the non-classicality indicator defined in equation 3.40 and the Cauchy-Schwarz inequality. We then presented numerical simulations to study the effect of several parameters on the state of the generated photon pairs, such as spectral filtering width, disorder, pump propagation or pump losses, and we highlighted a variety of quantum correlations that can be generated in the spatial degree of freedom by tailoring the spatial distribution of the pump beam.

This chapter illustrates theoretically the panel of different spatial biphoton states that can be generated using the device and shows that nonlinear waveguide arrays are a promising candidate to realize a versatile source of entanglement in the spatial degree of freedom. In the following chapters, we will present the next steps towards the experimental realization of controllable spatial entanglement generation, by first presenting in chapter 4 the design and clean room fabrication of AlGaAs waveguide arrays, and then in chapter 5 the measurement of spatial correlations in the fabricated waveguide arrays.

Chapter 4

Design and fabrication of AlGaAs waveguide arrays

The previous chapter described the theory of path entanglement generated by SPDC in waveguide arrays. Here we turn to the design and fabrication of such waveguide arrays. We first describe the electromagnetic simulations of the relevant parameters of the waveguide array and provide a structure for the array allowing the experimental generation and measurement of spatial correlations. We then present the clean room fabrication process and preliminary characterization techniques of the AlGaAs waveguide arrays.

Contents

4.1 Design of the structure

We describe in this section the design of the waveguide arrays that we will use. This is an important step for the experimental realization of cascaded quantum random walks via SPDC, as we need not only to fabricate waveguide arrays with efficient coupling between the waveguides, but also to design it in a way that it is measurable in a practical manner. We present here the different steps involved in the design of such a structure, sketched on figure 4.1.

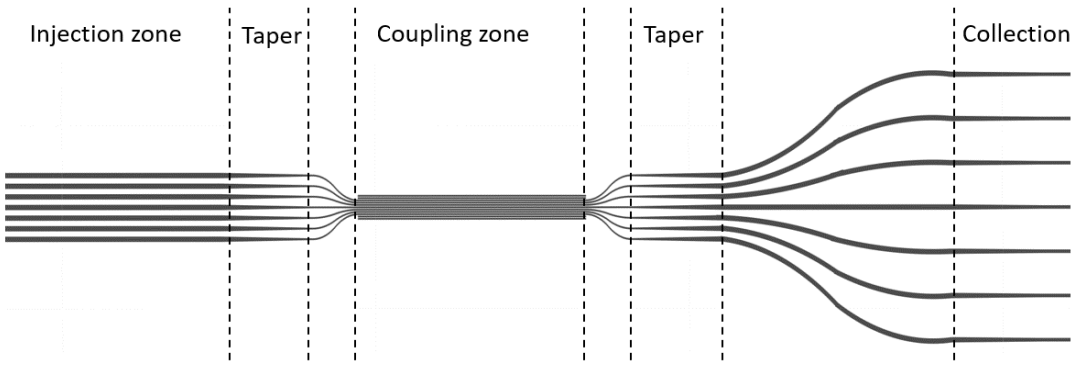

Figure 4.1: Sketch of the designed structure for the waveguide array, with injection, coupling and collection zones, tapers and bent waveguides.

4.1.1 Numerical simulations of the coupling constants

The first parameter of interest in the waveguide array is the coupling constant. To enhance the quantum random walks undergone by photons in the array, it should be the highest possible for the SPDC photons at telecom wavelengths, while simultaneously keeping the coupling constant low for the pump beam, so as to stay as close as possible to the theoretical case considered in chapter 3.

Since our structure will consist of an array of ridge waveguides etched into the epitaxial structure, the main parameters we have control over are the width of the waveguides, the distance between the waveguides, and the depth of the etching (see figure 4.2). The epitaxial structure we consider in this case consists of a piling of six Bragg mirrors above and below a propagation core where the optical modes are confined, made from AlGaAs layers with different Aluminum concentrations (see chapter 1). The possible range of these parameters depends on the fabrication process, described in the following section, which will involve electron-beam lithography and Inductively Coupled Plasma (ICP) etching. Electron beam lithography offers a good resolution for nano-fabricated devices, allowing to fabricate nano-devices with accuracy in the nanometre range. In order to have sufficient reproducibility for the coupling constant in the fabricated waveguide arrays, we initially chose to use gaps around 500 nm between the waveguides to keep the relative variance of the gap values as low as possible, and to allow for a not too high aspect ratio between the etching depth and the width of the gaps during the ICP etching process, ensuring a good verticality of the etched ridges. We also chose to use 2 μm wide waveguides, in order to reach a compromise between the losses, which increase when the width decreases, and the evanescent coupling, which is enhanced when the field has non-zero value outside the waveguide, an effect that is favoured for small width values. Simulations showed that the coupling constant for such parameters is sufficient to allow several steps of the quantum walks for array lengths of only a few millimetres.

We use Lumerical to simulate the coupling constants C at 1550 nm for different values of the etching depth between the waveguides, by defining a structure consisting of two adjacent waveguides etched in the considered epitaxial structure, with a 2 μm width, and separated by a 500 nm gap (figure 4.3). To determine the coupling constant of the modes, according to the previous chapter, we have two different methods: we can compute

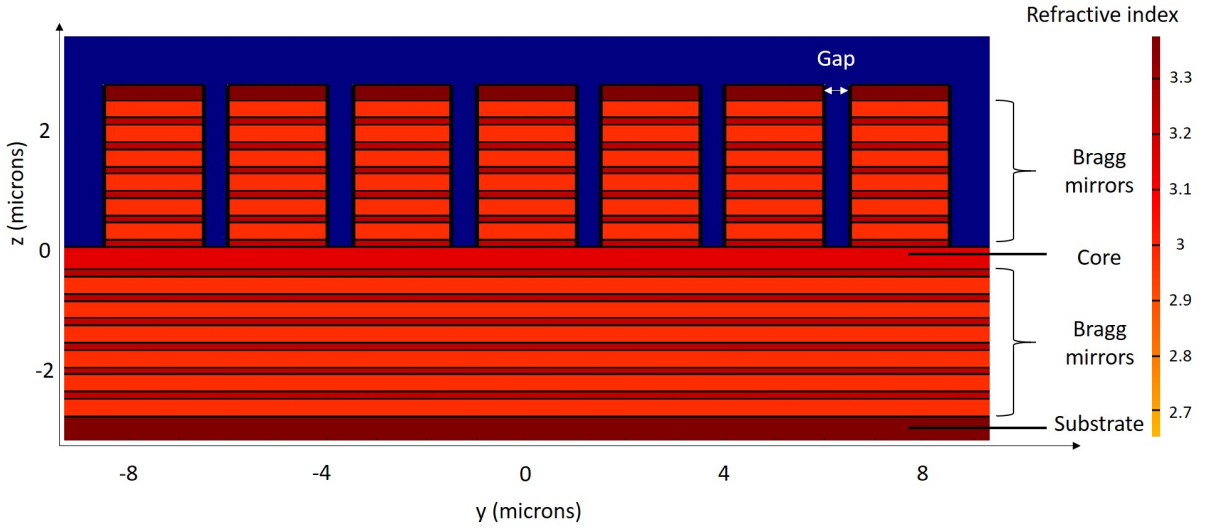

Figure 4.2: Simulated structure for a waveguide array consisting of 7 waveguides. The width of the waveguides, etching depth and gap are shown in the figure, and the colours indicate the refractive index of the different layers. The separation between the waveguides is 500 nm, and the guides are etched until the top of the core layer with an etching depth of 2.95 μm.

the difference between the propagation constants of the symmetrical and antisymmetrical modes, which will give $\beta_a - \beta_s = 2C$, or we can inject light in the first waveguide in the considered mode and simulate the propagation to determine the coupling length $L_c = \pi/2C$ that the optical power takes to travel completely to the second waveguide, called the half-beat length.

We here report the results using the propagation method, as it directly correlates to the physical phenomenon we want to observe, and is less dependent on possible index simulation errors. Simulations show an oscillation of the optical field, going back and forth between the two waveguides (see figure 4.4 for an example using the TE-polarized mode at 1550 nm, for a 500 nm gap and an etching depth of 2.590 μm), yielding $L_c = 278$ μm and $C = 5.65$ mm^{-1}.

Using this method, we determine the coupling lengths, for the TE and TM fundamental modes at 1550 nm, as a function of the etching depth of the two waveguides. The results of the simulations are presented in figure 4.5 (the core is located between 2590 nm and 2945 nm). The coupling length for the TE fundamental mode is 15 to 20% smaller than that of the TM fundamental mode at 1550 nm, highlighting an effect of the anisotropy of the waveguide and the epitaxial structure. We observe that the deeper the etching, the weaker the coupling between the waveguides (higher coupling length), which is expected since the modes are more and more confined in the waveguides. In the following, we will consider an etching depth of 2.590 μm, corresponding to the top of the core layer.

Additionally, we also simulate the frequency dependence of the coupling length, as it is necessary to conduct numerical simulations of the photonic states produced by SPDC in the waveguide array. The corresponding coupling length are represented for the TE and TM fundamental modes, as a function of wavelength, on figure 4.6, for an etching depth of $d = 2.590$ μm. The total variation of coupling over the 100 nm wavelength range for the two modes is around 15%, while the ratio between the coupling lengths for both polariza-

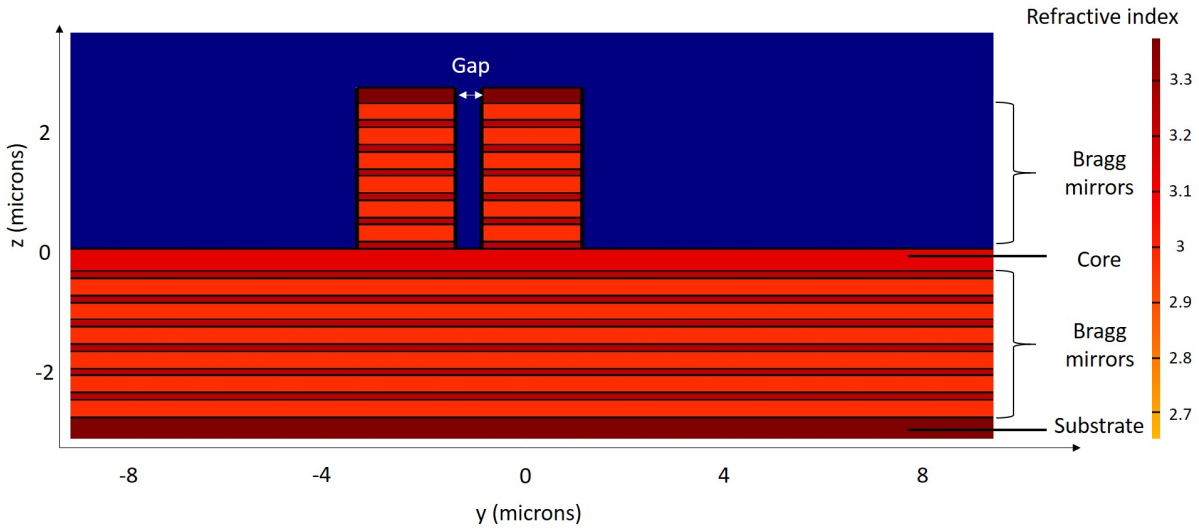

Figure 4.3: Simulated structure for the determination of the propagation constant, consisting of two adjacent waveguides. The separation between the waveguides is 500 nm, and the guides are etched until the top of the core layer with an etching depth of 2.590 μm.

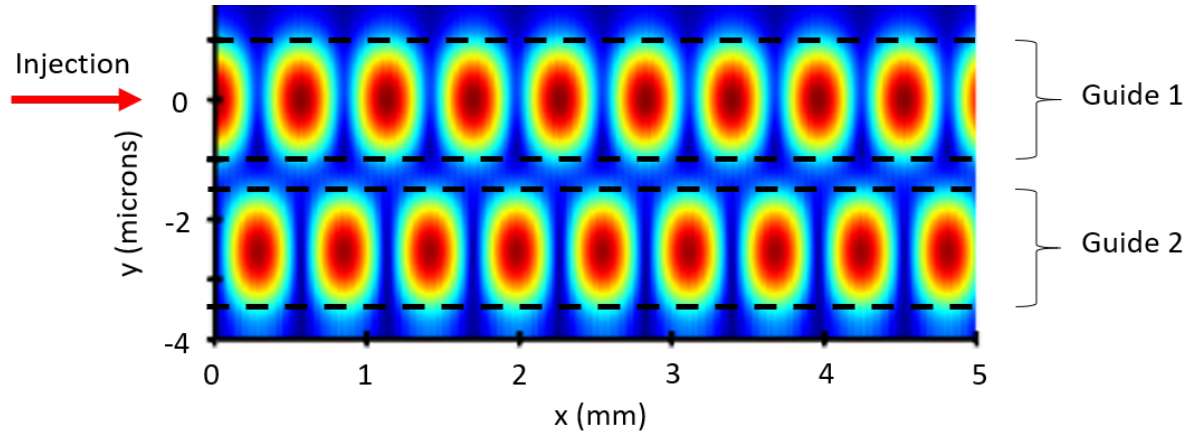

Figure 4.4: Power oscillation for the fundamental TE mode at 1550 nm, in a structure consisting of two 2 μm wide waveguides separated by a 500 nm gap for an etching depth of $d = 2.590$ μm.

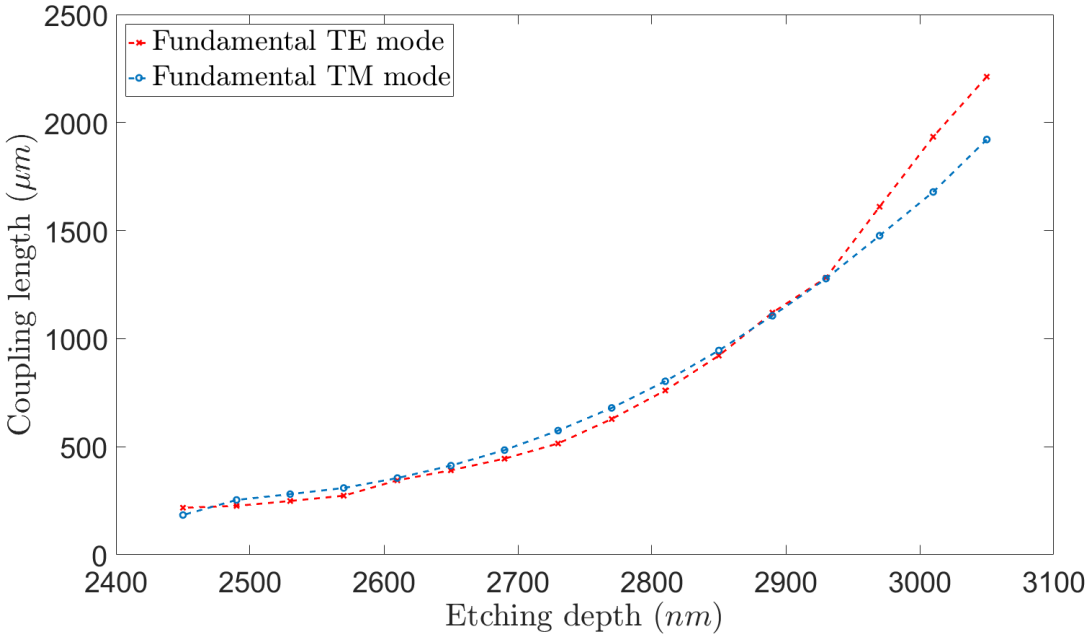

Figure 4.5: Simulated coupling length as a function of etching depth, for the fundamental TE and TM modes at 1550 nm, in a structure consisting of two 2 μm wide waveguides separated by a 500 nm gap.

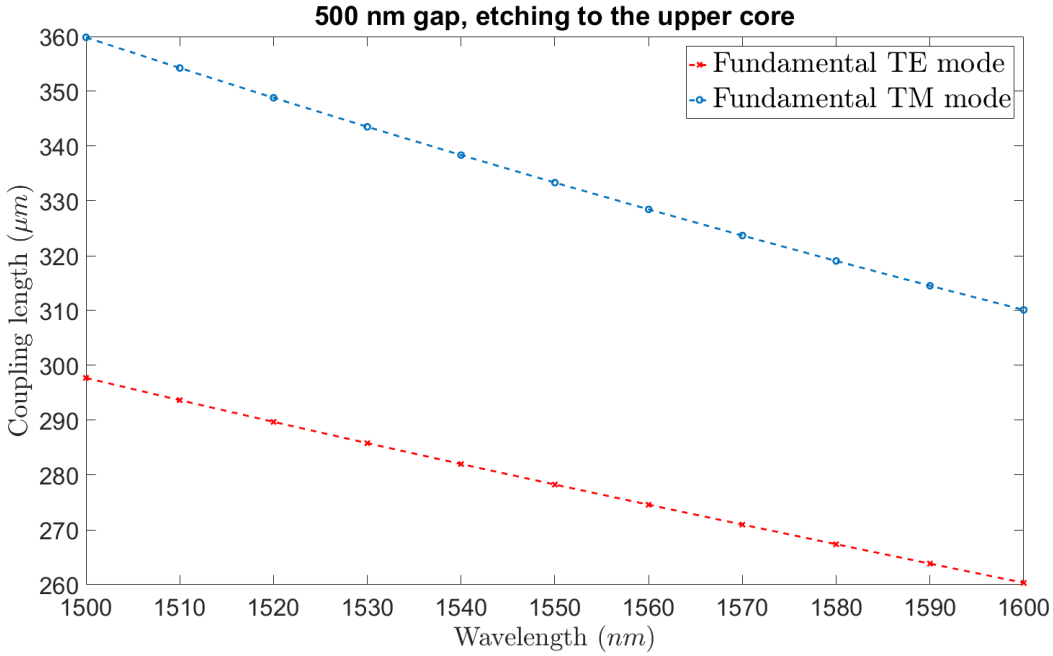

Figure 4.6: Simulated coupling length as a function of wavelength, for the fundamental TE and TM modes, in a structure consisting of two 2 μm wide waveguides separated by a 500 nm gap and etched to the top of the core epitaxial layer with etching depth $d = 2.590$ μm.

tions is almost constant over this wavelength range, with the coupling length for the TM fundamental mode roughly 20% higher than that of the TE fundamental mode. When the wavelength increases, the field spreads over a larger length scale, hence the evanescent coupling is more efficient, and the coupling length decreases. The frequency dependence contributes to the coupling between the spatial and spectral degrees of freedom (section 3.1.2.2), which can be eliminated by spectral filtering.

4.1.2 Experimental constraints and structure design

Having simulated the coupling lengths, we can now turn to the design of the sample and the structure that we will fabricate. This is an important step, as it involves the design of a structure that is experimentally measurable in a practical way. In our case, we want to be able to measure the spatial distribution of SPDC photons produced in a waveguide array, while being able to pump each waveguide individually, in order to realize spatial tailoring of the pump beam. This imposes several constraints on the sample. The sample (sketched in figure 4.1) must have an injection zone, consisting of input waveguides separated enough so that we can couple only one of them to an incoming pump beam, and a collection zone, with output waveguides separated enough so that we can couple the outgoing photons to different single-photon detectors to realize coincidence measurements. It must also have a coupling zone, i.e. an area where the waveguides are close enough to be coupled, and thus form a waveguide array. Finally, the SPDC must only take place in the coupling zone, and not in the injection or collection zone.

To allow for different spacing between the waveguides in the different zones, we use bent waveguides so that we can modify the spacing between the waveguides along the propagation. To allow generation in the coupling zone only, we use linear tapering to change the width of the waveguides between the coupling zone and the injection or collection zones, thus changing the phase-matching resonance by modifying the effective indices of the different modes involved in the SPDC process.

In our case, the gap between the waveguides in the coupling zone is chosen to be of the order of 500 nm, and we choose the value for the spacing in the injection zone to be 12 μm, providing enough separation between the waveguides so that they are not evanescently coupled to each other, while keeping them close enough to be addressed easily by a pump beam using a microscope objective without significantly modifying the alignment. We choose the width of the waveguides in the injection and collection zones to be 6 μm (compared to 2 μm in the coupling zone), which significantly shifts the SPDC resonance (by about 10 nm lower in wavelength) and ensures low propagation losses for photons in the telecom range ($\simeq 0.2$ cm^{-1}). On the other end, for the collection zone, we would like to be able to collect the output photons using a commercial fiber array, to send them simultaneously to several detectors (see section 5.1.2.1). For this, we use a Vanguard lensed fiber array, with a 127 μm pitch, which sets the spacing between the waveguides in our collection zone. We choose a waveguide width of 2.5 μm for the final part of the collection zone, so as to match the mode-field diameter of the lensed fiber array while shifting the resonance by about 1.2 nm lower in wavelength.

In order to quantify the losses induced by the bending in the injection and collection zones, we simulated a bent waveguide in Lumerical, for 6 μm and 2.5 μm widths, using the minimal bending radius necessary to achieve a separation of 127 μm of the waveguides over

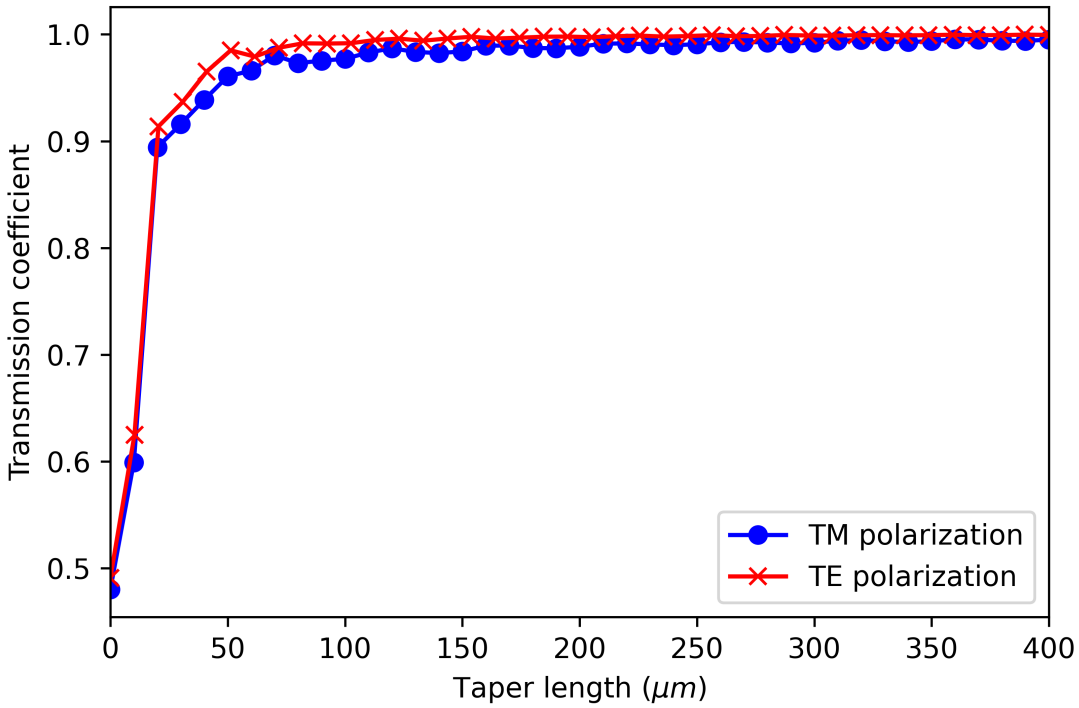

Figure 4.7: Simulated transmission for a taper taking the width of a waveguide from 6 to 2 μm at 1550 nm.

a 1 mm length (the values we used in our design), which was 360 μm. This bending radius generates losses of 0.96 dB/cm at 1550 nm for both 6 μm and 2.5 μm wide waveguides (i.e. a signal transmission of 95% over 1 mm).

We also quantified the losses induced by the tapers by simulating the transmission of the telecom modes for different linear taper lengths, for tapering from 6 to 2 μm. The results of the simulation are given in figure 4.7 for both polarizations. We observe that the power transmission is above 99% for taper lengths over 100 μm, and that no significant transmission advantage is gained by increasing the length of the taper further from that point, while it would increase the footprint of the structure. We thus use a tapering length of 100 μm.

A sketch of the final structure is schematically shown in figure 4.1, where the injection, coupling and collection zones are visible, as well as the bending and tapering zones. This type of structures will serve as our main measurement support for the spatial correlations of the SPDC photon pairs. Additionally, we will use simple waveguide arrays (i.e. structures with only coupling zones) and single waveguides to make characterization measurements, such as losses measurements, or Second Harmonic Generation measurements.

4.2 Cleanroom fabrication

In this section, we describe the clean room processes used for the fabrication of the AlGaAs waveguide arrays that we measured during this thesis. In order to fabricate the samples,

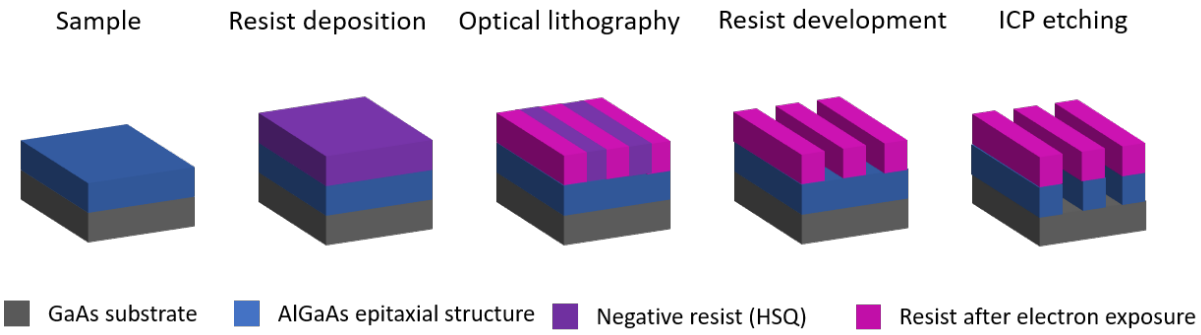

Figure 4.8: Principle of the electron-beam lithography process. The negative resist is exposed, and the non-exposed part is developed and discarded, while the exposed resist serves as a protective mask during the ICP etching.

we decided to use electron beam lithography and Inductively Coupled Plasma (ICP) etching, since this method has proven efficient to realize nano-fabricated devices with high accuracy. The fabrication process took place in three different cleanrooms: the cleanroom at Université Paris Cité for sample preparation, reactive ion etching, ICP etching and metal deposition, the ENS cleanroom where Fixed Beam Moving Stage electron beam lithography was performed, and C2N where the molecular beam epitaxy was done, as well as electron beam lithography and ICP etching.

4.2.1 Electron beam lithography

We first describe the electron beam lithography process. The procedure is summarized graphically in figure 4.8.

The electron-beam lithography consists of the exposure of an electron-sensitive resist using an electron beam, which allows the drawing of custom patterns inside the resist to realize micro- and nano-structures with high resolution, typically in the 10 nm range. For the fabrication of our samples, we use HSQ (hydrogen silsequioxane) resists, which are negative electron-sensitive resists. We first deposit a thin SiO_2 layer on our sample (typically 10 nm), which will serve as an adherence layer for the resist to properly deposit on the sample surface. We then spin-coat the HSQ resist on the surface of our sample, to form a thick layer of resist (200 to 600 nm, depending on the processes) that will serve as a mask during the etching process. The resist is then exposed using electron beam lithography, in the pattern corresponding to the desired outlay for the design of the structure. The resist is finally developed, only leaving the exposed pattern, which can now serve as a mask during the ICP dry etching, after eliminating the SiO_2 adherence layer using Reactive Ion Etching (RIE).

We first chose to use the 30 keV Raith eLine lithographic system from the ENS clean room, with a 200 nm layer of HSQ manufactured by AQM. This lithographic system allows to use the fixed beam moving stage (FBMS) mode for the electronic exposure of the resist, a method in which the sample, mounted on a moving stage, is moved under the immobile electron beam to realize the exposure with the desired pattern. This method enables the fast exposure of long structures with a fixed width, such as waveguides, and avoids stitching errors, but is not naturally suited for elements with varying width, such

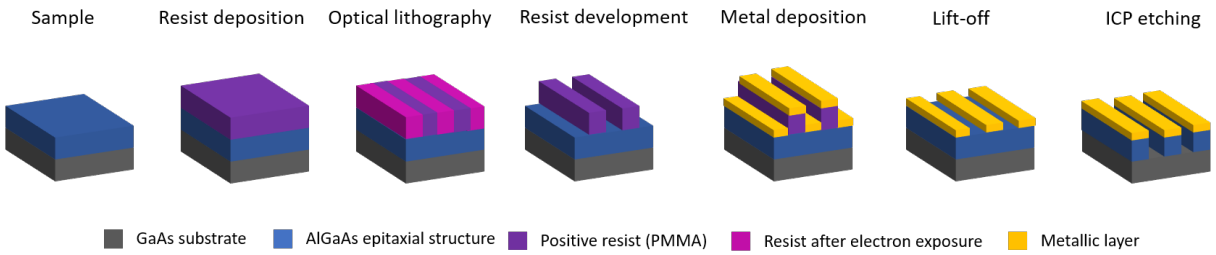

Figure 4.9: Principle of the double-mask electron-beam lithography, where we use a positive resist as a mask to deposit a metallic layer by evaporation. The metallic layer is then used as a protective layer during the ICP etching.

as tapers. Hence the method we used for taper exposure using the FBMS mode was to first expose the external contour of the taper, and then fill the interior of the taper with rectangles. This process is well-suited for straight arrays of waveguides, without injection or collection zones, but can result in alignment errors for the tapered structures. Several tests were conducted to determine the correct exposure dose to achieve a satisfying compromise between the exposure time and the resolution of the lithography (the exposure time took up to 3 hours per structure because the maximum acceleration voltage of the electrons was 30 keV).

The second system we used was a 100 keV lithographic system from the C2N cleanroom, using a 600 nm Dow Corning HSQ layer. This device didn't allow for the use of the FBMS mode, but allowed for faster exposure of the samples because of the higher electron energy available in this system, which additionally offered higher lithographic resolution. The stitching field error and misalignment was negligible, and the exposure was much shorter (approximately 3 hours for 6 structures with injection, collection and coupling zones).

Additionally, we also investigated a double-mask exposure technique, using a positive PMMA resist and a metallic nickel mask deposited by evaporation, which we sketch in figure 4.9. As this technique did not significantly improve the resolution of the electron-beam lithography but increased the complexity of the overall process, we did not end up using it to fabricate actual samples.

4.2.2 ICP dry etching

In order to etch our structure into the epitaxial layers, we use ICP etching, after the resist is developed. The surface of the sample is bombarded by a plasma, which chemically reacts with the material on the surface and simultaneously ejects some material through the high-energy collisions. The plasma is electrically accelerated in order to have a highly directional and anisotropic etching in the direction of the plasma acceleration (i.e. generally orthogonally to the surface), in contrast with wet chemical etching where the etching simultaneously occurs in every direction at once. This process allows to create etching profiles with vertical sidewalls, making it suitable for the fabrication of ridge waveguides.

For the fabrication of our samples, we use a Sentech SI500 machine, and the recipe consists of a low plasma power of 20 W, with 3 sccm[1] of $SiCl_4$ and Ar accelerated at

[1] 1 sccm corresponds to one standard cubic centimeter per minute, and is the usual unit used to

approximately 117 V and 15 W. Since we want to control the etching depth in the gaps between the waveguides in our waveguide arrays, we need to characterize the etching rate provided by this recipe. The etching depth is usually directly observed using the reflected power of a laser on the surface of the sample, which is dependent on the thickness of the uppermost epitaxial layer. However, since the gaps between the waveguides are smaller than the laser spot size, it is not possible to directly observe the etching depth within the gaps, where the etching is slower because of the narrow aperture which limits the amount of plasma that can be used for etching in this area. We thus realized several tests to determine the ratio between the etching speed inside and outside the gaps. This recipe gives a low etching rate around 15 nm/min inside the gaps, making the total etching duration for the complete etching process 6 hours, while the etching outside the gaps is closer to 25 nm/min.

At C2N we employ a different etching recipe, using HBr and O_2 as the etching chemical species, and a higher plasma power, giving an etching speed inside the gaps of 130 nm/min.

SEM images of waveguide arrays fabricated using this process are shown in figure 4.10, where we observe the facet of the array after cleaving, as well as a top inclined view showing a full structure including the injection and collection zones on figure 4.11.

4.3 Samples characterization

We now present some characterizations measurements performed on the fabricated samples, where we want to characterize the losses, the strength of the nonlinear processes through Second Harmonic Generation (SHG), and the transverse propagation of the photons at telecom wavelength.

4.3.1 Propagation Losses

The losses in the waveguide arrays are not easily accessible, and we cannot use the method presented in section 2.2.1.2, as the waveguide array supports several collective modes with different propagation constants. This yields a complex beating pattern that reduces the effective visibility of the Fabry-Pérot oscillations, as we change the wavelength of the transmitted laser. Figure 4.12 shows the result of a measurement of the transmitted power through a waveguide array, as a function of the laser wavelength. We observe that the oscillation does not present a sinusoidal shape, as we would expect from a monomodal system (see figure 2.3), making the method we used to measure losses in chapter 2 impractical. We can however measure the losses in a single waveguide, with a 2 μm width, coming from the same sample and placed next to the corresponding waveguide array, to estimate as well as possible the propagation losses from the fabrication process. The results of the measurement are presented in figure 4.13. Using the simulated reflection coefficients, we estimate the losses to be around 0.2 cm^{-1} for the TE-polarized guided mode and 1.2 cm^{-1} for the TM-polarized guided mode[2].

describe the flow of a gaz in clean room processes.

[2]We typically observe in our samples that the TE mode has less propagation losses than the TM mode, and the difference between the two increases when the waveguide width is reduced.

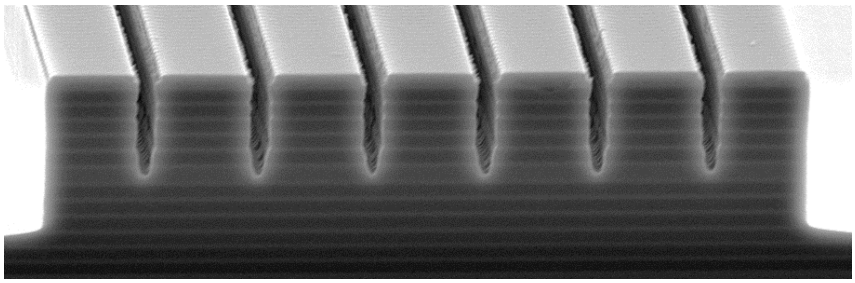

Figure 4.10: SEM image of a waveguide array fabricated using e-beam lithography and ICP etching.

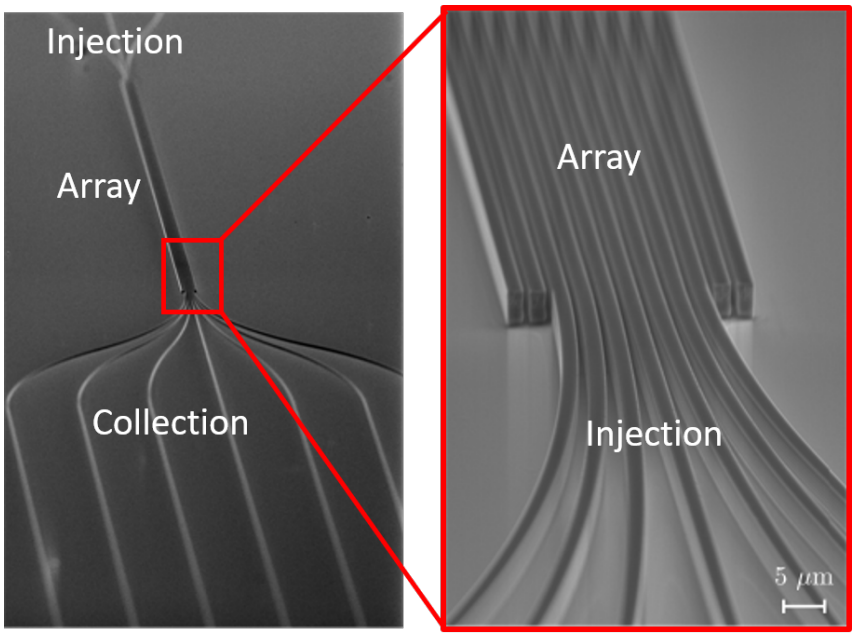

Figure 4.11: SEM image in top view of a waveguide array with injection, coupling and collection zones.

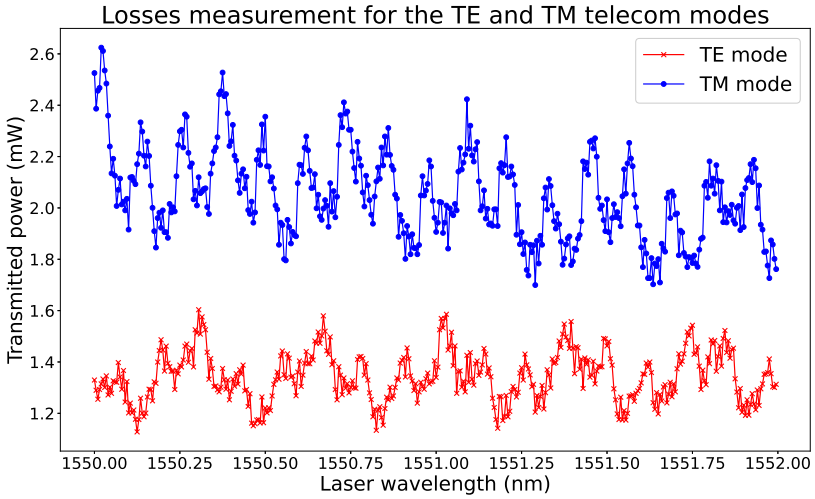

Figure 4.12: Results of the losses measurement on a waveguide array with 15 2 μm wide waveguides and a 600 nm gap, for the TE and TM fundamental modes at 1550 nm with an input power of 30 mW and a waveguide length of 3 mm.

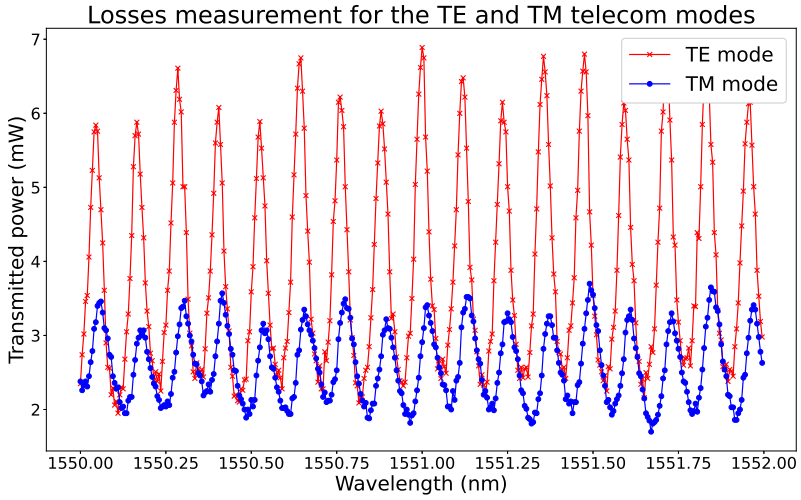

Figure 4.13: Results of the losses measurement on a single 2 μm wide waveguide, for the TE and TM fundamental modes at 1550 nm, with an input power of 30 mW and a waveguide length of 3 mm.

4.3.2 Second Harmonic Generation

Another characterization measurement that can be useful in our case is the Second Harmonic Generation (SHG) measurement, which allows to determine quickly by simply scanning the wavelength of a telecom laser the position of the nonlinear resonances (since the SHG is the reverse process of SPDC at degeneracy and involves the same phase-matching function) which will then be used for tuning the pump laser wavelength for the SPDC process.

The measurement is performed in the following way: a continuous-wave Tunics laser is amplified using an Erbium amplifier and injected in the waveguide array at telecom wavelength. The incoming telecom photons (around 1560 nm) are converted to visible photons (around 780 nm). We can measure the process for the different nonlinear interactions by changing the polarization of the incoming laser: TM for the type 0 SHG, TE for the type I SHG, and diagonal for type II SHG which requires both TM- and TE-polarized input fields (see section 1.1.4). The generated second harmonic signal is sent through a shortpass filter at 900 nm to filter out the telecom laser beam, and then sent to a photodiode to measure the output power. To increase the Signal-to-Noise Ratio (SNR) and the sensitivity of the measurement, we employ a synchronous detection scheme. A chopper, coupled to a lock-in amplifier, is added to the optical path, and the photodiode is connected to the lock-in amplifier to ensure we only take the periodic component of the signal determined by the frequency of the chopper.

We measure the Second Harmonic Generation (SHG) in a straight waveguide array from sample K7AD119-A3, which consists of 11 waveguides separated by 600 nm gaps and etched down to the core layer. The output power in the visible range is measured at the output of the waveguide array and the results of the measurement are shown in figure 4.14. We can see that the sample produces an SHG signal for a 45° input polarization, which indicates type II SHG, and for a TM input polarization, corresponding to type 0 SHG. We did not include the results for a TE polarized injected laser beam (type I), as there was no measurable output power in this case. This measurement serves as proof that the structure presents the nonlinearity necessary for type II and type 0 three-wave-mixing nonlinear processes that will later be exploited for SPDC generation in the arrays.

4.3.3 Transverse propagation in waveguide arrays

In order to characterize the transverse propagation in our waveguide arrays, and verify that there is effectively a good coupling between the waveguides, we inject a laser at 1550 nm at the input of the central waveguide of the array and image the output facet of the waveguide array using an infrared CCD camera. The results are shown on figure 4.15b in correspondence with the SEM image of the sample (figure 4.15a). Each lobe corresponds to the optical mode of one waveguide, and the extended light distribution shows that the light, initially localized in the central waveguide ($n = 0$), has effectively propagated throughout the whole waveguide array by experiencing discrete diffraction (figure 3.3), with a longitudinal propagation length of 7 mm. This measurement, although purely classical, indicates that the coupling in our waveguide arrays will be sufficient to make the photons undergo several ”steps” of transverse propagation, which is a necessary condition to generate spatial entanglement from cascaded quantum random walks of SPDC photon

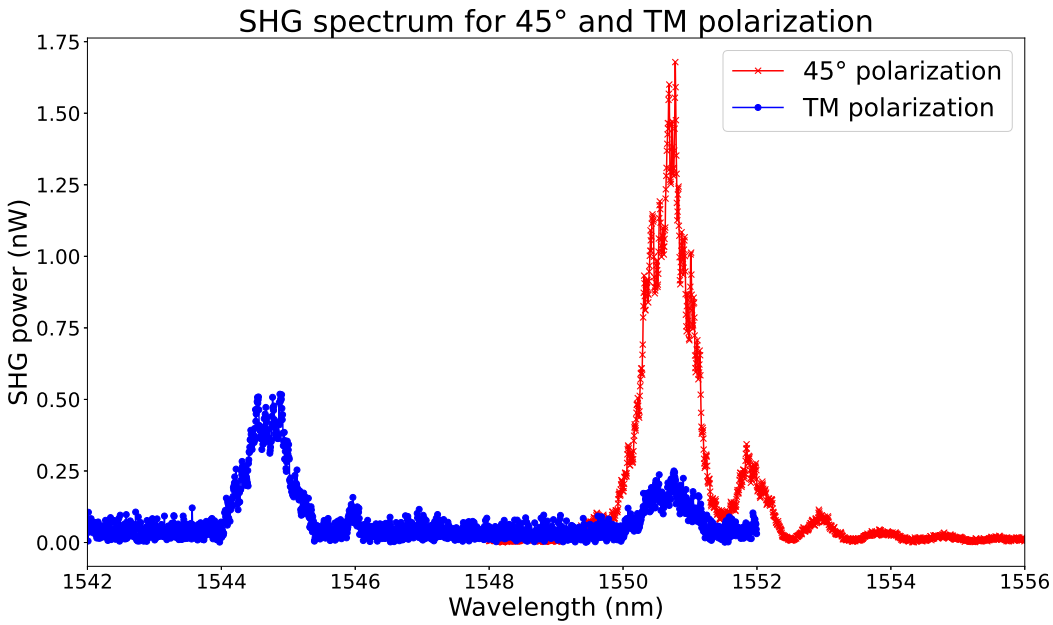

Figure 4.14: SHG power measured in a waveguide array of 11 2 μm wide waveguides, with a 600 nm gap, for a laser at telecom wavelength injected with a 45° diagonal polarization and with a TM polarization. The injection power is 30 mW.

pairs. Here the light intensity travels in a significant manner up to at least 6 sites from the central waveguide.

We additionally imaged the output facet of the waveguide array while injecting a laser at 775 nm instead (figure 4.15c). It is visible that the Bragg mode in the visible wavelength propagates much less than the telecom mode, confirming that the experimental conditions are compatible with the hypothesis that the coupling constant for the pump mode is greatly smaller than the coupling constant of the telecom modes.

The performed characterizations (losses, SHG and efficient transverse propagation) allow to check the good quality of the samples on which quantum measurements can then be performed, as we detail in the next chapter.

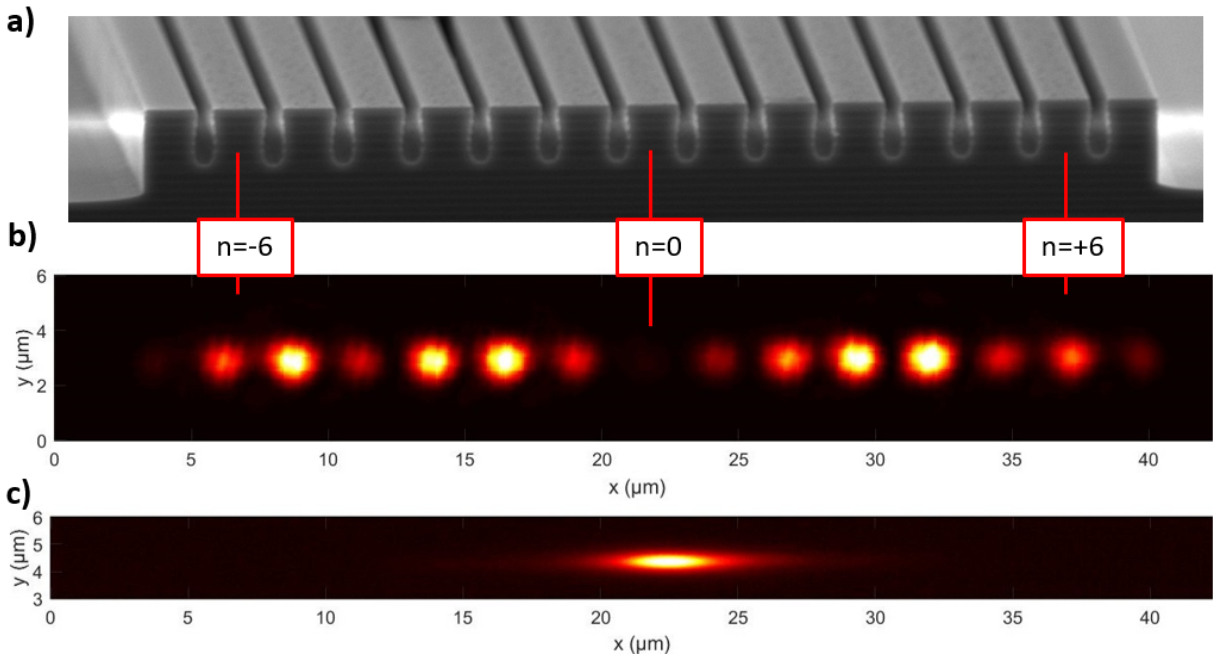

Figure 4.15: a) SEM image of a waveguide array, superimposed with b) infrared CCD image of the spatial distribution of the power at the output after injection of a laser beam at 1550 nm in one input waveguide, labeled $n = 0$, and c) after injection of a laser beam at 775 nm in one input waveguide. The telecom light is spread across multiple waveguides in the array, indicating that the coupling constant in the array is sufficient for the photons to travel several waveguides away from their starting waveguide during the propagation length, while the visible light around 775 nm stays well confined in its input waveguide.

Chapter 5

Experimental realization of spatially entangled states in AlGaAs waveguide arrays

In this chapter, we describe the experimental measurements made on the waveguide arrays whose fabrication was described in the previous chapter. We first present the experimental set-up and the method for the measurement of spatial intensity correlations through a coincidence scheme, and then present the experimental results demonstrating the on-chip generation of spatially entangled photon pairs.

Contents

5.1 Detailed experimental set-up and methods

5.1.1 Principle of the experiment and instrumentation

In this experiment, we are interested in the measurement of the spatial correlations of photon pairs produced by SPDC in a nonlinear waveguide array. A way to quantify these correlations is to measure the two-photon coincidence rates between all pairs of waveguides, which will give a quantity proportional to the spatial correlation function Γ_{n_s,n_i} (equation 3.31). Thus we have to be able to measure the coincidences between the different output waveguides (interguide coincidences) as well as within each waveguide (intraguide coincidences).

A scheme of the experiment is presented in figure 5.1. Here, we pump one waveguide of the array using a continuous-wave Toptica laser, operating in the visible range (around 780 nm) with a narrow spectral width of $\simeq$ 100kHz (or 1.3 fm) and thus placing us in experimental conditions compatible with the numerical simulations assuming a monochromatic pump beam. The pump power employed is approximately of 30 mW, measured in free space before the injection, for all the SPDC measurements performed. We use a microscope objective (x60, NA = 0.95) to properly focus the pump beam into the input waveguide of the sample, after a half-waveplate and a polarizer to control the polarization of the pump beam. SPDC photon pairs are generated inside the array and undergo correlated quantum random walks as they propagate. To measure the spatial intensity correlation between two different waveguides, we select a pair of waveguides and collect the output photons to send them to Superconducting Nanowires Single Photon Detectors (SNSPDs), which we connect to a Swabian TimeTagger Ultra to record the time of arrival of the photons, with time bins of 80 ps. We then proceed to a start-stop coincidence measurement[1] by selecting a specific time window for the relative arrival times of the photon pair. Here, in contrast to chapter 2, we do not use a trigger for the coincidence measurement since the pump is continuously generating photon pairs.

Let us first consider the measurement of the intraguide coincidences in waveguide n (i.e. the $\Gamma_{n,n}$). For this we simply connect the output waveguide n to a beamsplitter, connect each output port to an SNSPD, and perform a coincidence measurement on these

[1]The majority of accidental coincidences comes from the detection of a single photon from a pair (where the second photon has been lost or undetected) with a noise photon, that can come from the pump, the luminescence, the multi-pair generation or the dark counts of the detectors.

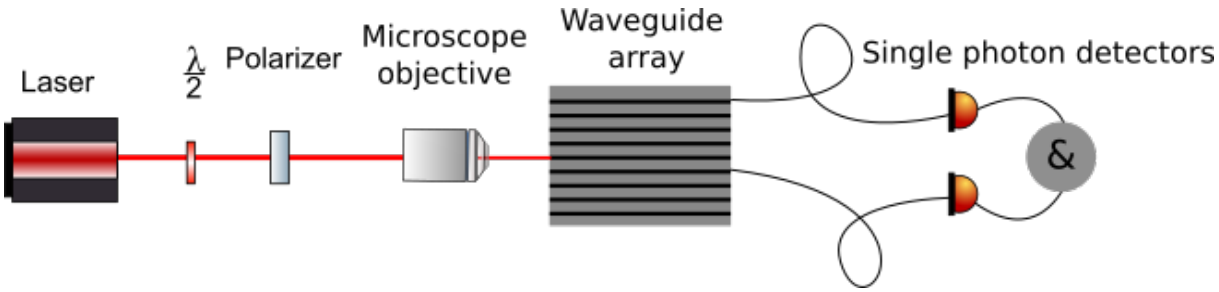

Figure 5.1: Simplified scheme of the SPDC experiment in a waveguide array: the waveguide array is pumped with a continuous wave laser, and we measure the coincidences between two waveguides for the photon pairs produced by SPDC inside the waveguide array. The half-waveplate and the polarizer allow to choose the polarization of the pump beam.

two detectors. A typical result is shown in figure 5.2. We can see that the coincidences are mainly located in a narrow time window, mainly determined by the jitter of the detectors (approximately 90 ps) and by the resolution of the TimeTagger (42 ps)[2], which we can use as our selection window for the coincidences and use the rest of the time bins to quantify the noise in the experiment. The measured raw coincidence rate is here 65 Hz, with a Coincidence to Accidental Ratio (CAR) of 316.

5.1.2 Measurement of interguide correlations

We now turn to the measurement of correlations between two different output waveguides (interguide correlations). The experimental challenge in this case is the simultaneous measurement and alignment of two output waveguides for photon detection. Here we present two different schemes that we have experimentally investigated, with their respective advantages and drawbacks.

5.1.2.1 Scheme for the simultaneous measurement of the interguide correlations

We first describe a scheme for the simultaneous measurement of all the elements of the correlations matrix, which would allow for a short integration time for the detection of the coincidences. To realize this, every waveguide of the waveguide array must have its output connected to a single-photon detector. In order to do this, we connected the output waveguides to a lensed fiber array, which allowed to connect each waveguide to a fibered channel that can simply be sent towards the detectors. The lensed fiber array consists of a set of Single-Mode Fibers equally spaced with the same orientation, with microlenses at the end of the fibers that allow to properly match the mode-field diameter of the output waveguides with the mode-field diameter of the fibers. The fiber array we used was made by Vanguard, had a 127 μm pitch and a 2 μm mode-field diameter. The procedure for the alignment of fiber arrays can be quite complex, since one has to simultaneously overlap the modes of numerous fibers and waveguides in a efficient manner. The alignment of one lensed fiber to one waveguide usually requires five alignment parameters: three

[2]In all measurements, the bandwidth of the photons is greater than 1 nm, corresponding to a coherence time of 2 ps; so the coherence time of the photons is negligible compared to the detection jitters.

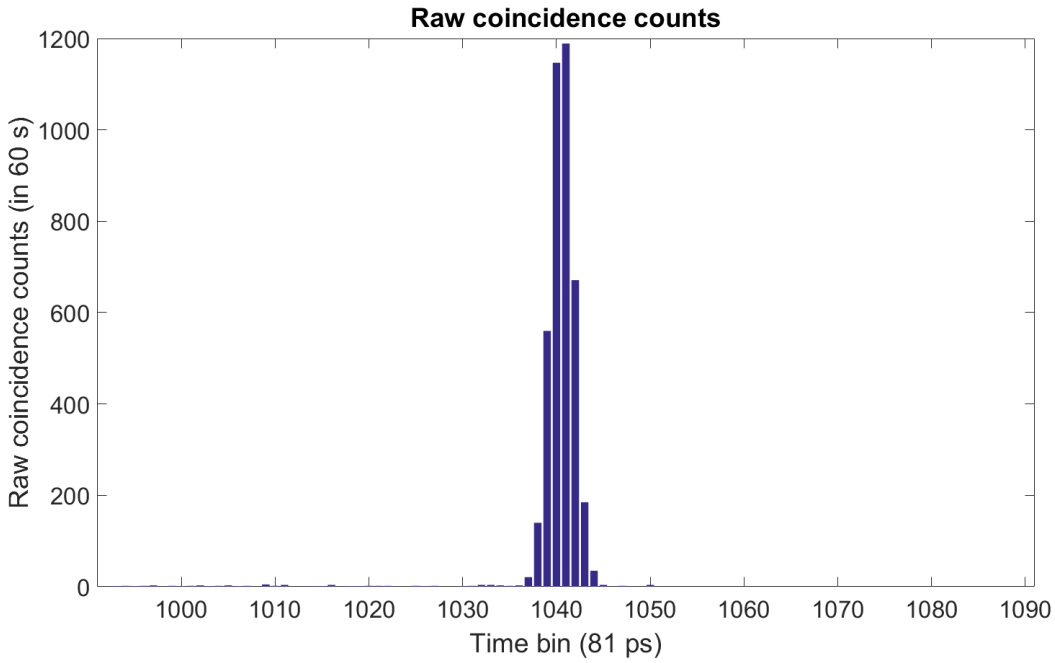

Figure 5.2: Results of a raw intraguide coincidence measurement inside one waveguide of an array, for a 60s integration time. Here the coincidences are concentrated in a 6 bins window, with a CAR of 315.

translational degrees of freedom for the relative position of the fiber to the waveguide, and two rotational degrees of freedom for the alignment of the propagation directions. Note that in the case of only one fiber, since the problem is invariant by rotation around the optical axis, this rotation does not affect the efficient coupling of the fiber and the waveguide. In the case of the fiber array, however, this rotation needs to be aligned as well to allow the fibers to be simultaneously aligned with all waveguides.

The alignment procedure that we developed goes as follows: we define three axes, the optical axis x, horizontal, defined by the direction of the pump beam and corresponding to the propagation axis of the photons, the horizontal perpendicular axis y, and the vertical axis z (figure 5.3).

The alignment around the y-axis is ensured by making the optical axis as horizontal as possible, and using a flat horizontal platform as a support for the fibered array. The sample is first aligned along the x-axis using the reflection of a laser beam on the cleaved facet by rotating the sample support around the y and z axes, ensuring that the facet is orthogonal to the optical axis. We then use a 5-axes Newport manual alignment stage to align the fiber array while keeping the sample fixed, with rotations around the x and z axes and translations on all three axes. We first visually align for the rotation around the z-axis using a binocular, and placing the fiber array along the facet of the sample. In our case, it is hard to use the transmitted power through the array to align this angle, since the working distance is very low for the lenses of the fibers ($\simeq 10$ μm) and this rotation can make some of the fibers crash against the facet of the sample and damage it. We then align the translational degrees of freedom along x, y and z by injecting a Tunics laser at telecom wavelength (1550 nm) into the central fiber of the fiber array and coupling it into the central waveguide of the waveguide array, and maximizing the output power on

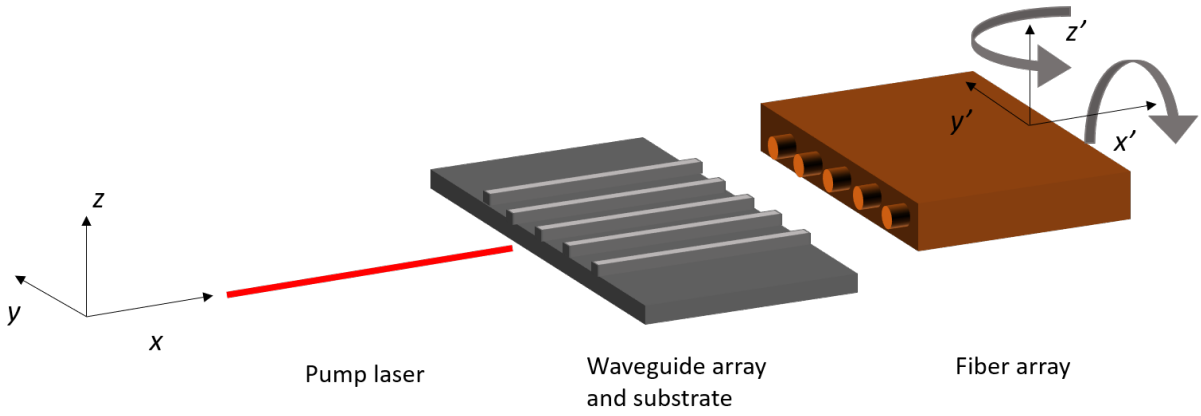

Figure 5.3: Sketch of the alignment of the fiber array with respect to the waveguide array.

the other side of the sample. Finally, to align the rotation around the x-axis, we identify the rotation axis of the manual alignment stages x'. We align the central fiber with the central waveguide, then align the farthest waveguide with the farthest fiber from the x' axis using only the rotational degree of freedom then align the closest waveguide with the closest fiber to the x' axis using translation along z, and repeat this method until we reach convergence on the alignment with the waveguide array (in our case, we considered the alignment satisfactory if the transmitted power through the waveguide array for the two extreme fibers was simultaneously 90% of the maximum power or higher).

The pump beam is injected on the other side of the sample, measuring the output power at 775 nm at the output of the fiber array to ensure a good alignment on the injection side of the experiment.

We can then connect every fiber to a single-photon detector, and perform a simultaneous coincidence measurement on all the waveguide pairs by recording the arrival times of photons on each detector using the time tagger, and then compute the coincidence histograms for every single pair of waveguides. To reduce noise stemming from the residual pump photons and luminescence, we add in the output arms bandpass filters around 1560 nm. We also add a fibered polarization controller to optimize the arrival polarization of the photons on the detectors, since the detection efficiency is polarization-dependent. To measure the diagonal matrix elements $\Gamma_{n,n}$ and the corresponding coincidences, we can use a fibered beamsplitter on any fiber at the output of the fiber array, send the two output ports of the beamsplitter to the single-photon detectors and measure the histogram of coincidences to get the intraguide coincidence rate.

This method has the advantage of allowing for a fast measurement of the correlation matrix, while aligning the pump beam only once, ensuring that the measurement for all of the matrix elements is always done in the same conditions. To give an idea of the improvement in measurement time, let us note that to measure a complete correlation matrix for N guides, one has to measure the diagonal, which is N points, and then $\frac{N^2-N}{2}$ for the rest of the points, with the division by two because $\Gamma_{n_s,n_i} = \Gamma_{n_i,n_s}$. This requires $\frac{N(N+1)}{2}$ measurements if done separately on each matrix point, i.e. a quadratic scaling of the measurement time with the number of waveguides. By contrast, using a fiber array the whole correlation matrix can be measured in a single acquisition with $2N$ detectors, or 3 acquisitions with N detectors. When implementing this fiber-array

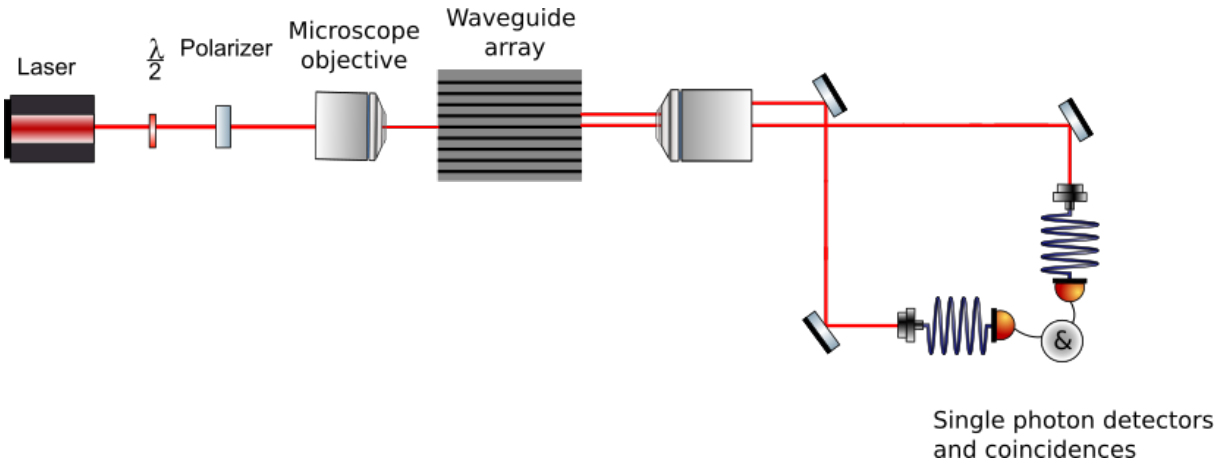

Figure 5.4: Simplified experimental set-up for the measurement of interguide correlations in free space using collimators.

based technique, a practical difficulty that we encountered, however, is that it is more sensitive to luminescence and pump noise, both guided and in free space, than when collecting with a microscope objective. Indeed, because of the very short working distance between the microlenses of the fibers and the facet of the sample (10 μm), the spectral and spatial selectivity is reduced compared to a technique based on collection with an objective and collimation of the free-space beam (after tens of centimeters of optical path) into single-mode fibers. Hence a heavier spectral filtering is needed. In addition, our first experimental implementation was complicated by a more circumstantial difficulty, namely the fact that the collection efficiency of the commercial fiber array that we used, which we measured to be of the order of 10%, turned out to be much lower than the specifications. We ordered a new fiber array (with longer working distance) but in the meantime, we resorted to free-space measurements, as described in the next paragraph. We plan however to come back to the fiber array technique as soon as possible, as it provides a very interesting scaling in view of measuring high-dimensional entangled states.

5.1.2.2 Free-space measurement of the correlation matrix

In this paragraph, we describe the measurement of spatial intensity correlations in our waveguide array in free space using a microscope objective. By focusing the objective on the facet of the sample, the outgoing photons from each waveguide can be spatially separated and coupled to different fiber collimators to be sent to different single-photon detectors.

The experimental set-up used for this measurement is depicted in figure 5.4. The injection scheme is the same, with the pump beam being focused on the input facet of the array. The SPDC photons are then collected through a microscope objective and a mirror is used to reflect one of them in an orthogonal direction, before being collimated into single-mode fibers connected to SNSPDs.

In order to properly collect the photons in the collimators and to correctly align the corresponding optical paths, we proceed in the following way: we inject a telecom wavelength laser beam into the central waveguide of our waveguide array. Using the transmitted power which is spread over all waveguides because of the coupling in the array,

one can identify the beams transmitted by the different waveguides, for instance using an infrared card to visualize the spots formed by the transmitted light. The transmission paths for two adjacent waveguide are separated by a distance of the order of 5 mm a few centimeters after the objective, making it possible to distinguish two waveguides. We then choose the first waveguide number n_s that we want to measure, and align the corresponding transmitted light with a fibered collimator by maximizing the power at the output using the alignment of the two transmission mirrors in figure 5.4. We then select the second waveguide number n_i, and reflect the corresponding spot on two mirrors to couple it to a second fibered collimator, using the same alignment procedure to ensure efficient collection of the photons through the collimator. We also place free-space longpass filters on the paths of the photons to ensure proper filtering of the residual pump and luminescence photons. The spatial and spectral selectivity in this case is excellent [3], so that only one filter with 40 dB rejection is sufficient in each arm. The collection efficiency is estimated to be 0.7 for the microscope objective, 0.5 for the collimators, and 0.8 for the filters, making the total collection efficiency for each arm 0.28, i.e. 5.5 dB of losses.

We then switch back to pumping the central waveguide at 775 nm. To ensure the pump is properly aligned, we measure the output power in free space after the microscope objective and maximize it in the central waveguide. We then measure the SPDC photons coincidences between the two detectors coupled to waveguides n_s and n_i, giving Γ_{n_s,n_i}. Note that, as previously, to measure the diagonal matrix elements Γ_{n_s,n_s}, we can connect a beamsplitter to the collimator coupled to waveguide n_s and measure the coincidences between the two output arms of the beamsplitter. In order to minimize the alignment procedure for each measurement, we fix the waveguide number n_s and measure every corresponding (n_s, n_i) matrix element, which allows to only align one arm of the collection path at a time to change n_i while keeping the same alignment for the collimator coupled to waveguide n_s before switching to the following waveguide $n_s + 1$.

This measurement method is more time-consuming, since it requires multiple alignments to measure the intensity correlation matrix. However, it gave better signal levels and better CARs than the fiber array method in its current state, and thus we chose to use it in the following measurements to characterize the spatial intensity correlations.

5.2 Experimental measurement and data analysis

In this section, we present the experimental realization and measurements of spatially entangled photon pairs generated by SPDC in the waveguide arrays, and discuss their interpretation in terms of non-classicality of the state. The measured photon pairs were produced using type II SPDC with a TE-polarized pump, since the signal was the strongest for this interaction.

[3] The longer path for the photons ensures the divergence of the modes for which the set-up is not aligned and focused, thus reducing the accidental coincidences.

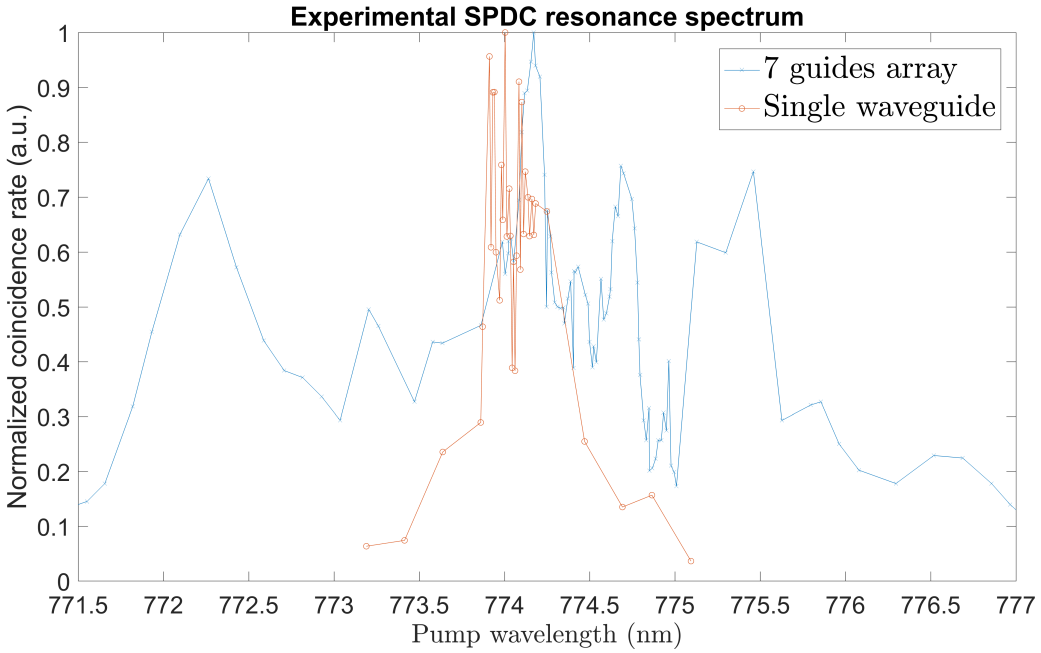

Figure 5.5: Experimentally measured SPDC resonance spectrum, in an array of 7 waveguides (blue points) and in a single waveguide (red points), normalized.

5.2.1 Results

5.2.1.1 Measurement of the SPDC resonance spectrum

This paragraph first presents the measurement of the SPDC efficiency in a waveguide array as a function of the pump wavelength, experimentally highlighting the enlargement effect mentioned in paragraph 3.2.1.3.

We first measured the SPDC in a straight array of waveguides, without collection or injection zones. These structures are convenient to use for this type of measurement because since they are very compact, one can collect the output of all waveguides in a single collimator with the use of a single microscope objective, allowing to get the total coincidence rate of the SPDC photons (i.e. the sum over all matrix elements $\Gamma_{tot} = \sum_{n_s,n_i} \Gamma_{n_s,n_i}$). The coincidence measurement was realized in free space, using a microscope objective, on a waveguide array[4] consisting of 7 waveguides, 2 μm wide, 6 mm long and with a 500 nm gap between them, and using a longpass filter with a 1400 nm cutoff. Figure 5.5 shows the measured raw coincidence rate as a function of the pump wavelength (blue points), along with a similar measurement realized on a single 2 μm wide waveguide (red points). One can observe that the full width at half maximum is around 3.7 nm, while for a single waveguide the FWHM is 0.3 nm, providing a clear experimental confirmation of the enlargement of the SPDC efficiency from the coupling between the waveguides (paragraph 3.2.1.3). We can also observe that the SPDC spectrum presents several peaks, highlighting the presence of a discrete number of collective modes involved in SPDC for the signal and idler photons[5].

[4]Sample K7AD119-A1.

[5]In the limit of an infinite array, the spectrum becomes smooth (see figure 3.6)

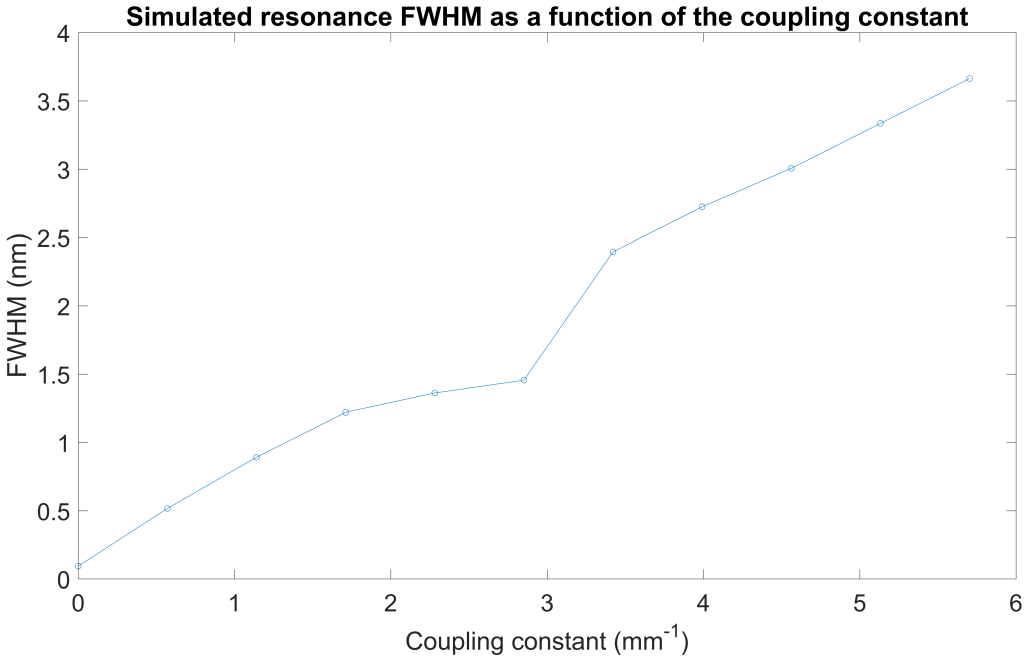

Figure 5.6: Simulation of the FWHM of the SPDC resonance spectrum for a 6 mm-long array consisting of 7 waveguides, with a 320 nm spectral filtering width, as a function of the coupling constant for the TE-polarized telecom mode.

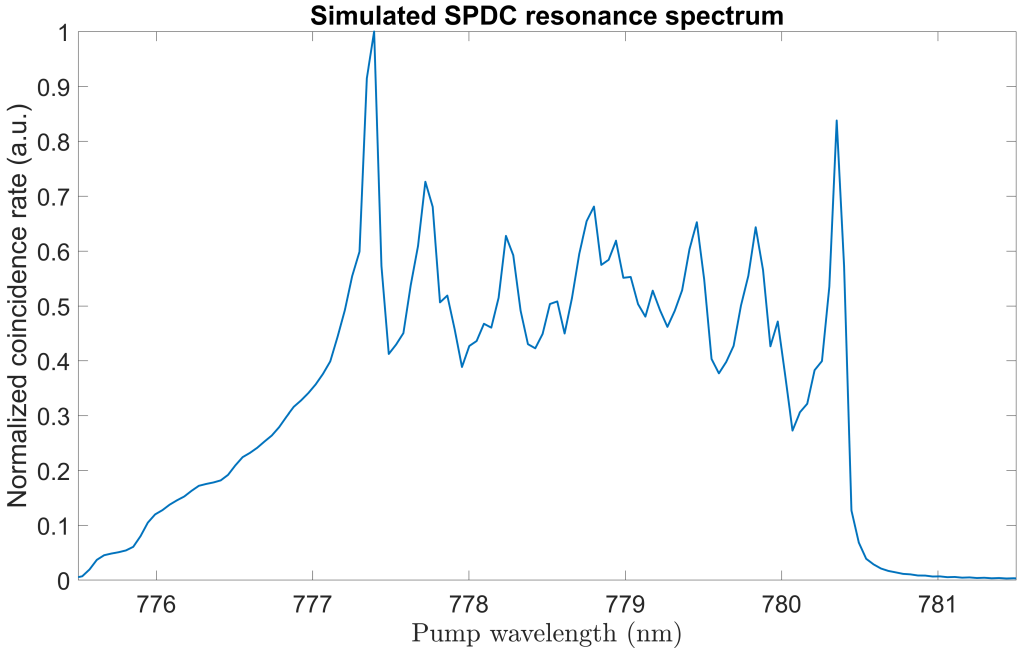

Figure 5.7: Simulation of the SPDC resonance spectrum (i.e. the total coincidence rate $\Gamma_{tot} = \sum_{n_s,n_i} \Gamma_{n_s,n_i}$) for an array consisting of 7 waveguides, with a 320 nm spectral filtering width.

We can simulate the type II SPDC resonance spectrum for a finite array with 7 waveguides and compare it with these experimental results, for instance using the width of the resonance to estimate the actual value of the coupling constant. We present in figure 5.6 the results of the simulation for the width of the resonance as a function of the coupling constant, considering a 320 nm spectral bandwidth for the SPDC photons as in the experiment[6]. As expected, the width of the resonance increases with the coupling constant[7], as the latter governs the dispersion of the collective modes. Comparing the experimental FWHM of the resonance to the simulation yields an estimated coupling constant of $C \simeq 4.8$ mm^{-1}, corresponding to a coupling length $L_c \simeq 330$ μm. This value is in good agreement (within 15%) with the coupling length determined from electromagnetic simulations using the nominal parameters of the structure. Figure 5.7 shows the result of the full SPDC resonance spectrum simulated using the estimated coupling constant. Except for a slight shift in the central wavelength (likely due to a small deviation of the actual epitaxial structure from the nominal one), the overall multi-peaked shape is in good qualitative agreement with the experiment.

We also measured the SPDC resonance spectrum for another waveguide array[8], this time presenting injection and collection zones. The injection, coupling and collection zones are each approximately 2 mm long and the waveguides are 2 μm wide with a 650 nm gap. We measure coincidences at the output of the central waveguide ($\Gamma_{0,0}$), where the pump is injected, and at the first diagonal and antidiagonal points of the intensity correlation matrix $\Gamma_{1,1}$ and $\Gamma_{1,-1}$. The results are presented in figure 5.8 for the central waveguide (blue), diagonal (red) and antidiagonal (yellow). This time, the used filter was a longpass filter with a 1500 nm cutoff, giving a spectral width of $\simeq$ 120 nm for the measured biphoton state.

In this case, we see that SPDC is most efficient around 779.43 nm, which corresponds in this sample to generation in the coupling zone where the waveguides are 2 μm wide. The measurement of the spectrum over the diagonal and antidiagonal serves to determine the optimal pumping wavelength for the generation of spatially entangled photon pairs, as the pump wavelength induces resonant effects on the spatial correlations (section 3.2.1.5).

We can additionally observe that the FWHM of the resonance peak for the waveguide array is this time reduced to $\Delta\lambda \simeq 1$ nm, showing that the resonance is narrower than what was obtained previously when measuring the total coincidence rate $\sum_{n_s,n_i} \Gamma_{n_s,n_i}$ (figure 5.5). We verified however that it is consistent with numerical simulations of coincidences within a single waveguide for this filtering bandwidth, which results in a narrowing of the spectral resonance.

5.2.1.2 Measurement of the correlation matrix

We now present the result of the measurement of the correlation matrix for the last sample presented, with injection and coupling zones. We chose a pump wavelength of $\lambda_p = 779.430$ nm, corresponding to the maximum of the diagonal and off-diagonal correlations (figure 5.8).

[6]The degeneracy wavelength is around 1560 nm, and we use longpass filters with a 1400 nm cutoff.

[7]Here the shape of the FWHM versus C shows irregularities around $C = 2.5\text{mm}^{-1}$, which stem from the complex multi-peaked structure of the SPDC spectrum of the finite array, unlike the case of an infinite array (figure 3.6), yielding an almost linear increase of the resonance width with C.

[8]From sample K7AD119-A7.

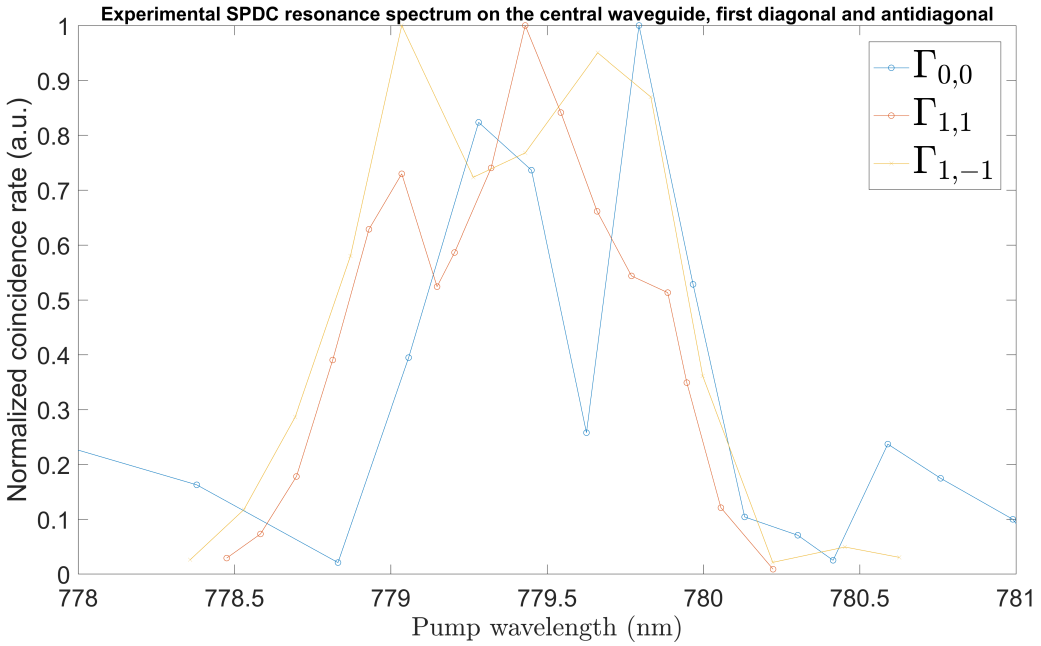

Figure 5.8: Central ($\Gamma_{0,0}$), first diagonal ($\Gamma_{1,1}$) and first antidiagonal ($\Gamma_{-1,1}$) coincidence rates as a function of the pump wavelength, normalized, in an array with 11 waveguides and 120 nm filtering width.

To realize the measurement, we employ the method given in the previous section for the free-space measurement of the coincidences, by coupling simultaneously two output waveguides to two collimators connected to single-photon detectors. The microscope objective that we use for the collection of the SPDC photons, with a 0.65 aperture and a 40× image enlargement, allows to simultaneously collect 5 output waveguides. Thus, we focus on the measurement of the central part of the correlation matrix (the structure consists of 11 coupled waveguides in total, of which we measure the central 5). To measure the diagonal points of the intensity correlation matrix Γ_{n_s,n_s}, we additionally use a polarizing beam splitter (PBS) with its two output ports connected to two detectors, and a fiber polarization controller before its input port to correctly adjust the splitting of the photons, so that the TE-polarized photons always go into one arm and the TM-polarized ones in the other, which we realize experimentally by maximizing the coincidence rate.

The waveguide array was pumped with 30 mW CW external pump power (measured before the injection objective, and corresponding to an estimated internal pump power of 1 mW)[9] at 779.430 nm. When aligning the measurement, we also measured the transmission through the waveguide array at 1560 nm by injecting laser light through the collection collimators (i.e. in the reverse direction of the experiment) to quantify the collection efficiency and normalize the corresponding coincidences. This ensures that the quality of the different collection waveguides and the collection efficiency from the specific alignment does not affect the measured correlations. We used two longpass filters with a 1500 nm cutoff before the collection collimators to filter out the pump noise and

[9]The internal pump power is limited by the overlap of the Gaussian free-space pump mode with the Bragg mode (see figures 1.7c and 1.7d).

n_s/n_i	Normalized coincidence rate (120 nm width) (Hz)	CAR	Normalized coincidence rate (40 nm width) (Hz)	CAR
0/0	563.31	38.1	249.01	37.7
0/1	30.47	2.8	15.90	9.1
0/2	29.60	2.8	15.29	8
0/-1	22.46	4	14.25	15.5
0/-2	22.72	11.6	5.36	20.4
1/1	142.57	315.9	51.26	603
1/2	101.23	16.2	36.09	36.9
1/-1	119.87	66.4	29.33	101.1
1/-2	52.61	35.3	33.24	89.5
2/2	90.80	111.4	15.10	45.2
2/-1	28.16	23.9	15.64	41.4
2/-2	75.57	51.7	24.65	93.5
-1/-1	152.52	480.6	49.46	562.1
-1/-2	39.10	101.6	13.94	172.8
-2/-2	115.49	343.1	18.00	225.8

Table 5.1: Table of the coincidence measurement results

reduce the spectral width of the state. Note that, in this case, the state has a spectral width of 120 nm, which according to the simulations gives a purity of 0.5 for the reduced spatial density matrix, meaning that the measured state is mixed. The normalized coincidence rates, and the corresponding Coincidence to Accidental Ratios are given in table 5.1 (second and third columns). The normalized coincidence rate is computed in the following way: defining $T(n)$ as the total collection efficiency through waveguide n and $R^m_{n_s,n_i}$ the measured raw coincidence rate, the normalized coincidence rate is defined as $R_{n_s,n_i} = R^m_{n_s,n_i} \frac{\max_n(T(n))^2}{T(n_s)T(n_i)}$. The measurement was also performed using additional fibered bandpass filters between the collimators and the detectors, to restrict the spectral width of the measured state to roughly 40 nm, for which the expected purity is approximately 95% according to numerical simulations. The results are presented in the right part of table 5.1.

The total measured raw coincidence rate (summed over all matrix elements) is 447 Hz for the 120 nm bandwidth measurement, and 162 Hz for the 40 nm bandwidth measurement. Note that this is not the exact total coincidence rate generated by the array, since only 5 waveguides were measured, but it is a close approximate since most of the coincidences are expected to be located near the center of the correlation matrix. We can observe that reducing the spectral filtering width to a third of its initial value almost divides the total coincidences threefold, confirming that the signal and idler wavelength distribution is spread over a large spectral range (in agreement with the simulations presented in figure 3.7a).

The results are presented in a graphical manner in figures 5.9a (120 nm state) and 5.9b (40 nm state), with a comparison to the corresponding simulated spatial intensity correlations (5.9c and 5.9d). We can observe that, in agreement with the simulations, the correlations are mainly located on the diagonal and antidiagonal points of the matrix. For the state with 40 nm filtering, the antidiagonal points are less intense, which might

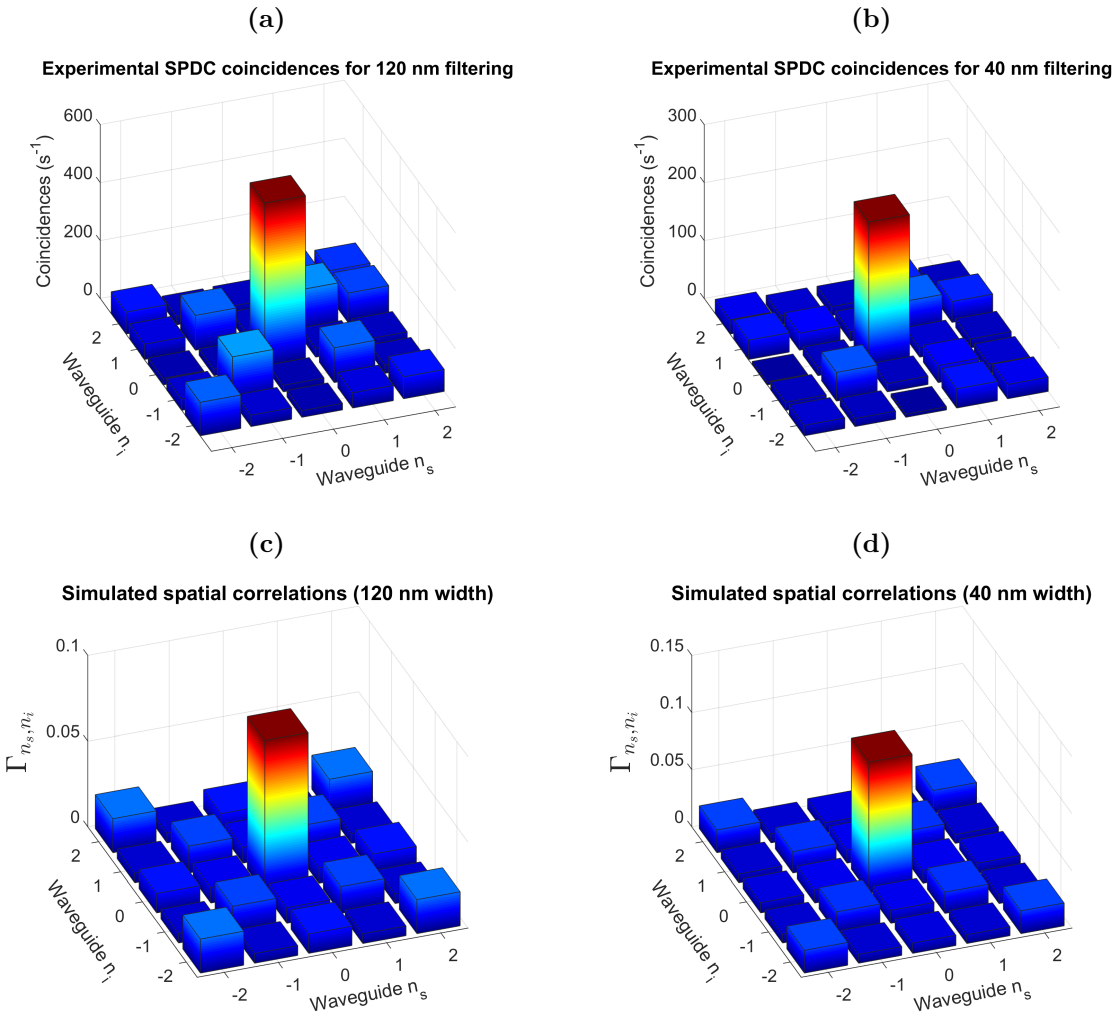

Figure 5.9: a) Measured and c) simulated intensity correlation matrices for filtering with a 120 nm bandwidth, and b) measured and d) simulated intensity correlation matrices for filtering with a 40 nm bandwidth.

be stemming from a drift of the alignment during the measurement.

An interesting parameter for the comparison with the simulation is the non-classicality indicator I_{NC} (equation 3.40), which we expect to be high for a state with intensity correlations located mainly along the diagonal and antidiagonal points of the matrix. We compute the experimental value of this indicator for every point of the intensity correlation matrix, and present the results in figure 5.10a for the 120 nm state and 5.10b for the 40 nm state, in comparison with the corresponding numerical simulations in 5.10c and 5.10d. The criterion is experimentally violated by up to 60 standard deviations on the off-diagonal central points for the 120 nm wide state, and by 28 standard deviations on the same points for the 40 nm wide state. The spatial shape of the violation matrix is consistent with the simulations, and presents strong indication that the generated spatial correlations present important non-classical features.

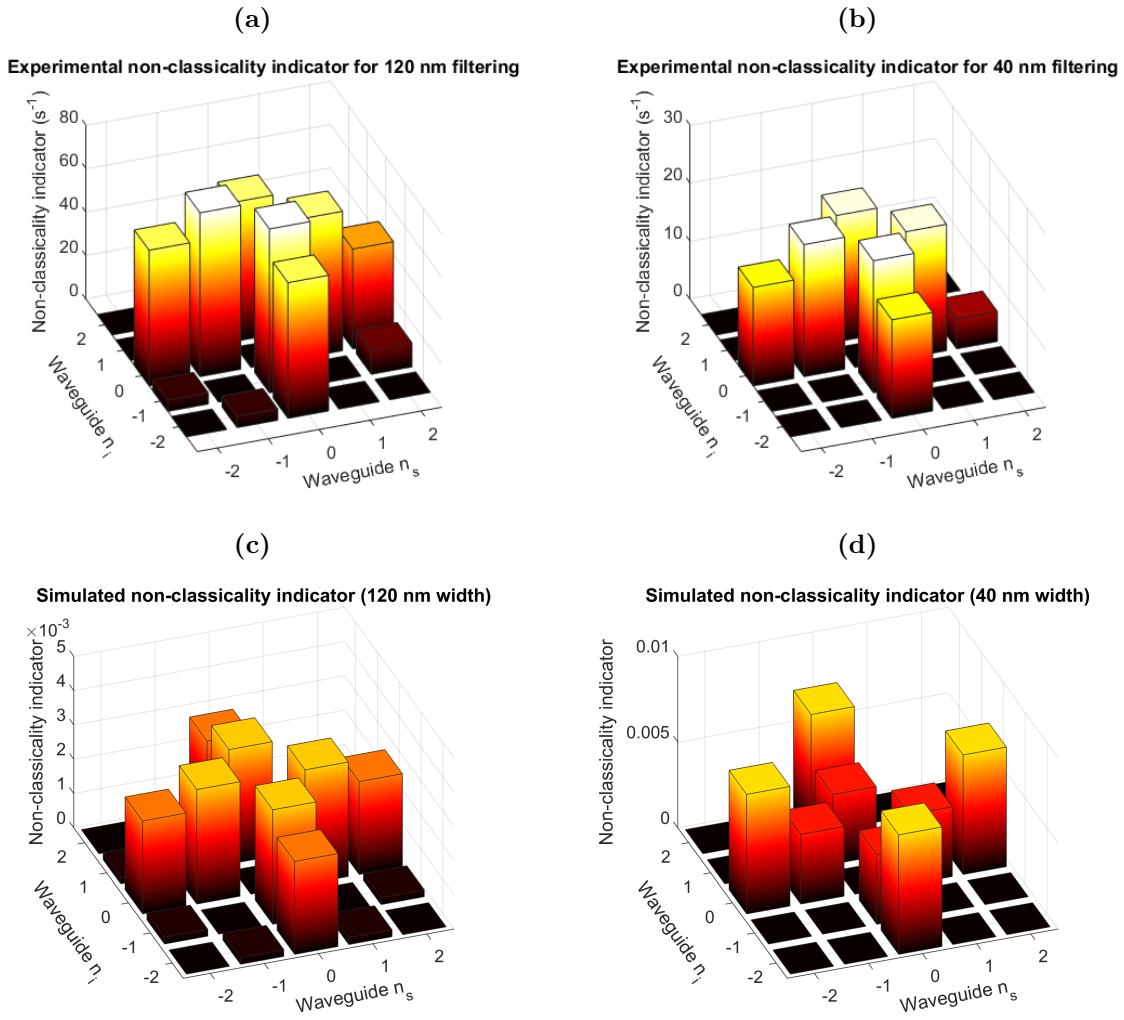

Figure 5.10: a) Measured and c) simulated non-classicality indicator for filtering with a 120 nm bandwidth, and b) measured and d) simulated non-classicality indicator for filtering with a 40 nm bandwidth.

5.2.2 Perspectives on further measurements

The results presented in this chapter provide a first experimental demonstration for the use of AlGaAs waveguide arrays as a support for the generation of entanglement in the spatial degree of freedom for photon pairs, that can trigger further developments in the generation of this type of photonic quantum states. Additionally, the waveguide array platform itself can serve as a simulation of tight-binding Hamiltonians for electrons in condensed matter systems as already mentioned in chapter 3. Here, we present two axes for further developments of the experiments.

5.2.2.1 Reconfigurable generation of spatially entangled photon pairs

As discussed in section 3.2.1.6, it is possible to use tailoring of the spatial distribution of the pump beam to generate spatial entanglement in a reconfigurable way. The experiment can be improved in this direction, by coherently pumping several waveguides in a controllable manner and tuning the wavelength and polarization of the pump to implement type 0 SPDC.

In order to implement the control of spatial correlations, the simplest possible scheme consists in the splitting of the pump beam for injection in two different guides, with a controllable phase-shifter in one path to control the relative phase of the two injected beams. The splitting can be realized in free space and the split paths properly aligned using mirrors to ensure proper injections in the desired waveguide, taking care of the thermal and mechanical stability of the two optical paths. This would allow to selectively enhance either the bunching or antibunching components of the spatial correlations, as detailed in section 3.2.1.6.

In order to implement more complex state control, the pump beam can also be split using and $N-$fiber splitter and sent to a fiber array. Each arm of the fiber array can be individually equipped with a controllable phase-shifter and a variable attenuator in order to achieve complete control over the spatial distribution of the pump laser at the input of the waveguide array[10]. This is expected to allow for the generation of a wide zoology of spatially entangled states, as described in section 3.2.1.6. Finally, the multimode character of the generated spatial states can be increased by fabricating samples with stronger coupling between the waveguides, leading to enhanced transverse propagation of the photons in the array.

Overall, these experimental developments would lead to a compact and reconfigurable source of spatially entangled states, operating at room temperature and telecom wavelength, that can serve for the implementation of quantum information protocols.

5.2.2.2 Quantum simulation of controllable tight-binding Hamiltonians

The second perspective that we present here is the use of waveguide arrays as a platform for quantum simulations, in particular of condensed matter-type problems. Indeed, as discussed in section 3.1.1.2, the transverse propagation of light in a waveguide array can be modeled by a tight-binding Hamiltonian, in direct analogy with electrons on an atomic chain or in a crystal, with the propagation direction playing the role of an effective time.

[10] In the long term, this pump control stage could be implemented on-chip by using integrated splitters and phase-shifters.

As described by equation 3.23, the tight-binding Hamiltonian is determined by the on-site energies (which are mapped to the propagation constants of the waveguides in the case of the waveguide array) and the coupling between the sites (mapped to the evanescent coupling between the waveguides). The on-site energies can be controlled through the modal refractive index of each waveguide, e.g. by individually varying the width of the waveguides, while the coupling constants can be controlled through the distances between the waveguides. Both parameters can be engineered at the fabrication stage through the design of the waveguide array, resulting in a static control over the simulated Hamiltonian. Dynamic control could also be achieved by using the strong electro-optic effect of AlGaAs to modify the modal refractive indices and the evanescent coupling between the waveguides in situ and in a reconfigurable manner.

Such tailoring of the lattice Hamiltonian is particularly interesting for the simulation of two classes of phenomena. First, we can simulate for instance Anderson-type localization in disordered systems (see section 3.2.2.3) of correlated particles, by introducing controlled disorder either in the on-site energies or in the coupling between the sites. While the parameters of the Hamiltonian are difficult to control and access in typical electronic systems, waveguide arrays constitute a flexible and reconfigurable platform for the study of localization phenomena in a controlled setting. Studying the effect of disorder in nonlinear waveguide arrays also offers the interest to investigate two-particle (rather than single-particle) localization problems, and also the possibility to study the interplay between the localization phenomenon and the nonlinear resonances of the system, further enriching the study compared to the usual condensed-matter situation.

Secondly, control over the parameters of the Hamiltonian can enable the simulation of topological behaviours of photons in the waveguide array. Topological effects have been investigated heavily in the recent years, both in solid-state systems in which the effects were originally discovered, enabling the realization of topological insulators that can support electrical edge currents without dissipation [180], and in classical photonics [181–183], where they enable the propagation of disorder-independent edge modes without back-scattering [184]. Recent photonics experiment have focused on the study of topological effects in the quantum regime [82, 83, 185] and nonlinear waveguide arrays have been proposed as a platform to harness topological effects [82, 83, 186, 187].

The simplest Hamiltonian presenting topological properties is the Su-Schrieffer-Heeger Hamiltonian [171], which is a tight-binding Hamiltonian with alternate values of the coupling between the two sites. If a structural defect is introduced in the chain (for instance by setting two successive high values of the coupling constant instead of perfect alternance) then an interface between two distinct topological phases is created, leading to the emergence of a topologically protected edge state.

This type of Hamiltonians is straightforward to simulate using waveguide arrays: by alternating long and short gaps between the waveguides at the fabrication stage (figure 5.11a), we can modulate the coupling constant from high to low values. In this case, the inclusion of a topological defect leads to a topological mode that localizes the propagation of photons at the interface (figure 5.11b), and both the existence and propagation constant of this topological mode are protected against disorder[11]. Waveguide arrays thus offer the

[11]More precisely against off-diagonal disorder, i.e. disorder in the tunnel couplings, and within the limit of the extension of the topological band gap which depends on the contrast between the low and high coupling constants.

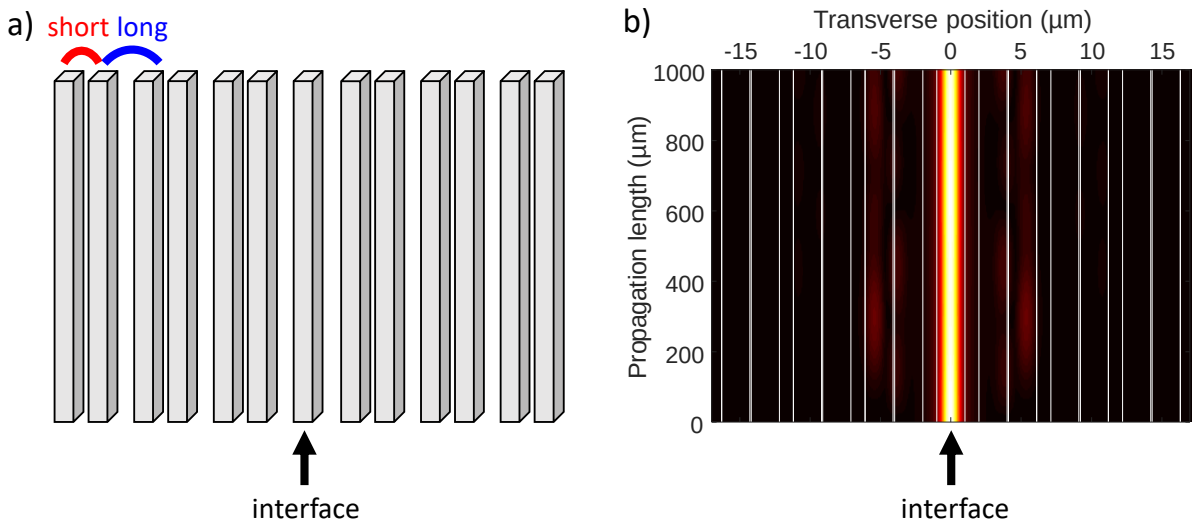

Figure 5.11: a) Scheme of a waveguide array with alternating long and short gaps and a long-long defect in the center. b) Propagation simulation of a coherent state in the topological mode located at the long-long interface in the waveguide array.

possibility to study the transition between the spatial entanglement provided by transverse propagation and the topological localization of the quantum states, as well as the entanglement between topologically protected modes and propagating modes [186]. More complex lattice geometries can also be realized using this platform, opening the path to the realization of photonic devices robust to fabrication defects and to the implementation of the protected transport of quantum states.

Conclusion

Summary of the thesis

This PhD thesis has focused on the study of two different AlGaAs-based devices for the generation of photon pairs, producing entanglement into the high-dimensional frequency and spatial degrees of freedom respectively. The two studied sources offer flexible control over the output quantum state of the photon pairs directly at the generation stage.

In the first chapter, we initially introduced the theoretical framework necessary to describe the photon pair generation in AlGaAs waveguides from the second-order nonlinear SPDC process, in particular the Joint Spectral Amplitude of the photon pairs to describe its state in the frequency degree of freedom. We then highlighted the working principles of the two studied sources.

In the second chapter, we focused on the counterpropagating source and theoretically studied the manipulation of the exchange statistics of the generated photons as well as their measurement through HOM interferometry. We then described the experimental procedure for the measurement of the Joint Spectral Intensity and of the HOM interferograms corresponding to anyonic exchange statistics. The reported measurements indeed demonstrate that control over the exchange statistics of the SPDC photons was achieved and allowed for the mimicking of anyonic behaviour in a HOM interferometer.

In the third chapter, we switched to the theoretical description of the second investigated device, which consists in an array of coupled nonlinear waveguides for the generation of spatially entangled states. We developed the theory of random quantum walks of correlated photons, and then derived the quantum state generated by SPDC in waveguide arrays. We introduced metrics to quantify the non-classicality of the produced states, and then presented various numerical simulations giving a zoology of the quantum states that can be engineered using this device, including the effects of various experimental parameters.

In the fourth chapter, we reported the design and clean-room fabrication of the samples for the experimental realization of spatially entangled photon pairs. We performed electromagnetic simulations of the structure to properly design the relevant parameters of the AlGaAs waveguide arrays and developed and optimized a fabrication process based on electron-beam lithography and ICP etching to fabricate suitable waveguide arrays, which was an important and demanding aspect of this PhD work.

Finally, in the fifth chapter, we described the experimental realization of spatially entangled photon pairs by SPDC in waveguide arrays. The measurement demonstrates enlargement of the SPDC resonance from the coupling between the waveguides, a key signature of the emergence of collective modes in the arrays. The measured spatial correlations are also in good qualitative agreement with the simulations and present strong

indications of non-classical features, which constitutes a first experimental demonstration for the on-chip generation of spatially entangled states of light using AlGaAs waveguide arrays.

The two devices that we have presented have the advantage of working at room temperature and telecom wavelength, enabling reliable long-distance transmission of the generated photon pairs into optical fibers. They present a strong potential for integration within more complex AlGaAs photonic circuits, taking advantage of the assets of this platform such as its direct band-gap for electrical injection, its high electro-optic effect and its integrability with on-chip superconducting nanowire detectors, and are thus promising candidates for the all-integrated implementation of quantum information protocols on photonic chips.

Perspectives

We conclude this manuscript by giving an outlook on the future perspectives open by the presented results.

We experimentally demonstrated the possibility to reconfigure the exchange statistics of entangled photon pairs in the frequency degree of freedom and to mimic arbitrary exchange statistics, in particular to reproduce the behaviour of anyons in a HOM setup. This could be harnessed for the realization of quantum information protocols exploiting the robustness of the braiding process to noise, such as error correction codes [146,147] and fault-tolerant topological quantum computing. The frequency degree of freedom can also be coupled to polarization by simultaneously exploiting the two interactions for type II SPDC supported by the source, enabling the generation of hybrid frequency/polarization entangled states [136]. This hybrid degree of freedom could in turn be used for the entanglement distribution to quantum systems with disparate energy levels [156] or as a resource for precise time measurements in metrology [155]. Moreover, more complex configurations of the pumping scheme could also be implemented to generate a more diverse zoology of frequency quantum states [157], with fine-patterned phase structure that can again provide a resource for quantum metrology [158, 159].

On the other hand, we have demonstrated the generation of spatially-entangled photon pairs from quantum walks in nonlinear AlGaAs waveguide arrays. In the future, this platform could be used to generate controllable spatial entanglement of photon pairs by tailoring the spatial distribution of the pump beam in the array. Waveguide arrays additionally offer a natural workbench for the quantum simulation of tight-binding Hamiltonians with controllable on-site energies and coupling rates. The parameters can either be chosen directly at the fabrication stage or dynamically varied by exploiting the electro-optic effect in AlGaAs. With accurate control over the Hamiltonian, waveguide arrays can thus enable the simulation of condensed-matter type problems such as the Anderson localization of bipartite quantum states. They also offer the possibility to simulate and exploit topological effects to realize dissipation-free optical transmission in the quantum regime [185]. Indeed, it is possible to properly engineer the coupling constants and their periodicity inside the array to simulate Hamiltonians with topological properties, such as the Su-Schrieffer-Heeger Hamiltonian [171], and to introduce a structural defect to create an interface between two distinct topological phases. This leads to the emergence of topologically protected edge states which have properties robust to disorder. Using this

scheme, waveguide arrays could be exploited to study the interplay between quantum correlations in the spatial degree of freedom and the topological protection of quantum states, especially for SPDC-generated photon pairs.

Both the counter-propagating source and the nonlinear waveguide array offer versatile generation of entangled photon pairs in a reconfigurable manner and can be integrated with photonic circuits for further manipulation of the generated photons. They offer various perspectives in terms of metrology and quantum simulation, and their development and on-chip integration constitute a step in the direction of low-footprint, chip-integrated quantum protocols for future real-world implementation of quantum information technologies.

Appendix A

List of publications

Journal articles :

- A. Raymond, S. Francesconi, J.Palomo, P. Filloux, M. Morassi, A. Lemaître, F. Raineri, M. Amanti, S. Ducci and F. Baboux, "Generation of spatially entangled states of light in nonlinear waveguide arrays", *in preparation*.
- S. Francesconi, A. Raymond, N. Fabre, A. Lemaître, M. Amanti, P. Milman, F. Baboux and S. Ducci, "On-chip generation of hybrid polarization-frequency entangled biphoton states", *preprint*.
- S. Francesconi, A. Raymond, N. Fabre, A. Lemaître, M. Amanti, P. Milman, F. Baboux and S. Ducci, "Anyonic Two-Photon Statistics with a Semiconductor Chip", *ACS Photonics*, vol. 8, no. 9, pp. 2764-2769, 2021.
- S. Francesconi, F. Baboux, A. Raymond, N. Fabre, G. Boucher, A. Lemaître, M. Amanti, P. Milman and S. Ducci, "Engineering two-photon wavefunction and exchange statistics in a semiconductor chip", *Optica*, vol. 7, no. 4, pp. 316-322, 2020.

Conference presentations :

- A. Raymond, S. Francesconi, J.Palomo, P. Filloux, M. Morassi, A. Lemaître, F. Raineri, M. Amanti, S. Ducci and F. Baboux, "Generation of spatially entangled states of light in nonlinear waveguide arrays", *contributed talk at IQFA'XIII*, Palaiseau, France, 2022.
- A. Raymond, S. Francesconi, N. Fabre, A. Lemaître, M. Amanti, P. Milman, F. Baboux and S. Ducci, "Anyonic two-photon statistics with a semiconductor chip", *contributed talk at IQFA'XII*, Lyon, France, 2021.
- A. Raymond, S. Francesconi, N. Fabre, A. Lemaître, M. Amanti, P. Milman, F. Baboux and S. Ducci, "Anyonic two-photon statistics and hybrid entanglement with a semiconductor chip", *poster presentation at Optique Dijon*, Dijon, France, 2021.

Appendix B

Derivation of the non-classicality indicator

In the context of photonic quantum walks in waveguide arrays, the definition of the correlation between waveguides is given by :

$$\Gamma_{q,r} = \langle a_r^\dagger a_q^\dagger a_r a_q \rangle \tag{B.1}$$

and its classical analog is

$$\Gamma_{q,r} = \langle A_r^* A_q^* A_r A_q \rangle = \langle |A_r|^2 |A_q|^2 \rangle \tag{B.2}$$

where the brackets denote the temporal average in the classical case, and the mean operator value in the quantum case.

The non-classicality criterion was given in [79] :

$$\Gamma_{q,r} < \frac{1}{3}\sqrt{\Gamma_{q,q}\Gamma_{r,r}}. \tag{B.3}$$

in the context of two incoherent sources injected in two different waveguides. We present here a derivation of this criterion. We assume that we inject in guide l an amplitude $A_l(t)$, and in guide $k \neq l$ an amplitude $A_k(t)$, which is incoherent with $A_l(t)$ in the sense that the temporal mean $\langle A_l^* A_k \rangle = 0$, and both with intensity $I_0 = \langle |A_l|^2 \rangle = \langle |A_k|^2 \rangle$. We additionally consider that $|A_k| = |A_l| = \sqrt{I_0}$ at all times, so that we have as well : $\langle |A_l^* A_l|^2 \rangle = \langle |A_k^* A_k|^2 \rangle = \langle |A_k^* A_l|^2 \rangle = I_0^2$.

We consider that the array makes the amplitudes evolve according to a unitary matrix U (which can be obtained through the Hamiltonian evolution in the quantum case):

$$A_i^{out} = \sum_j U_{i,j} A_j^{in} \tag{B.4}$$

If we now consider two waveguides q and r, with $q \neq r$, we have :

$$\begin{aligned} A_q(t) &= U_{q,l} A_l(t) + U_{q,k} A_k(t) \\ A_r(t) &= U_{r,l} A_l(t) + U_{r,k} A_k(t) \end{aligned} \tag{B.5}$$

where we dropped the *in* and *out* labels for clarity. We can then compute $\Gamma_{q,r}$, $\Gamma_{q,q}$ and $\Gamma_{r,r}$, starting with the product $A_q A_r$:

$$\begin{aligned} A_q(t)A_r(t) &= \left(U_{q,l}U_{r,k} + U_{r,l}U_{q,k}\right) A_l(t)A_k(t) \\ &+ U_{q,k}U_{r,k}A_k(t)^2 + U_{q,l}U_{r,l}A_l(t)^2 \end{aligned} \tag{B.6}$$

and

$$\begin{aligned} \Gamma_{q,r} &= \langle \Big(\left(U_{q,l}U_{r,k} + U_{r,l}U_{q,k}\right) A_l A_k + U_{q,k}U_{r,k}A_k^2 + U_{q,l}U_{r,l}A_l^2 \Big) \\ &\cdot \Big(\left(U_{q,l}^* U_{r,k}^* + U_{r,l}^* U_{q,k}^*\right) A_l^* A_k^* + U_{q,k}^* U_{r,k}^* A_k^{*2} + U_{q,l}^* U_{r,l}^* A_l^{*2} \Big) \rangle \\ &= \langle |U_{q,l}U_{r,k} + U_{r,l}U_{q,k}|^2 |A_l(t)A_k(t)|^2 + |U_{q,l}U_{r,l}|^2 \left(A_l^* A_l\right)^2 + |U_{q,k}U_{r,k}|^2 \left(A_k^* A_k\right)^2 \rangle \\ &+ \langle \left(U_{q,l}U_{r,k} + U_{r,l}U_{q,k}\right) A_l A_k U_{q,k}^* U_{r,k}^* A_k^{*2} + \left(U_{q,l}U_{r,k} + U_{r,l}U_{q,k}\right) A_l A_k U_{q,l}^* U_{r,l}^* A_l^{*2} \\ &+ U_{q,k}U_{r,k}A_k^2 U_{q,l}^* U_{r,l}^* A_l^{*2} + \textbf{c.c.} \rangle \end{aligned} \tag{B.7}$$

where **c.c.** denotes the complex conjugate. The second term in the last equality is made up of incoherent terms, with incoherent phases, so that its temporal average is zero. Then we simply get

$$\Gamma_{q,r} = I_0^2 \left(|U_{q,l}U_{r,k} + U_{r,l}U_{q,k}|^2 + |U_{q,l}U_{r,l}|^2 + |U_{q,k}U_{r,k}|^2 \right) \tag{B.8}$$

Through similar computations, one can get :

$$\begin{aligned} \Gamma_{q,q} &= I_0^2 \left(4|U_{q,l}U_{q,k}|^2 + |U_{q,l}U_{q,l}|^2 + |U_{q,k}U_{q,k}|^2 \right) \\ \Gamma_{r,r} &= I_0^2 \left(4|U_{r,l}U_{r,k}|^2 + |U_{r,l}U_{r,l}|^2 + |U_{r,k}U_{r,k}|^2 \right) \end{aligned} \tag{B.9}$$

We now define

$$\begin{aligned} a &= U_{q,l} \\ b &= U_{r,k} \\ c &= U_{q,k} \\ d &= U_{r,l} \end{aligned} \tag{B.10}$$

which yields, if we divide by I_0^2

$$\begin{aligned} \Gamma_{q,r} &= |ab + cd|^2 + |ad|^2 + |cb|^2 \\ \Gamma_{q,q} &= 4|ac|^2 + |a^2|^2 + |c^2|^2 \\ \Gamma_{r,r} &= 4|bd|^2 + |b^2|^2 + |d^2|^2 \end{aligned} \tag{B.11}$$

We now want to demonstrate that $\sqrt{\Gamma_{q,q}\Gamma_{r,r}} \leq 3\Gamma_{q,r}$. For this, we notice that

$$\begin{aligned} \Gamma_{q,q}\Gamma_{r,r} &= \Big(\left(|a|^2 + |c|^2\right)^2 + 2|ac|^2 \Big) \Big(\left(|b|^2 + |d|^2\right)^2 + 2|bd|^2 \Big) \\ &\leq \frac{3}{2}^2 \left(|a|^2 + |c|^2\right)^2 \left(|b|^2 + |d|^2\right)^2 \end{aligned} \tag{B.12}$$

since $2AB \leq \frac{1}{2}(A+B)^2$ for any A, B real from remarkable identities. Taking the square root of the inequality, one gets :

$$
\begin{aligned}
\sqrt{\Gamma_{q,q}\Gamma_{r,r}} &\leq \frac{3}{2}\left(|a|^2+|c|^2\right)\left(|b|^2+|d|^2\right) \\
&= \frac{3}{2}\left(|ab|^2+|ad|^2+|bc|^2+|cd|^2\right) \\
&\leq \frac{3}{2}\left(|ab|^2+|cd|^2\ +|bc|^2+|ad|^2\right)+\frac{3}{2}\left(|bc|^2+|ad|^2-2|abcd|\right) \\
&= 3\left(|bc|^2+|ad|^2\right)+\frac{3}{2}||ab|-|cd||^2 \\
&\leq 3\left(|bc|^2+|ad|^2\right)+3||ab|-|cd||^2 \\
&\leq 3\left(|bc|^2+|ad|^2\right)+3|ab+cd|^2 \\
&= 3\Gamma_{q,r}
\end{aligned}
\tag{B.13}
$$

where the lasts inequality simply stems from $|A+B| > ||A|-|B||$, which establishes the inequality used in [79]. We thank Y. Bromberg for fruitful discussion on this topic.

References

[1] J. S. Bell, "On the Einstein Podolsky Rosen paradox," *Physics Physique Fizika*, vol. 1, no. 3, p. 195, 1964. (Cited on page 13.)

[2] A. Aspect, P. Grangier, and G. Roger, "Experimental tests of realistic local theories via Bell's theorem," *Physical review letters*, vol. 47, no. 7, p. 460, 1981. (Cited on page 13.)

[3] A. Einstein, B. Podolsky, and N. Rosen, "Can quantum-mechanical description of physical reality be considered complete?," *Physical review*, vol. 47, no. 10, p. 777, 1935. (Cited on page 13.)

[4] R. P. Feynman, ""simulating physics with quantum computers"," *Inernational Journal of Theoretical Physics*, vol. 21, no. 7, 1982. (Cited on page 13.)

[5] G. Brassard and C. Bennett, "Quantum cryptography: Public key distribution and coin tossing," in *International conference on computers, systems and signal processing*, 1984. (Cited on page 13.)

[6] C. H. Bennett, G. Brassard, and N. D. Mermin, "Quantum cryptography without Bell's theorem," *Physical review letters*, vol. 68, no. 5, p. 557, 1992. (Cited on page 13.)

[7] D. Deutsch and R. Jozsa, "Rapid solution of problems by quantum computation," *Proceedings of the Royal Society of London. Series A: Mathematical and Physical Sciences*, vol. 439, no. 1907, pp. 553–558, 1992. (Cited on page 13.)

[8] P. W. Shor, "Algorithms for quantum computation: discrete logarithms and factoring," in *Proceedings 35th annual symposium on foundations of computer science*, pp. 124–134, Ieee, 1994. (Cited on page 13.)

[9] L. K. Grover, "A fast quantum mechanical algorithm for database search," in *Proceedings of the twenty-eighth annual ACM symposium on Theory of computing*, pp. 212–219, 1996. (Cited on page 13.)

[10] F. Arute, K. Arya, R. Babbush, D. Bacon, J. C. Bardin, R. Barends, R. Biswas, S. Boixo, F. G. Brandao, D. A. Buell, *et al.*, "Quantum supremacy using a programmable superconducting processor," *Nature*, vol. 574, no. 7779, pp. 505–510, 2019. (Cited on pages 13 and 14.)

[11] K. Satzinger, Y.-J. Liu, A. Smith, C. Knapp, M. Newman, C. Jones, Z. Chen, C. Quintana, X. Mi, A. Dunsworth, *et al.*, "Realizing topologically ordered states on a quantum processor," *Science*, vol. 374, no. 6572, pp. 1237–1241, 2021. (Cited on page 13.)

[12] S. Geyer, L. C. Camenzind, L. Czornomaz, V. Deshpande, A. Fuhrer, R. J. Warburton, D. M. Zumbühl, and A. V. Kuhlmann, "Self-aligned gates for scalable silicon quantum computing," *Applied Physics Letters*, vol. 118, no. 10, p. 104004, 2021. (Cited on page 13.)

[13] L. S. Madsen, F. Laudenbach, M. F. Askarani, F. Rortais, T. Vincent, J. F. Bulmer, F. M. Miatto, L. Neuhaus, L. G. Helt, M. J. Collins, *et al.*, "Quantum computational advantage with a programmable photonic processor," *Nature*, vol. 606, no. 7912, pp. 75–81, 2022. (Cited on page 13.)

[14] D. P. DiVincenzo, "The physical implementation of quantum computation," *Fortschritte der Physik: Progress of Physics*, vol. 48, no. 9-11, pp. 771–783, 2000. (Cited on page 13.)

[15] J. Dalibard, S. Reynaud, and C. Cohen-Tannoudji, "Potentialities of a new σ+-σ-laser configuration for radiative cooling and trapping," *Journal of Physics B: Atomic and Molecular Physics (1968-1987)*, vol. 17, no. 22, p. 4577, 1984. (Cited on page 13.)

[16] A. Ashkin, J. M. Dziedzic, J. E. Bjorkholm, and S. Chu, "Observation of a single-beam gradient force optical trap for dielectric particles," *Optics letters*, vol. 11, no. 5, pp. 288–290, 1986. (Cited on page 13.)

[17] K. Kiepenheuer, "Über zählrohre für das sichtbare spektralgebiet," *Zeitschrift für Physik*, vol. 107, no. 3, pp. 145–152, 1937. (Cited on page 13.)

[18] J. S. Allen, "The detection of single positive ions, electrons and photons by a secondary electron multiplier," *Physical Review*, vol. 55, no. 10, p. 966, 1939. (Cited on page 13.)

[19] D. E. Groom, "Silicon photodiode detection of bismuth germanate scintillation light," *Nuclear Instruments and Methods in Physics Research*, vol. 219, no. 1, pp. 141–148, 1984. (Cited on page 13.)

[20] M. Saffman, "Quantum computing with atomic qubits and rydberg interactions: progress and challenges," *Journal of Physics B: Atomic, Molecular and Optical Physics*, vol. 49, no. 20, p. 202001, 2016. (Cited on page 13.)

[21] C. D. Bruzewicz, J. Chiaverini, R. McConnell, and J. M. Sage, "Trapped-ion quantum computing: Progress and challenges," *Applied Physics Reviews*, vol. 6, no. 2, p. 021314, 2019. (Cited on page 13.)

[22] I. Bloch, J. Dalibard, and S. Nascimbene, "Quantum simulations with ultracold quantum gases," *Nature Physics*, vol. 8, no. 4, pp. 267–276, 2012. (Cited on page 14.)

[23] C. Gross and I. Bloch, "Quantum simulations with ultracold atoms in optical lattices," *Science*, vol. 357, no. 6355, pp. 995–1001, 2017. (Cited on page 14.)

[24] C. Monroe, D. M. Meekhof, B. E. King, W. M. Itano, and D. J. Wineland, "Demonstration of a fundamental quantum logic gate," *Physical review letters*, vol. 75, no. 25, p. 4714, 1995. (Cited on page 14.)

[25] S. Gulde, H. Häffner, M. Riebe, G. Lancaster, C. Becher, J. Eschner, F. Schmidt-Kaler, I. Chuang, and R. Blatt, "Quantum information processing with trapped ca+ ions," *Philosophical Transactions of the Royal Society of London. Series A: Mathematical, Physical and Engineering Sciences*, vol. 361, no. 1808, pp. 1363–1374, 2003. (Cited on page 14.)

[26] P. Schindler, D. Nigg, T. Monz, J. T. Barreiro, E. Martinez, S. X. Wang, S. Quint, M. F. Brandl, V. Nebendahl, C. F. Roos, *et al.*, "A quantum information processor with trapped ions," *New Journal of Physics*, vol. 15, no. 12, p. 123012, 2013. (Cited on page 14.)

[27] D. Loss and D. P. DiVincenzo, "Quantum computation with quantum dots," *Physical Review A*, vol. 57, no. 1, p. 120, 1998. (Cited on page 14.)

[28] L. Childress and R. Hanson, "Diamond nv centers for quantum computing and quantum networks," *MRS bulletin*, vol. 38, no. 2, pp. 134–138, 2013. (Cited on page 14.)

[29] C. Kloeffel and D. Loss, "Prospects for spin-based quantum computing in quantum dots," *Annu. Rev. Condens. Matter Phys.*, vol. 4, no. 1, pp. 51–81, 2013. (Cited on page 14.)

[30] J. Zhang, S. S. Hegde, and D. Suter, "Efficient implementation of a quantum algorithm in a single nitrogen-vacancy center of diamond," *Physical Review Letters*, vol. 125, no. 3, p. 030501, 2020. (Cited on page 14.)

[31] W. Yang, Z. Yin, Y. Hu, M. Feng, and J. Du, "High-fidelity quantum memory using nitrogen-vacancy center ensemble for hybrid quantum computation," *Physical Review A*, vol. 84, no. 1, p. 010301, 2011. (Cited on page 14.)

[32] K. Heshami, C. Santori, B. Khanaliloo, C. Healey, V. M. Acosta, P. E. Barclay, and C. Simon, "Raman quantum memory based on an ensemble of nitrogen-vacancy centers coupled to a microcavity," *Physical Review A*, vol. 89, no. 4, p. 040301, 2014. (Cited on page 14.)

[33] M. Kjaergaard, M. E. Schwartz, J. Braumüller, P. Krantz, J. I.-J. Wang, S. Gustavsson, and W. D. Oliver, "Superconducting qubits: Current state of play," *Annual Review of Condensed Matter Physics*, vol. 11, pp. 369–395, 2020. (Cited on page 14.)

[34] Y. Nakamura, Y. A. Pashkin, and J. Tsai, "Coherent control of macroscopic quantum states in a single-cooper-pair box," *nature*, vol. 398, no. 6730, pp. 786–788, 1999. (Cited on page 14.)

[35] T. Orlando, J. Mooij, L. Tian, C. H. Van Der Wal, L. Levitov, S. Lloyd, and J. Mazo, "Superconducting persistent-current qubit," *Physical Review B*, vol. 60, no. 22, p. 15398, 1999. (Cited on page 14.)

[36] J. M. Martinis, "Superconducting phase qubits," *Quantum information processing*, vol. 8, no. 2, pp. 81–103, 2009. (Cited on page 14.)

[37] J. Plantenberg, P. De Groot, C. Harmans, and J. Mooij, "Demonstration of controlled-not quantum gates on a pair of superconducting quantum bits," *Nature*, vol. 447, no. 7146, pp. 836–839, 2007. (Cited on page 14.)

[38] N. Gisin and R. Thew, "Quantum communication," *Nature photonics*, vol. 1, no. 3, pp. 165–171, 2007. (Cited on page 14.)

[39] S.-K. Liao, W.-Q. Cai, W.-Y. Liu, L. Zhang, Y. Li, J.-G. Ren, J. Yin, Q. Shen, Y. Cao, Z.-P. Li, *et al.*, "Satellite-to-ground quantum key distribution," *Nature*, vol. 549, no. 7670, pp. 43–47, 2017. (Cited on page 14.)

[40] F. Flamini, N. Spagnolo, and F. Sciarrino, "Photonic quantum information processing: a review," *Reports on Progress in Physics*, vol. 82, no. 1, p. 016001, 2018. (Cited on page 14.)

[41] E. Knill, R. Laflamme, and G. J. Milburn, "A scheme for efficient quantum computation with linear optics," *nature*, vol. 409, no. 6816, pp. 46–52, 2001. (Cited on page 14.)

[42] R. Raussendorf and H. J. Briegel, "A one-way quantum computer," *Physical review letters*, vol. 86, no. 22, p. 5188, 2001. (Cited on page 14.)

[43] N. Spagnolo, C. Vitelli, M. Bentivegna, D. J. Brod, A. Crespi, F. Flamini, S. Giacomini, G. Milani, R. Ramponi, P. Mataloni, *et al.*, "Experimental validation of photonic boson sampling," *Nature Photonics*, vol. 8, no. 8, pp. 615–620, 2014. (Cited on pages 14 and 16.)

[44] C. Sparrow, E. Martín-López, N. Maraviglia, A. Neville, C. Harrold, J. Carolan, Y. N. Joglekar, T. Hashimoto, N. Matsuda, J. L. O'Brien, *et al.*, "Simulating the vibrational quantum dynamics of molecules using photonics," *Nature*, vol. 557, no. 7707, pp. 660–667, 2018. (Cited on page 14.)

[45] C.-Y. Lu, D. E. Browne, T. Yang, and J.-W. Pan, "Demonstration of a compiled version of shor's quantum factoring algorithm using photonic qubits," *Physical Review Letters*, vol. 99, no. 25, p. 250504, 2007. (Cited on page 14.)

[46] A. Politi, J. C. Matthews, and J. L. O'brien, "Shor's quantum factoring algorithm on a photonic chip," *Science*, vol. 325, no. 5945, pp. 1221–1221, 2009. (Cited on pages 14 and 59.)

[47] J. Aasi, J. Abadie, B. Abbott, R. Abbott, T. Abbott, M. Abernathy, C. Adams, T. Adams, P. Addesso, R. Adhikari, *et al.*, "Enhanced sensitivity of the ligo gravitational wave detector by using squeezed states of light," *Nature Photonics*, vol. 7, no. 8, pp. 613–619, 2013. (Cited on page 14.)

[48] H. Grote, K. Danzmann, K. Dooley, R. Schnabel, J. Slutsky, and H. Vahlbruch, "First long-term application of squeezed states of light in a gravitational-wave observatory," *Physical review letters*, vol. 110, no. 18, p. 181101, 2013. (Cited on page 14.)

[49] V. Giovannetti, S. Lloyd, and L. Maccone, "Advances in quantum metrology," *Nature photonics*, vol. 5, no. 4, pp. 222–229, 2011. (Cited on page 14.)

[50] K. R. Motes, J. P. Olson, E. J. Rabeaux, J. P. Dowling, S. J. Olson, and P. P. Rohde, "Linear optical quantum metrology with single photons: exploiting spontaneously generated entanglement to beat the shot-noise limit," *Physical review letters*, vol. 114, no. 17, p. 170802, 2015. (Cited on page 14.)

[51] X. Guo, C. R. Breum, J. Borregaard, S. Izumi, M. V. Larsen, T. Gehring, M. Christandl, J. S. Neergaard-Nielsen, and U. L. Andersen, "Distributed quantum sensing in a continuous-variable entangled network," *Nature Physics*, vol. 16, no. 3, pp. 281–284, 2020. (Cited on page 14.)

[52] H. J. Kimble, "The quantum internet," *Nature*, vol. 453, no. 7198, pp. 1023–1030, 2008. (Cited on page 14.)

[53] S. Wehner, D. Elkouss, and R. Hanson, "Quantum internet: A vision for the road ahead," *Science*, vol. 362, no. 6412, p. eaam9288, 2018. (Cited on page 14.)

[54] D. F. Walls, "Squeezed states of light," *nature*, vol. 306, no. 5939, pp. 141–146, 1983. (Cited on page 14.)

[55] R. Slusher, L. Hollberg, B. Yurke, J. Mertz, and J. Valley, "Observation of squeezed states generated by four-wave mixing in an optical cavity," *Physical review letters*, vol. 55, no. 22, p. 2409, 1985. (Cited on pages 14 and 15.)

[56] S. L. Braunstein and P. Van Loock, "Quantum information with continuous variables," *Reviews of modern physics*, vol. 77, no. 2, p. 513, 2005. (Cited on page 14.)

[57] U. L. Andersen, G. Leuchs, and C. Silberhorn, "Continuous-variable quantum information processing," *Laser & Photonics Reviews*, vol. 4, no. 3, pp. 337–354, 2010. (Cited on page 14.)

[58] Y.-H. Kim, S. P. Kulik, and Y. Shih, "Quantum teleportation of a polarization state with a complete bell state measurement," *Physical Review Letters*, vol. 86, no. 7, p. 1370, 2001. (Cited on page 14.)

[59] C. Ma, W. D. Sacher, Z. Tang, J. C. Mikkelsen, Y. Yang, F. Xu, T. Thiessen, H.-K. Lo, and J. K. Poon, "Silicon photonic transmitter for polarization-encoded quantum key distribution," *Optica*, vol. 3, no. 11, pp. 1274–1278, 2016. (Cited on page 14.)

[60] P. Walther, K. J. Resch, T. Rudolph, E. Schenck, H. Weinfurter, V. Vedral, M. Aspelmeyer, and A. Zeilinger, "Experimental one-way quantum computing," *Nature*, vol. 434, no. 7030, pp. 169–176, 2005. (Cited on page 14.)

[61] R. Prevedel, P. Walther, F. Tiefenbacher, P. Böhi, R. Kaltenbaek, T. Jennewein, and A. Zeilinger, "High-speed linear optics quantum computing using active feed-forward," *Nature*, vol. 445, no. 7123, pp. 65–69, 2007. (Cited on page 14.)

[62] S. Barz, I. Kassal, M. Ringbauer, Y. O. Lipp, B. Dakić, A. Aspuru-Guzik, and P. Walther, "A two-qubit photonic quantum processor and its application to solving systems of linear equations," *Scientific reports*, vol. 4, no. 1, pp. 1–5, 2014. (Cited on page 14.)

[63] L. Sansoni, F. Sciarrino, G. Vallone, P. Mataloni, A. Crespi, R. Ramponi, and R. Osellame, "Two-particle bosonic-fermionic quantum walk via integrated photonics," *Physical review letters*, vol. 108, no. 1, p. 010502, 2012. (Cited on pages 14 and 57.)

[64] J. C. Matthews, K. Poulios, J. D. Meinecke, A. Politi, A. Peruzzo, N. Ismail, K. Wörhoff, M. G. Thompson, and J. L. O'Brien, "Observing fermionic statistics with photons in arbitrary processes," *Scientific reports*, vol. 3, no. 1, pp. 1–7, 2013. (Cited on pages 14 and 57.)

[65] I. Ali-Khan, C. J. Broadbent, and J. C. Howell, "Large-alphabet quantum key distribution using energy-time entangled bipartite states," *Physical review letters*, vol. 98, no. 6, p. 060503, 2007. (Cited on page 14.)

[66] D. Cozzolino, B. Da Lio, D. Bacco, and L. K. Oxenløwe, "High-dimensional quantum communication: benefits, progress, and future challenges," *Advanced Quantum Technologies*, vol. 2, no. 12, p. 1900038, 2019. (Cited on pages 14 and 15.)

[67] B. P. Lanyon, M. Barbieri, M. P. Almeida, T. Jennewein, T. C. Ralph, K. J. Resch, G. J. Pryde, J. L. O'brien, A. Gilchrist, and A. G. White, "Simplifying quantum logic using higher-dimensional hilbert spaces," *Nature Physics*, vol. 5, no. 2, pp. 134–140, 2009. (Cited on page 14.)

[68] Y. Wang, Z. Hu, B. C. Sanders, and S. Kais, "Qudits and high-dimensional quantum computing," *Frontiers in Physics*, vol. 8, p. 589504, 2020. (Cited on page 14.)

[69] M. Erhard, R. Fickler, M. Krenn, and A. Zeilinger, "Twisted photons: new quantum perspectives in high dimensions," *Light: Science & Applications*, vol. 7, no. 3, pp. 17146–17146, 2018. (Cited on page 14.)

[70] M. Krenn, R. Fickler, M. Fink, J. Handsteiner, M. Malik, T. Scheidl, R. Ursin, and A. Zeilinger, "Communication with spatially modulated light through turbulent air across vienna," *New Journal of Physics*, vol. 16, no. 11, p. 113028, 2014. (Cited on page 15.)

[71] M. Mirhosseini, O. S. Magaña-Loaiza, M. N. O'Sullivan, B. Rodenburg, M. Malik, M. P. Lavery, M. J. Padgett, D. J. Gauthier, and R. W. Boyd, "High-dimensional quantum cryptography with twisted light," *New Journal of Physics*, vol. 17, no. 3, p. 033033, 2015. (Cited on page 15.)

[72] I. Marcikic, H. De Riedmatten, W. Tittel, H. Zbinden, and N. Gisin, "Long-distance teleportation of qubits at telecommunication wavelengths," *Nature*, vol. 421, no. 6922, pp. 509–513, 2003. (Cited on page 15.)

[73] O. Landry, J. A. W. van Houwelingen, A. Beveratos, H. Zbinden, and N. Gisin, "Quantum teleportation over the swisscom telecommunication network," *JOSA B*, vol. 24, no. 2, pp. 398–403, 2007. (Cited on page 15.)

[74] A. Boaron, G. Boso, D. Rusca, C. Vulliez, C. Autebert, M. Caloz, M. Perrenoud, G. Gras, F. Bussières, M.-J. Li, *et al.*, "Secure quantum key distribution over 421 km of optical fiber," *Physical review letters*, vol. 121, no. 19, p. 190502, 2018. (Cited on page 15.)

[75] N. T. Islam, C. C. W. Lim, C. Cahall, B. Qi, J. Kim, and D. J. Gauthier, "Scalable high-rate, high-dimensional time-bin encoding quantum key distribution," *Quantum Science and Technology*, vol. 4, no. 3, p. 035008, 2019. (Cited on page 15.)

[76] L. Olislager, E. Woodhead, K. P. Huy, J.-M. Merolla, P. Emplit, and S. Massar, "Creating and manipulating entangled optical qubits in the frequency domain," *Physical Review A*, vol. 89, no. 5, p. 052323, 2014. (Cited on page 15.)

[77] M. Kues, C. Reimer, P. Roztocki, L. R. Cortés, S. Sciara, B. Wetzel, Y. Zhang, A. Cino, S. T. Chu, B. E. Little, *et al.*, "On-chip generation of high-dimensional entangled quantum states and their coherent control," *Nature*, vol. 546, no. 7660, pp. 622–626, 2017. (Cited on page 15.)

[78] J. Cussey, F. Patois, N. Pelloquin, and J.-M. Merolla, "High frequency spectral domain qkd architecture with dispersion management for wdm network," in *Optical Fiber Communication Conference*, p. OWJ3, Optica Publishing Group, 2008. (Cited on page 15.)

[79] Y. Bromberg, Y. Lahini, R. Morandotti, and Y. Silberberg, "Quantum and classical correlations in waveguide lattices," *Physical review letters*, vol. 102, no. 25, p. 253904, 2009. (Cited on pages 15, 69, 70, 83, 147, and 149.)

[80] A. S. Solntsev, A. A. Sukhorukov, D. N. Neshev, and Y. S. Kivshar, "Spontaneous parametric down-conversion and quantum walks in arrays of quadratic nonlinear waveguides," *Physical Review Letters*, vol. 108, no. 2, p. 023601, 2012. (Cited on pages 15, 70, and 71.)

[81] A. Crespi, R. Osellame, R. Ramponi, V. Giovannetti, R. Fazio, L. Sansoni, F. De Nicola, F. Sciarrino, and P. Mataloni, "Anderson localization of entangled photons in an integrated quantum walk," *Nature Photonics*, vol. 7, no. 4, pp. 322–328, 2013. (Cited on pages 15, 16, 17, 59, 60, 105, and 168.)

[82] A. Blanco-Redondo, B. Bell, D. Oren, B. J. Eggleton, and M. Segev, "Topological protection of biphoton states," *Science*, vol. 362, no. 6414, pp. 568–571, 2018. (Cited on pages 15, 59, 80, 82, and 138.)

[83] J.-L. Tambasco, G. Corrielli, R. J. Chapman, A. Crespi, O. Zilberberg, R. Osellame, and A. Peruzzo, "Quantum interference of topological states of light," *Science advances*, vol. 4, no. 9, p. eaat3187, 2018. (Cited on pages 15 and 138.)

[84] J. Carolan, C. Harrold, C. Sparrow, E. Martín-López, N. J. Russell, J. W. Silverstone, P. J. Shadbolt, N. Matsuda, M. Oguma, M. Itoh, *et al.*, "Universal linear optics," *Science*, vol. 349, no. 6249, pp. 711–716, 2015. (Cited on page 15.)

[85] J. Wang, S. Paesani, Y. Ding, R. Santagati, P. Skrzypczyk, A. Salavrakos, J. Tura, R. Augusiak, L. Mančinska, D. Bacco, *et al.*, "Multidimensional quantum entanglement with large-scale integrated optics," *Science*, vol. 360, no. 6386, pp. 285–291, 2018. (Cited on page 15.)

[86] P. G. Kwiat, K. Mattle, H. Weinfurter, A. Zeilinger, A. V. Sergienko, and Y. Shih, "New high-intensity source of polarization-entangled photon pairs," *Physical Review Letters*, vol. 75, no. 24, p. 4337, 1995. (Cited on pages 15 and 31.)

[87] C. Kurtsiefer, M. Oberparleiter, and H. Weinfurter, "High-efficiency entangled photon pair collection in type-ii parametric fluorescence," *Physical Review A*, vol. 64, no. 2, p. 023802, 2001. (Cited on page 15.)

[88] L.-A. Wu, M. Xiao, and H. Kimble, "Squeezed states of light from an optical parametric oscillator," *JOSA B*, vol. 4, no. 10, pp. 1465–1475, 1987. (Cited on page 15.)

[89] C. H. Bennett, F. Bessette, G. Brassard, L. Salvail, and J. Smolin, "Experimental quantum cryptography," *Journal of cryptology*, vol. 5, no. 1, pp. 3–28, 1992. (Cited on page 15.)

[90] D. Bouwmeester, J.-W. Pan, K. Mattle, M. Eibl, H. Weinfurter, and A. Zeilinger, "Experimental quantum teleportation," *Nature*, vol. 390, no. 6660, pp. 575–579, 1997. (Cited on page 15.)

[91] D. Boschi, S. Branca, F. De Martini, L. Hardy, and S. Popescu, "Experimental realization of teleporting an unknown pure quantum state via dual classical and einstein-podolsky-rosen channels," *Physical Review Letters*, vol. 80, no. 6, p. 1121, 1998. (Cited on page 15.)

[92] S. Clemmen, K. P. Huy, W. Bogaerts, R. G. Baets, P. Emplit, and S. Massar, "Continuous wave photon pair generation in silicon-on-insulator waveguides and ring resonators," *Optics express*, vol. 17, no. 19, pp. 16558–16570, 2009. (Cited on page 15.)

[93] X. Qiang, X. Zhou, J. Wang, C. M. Wilkes, T. Loke, S. O'Gara, L. Kling, G. D. Marshall, R. Santagati, T. C. Ralph, *et al.*, "Large-scale silicon quantum photonics implementing arbitrary two-qubit processing," *Nature photonics*, vol. 12, no. 9, pp. 534–539, 2018. (Cited on page 15.)

[94] W. H. Pernice, C. Schuck, O. Minaeva, M. Li, G. Goltsman, A. Sergienko, and H. Tang, "High-speed and high-efficiency travelling wave single-photon detectors embedded in nanophotonic circuits," *Nature communications*, vol. 3, no. 1, pp. 1–10, 2012. (Cited on page 15.)

[95] J. F. Bauters, M. J. Heck, D. D. John, J. S. Barton, C. M. Bruinink, A. Leinse, R. G. Heideman, D. J. Blumenthal, and J. E. Bowers, "Planar waveguides with less than 0.1 db/m propagation loss fabricated with wafer bonding," *Optics express*, vol. 19, no. 24, pp. 24090–24101, 2011. (Cited on page 15.)

[96] A. Politi, M. J. Cryan, J. G. Rarity, S. Yu, and J. L. O'brien, "Silica-on-silicon waveguide quantum circuits," *Science*, vol. 320, no. 5876, pp. 646–649, 2008. (Cited on page 15.)

[97] C. Taballione, T. A. Wolterink, J. Lugani, A. Eckstein, B. A. Bell, R. Grootjans, I. Visscher, D. Geskus, C. G. Roeloffzen, J. J. Renema, *et al.*, "8× 8 reconfigurable quantum photonic processor based on silicon nitride waveguides," *Optics express*, vol. 27, no. 19, pp. 26842–26857, 2019. (Cited on page 16.)

[98] J. M. Arrazola, V. Bergholm, K. Brádler, T. R. Bromley, M. J. Collins, I. Dhand, A. Fumagalli, T. Gerrits, A. Goussev, L. G. Helt, *et al.*, "Quantum circuits with many photons on a programmable nanophotonic chip," *Nature*, vol. 591, no. 7848, pp. 54–60, 2021. (Cited on page 16.)

[99] P. Imany, J. A. Jaramillo-Villegas, O. D. Odele, K. Han, D. E. Leaird, J. M. Lukens, P. Lougovski, M. Qi, and A. M. Weiner, "50-ghz-spaced comb of high-dimensional frequency-bin entangled photons from an on-chip silicon nitride microresonator," *Optics express*, vol. 26, no. 2, pp. 1825–1840, 2018. (Cited on page 16.)

[100] A. Peruzzo, M. Lobino, J. C. Matthews, N. Matsuda, A. Politi, K. Poulios, X.-Q. Zhou, Y. Lahini, N. Ismail, K. Wörhoff, *et al.*, "Quantum walks of correlated photons," *Science*, vol. 329, no. 5998, pp. 1500–1503, 2010. (Cited on pages 16, 59, 60, 70, and 168.)

[101] S. Tanzilli, H. De Riedmatten, W. Tittel, H. Zbinden, P. Baldi, M. De Micheli, D. B. Ostrowsky, and N. Gisin, "Highly efficient photon-pair source using periodically poled lithium niobate waveguide," *Electronics Letters*, vol. 37, no. 1, pp. 26–28, 2001. (Cited on page 16.)

[102] H. Jin, F. Liu, P. Xu, J. Xia, M. Zhong, Y. Yuan, J. Zhou, Y. Gong, W. Wang, and S. Zhu, "On-chip generation and manipulation of entangled photons based on reconfigurable lithium-niobate waveguide circuits," *Physical review letters*, vol. 113, no. 10, p. 103601, 2014. (Cited on page 16.)

[103] K.-H. Luo, S. Brauner, C. Eigner, P. R. Sharapova, R. Ricken, T. Meier, H. Herrmann, and C. Silberhorn, "Nonlinear integrated quantum electro-optic circuits," *Science advances*, vol. 5, no. 1, p. eaat1451, 2019. (Cited on page 16.)

[104] A. S. Solntsev, F. Setzpfandt, A. S. Clark, C. W. Wu, M. J. Collins, C. Xiong, A. Schreiber, F. Katzschmann, F. Eilenberger, R. Schiek, *et al.*, "Generation of nonclassical biphoton states through cascaded quantum walks on a nonlinear chip," *Physical Review X*, vol. 4, no. 3, p. 031007, 2014. (Cited on pages 16, 59, and 104.)

[105] F. Graffitti, D. Kundys, D. T. Reid, A. M. Brańczyk, and A. Fedrizzi, "Pure down-conversion photons through sub-coherence-length domain engineering," *Quantum Science and Technology*, vol. 2, no. 3, p. 035001, 2017. (Cited on page 16.)

[106] F. Graffitti, P. Barrow, A. Pickston, A. M. Brańczyk, and A. Fedrizzi, "Direct generation of tailored pulse-mode entanglement," *Physical Review Letters*, vol. 124, no. 5, p. 053603, 2020. (Cited on page 16.)

[107] P. Rabiei, J. Ma, S. Khan, J. Chiles, and S. Fathpour, "Heterogeneous lithium niobate photonics on silicon substrates," *Optics express*, vol. 21, no. 21, pp. 25573–25581, 2013. (Cited on page 16.)

[108] L. Lanco, S. Ducci, J.-P. Likforman, X. Marcadet, J. Van Houwelingen, H. Zbinden, G. Leo, and V. Berger, "Semiconductor waveguide source of counterpropagating twin photons," *Physical review letters*, vol. 97, no. 17, p. 173901, 2006. (Cited on page 16.)

[109] R. Horn, P. Abolghasem, B. J. Bijlani, D. Kang, A. Helmy, and G. Weihs, "Monolithic source of photon pairs," *Physical review letters*, vol. 108, no. 15, p. 153605, 2012. (Cited on page 16.)

[110] P. Sarrafi, E. Y. Zhu, K. Dolgaleva, B. M. Holmes, D. C. Hutchings, J. S. Aitchison, and L. Qian, "Continuous-wave quasi-phase-matched waveguide correlated photon pair source on a iii–v chip," *Applied Physics Letters*, vol. 103, no. 25, p. 251115, 2013. (Cited on page 16.)

[111] A. Orieux, A. Eckstein, A. Lemaître, P. Filloux, I. Favero, G. Leo, T. Coudreau, A. Keller, P. Milman, and S. Ducci, "Direct bell states generation on a iii-v semiconductor chip at room temperature," *Physical review letters*, vol. 110, no. 16, p. 160502, 2013. (Cited on page 16.)

[112] C. Autebert, N. Bruno, A. Martin, A. Lemaitre, C. G. Carbonell, I. Favero, G. Leo, H. Zbinden, and S. Ducci, "Integrated algaas source of highly indistinguishable and energy-time entangled photons," *Optica*, vol. 3, no. 2, pp. 143–146, 2016. (Cited on page 16.)

[113] P. Kultavewuti, E. Y. Zhu, L. Qian, V. Pusino, M. Sorel, and J. S. Aitchison, "Correlated photon pair generation in algaas nanowaveguides via spontaneous four-wave mixing," *Optics express*, vol. 24, no. 4, pp. 3365–3376, 2016. (Cited on page 16.)

[114] H. Mahmudlu, S. May, A. Angulo, M. Sorel, and M. Kues, "Algaas-on-insulator waveguide for highly efficient photon-pair generation via spontaneous four-wave mixing," *Optics Letters*, vol. 46, no. 5, pp. 1061–1064, 2021. (Cited on page 16.)

[115] T. J. Steiner, J. E. Castro, L. Chang, Q. Dang, W. Xie, J. Norman, J. E. Bowers, and G. Moody, "Ultrabright entangled-photon-pair generation from an al ga as-on-insulator microring resonator," *PRX Quantum*, vol. 2, no. 1, p. 010337, 2021. (Cited on page 16.)

[116] L. Monniello, C. Tonin, R. Hostein, A. Lemaitre, A. Martinez, V. Voliotis, and R. Grousson, "Excitation-induced dephasing in a resonantly driven inas/gaas quantum dot," *Physical Review Letters*, vol. 111, no. 2, p. 026403, 2013. (Cited on page 16.)

[117] N. Somaschi, V. Giesz, L. De Santis, J. Loredo, M. P. Almeida, G. Hornecker, S. L. Portalupi, T. Grange, C. Anton, J. Demory, *et al.*, "Near-optimal single-photon sources in the solid state," *Nature Photonics*, vol. 10, no. 5, pp. 340–345, 2016. (Cited on page 16.)

[118] F. Boitier, A. Orieux, C. Autebert, A. Lemaître, E. Galopin, C. Manquest, C. Sirtori, I. Favero, G. Leo, and S. Ducci, "Electrically injected photon-pair source at room temperature," *Physical review letters*, vol. 112, no. 18, p. 183901, 2014. (Cited on page 16.)

[119] Z. Yuan, B. E. Kardynal, R. M. Stevenson, A. J. Shields, C. J. Lobo, K. Cooper, N. S. Beattie, D. A. Ritchie, and M. Pepper, "Electrically driven single-photon source," *science*, vol. 295, no. 5552, pp. 102–105, 2002. (Cited on page 16.)

[120] S. Deshpande, J. Heo, A. Das, and P. Bhattacharya, "Electrically driven polarized single-photon emission from an ingan quantum dot in a gan nanowire," *Nature communications*, vol. 4, no. 1, pp. 1–8, 2013. (Cited on page 16.)

[121] D. Szymanski, B. Jones, M. Skolnick, A. Fox, D. O'Brien, T. Krauss, and J. Roberts, "Ultrafast all-optical switching in algaas photonic crystal waveguide interferometers," *Applied Physics Letters*, vol. 95, no. 14, p. 141108, 2009. (Cited on page 16.)

[122] J. Sprengers, A. Gaggero, D. Sahin, S. Jahanmirinejad, G. Frucci, F. Mattioli, R. Leoni, J. Beetz, M. Lermer, M. Kamp, *et al.*, "Waveguide superconducting single-photon detectors for integrated quantum photonic circuits," *Applied Physics Letters*, vol. 99, no. 18, p. 181110, 2011. (Cited on page 16.)

[123] M. Schwartz, E. Schmidt, U. Rengstl, F. Hornung, S. Hepp, S. L. Portalupi, K. Llin, M. Jetter, M. Siegel, and P. Michler, "Fully on-chip single-photon hanbury-brown and twiss experiment on a monolithic semiconductor–superconductor platform," *Nano Letters*, vol. 18, no. 11, pp. 6892–6897, 2018. (Cited on page 16.)

[124] V. Ansari, J. M. Donohue, B. Brecht, and C. Silberhorn, "Tailoring nonlinear processes for quantum optics with pulsed temporal-mode encodings," *Optica*, vol. 5, no. 5, pp. 534–550, 2018. (Cited on page 16.)

[125] H. G. de Chatellus, A. V. Sergienko, B. E. Saleh, M. C. Teich, and G. Di Giuseppe, "Non-collinear and non-degenerate polarization-entangled photon generation via concurrent type-i parametric downconversion in ppln," *Optics express*, vol. 14, no. 21, pp. 10060–10072, 2006. (Cited on page 31.)

[126] M. Halder, A. Beveratos, R. T. Thew, C. Jorel, H. Zbinden, and N. Gisin, "High coherence photon pair source for quantum communication," *New Journal of Physics*, vol. 10, no. 2, p. 023027, 2008. (Cited on page 31.)

[127] M. Fiorentino, S. M. Spillane, R. G. Beausoleil, T. D. Roberts, P. Battle, and M. W. Munro, "Spontaneous parametric down-conversion in periodically poled ktp waveguides and bulk crystals," *Optics express*, vol. 15, no. 12, pp. 7479–7488, 2007. (Cited on page 31.)

[128] K. L. Vodopyanov, O. Levi, P. Kuo, T. Pinguet, J. Harris, M. Fejer, B. Gerard, L. Becouarn, and E. Lallier, "Optical parametric oscillation in quasi-phase-matched gaas," *Optics letters*, vol. 29, no. 16, pp. 1912–1914, 2004. (Cited on page 31.)

[129] J. Ota, W. Narita, I. Ohta, T. Matsushita, and T. Kondo, "Fabrication of periodically-inverted algaas waveguides for quasi-phase-matched wavelength conversion at 1.55 μm," *Japanese Journal of Applied Physics*, vol. 48, no. 4S, p. 04C110, 2009. (Cited on page 31.)

[130] E. Rafailov, P. Loza-Alvarez, C. Brown, W. Sibbett, R. De La Rue, P. Millar, D. Yanson, J. Roberts, and P. Houston, "Second-harmonic generation from a first-order quasi-phase-matched gaas/algaas waveguide crystal," *Optics Letters*, vol. 26, no. 24, pp. 1984–1986, 2001. (Cited on page 31.)

[131] P. S. Kuo, J. Bravo-Abad, and G. S. Solomon, "Second-harmonic generation using-quasi-phasematching in a gaas whispering-gallery-mode microcavity," *Nature communications*, vol. 5, no. 1, pp. 1–7, 2014. (Cited on page 31.)

[132] S. Mariani, A. Andronico, A. Lemaître, I. Favero, S. Ducci, and G. Leo, "Second-harmonic generation in algaas microdisks in the telecom range," *Optics letters*, vol. 39, no. 10, pp. 3062–3065, 2014. (Cited on page 31.)

[133] N. Morais, I. Roland, M. Ravaro, W. Hease, A. Lemaître, C. Gomez, S. Wabnitz, M. De Rosa, I. Favero, and G. Leo, "Directionally induced quasi-phase matching in homogeneous algaas waveguides," *Optics Letters*, vol. 42, no. 21, pp. 4287–4290, 2017. (Cited on page 31.)

[134] X. Caillet, *Une microcavité semiconductrice source de photons jumeaux contrapropageants à température ambiante*. PhD thesis, Université Paris Diderot, 2009. (Cited on pages 32 and 50.)

[135] G. Boucher, *Biphoton Frequency-Correlations Engineering and Measurement with a Semiconductor Microcavity*. PhD thesis, Université Paris Diderot, 2016. (Cited on pages 32 and 44.)

[136] S. Francesconi, A. Raymond, M. Amanti, A. Lemaître, P. Milman, F. Baboux, and S. Ducci, "On-chip generation of hybrid polarization-frequency entangled biphoton states," *arXiv preprint arXiv:2207.10943*, 2022. (Cited on pages 35, 57, and 142.)

[137] S. Francesconi, *On-chip generation of high-dimensional entangled states of light*. PhD thesis, Université Paris Cité, 2020. (Cited on pages 41, 44, and 52.)

[138] C.-K. Hong, Z.-Y. Ou, and L. Mandel, "Measurement of subpicosecond time intervals between two photons by interference," *Physical review letters*, vol. 59, no. 18, p. 2044, 1987. (Cited on page 46.)

[139] F. Wilczek, "Quantum mechanics of fractional-spin particles," *Physical review letters*, vol. 49, no. 14, p. 957, 1982. (Cited on page 48.)

[140] F. D. M. Haldane, "'fractional statistics''in arbitrary dimensions: a generalization of the pauli principle," *Physical review letters*, vol. 67, no. 8, p. 937, 1991. (Cited on page 48.)

[141] B. I. Halperin, "Statistics of quasiparticles and the hierarchy of fractional quantized hall states," *Physical Review Letters*, vol. 52, no. 18, p. 1583, 1984. (Cited on page 48.)

[142] D. Arovas, J. R. Schrieffer, and F. Wilczek, "Fractional statistics and the quantum hall effect," *Physical review letters*, vol. 53, no. 7, p. 722, 1984. (Cited on page 48.)

[143] H.-N. Dai, B. Yang, A. Reingruber, H. Sun, X.-F. Xu, Y.-A. Chen, Z.-S. Yuan, and J.-W. Pan, "Four-body ring-exchange interactions and anyonic statistics within a minimal toric-code hamiltonian," *Nature Physics*, vol. 13, no. 12, pp. 1195–1200, 2017. (Cited on page 48.)

[144] C. Song, D. Xu, P. Zhang, J. Wang, Q. Guo, W. Liu, K. Xu, H. Deng, K. Huang, D. Zheng, *et al.*, "Demonstration of topological robustness of anyonic braiding statistics with a superconducting quantum circuit," *Physical Review Letters*, vol. 121, no. 3, p. 030502, 2018. (Cited on page 48.)

[145] C. Liu, H.-L. Huang, C. Chen, B.-Y. Wang, X.-L. Wang, T. Yang, L. Li, N.-L. Liu, J. P. Dowling, T. Byrnes, *et al.*, "Demonstration of topologically path-independent anyonic braiding in a nine-qubit planar code," *Optica*, vol. 6, no. 3, pp. 264–268, 2019. (Cited on pages 48 and 49.)

[146] A. Y. Kitaev, "Fault-tolerant quantum computation by anyons," *Annals of Physics*, vol. 303, no. 1, pp. 2–30, 2003. (Cited on pages 49 and 142.)

[147] C. Nayak, S. H. Simon, A. Stern, M. Freedman, and S. D. Sarma, "Non-abelian anyons and topological quantum computation," *Reviews of Modern Physics*, vol. 80, no. 3, p. 1083, 2008. (Cited on pages 49 and 142.)

[148] C. Autebert, *AlGaAs photonic devices : from quantum state generation to quantum communications*. PhD thesis, Université Paris Diderot, 2016. (Cited on page 50.)

[149] I. Jizan, B. Bell, L. G. Helt, A. C. Bedoya, C. Xiong, and B. J. Eggleton, "Phase-sensitive tomography of the joint spectral amplitude of photon pair sources," *Optics letters*, vol. 41, no. 20, pp. 4803–4806, 2016. (Cited on page 52.)

[150] Y.-H. Kim and W. P. Grice, "Measurement of the spectral properties of the two-photon state generated via type ii spontaneous parametric downconversion," *Optics Letters*, vol. 30, no. 8, pp. 908–910, 2005. (Cited on page 52.)

[151] W. Wasilewski, P. Wasylczyk, P. Kolenderski, K. Banaszek, and C. Radzewicz, "Joint spectrum of photon pairs measured by coincidence fourier spectroscopy," *Optics Letters*, vol. 31, no. 8, pp. 1130–1132, 2006. (Cited on page 52.)

[152] S. Francesconi, F. Baboux, A. Raymond, N. Fabre, G. Boucher, A. Lemaitre, P. Milman, M. I. Amanti, and S. Ducci, "Engineering two-photon wavefunction and exchange statistics in a semiconductor chip," *Optica*, vol. 7, no. 4, pp. 316–322, 2020. (Cited on page 54.)

[153] J. Pachos, W. Wieczorek, C. Schmid, N. Kiesel, R. Pohlner, and H. Weinfurter, "Revealing anyonic features in a toric code quantum simulation," *New Journal of Physics*, vol. 11, no. 8, p. 083010, 2009. (Cited on page 57.)

[154] C.-Y. Lu, W.-B. Gao, O. Gühne, X.-Q. Zhou, Z.-B. Chen, and J.-W. Pan, "Demonstrating anyonic fractional statistics with a six-qubit quantum simulator," *Physical review letters*, vol. 102, no. 3, p. 030502, 2009. (Cited on page 57.)

[155] Y. Chen, M. Fink, F. Steinlechner, J. P. Torres, and R. Ursin, "Hong-ou-mandel interferometry on a biphoton beat note," *npj Quantum Information*, vol. 5, no. 1, pp. 1–6, 2019. (Cited on pages 57 and 142.)

[156] S. Olmschenk, D. Matsukevich, P. Maunz, D. Hayes, L.-M. Duan, and C. Monroe, "Quantum teleportation between distant matter qubits," *Science*, vol. 323, no. 5913, pp. 486–489, 2009. (Cited on pages 57 and 142.)

[157] G. Boucher, T. Douce, D. Bresteau, S. P. Walborn, A. Keller, T. Coudreau, S. Ducci, and P. Milman, "Toolbox for continuous-variable entanglement production and measurement using spontaneous parametric down-conversion," *Physical Review A*, vol. 92, no. 2, p. 023804, 2015. (Cited on pages 57 and 142.)

[158] W. H. Zurek, "Sub-planck structure in phase space and its relevance for quantum decoherence," *Nature*, vol. 412, no. 6848, pp. 712–717, 2001. (Cited on pages 57 and 142.)

[159] F. Toscano, D. A. Dalvit, L. Davidovich, and W. H. Zurek, "Sub-planck phase-space structures and heisenberg-limited measurements," *Physical Review A*, vol. 73, no. 2, p. 023803, 2006. (Cited on pages 57 and 142.)

[160] S. Francesconi, A. Raymond, N. Fabre, A. Lemaître, M. I. Amanti, P. Milman, F. Baboux, and S. Ducci, "Anyonic two-photon statistics with a semiconductor chip," *ACS photonics*, vol. 8, no. 9, pp. 2764–2769, 2021. (Cited on page 57.)

[161] J. Kempe, "Quantum random walks: an introductory overview," *Contemporary Physics*, vol. 44, no. 4, pp. 307–327, 2003. (Cited on page 59.)

[162] J. B. Spring, B. J. Metcalf, P. C. Humphreys, W. S. Kolthammer, X.-M. Jin, M. Barbieri, A. Datta, N. Thomas-Peter, N. K. Langford, D. Kundys, *et al.*, "Boson sampling on a photonic chip," *Science*, vol. 339, no. 6121, pp. 798–801, 2013. (Cited on page 59.)

[163] Y. Aharonov, L. Davidovich, and N. Zagury, "Quantum random walks," *Physical Review A*, vol. 48, no. 2, p. 1687, 1993. (Cited on page 59.)

[164] E. Farhi and S. Gutmann, "Quantum computation and decision trees," *Physical Review A*, vol. 58, no. 2, p. 915, 1998. (Cited on page 59.)

[165] A. Crespi, R. Osellame, R. Ramponi, D. J. Brod, E. F. Galvao, N. Spagnolo, C. Vitelli, E. Maiorino, P. Mataloni, and F. Sciarrino, "Integrated multimode interferometers with arbitrary designs for photonic boson sampling," *Nature photonics*, vol. 7, no. 7, pp. 545–549, 2013. (Cited on page 59.)

[166] S. Paesani, Y. Ding, R. Santagati, L. Chakhmakhchyan, C. Vigliar, K. Rottwitt, L. K. Oxenløwe, J. Wang, M. G. Thompson, and A. Laing, "Generation and sampling of quantum states of light in a silicon chip," *Nature Physics*, vol. 15, no. 9, pp. 925–929, 2019. (Cited on page 59.)

[167] D. N. Christodoulides, F. Lederer, and Y. Silberberg, "Discretizing light behaviour in linear and nonlinear waveguide lattices," *Nature*, vol. 424, no. 6950, pp. 817–823, 2003. (Cited on pages 59, 66, and 67.)

[168] D. Barral, K. Bencheikh, N. Belabas, and J. A. Levenson, "Zero supermode-based multipartite entanglement in χ (2) nonlinear waveguide arrays," *Physical Review A*, vol. 99, no. 5, p. 051801, 2019. (Cited on page 59.)

[169] D. Barral, M. Walschaers, K. Bencheikh, V. Parigi, J. A. Levenson, N. Treps, and N. Belabas, "Quantum state engineering in arrays of nonlinear waveguides," *Physical Review A*, vol. 102, no. 4, p. 043706, 2020. (Cited on page 59.)

[170] D. Barral, K. Bencheikh, J. A. Levenson, and N. Belabas, "Scalable multimode entanglement based on efficient squeezing of propagation eigenmodes," *Physical Review Research*, vol. 3, no. 1, p. 013068, 2021. (Cited on page 59.)

[171] W. Su, J. Schrieffer, and A. J. Heeger, "Solitons in polyacetylene," *Physical review letters*, vol. 42, no. 25, p. 1698, 1979. (Cited on pages 66, 138, and 142.)

[172] H. B. Perets, Y. Lahini, F. Pozzi, M. Sorel, R. Morandotti, and Y. Silberberg, "Realization of quantum walks with negligible decoherence in waveguide lattices," *Physical review letters*, vol. 100, no. 17, p. 170506, 2008. (Cited on page 66.)

[173] R. Kruse, F. Katzschmann, A. Christ, A. Schreiber, S. Wilhelm, K. Laiho, A. Gábris, C. S. Hamilton, I. Jex, and C. Silberhorn, "Spatio-spectral characteristics of parametric down-conversion in waveguide arrays," *New Journal of Physics*, vol. 15, no. 8, p. 083046, 2013. (Cited on page 77.)

[174] F. Setzpfandt, A. S. Solntsev, and A. A. Sukhorukov, "Nonlocal splitting of photons on a nonlinear chip," *Optics Letters*, vol. 41, no. 23, pp. 5604–5607, 2016. (Cited on page 81.)

[175] D. A. Antonosyan, A. S. Solntsev, and A. A. Sukhorukov, "Effect of loss on photon-pair generation in nonlinear waveguide arrays," *Physical Review A*, vol. 90, no. 4, p. 043845, 2014. (Cited on page 81.)

[176] A. Ekert and P. L. Knight, "Entangled quantum systems and the schmidt decomposition," *American Journal of Physics*, vol. 63, no. 5, pp. 415–423, 1995. (Cited on page 91.)

[177] P. W. Anderson, "Absence of diffusion in certain random lattices," *Physical review*, vol. 109, no. 5, p. 1492, 1958. (Cited on page 104.)

[178] Y. Lahini, A. Avidan, F. Pozzi, M. Sorel, R. Morandotti, D. N. Christodoulides, and Y. Silberberg, "Anderson localization and nonlinearity in one-dimensional disordered photonic lattices," *Physical Review Letters*, vol. 100, no. 1, p. 013906, 2008. (Cited on page 104.)

[179] Y. Bai, P. Xu, L. Lu, M. Zhong, and S. Zhu, "Two-photon anderson localization in a disordered quadratic waveguide array," *Journal of Optics*, vol. 18, no. 5, p. 055201, 2016. (Cited on page 104.)

[180] M. Z. Hasan and C. L. Kane, "Topological insulators," *Reviews of modern physics*, vol. 82, no. 4, p. 3045, 2010. (Cited on page 138.)

[181] A. Blanco-Redondo, I. Andonegui, M. J. Collins, G. Harari, Y. Lumer, M. C. Rechtsman, B. J. Eggleton, and M. Segev, "Topological optical waveguiding in silicon and the transition between topological and trivial defect states," *Physical review letters*, vol. 116, no. 16, p. 163901, 2016. (Cited on page 138.)

[182] P. St-Jean, V. Goblot, E. Galopin, A. Lemaître, T. Ozawa, L. Le Gratiet, I. Sagnes, J. Bloch, and A. Amo, "Lasing in topological edge states of a one-dimensional lattice," *Nature Photonics*, vol. 11, no. 10, pp. 651–656, 2017. (Cited on page 138.)

[183] T. Ozawa, H. M. Price, A. Amo, N. Goldman, M. Hafezi, L. Lu, M. C. Rechtsman, D. Schuster, J. Simon, O. Zilberberg, *et al.*, "Topological photonics," *Reviews of Modern Physics*, vol. 91, no. 1, p. 015006, 2019. (Cited on page 138.)

[184] Z. Wang, Y. Chong, J. D. Joannopoulos, and M. Soljačić, "Observation of unidirectional backscattering-immune topological electromagnetic states," *Nature*, vol. 461, no. 7265, pp. 772–775, 2009. (Cited on page 138.)

[185] Y. Wang, X.-L. Pang, Y.-H. Lu, J. Gao, Y.-J. Chang, L.-F. Qiao, Z.-Q. Jiao, H. Tang, and X.-M. Jin, "Topological protection of two-photon quantum correlation on a photonic chip," *Optica*, vol. 6, no. 8, pp. 955–960, 2019. (Cited on pages 138 and 142.)

[186] D. Leykam, A. S. Solntsev, A. A. Sukhorukov, and A. S. Desyatnikov, "Lattice topology and spontaneous parametric down-conversion in quadratic nonlinear waveguide arrays," *Physical Review A*, vol. 92, no. 3, p. 033815, 2015. (Cited on pages 138 and 139.)

[187] S. Mittal, V. V. Orre, E. A. Goldschmidt, and M. Hafezi, "Tunable quantum interference using a topological source of indistinguishable photon pairs," *Nature Photonics*, vol. 15, no. 7, pp. 542–548, 2021. (Cited on page 138.)

List of Figures

List of Tables